Equilibrium Phase Behavior and Mass Transport in Neutral and Oppositely Charged Polymer Assemblies

by

Ali Salehi

A dissertation submitted in partial fulfillment
of the requirements for the degree of
Doctor of Philosophy
(Chemical Engineering)
in the University of Michigan
2018

Doctoral Committee:

Professor Ronald G. Larson, Chair
Professor Sharon C. Glotzer
Professor Nicholas Kotov
Professor Katsuyo S. Thornton

Ali Salehi

salehi@umich.edu

ORCID ID: 0000-0003-3242-8186

2018

Dedicated to

My beloved parents, Bahram Salehi & Omolbanin (Mondana) Gholami, my siblings, Elaheh and Sourena Salehi.

Acknowledgments

First and foremost, I should thank my advisor Prof. Ronald G. Larson for accepting me as a student in his group and for affording me the latitude to enter an underdeveloped and challenging research area and choosing the direction of my doctoral research. I have always admired him as a scholar and a human being and greatly appreciated his work ethic. He has guided, encouraged and supported me through my toughest moments in my research and always challenged me to comprehend the underlying physics of any subject that is sometimes lost beneath piles of mathematical manipulations. He has been a great mentor to me, both professionally and personally and has been nothing but patient with me when I faced setbacks in research. He has shared many personal stories and invited me and other lab members to his house every summer and thanksgiving holiday, which I will keep as my fondest memories for many years to come.

I acknowledge the partial funding from the National Science Foundation and the Dow chemical Company with which I had the opportunity to work as a part of my doctoral research. I greatly appreciate the input and stimulating discussions with my collaborators there, in particular Dr. William "Trey" Porter III and Jin Zhao whose carefully designed experiments informed my transport model of drug release from polymeric tablets, presented in chapter 4.

I had many fruitful and stimulating discussions with Prof. Charles W. Monroe and former Larson group members, Dr. Prateek K. Jha and Dr. Priyanka S. Desai. I enjoyed the great support and friendship of my Larson group members who made my doctoral research a wonderful experience. I would also like to thank the administrative staff at the department of chemical engineering, especially graduate student coordinator, Ms. Susan Hamlin, whose support was there for me whenever I needed assistance with legal and administrative issues.

Finally, I cannot do the justice in thanking my parents, Bahram Salehi and Omolbanin (Mondana) Gholami and my siblings, Sourena and Elaheh for their patience, love and support throughout my doctoral research abroad and away from my family and for igniting a passion in me to pursue excellence in life.

Table of Contents

List of Figures

List of Tables

Abstract

Polyelectrolyte (PE) complexation (PEC) occurs upon mixing solutions of oppositely charged polyelectrolytes. This electrostatic self-assembly paradigm is also extended to layer-by-layer (LbL) assembled polyelectrolyte multilayers (PEM). Despite the broad applications of both PEC and PEM, bulk phase behavior of PEC and mass transport controlling the structure and film growth rate of PEMs and their connection is poorly understood. In this doctoral work, we present a combined experimental and theoretical investigation of PEC and PEM LbL assembly. We first observe that polymer-specific interactions have a profound effect on both PEC and LbL growth rate while salinity has a non-monotonic and a rather universal effect on LbL growth rate of fully ionized polyelectrolytes when normalized by the critical salinity required to suppress PEC. We next develop a free energy model of PEC by incorporating counterion association-dissociation, cross-chain ion pairing (IP) and protonation, treating each as a reversible reaction using laws of mass action. The importance of each reaction is controlled by a corresponding chemistry-dependent standard free energy input parameter that could be measured via experimentation or molecular simulations. In monophasic systems, the thermodynamic model can qualitatively explain the shifts in acidity and basicity observed in potentiometric titration of weak PEs in the presence of salt and oppositely charged PEs in accordance with Le Châtelier's principle. We demonstrate how a competition between counterion condensation and IP can explain the complex coacervation of strongly charged PEs. Binodal diagrams predicted in our model are most sensitive to IP strength both for weak and strong PEs. We compare binodal diagrams predicted by our model against experimental data, and find a plausible parameter set that leads to agreement between them. Finally, we develop a transport modeling framework for LbL assembly by variational minimization of the Rayleighian of a mixture of oppositely charged PEs, simple salt and water with respect to species velocities yielding species flux laws that equate the net mutual friction between components with the diffusional driving force on each species. The latter includes gradients in the conventional mixing chemical potential, electrostatic potential and mechanical stress (only for PEs). We also develop a constitutive equation for mixtures of PEs that accounts for solvent imbibition and IP. The result is a modification of the upper-convected Maxwell model. Our LbL transport model captures PE adsorption and film swelling in the equilibrium limit. A dynamic coupling of elastic stress and diffusion is applied in a different context to an electroneutral system involving drug release from polymer tablets, capturing Fickian, anomalous and case II modes of drug transport that arise naturally from the model. In addition to LbL, the transport framework proposed in this work can be applied to any system of charged and neutral components.

Chapter 1: Introduction

1.1 Polyelectrolyte Complex Coacervation

Mixtures of oppositely charged macromolecules, i.e. polyelectrolytes (PEs), undergo associative phase separation, yielding inter-PE complexes at the meso scale or a dense turbid liquid-like coacervate or solid-like precipitate at the macro scale that coexists in equilibrium with a solvent-rich phase depleted in both PEs, depending on the physiochemical conditions, e.g. monomer concentration, pH, ionic strength and temperature. Throughout this dissertation we refer to positively and negatively charged polyelectrolytes as 'polycation' and 'polyanion', respectively. Figure 1-1 depicts schematically macro phase separation of PEs upon mixing, occurring at high monomer concentration, referred to as PE complex coacervation\precipitation (PEC\P), first observed by Bungenberg de Jong,[1] has proven to be a versatile means of assembling materials useful in numerous applications due to the relative ease of fabrication as well as wide variety of polymer chemistries of both biological and synthetic origin that can be employed. In fact, charge-driven assemblies have been historically invoked in origin of life theories. Promising biomedical applications of PEC have emerged over the past two decades in areas that include DNA condensation for gene delivery,[2,3] non-viral gene therapy[4–7] delivery of various biotherapeutics,[8–13] cell encapsulation[14–16] and culture,[17] tissue engineering,[18] as well as additives in the cosmetics and food industries.[19,20]

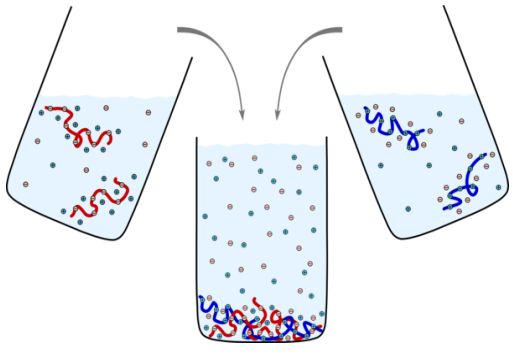

Figure 1-1: Polyelectrolyte complex coacervation/precipitation upon mixing two oppositely charged polyelectrolytes. Red and blue chains represent (negatively charged) polyanions and (positively charged) polycations, respectively. Figure adapted from ref [21].

Shortly after observation of PEC by Bungenberg de Jong,[1] theoretical treatments emerged, beginning with the early work of Overbeek and Voorn (VO) in 1957.[22] Experimental studies have led to identification of parameters influencing PEC/P, including chain length, salinity, pH, charge ratio etc. Most notably, PEC\P can be suppressed at high enough concentration of simple salts the exact amount is determined by pH, monomer concentration, pH and temperature among others.[1] PEC\P in the context of the VO model was described as a competition between the entropy of simple salt ions, loss of PE chains' translational entropy, short-range van der Waals (VdW) interactions and a reduction in electrostatic correlation free energy. Combining the well-celebrated Flory-Huggins (FH) free energy model[23] of neutral polymers and Debye-Hückel electrostatic free energy[24] of simple electrolyte solutions, VO model, in essence, rationalized the PEC\P by a favorable reduction of electrostatic free energy at the expense of negligible translational entropy of the chains. The VO model overlooks chain connectivity[25] and the highly correlated nature of electrostatic charges in the PE coacervate/precipitate phase; yet it remained the only continuum-level modeling framework for PEC\P for up to 50 years. We take a deep dive in recent modeling efforts and the shortcomings of the VO model in chapter 3. Therefore, utilization of oppositely charged PEs in applications by the experimental community has largely relied upon trial-and-error for design and optimization, given that the molecular and sophisticated field-theoretic simulations are still computationally expensive and emerging.[26,27]

1.2 Layer-by-Layer Assembly of Polyelectrolytes

About 40 years after the advent of the PEC\P's, it inspired the development of Layer-by-Layer (LbL) deposition of PE Multilayer (PEM) films[28] in which usually two oppositely charged PEs are alternately deposited onto a suitably primed substrate by either dipping the substrate in each PE solution or spraying the solution onto the substrate with possible rinsing steps with pure buffer intervening two consecutive polymer deposition steps. Figure 1-2 illustrates LbL assembly of PEM schematically. For simplicity, we refer to the polymer deposition steps as 'dipping step' regardless of the actual method used to do so, while the term 'rinsing step' is reserved for exposure of the PEM to polymer-free buffer solutions throughout this dissertation.

LbL assembly has allowed incorporation of various combinations of charged species, including synthetic and bio polymers,[29] clay minerals[30] and charged colloids[31] as constituents of the film. PEM films are not restricted to planar geometry. Indeed, extension of LbL assembly to organic

and inorganic substrates of arbitrary geometry brought about a burst of exciting applications in medicine, biotechnology and engineering, including microencapsulation,[32] nanocomposite assembly,[33] selective patterning,[34] enzyme-active coating,[35] drug delivery[36,37] and sensor fabrication[38] to cite but a few. A key attribute of LbL assembly is the wide range of polyelectrolytes that can be employed. However, control over the thickness, growth rate, and distribution of the components is of paramount importance,[39] and these attributes depend very sensitively on PE composition and conditions of salinity and pH.

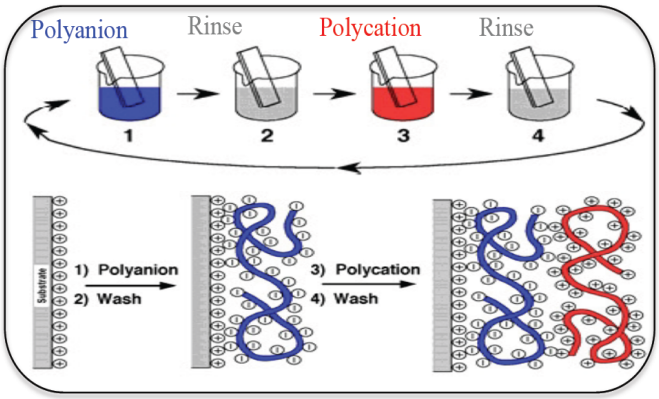

Figure 1-2: Layer-by-Layer (LbL) assembly of two oppositely charged polyelectrolytes on a charged substrate. Each cycle depicted above includes two dipping steps (in polyelectrolyte solutions) with two intervening rinsing steps with a buffer solution.

In addition to the thermodynamic factors controlling the equilibrium phase behavior of oppositely charged PE pairs used in the LbL process, dynamics factors most notably in-and-out diffusion of chains has been shown to significantly factor in the growth rate and structure of resulting PEMs over the past two decades.[40,41] In certain assembly conditions such as high salinity, PEM becomes unstable and dissolve in their surrounding media. This is largely believed to be caused by the loss of the so-called cross-chain "ion pairs" formed upon complexation of oppositely charged repeat units that act as junction points and create a temporary network and impart stability and viscoelasticity to PEM and complexes.[42]

Given that theoretical understanding and modeling of the thermodynamics of PEC\P is still an emerging area, however, it is not surprising that a definitive dynamic modeling framework for transport of charged constituents in LbL assembled multilayer does not exists. Additionally, mechanical stress evolution due to the deformation of the network of PEs in PEM has entirely been left out of PEM models to date. The length and time scales typically involved in an LbL

experiment, (10-1000) seconds, (1-1000) nm respectively, pose a major setback for any molecular scale simulations of LbL process. Therefore, most LbL models, reviewed extensively in chapter 5, are at a continuum level. There is, however, a great need for dynamic model of LbL process to be used as a robust predictive tool in design and optimization of the properties and stability of PEM films.

1.3 Drug Release from Polymer Matrix Tablets

Polymer matrices have long been used in controlled drug delivery devices. The release kinetics is dictated by the physiochemical structure and characteristics of the polymer matrix (excipient), drug -- i.e. the active pharmaceutical ingredient (API), and penetrant interactions. Mathematical modeling of drug release has been developed over the past two decades to help optimize the design of controlled release tablets and to minimize laborious *in vitro* drug release experiments. Upon contact with water or a physiological buffer solution, penetrant molecules diffuse into the polymer matrix, leading to swelling and expansion. That, in turn, increases segmental mobility of polymer chains and effective diffusion of drug molecules into the surrounding release medium in typical *in vitro* studies.

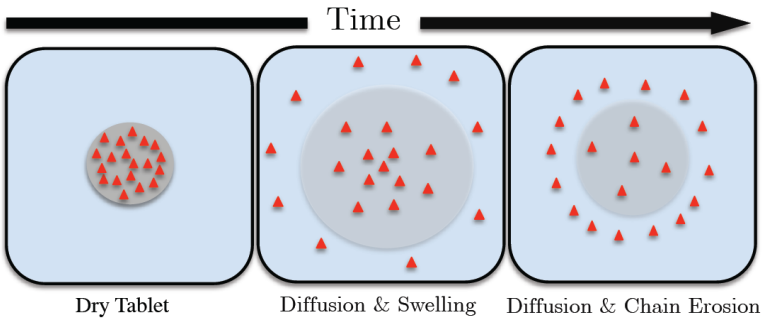

Figure 1-3: Water and API diffusion, swelling and surface erosion during the release of API molecules, represented by the red triangles, from a chemically stable and well-entangled polymeric matrix tablet, grey circles into a large release medium shown above by the blue background.

If the polymer is unstable to degradation by hydrolysis in water, chain scission and matrix degradation will follow in which case the API release rate is further sped up. Even for chemically stable matrices, if the polymer matrix is not chemically cross-linked, penetrant-induced disentanglements lead to chain detachment and surface erosion. As a result, API release is controlled by the net effects of API diffusion, matrix swelling and possibly chain erosion and/or degradation. These different processes are illustrated schematically in Figure 1-3. Limited solubility of API can cause the released API to crystalize in the release medium, lowering the

bioavailability of the API. Hydrophilic polymers such as poly(*N*-vinylpyrrolidone), cellulose and its derivatives such as hydroxypropyl methylcellulose (HPMC) are commonly used in controlled release tablets due to their high water uptake, drug loading capability and nontoxicity.

A considerable body of theoretical work at different levels of rigor has been dedicated to modeling transport of solutes from matrix tablets over the past two decades.[42-46] In principle, water swollen API/excipient is a multicomponent system and, as such, amenable to transport laws derived from irreversible thermodynamics. Weinstein *et al*.[47,48] and Lustig *et al*.[49] have proposed formal theoretical frameworks for modeling of fluid-polymer systems. Due partially to the complexity of these models, they have so far attracted little attention in the experimental community. As a result, much of the theoretical effort has been focused on formulation of relatively simple continuum transport models, often with redundant fitting parameters that can connect readily to experimental studies. It is thus desirable to formulate a robust dynamic model of stress-diffusion coupling with minimal fitting parameters that can be used in predictions of API and polymer release profiles obtained experimentally. Previous literature in this area is extensively reviewed in chapter 4.

1.4 Project Overview

In the quest for a dynamic modeling framework of LbL process involving two oppositely charged PEs, we first present a systematic experimental investigation of the extent to which the growth rate of LbL assembled PEM correlates with the corresponding bulk thermodynamic phase behavior in chapter 2. The role of PE chemistry, mixing ratio, assembly pH and salinity was studied for three PE pairs. Informed by our own results in chapter 2 as well as more recent body of data on thermodynamic characterization of PE complexation, we next formulate a free energy model of PE complex coacervation in chapter 3 and compare our predictions with experimental results. We demonstrate that the thermodynamic model articulates the chemo-specificity of PE chains and simple salt utilizing laws of mass action in the context chemical reaction equilibria. We specifically aimed to derive explicit free energy expressions in chapter 3, as they can be readily incorporated in transport models. Before proceeding to develop a transport framework for LbL process involving two charged polymers, we present a multi-component transport model based on a dynamic coupling between mechanical stress and diffusion of small species in a closely related problem, namely API release and water sorption from and by a well-

entangled electroneutral polymeric tablet in chapter 4. In chapter 5, we derive a dynamic framework of LbL assembly that couples not only mass diffusion and mechanical stress but also the electrostatic field, informed by the crucial role of polymer stress relaxation in the transport of small species and dissolution of a single polymer. Finally, we close by the conclusion and suggestions for future work in chapter 6.

1.5 References

[1] Bungenberg de Jong, H. G. In *Colloid Science*; Kruyt, H. R.; Elsevier Publishing Co.; Amsterdam, The Netherlands, 1949; Vol. II, p 335.

[2] Davis, M. E.; Zuckerman, J. E.; Choi, C. H. J.; Seligson, D.; Tolcher, A.; Alabi, C. A.; Yen, Y.; Heidel, J. D.; Ribas, A. Evidence of RNAi in humans from systemically administered siRNA via targeted nanoparticles. *Nature* **2010,** *464,* 1067-1070.

[3] Tseng, Y. C.; Mozumdar, S.; Huang, L. *Adv. Drug Delivery Rev.* **2009,** *61,* 721-731.

[4] Duceppe, N.; Tabrizian, M. *Expert Opinion on Drug Delivery* **2010,** *7,* 1191-1207.

[5] Wang, C.; Pham, P. T. **2008,** *5,* 385-401.

[6] Park, T. G.; Jeong, J. H.; Kim, S. W. *Adv. Drug Delivery Rev.* **2006,** *58,* 467-486.

[7] Samal, S. K.; Dash, M.; Van Vlierberghe, S.; Kaplan, D. L.; Chiellini, E.; van Blitterswijk, C.; Mornoni, L.; Dubruel, P. *Chem. Soc. Rev.* **2012,** *41,* 7147-7194.

[8] De Koker, S.; De Cock, L. J.; Rivera-Gil, P.; Parak, W. J.; Velty, R. A.; Vervaet, C.; Remon, J. P.; Grooten, J.; De Geest, B. G. *Adv. Drug Delivery Rev.* **2011,** *63,* 748-761.

[9] Laga, R.; Carlisle, R.; Tangney, M.; Ulbrich, K.; Seymour, L. W. *J. Controlled Release* **2012,** *161,* 537-553.

[10] Yoon, H.; Dell, E. J.; Freyer, J. L.; Campos, L. M.; Jang, W.-D. *Polymer* **2014,** *55,* 453-464.

[11] Cooper, C. L.; Dubin, P. L. K. A. B.; Turksen, S. *Curr. Opin. Colloid Interface Sci.* **2005,** *10,* 52-78.

[12] Štajner, L.; Požar, J.; Kovačević, D. *Colloids abd Surfaces A: Physiochem. Eng. Aspects* **2015,** *483,* 171-180.

[13] Albertini, B.; Vitali, B.; Passerini, N.; Cruciani, F.; Di Sabatino, M.; Rodriguez, L.; Brigidi, P. *European Journal of Pharmaceutical Sciences* **2010,** *40,* 359-366.

[14] Bhatia, S. R.; Khattak, S. F.; Roberts, S. C. *Curr. Opin. Colloid Interface Sci.* **2005,** *10,* 45-51.

[15] Butstraen, C.; Salaün, F. *Carbohydrate Polymers* **2014,** *99,* 608-616.

[16] Gonçalves, A.; Estevinho, B. N.; Rocha, F. *Trends in Food Science & Technology* **2016,** *51,* 76-87.

[17] Tai, B. C. U.; Wan, A. C. A.; Ying, J. Y. *Biomaterials* **2010,** *31,* 5927-5935.

[18] Costa, R. R.; Costa, A. M. S.; Caridade, S. G.; Mano, J. F. *Chem. Mater.* **2015,** *27,* 7490-7502.

[19] Alonso, D.; Gimeno, M.; Sepúlveda-Sánchez, J. D.; Shirai, K. *Carbohydrate Research* **2010,** *345,* 854-859.

[20] Schmitt, C.; Turgeon, S. L. *Advances in Colloid and Interface Science* **2011,** *167,* 63-70.

[21] van der Gucht, J.; Spruijt, E.; Lemmers, M.; Cohen Stuart, M.A. *J. Coll. Int. Sci.* **2011**, 361, 407-422.

[22] Overbeek, J.T.G; Voorn, M.J. *J. Cell. Compar. Physiol.* **1957**, 49, 7–22.

[23] Flory, P.J. Principles of Polymer Chemistry, Cornell University Press, Ithaca, NY, 1953.

[24] McQuarrie, D.A. Statistical Mechanics, University Science Books, Mill Valley, CA, 2000.

[25] Sing, C. E. *Adv. Colloid Interface Sci.* **2017**, 239, 2-16.

[26] Radhakrishna, M.; basu, K.; Liu, Y.; Shamsi, R.; Perry, S.L.; Sing, C.E. *Macromolecules* **2017**, 50, 3030-3037.

[27] Delaney, K.T.; Fredrickson, G.H. *J. Chem. Phys.* **2017**, 146, 224902-14.

[28] Decher, G. *Science* **1997**, 277, 1232–1237.

[29] Lvov, Y.M.; Lu, Z.; Schenkman, J.B.; Rusling, J.F. *J. Am. Chem. Soc.* **1998**, 120, 4073–4080.

[30] Kleinfeld, E. R.; Ferguson, G. S. *Science* **1994**, 265, 370–373.

[31] Feldheim, D. L.; Grabar, K. C.; Natan, M. J.; Mallouk, T. C. *J. Am. Chem. Soc.***1996**, 118, 7640–7641.

[32] De Temmerman, M.L.; Demeester, J.; De Smedt, S.C.; Rejman, J. *Nanomedicine* **2012**, 7, 771–788.

[33] Andres. C.M.; Larraza, I.; Corrales, T.; Kotov, N.A. *Adv. Mat.* **2012**, 24, 4597–4600.

[34] Hammond, P. T.; Whitesides, G. M. *Macromolecules* **1995**, 28, 7569–7571.

[35] Onda, M.; Lvov, Y.; Ariga, K.; Kunitake, T. *Biotechnol. Bioeng.* **1996**, 51, 163–167.

[36] Wohl, B.M.; Engbersen, J.F.J *J. Controlled Release* **2012**, 158, 2–14.

[37] De Koker, S.; De Cock, L.J.; Rivera-Gill, P.; Parak, W.J.; Velty, A.Z.; Vervaet, C.; Remon, J.P.; Grooten, J.; De Gist, B.G. *Adv. Drug Delivery Rev.* **2011**, 63, 748–761.

[38] Sun, Y.; Zhang, X.; Sun, C.; Wang, B.; Shen, J. *Macromol. Chem. Phys.* **1996**, 197, 147–153.

[39] Glinel, K.; Jonas, A.M.; Laschewsky, A.; Vuillaume, P.Y. In *Multilayer Thin Films; Sequential Assembly of Nanocomposite Materials,* 1st ed.; Decher, G., Schlenoff, J.B.; Wiley-VCH, Weinheim, Germany, 2003; p 177.

[40] Lavalle, Ph.; Picart, C.; Mutterer, J.; Gergely, C.; Reiss, H.; Voegel, J.C.; Senger, B.; Schaaf, P. *J. Phys. Chem. B* **2004**, 108, 635-648.

[41] Picart, C.; Mutterer, J.; Richert, L.; Luo, Y.; Prestwich, G.D.; Schaaf, P.; Voegel, J.-C.; lavalle, P. *PNAS* **2002**, 99, 12531-12535.

[42] Spruijt, E.; Cohen Stuart, M.A.; van der Gucht, J. *Macromolecules* **2013**, 46, 1633-1641.

[43] N.A. Peppas, B. Narasimhan, *J. Control. Release* **2014**, 190, 75-81.

[44] J. Siepmann, F. Siepmann, *J. Control. Release* **2012**, 161, 351-362.

[45] J. Siepmann, N.A. Peppas, *Adv. Drug. Deliv. Rev.* **2012**, 64 , 163-174.
[46] E. Kaunisto, M. Marucci, P. Borgquist, A. Axelsson, *Int. J. Pharm.* **2011**, 418, 54-77.
[47] T.F. Weinstain, L.S. Benethum, J.H. Cushman, *J. Pharm. Sci.* **2008**, 97, 1878-1903.
[48] T.F. Weinstain, L.S. Benethum, J.H. Cushman, *J. Pharm. Sci.* **2008**, 97, 1904-1915.
[49] Lustig, S.R., J.M. Caruthers, N.A. Peppas, *Chem. Eng. Sci.* **1992**, 47, 3037-3057.

Chapter 2: Polyelectrolyte Bulk Complexation and Layer-by-Layer Film Growth Rate; Is There A Correlation?*

2.1 Introduction

The model of Overbeek and Voorn (OV),[1] though crude, captures the salient features of PEC\P, which were experimentally established by the time the model was published. In particular, longer and more hydrophobic chains are predicted to undergo phase separation more readily. Also, the more symmetric the charge ratio of the PEs, the broader will be the instability window, which is the set of conditions (such as salt concentration and fractional charge on either polymer) over which phase separation occurs.[2] The OV model was recently demonstrated to fit adequately the binodal phase diagrams of PE complexation for polyacrylic acid (PAA)/poly(N,N-dimethylaminoethyl methacrylate) (PDMAEMA) at various salt concentrations.[3] Theoretical treatment of PE phase separation is still an active area of research and some of the shortcomings of the Overbeek and Voorn[1] mean field model have been addressed by the random phase approximation and one-loop expansions.[4,5]

Much of the research on PE complexation is concerned with establishing the phase diagram. However, a definitive molecular description of the microstructure of the complex phase is still lacking. A PE complex phase is either a gel-like coacervate or a powdery solid precipitate, or in some cases possibly something in between. Chollakup *et al*.[6,7] and Priftis *et al*.[8,9] recently observed that at low ionic strength, precipitates form while higher salinity results in coacervation. Above a critical salt concentration, polyelectrolyte complex coacervation/ precipitation (PEC\P) is suppressed altogether and a single clear liquid phase appears. Although the transition around the critical salt concentration is rather well understood, the nature of the transition between precipitation and coacervation remains obscure, especially since

* This chapter is adapted from my publication in Macromolecules *48* (**2015**) pp. 400-409. Part of the research has been conducted in collaboration with Dr. Priyanka S. Desai.

distinguishing coacervation from precipitation often relies solely on visual inspection and microscopy. In fact, precipitation is commonly marked by formation of sediments of irregularly shaped particles of broad size distribution, whereas the coacervate phase is commonly dispersed as lyophobic droplets as shown in Figure 2-A-1 in the appendix; see section 2-5.

Oppositely charged PE coacervates can be classed as thermoreversible gels[10-12] wherein ion pairs between the two PE charged sites, the so-called stickers, serve as the physical cross-links. Consequently, the dynamics of PEs in complex phase features hindered chain reptation, termed "sticky diffusion" or "sticky reptation" in which the relaxation time and the inverse of the diffusivity are both proportional to the lifetime of ionic pairs. A complex coacervate, or gel, is more amenable to characterization techniques than is a precipitate. Recent studies of Spruijt *et al*.[13,14] bear witness to the thermoreversible network structure of the complex coacervate, characterized by an average mesh size and relaxation time that can be interpreted using the sticky diffusion model.[15,16] If this lifetime becomes long enough, the complex phase transitions to a kinetically frozen "glass," in which thermodynamic equilibration within the complex phase and the co-existing solution is frustrated. This interpretation identifies the precipitate as an arrested "glass" and the coacervate as an equilibrated liquid.

Chain dynamics inside PEMs can also be viewed from this standpoint[17] and play a central role in LbL assembly. Numerous studies have established that PEMs grow either linearly or exponentially with deposition time. The thickness of the former typically ranges between 20-100 nm while the latter typically varies between 100-1000 nm and a few microns in thickness, depending of course on the number of layers deposited, which is typically of order 5-10 or so. Cross-layer diffusion of either of the PEs into and out of the PEM during the LBL deposition is now generally held to be responsible for exponential growth,[18,19] although other models not featuring diffusion have been proposed. For instance, arguments based on surface coverage saturation,[20] similar to "in and out" diffusion, also predict a cross-over from exponential to linear film growth, amply observed experimentally. Also, a simple model premised upon charge overcompensation occurring over a constant length scale was also able to predict such a transition,[21] even though it is difficult to distinguish conceptually between charge overcompensation across many layers and cross-layer diffusion. Various studies have already proved the existence of diffusion of PEs into PEMs,[18] and the effect of some parameters on PEM

growth kinetics can be predicted using models featuring chain diffusion.[19] These models assert that if chain mobility is insufficient to allow at least one PE to diffuse over across the entire film thickness over the time scale of the deposition, then the resultant PEM grows linearly.

Unsurprisingly, parameters controlling properties of PEC\P and phase behavior influence the LbL film growth. Moreover, properties of PEMs closely resemble those of the complexes formed at similar conditions in the bulk.[22-25] Indeed, some authors have employed the underlying physics and observations established in microscale complexation of PEs to interpret the properties of PEMs.[26-28] The exchange energy upon formation of an ion pair in a PEM controls its lifetime in much the same way as it does in bulk complexation. Despite such similarities, bulk phase behavior of oppositely charged PEs and PEM growth characteristics have usually been studied independently, with few attempts to study both bulk phase behavior and LbL growth on the same PEs at the same salinity and pH. Indeed, PEMs are viewed as structures far removed from equilibrium even though the feasibility of PEM growth has been demonstrated using only considerations of equilibrium thermodynamics.[28,29] In light of the intriguing indications of correspondence between PEC\P and PEM assembly, we here report a systematic study of both the bulk phase behavior and PEM formation of three pairs of model PEs. The following presents our preliminary work aimed at elucidating how strong a connection can be made between bulk complexation behavior and LbL film growth. Since phase behavior studies are much faster and cheaper than LbL growth experiments, it would greatly speed design and optimization of LbL film deposition if information relevant to the rate of LbL growth could be inferred from the phase behavior of the corresponding polyelectrolyte pair. In what follows, we will investigate the hypothesis that "bulk precipitation leads to linear growth kinetics whereas bulk complex coacervation leads to exponential growth kinetics during PEM LbL assembly" and check how close a correlation can be found, if any, between bulk PEC/P and PEM LbL assembly. We wish, in addition, to determine more precisely how pH, salinity, and polyelectrolyte interactions influence phase behavior and LbL growth rate.

2.2 Materials and Methods

Poly(acrylic acid) (PAA) was used as a polyanion and three different positively charged polyelectrolytes as polycations, viz. poly(N,N-dimethylaminoethyl methacrylate) (PDMAEMA), poly(diallyldimethylammonium chloride) (PDADMAC), and poly(allylamine hydrochloride)

(PAH). Both PAA (M_n ~ 43,000 g/mol, M_w/M_n ~ 1.15), and PDMAEMA (M_n ~ 82,700 g/mol, M_w/M_n ~ 1.09) were purchased from Polymer Source as white powders. PDADMAC was purchased from Sigma Aldrich as a 35 wt. % solution in water with average M_w less than 100,000 g/mol. Branched polyethylenimine (BPEI), a strong polycation (M_w ~ 25,000 g/mol) was also purchased from Sigma Aldrich.

2.2.1 Preparation of Bulk PE Complexes

Mixtures of oppositely charged polyelectrolyte complexes, each having similar chain length (with degree of polymerization N ≈ 500), were prepared at a monomer concentration of 0.11M of each of the positive and negative repeat units, in a total volume of 1.5ml for the case of PAA/PDMAEMA and PAA/PDADMAC pairs and at a monomer concentration of 0.05M of each of the positive and negative repeat units for the case of the PAA/PAH pair. We varied the molar ratios of the chargeable groups by changing their pH from very acidic to very alkaline, viz. pH = 3, 5, 6, 7, and 9. Additionally, the total mixing ratio of negative to positive repeat units was varied between 4:1 to 1:4, with 1:1 corresponding to an equimolar ratio. Interactions of PE pairs were also tuned by making a series of solutions with increasing salt concentrations, from no salt conditions to 3M KCl. The procedure for preparing equimolar complexes from the PAA/PDMAEMA pair at a monomer concentration of 0.11M and pH 3 with varying levels of salt concentrations was as follows:

First, stock solutions of both PAA and PDMAEMA were prepared at an overall monomer concentration of 0.5M in deionized Milli-Q water. The stock solutions were adjusted to pH 3 using 0.1M KOH and 0.1M HCl keeping the concentration of the stock solution at 0.5M. Second, 0.33 ml of the PDMAEMA stock solution was added to a vial (V=1.5ml) containing 0.84ml of deionized Milli-Q water at a desired KCl salt concentration. Finally, 0.33ml of PAA stock solution was added to the microcentrifuge vial to give a mixture with a final volume of 1.5ml at pH 3 and an overall desired KCl salt concentration. After each sequential addition, the vial was vigorously shaken and well mixed. Note that the final pH of the complex did not vary considerably from the initial pH values of the individual components. Complexation occurred immediately after addition of the last component to the vial. In some cases, we observed a white powder that settled to the bottom of the vial, which we call a “precipitate,” while in some other cases we observed a soft transparent to semi-transparent gel-like polymer-rich phase that settled

to the bottom of the vial, which we call a "coacervate." The vials were then left to equilibrate for 5 days, after which the complexes were micro centrifuged at 1000g for 15 minutes. We then used bright field microscopy to differentiate between precipitates, coacervates and clear solutions.

2.2.2 Preparation of PEM Films

The films were grown on chrome/gold-plated quartz crystals, (resonance frequency ~ 5 MHz) purchased from Stanford Research Systems. The fresh as-received crystals were thoroughly cleaned in freshly made Piranha solution (3:1 v/v Sulfuric acid/30 %v/v hydrogen peroxide aqueous solution) at room temperature, rinsed with deionized water and dried out with a stream of air prior to use. BPEI was deposited first, as a precursor to the next layers, from a stagnant solution poured directly into the crystal holder cell, followed by rinsing the film for 2 minutes with a total of 35 ml of water devoid of KCl and adjusted to the same pH as that of the PE solutions. After rinsing, the film was dried with a gentle stream of air. The rinsing/drying steps were performed identically throughout. Shortly thereafter, the polyanion was deposited by exposing the film to polyanion solution for 20 minutes, followed by rinsing/drying. The polycation layer was then deposited onto the film from a solution of the same concentration, pH and salinity as that of the polyanion solution for 20 minutes. Finally, one more rinsing/drying step concluded the first cycle, ending in deposition of one bilayer. The concentrations of both PAA/PDMAEMA and PAA/PDADMAC pairs were fixed at 0.11 M of monomer while for PAA/PAH 0.05 M solutions were used. The deposition cycle was then repeated for the desired number of times, often up to 8 bilayers. The experiment was carried out at room temperature at relative humidity of ~50 %. After each rinsing/drying step the shift in the resonant frequency of the crystal/film ensemble was monitored on a quartz crystal microbalance QCM-200 (Stanford Research Systems, Sunnyvale, CA, USA) and converted to the adsorbed mass density of the film using the Sauerbrey[30] equation:

$$\Delta m = -C\,\Delta f$$

where the dried films were taken to be rigid at the first overtone frequency, such that the mass density was assumed to be linearly proportional to the measured frequency shift. Rinsing for two minutes sufficed for the films to reach a constant weight for all conditions studied. PEM films were deposited from solutions with exactly the same concentration of the PE, salinity and pH as those used in the determinations of bulk phase behavior.

2.3 Results

2.3.1 Phase Behavior

In what follows, we systematically try to change the strength of interaction with which repeat units of PE pairs interact. To this end, four routes were taken: the polycation, the pH, the ionic strength, and the mixing ratio of polycation/polyanion, were separately varied. It should be noted that PE pairs studied here experience a variety of interactions as the pH of the mixture changes, thus making it challenging to tune their interaction strength, and in turn, the dynamics in the bulk and in the PEM, merely by means of pH variation.

In equimolar mixtures of the PE pairs, the ratio of AA repeat units to the polycation repeat units is close to unity. At equimolar mixing ratio, phase diagrams for the PE pairs are depicted in Figure 2-1. Electrostatic interactions in equimolar mixtures are screened upon varying the total concentration of KCl from no salt to 3.5M. The critical salt concentration for the complexation of PAA with each of the three polycations at pH 7 varies as PAH>PDMAEMA>PDADMAC; see Figure 2-1. Therefore, PAH has the strongest electrostatic interaction with PAA while PDADMAC has the weakest. Being a primary amine with less steric hindrance compared to PDMAEMA and PDADMAC, PAH is capable of forming the strongest electrostatic interactions with PAA.

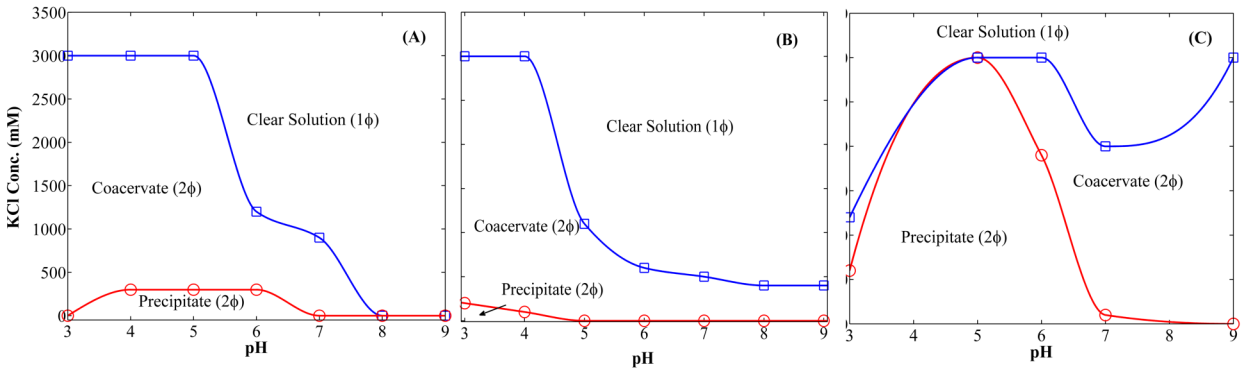

Figure 2-1: "Phase diagrams" of equimolar mixtures of (A) PAA/PDMAEMA (B) PAA/PDADMAC (C) PAA/PAH at room temperature. Solid lines, separating the three phases from each other, are guides to the eye. The red lines represent the precipitate-to-coacervate transition while the blue ones mark the critical salt concentration for a transition from coacervate to clear solution.

For PAA/PDMAEMA, all the complexes formed below the critical point concentration at pH 7 are coacervates. Consistent with Spruijt *et al.*[3], we established that the critical KCl concentration is roughly 1M for PAA/PDMAEMA at pH 7; Figure 2-1A. We do not imply that there is no

complexation above this critical salt concentration, but simply that any complexes formed are nano-sized, and remain dispersed in the solution. As can be seen in Figure 2-1A, addition of salt to PAA/PDMAEMA at pH 7 reduces the extent of complexation until the critical salinity of 1 M is reached where no bulk complexation is visible, although there may be water-dispersible inter-polyelectrolyte complexes (wIPCs) suspended in the solution. However, addition of salt does not suppress the complex coacervation at pH 3 all the way up to 3M KCl, implying that the interactions have not been weakened as much as they were at pH 7.

Another remarkable observation is that complexation of equimolar mixtures of PAA/PDMAEMA at pH 3 occurs over a salt concentration range roughly thrice as wide as at pH 7. In other words, in PAA/PDMAEMA, interactions that are primarily electrostatic at pH 7 are fully screened by 1 M KCl whereas interactions at pH 3 allow for complexation at salt concentrations well beyond the electrostatic critical point. A similar observation holds for PAA/PDADMAC where the critical salt concentration at pH 3 is a staggering five times that of pH 7. At pH 7 and 9, both PAA and PDADMAC are almost fully charged and thus we expect them to interact primarily via equally strong electrostatic interactions. The PAA/PDADMAC precipitate phase formed at pH 3 signifies either attractive interactions that are appreciably stronger than those at pH 7 and 9 where the complex phase is a coacervate or an insensitivity of the complexation at pH 3 to salt, or perhaps both. For PAA/PAH, where the pK_a of PAA is ~ 5-5.5[3] and the pK_b of PAH is ~ 8.5-9.3[18] in solution depending on the salt concentration, one would expect the phase behavior to be fairly symmetric around pH ~ 7 if electrostatics were the dominant interaction. On the contrary, we observe that the phase diagram for this system is markedly asymmetric around pH 7, Figure 2-1C. Similar asymmetry around pH 6 is evident for PAA/PDMAEMA, Figure 2-1A. We find that none of the above results can be fully explained in terms of electrostatics alone. This suggests the need to consider other interactions that might help elucidate these observations.

As an alternative to varying the pH, the charge ratio of polycation to polyanion can be controlled by varying their overall mixing ratio. The effect of mixing ratio on phase behavior of PAA/PDMAEMA and PAA/PDADMAC at various pH values is shown in Figure 2-2. Even though the mixing ratio, or equivalently the molar fraction of AA repeat units studied here, affects the phase behavior only marginally, its effect cannot be disregarded. At pH 3, the

coacervation of a PAA/PDMAEMA mixture with a 1:4 mixing ratio is prevented above a critical salt concentration of 1200 mM KCl, which is visibly lower than 3000 mM KCl necessary at all other mixing ratios at this pH. Similarly for PAA/PDADMAC at pH 5, as the fraction of acrylic acid (AA) units decreases, the critical KCl concentration falls sharply from 3000 mM to about 1000 mM. The critical KCl concentration is otherwise barely affected by the overall AA mole fraction.

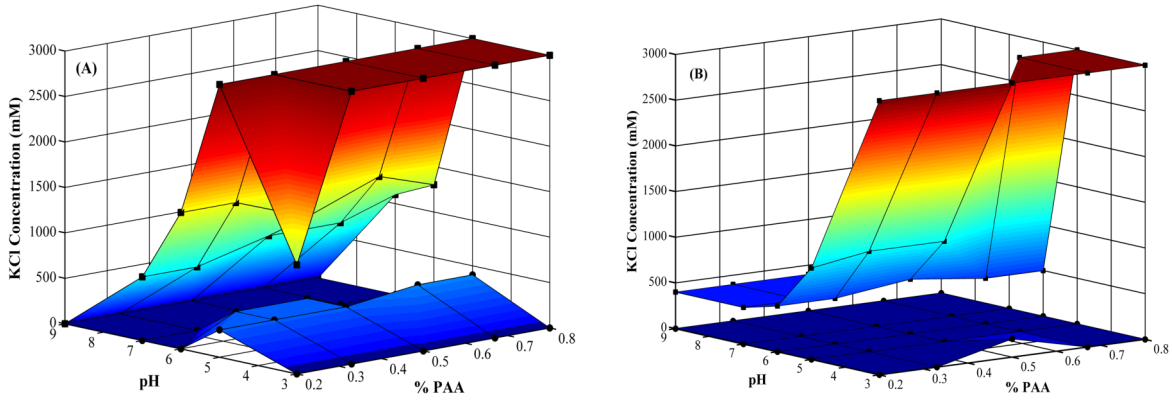

Figure 2-2: "Phase diagrams" of (A) PAA/PDMAEMA (B) PAA/PDADMAC at room temperature. The lower surfaces represent the precipitate-to-coacervate transition while the upper ones mark the critical salt concentration, required for a transition from coacervate to clear solution.

The precipitate-to-coacervate transition depends more weakly on mixing ratio than the critical KCl concentration does, according to Figure 2-2, which is consistent with a dynamically arrested state of precipitation. Prifitis *et al.*[8] have demonstrated that PEC/P formation is a two-step process in which microscopic ion-pairing between oppositely charged repeat units is followed by macroscopic phase separation. If ion-pairing is irreversibly favorable, the chain exchange in the following step will be largely eliminated, leading to a turbid mixture and precipitation. Since it is dominated by strong interactions at molecular level, precipitation is thus not expected to be noticeably affected by the macroscopic fraction of AA repeat units. In light of the marginal effect of mixing ratio on phase behavior of the two PE pairs, we will focus on pH, polycation type and salinity in the following LbL experiments.

2.3.2 Effect of pH on Salt-Free Systems

This section reports the effect of pH on growth kinetics of LbL on two polyelectrolyte pairs, namely, PAA/PDMAEMA and PAA/PDADMAC. Both the phase behavior and LbL kinetics for

PAA/PAH have been extensively studied.[6,7,32] Hence, we focus our attention on the other two pairs.

2.3.2.1 PAA/PDMAEMA

Depicted in Figure 2-3 is the growth kinetics of LbL films composed of PAA and PDMAEMA along with corresponding bulk phase behavior at various pH values and in the absence of salt. Given that both PAA and PDMAEMA are weak PEs (pK_a ~5-5.5[3], pK_b ~8[3] depending on salt concentration), pH affects the degree of protonation and thus their charge fractions. At pH 3, one would expect the two PEs to be highly asymmetric with respect to charge fraction (the polycation being much more charged than the polyanion) and accordingly, their electrostatic interactions should be weak. Despite this, we nevertheless observed under these conditions the formation of a "sticky precipitate" that could perhaps also be called a "high-modulus coacervate", as shown in Figure 2-3. Also, the film constructed at pH 3 grew exponentially and reached a greater mass density than was achieved under the other conditions studied in Figure 2-3. Conspicuous in Figure 2-3 at pH 3, is the rather asymmetric mass increments deposited upon alternating exposures to polycation and polyanion solutions, the so-called odd-even effect, also well-documented in the literature. As the pH is increased, clear-cut precipitation is observed at pH values of 5 and 6, as shown in Figure 2-3. Meanwhile, the film growth kinetics at these pH values slows down dramatically. Separate ellipsometric measurements (data provided in the appendix 2.5.1, Figure 2-A-1) indicate that film growth at pH 6 is even slower than at pH 5. At pH 7, where the charge fractions of PAA and PDMAEMA are roughly inverted relative to their charge fractions at pH 6, the phase behavior would be expected to mirror that observed at pH 6. However, instead of a precipitate, we observe a turbid coacervate. Interestingly, film growth at pH 7 obeys linear kinetics and the total mass of the film is considerably less than for the film grown at pH 5.

We observe that PEM growth at pH 3 is rapid and exponential and the corresponding bulk behavior is that of a high modulus, dense, coacervate. At pH 5, the film continues to grow exponentially; however its growth is much slower and we observe a precipitate in the bulk solution. A further increase in pH causes the growth kinetics to cross over to a linear growth regime while the corresponding bulk behavior shifts away from precipitation towards coacervation as observed in pH 7.

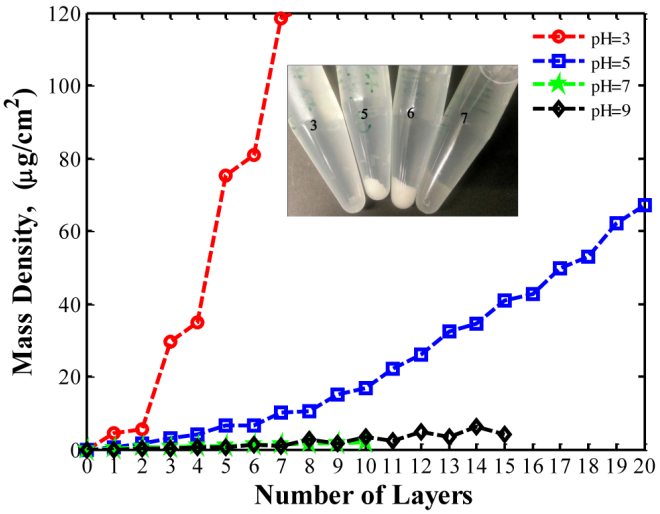

Figure 2-3: Effect of pH on PEM growth kinetics for PAA/PDAEMA in the absence of KCl at room temperature. The inset illustrates the physical form of the complex phases corresponding to LbL experiments. Numbers on the vials in the inset denote the pH of the contents. PAA was deposited at the odd-numbered steps, and produced larger increments in mass than the deposition of PDMAEMA on the even-numbered steps. Ellipsometry data for LbL growth at pH 6 are given in Figure 2-A-1 of appendix 2.5.1.

2.3.2.2 PAA/PDADMAC

For PAA/PDADMAC complexes at pH 3, we observe precipitation rather than coacervation that is observed for all other pH values investigated, as shown in Figure 2-4. Since PDADMAC remains fully protonated at all pH values considered, the strongest electrostatic interactions is experienced at pH 7 and 9 where PAA is fully charged. Quantum calculations have shown that steric hindrance reduces the electrostatic interactions of quaternary amines.[33] Although PDADMAC is a strong PE, the positive charge on its quaternary nitrogen atom experiences more steric hindrance to interaction with the carboxyl group on PAA, than is experienced by the tertiary nitrogen of PDMAEMA. Furthermore, the nitrogen atom in a quaternary amine possesses less partial positive charge than do tertiary amines, due to the presence of four neighboring electron-donor alkyl groups in the former. PDADMAC may therefore have weaker electrostatic interactions with PAA than does PDMAEMA. In agreement with this hypothesis, the complex phase for PAA/PDADMAC at both pH 7 and 9, where electrostatic interactions are predominant, is a coacervate. Furthermore, PAA/PDADMAC have the slowest growth rate in PEM build-up and have a linear character as shown in Figure 2-4. In contrast to PAA/PDMAEMA, where the overall film mass decreases monotonically with pH at acidic conditions, PAA/PDADMAC growth kinetics exhibits non-monotonic variation, with the fastest growth rate at pH 5 where

growth is exponential; see Figure 2-4. The corresponding bulk complex at pH 5 is a clear coacervate as is the case at pH 6, 7 and 9. PEM growth kinetics at pH 3 and 6 seem to fall in the intermediate but exponential regime while their bulk complex is a powdery precipitate and a coacervate respectively.

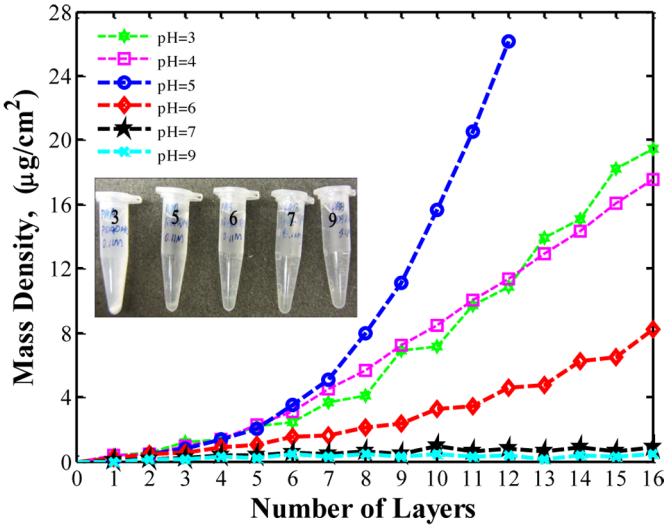

Figure 2-4: The same as Figure 2-3, for PAA/PDADMAC in the absence of KCl at room temperature.

2.3.3 Effect of Ionic Strength at pH 7

2.3.3.1 PAA/PDMAEMA

For PAA/PDMAEMA, addition of KCl leads to a non-monotonic variation of LbL growth rate with salt concentration as seen in Figure 2-5. It has been reported that in some cases addition of salt leads to a monotonic increase in the PEM growth rate whereas others show non-monotonic growth behavior, i.e. an increase in salt concentration first increases the growth rate and then decreases the rate at higher salinity.[28,34] Salt tends to destabilize the PEM through the charge screening effect, weakening the electrostatic interactions between opposite charges that holds the PEM film together. Salt-induced film re-dissolution of one or both PEs gives rise to saw-toothed curves in Figure 2-5 (particularly at 100 and 500 mM salt – the black and green curves). Interestingly, this has been reported for many PE pairs[35,36] and specifically for PAA/PDMAEMA[37,38] which might be caused by higher mobility of one of the PEs and formation of water-dispersible inter-polyelectrolyte complexes (wIPC's) that take some of the chains away from the film into the solution. Another likely explanation for the mass loss is the possible migration of one of the PEs out of the film during the rinsing step caused by an insufficient

electrostatic energy barrier at the solution-film interface. This in turn, might be caused by a small or even complete lack of surface charge overcompensation during the dipping step. Indeed, it has been recently demonstrated that surface charge overcompensation need not happen at both deposition steps in order to have net stable PEM film growth.[25,39]

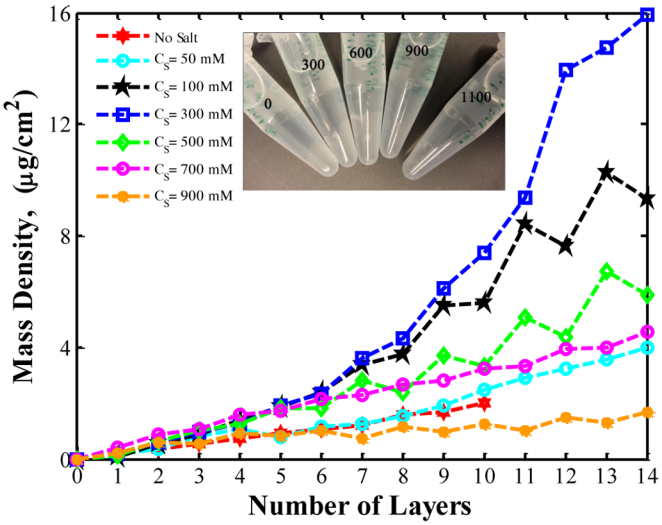

Figure 2-5: Effect of KCl concentration on PEM growth kinetics of PAA/PDMAEMA at pH 7 and room temperature. Numbers on the vials in the inset denote KCl concentration in (mM).

Despite the non-monotonic variation of the growth kinetics at pH 7 with salinity, addition of salt does not change the nature of the complex phase, Figure 2-5. In fact, all the complex phases formed at pH 7 are coacervates, which tend to become increasingly clearer and less viscous as the KCl concentration is increased. On the other hand, growth is linear and slow at KCl concentrations either below 50 mM or at or above 700 mM as is evident in Figure 5. At intermediate salt concentration region, namely, between 50 and 700 mM, growth is exponential.

2.3.3.2 PAA/PDADMAC

During growth of PAA/PDADMAC PEMs, film re-dissolution occurs on exposure of the films to PAA solution. Re-dissolution has previously been reported for PAA/PDADMAC[40] at 500 mM NaCl. Since re-dissolution, i.e. chain desorption, occurs for all salt concentrations during exposure to PAA, it must be the PDADMAC that is leaving the film during the PAA dipping step, resulting in a film with overall more uncompensated negative sites at least in topmost layers, so that PDADMAC can be adsorbed in the subsequent dipping in PDADMAC solution.

PDADMAC deposition on the subsequent dipping step is appreciable, due to complexation with surplus of carboxyl groups inside from the previous step.

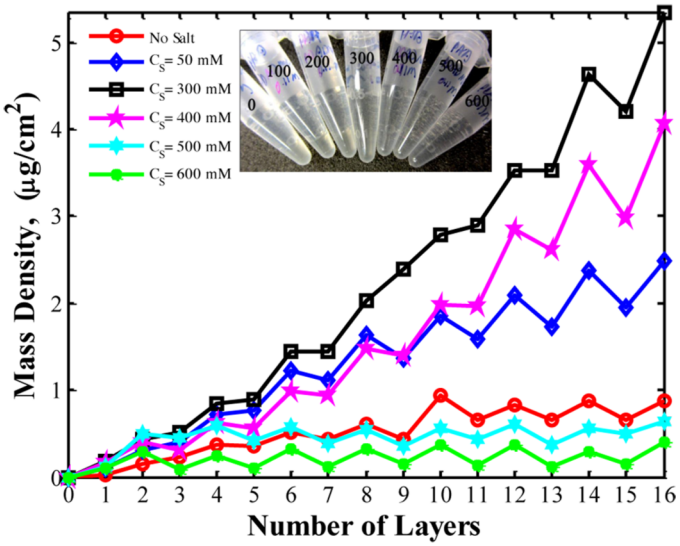

Figure 2-6: Effect of KCl concentration on PEM growth kinetics of PAA/PDADMAC system at pH 7 and room temperature. Numbers on the right denote KCl concentration in (mM).

Similar to PAA/PDMAEMA, film growth in PAA/PDADMAC is initially expedited with increasing salt concentration up to 300 mM, but further addition of salt slows down growth. Rapid LbL growth is accompanied by an exponential-like increase in film mass density with layer number, while slower growth kinetics, observed at either very low or very high salt concentration, tend to be linear. Despite such a non-monotonic response of growth kinetics to KCl concentration, there is no perceptible change in the bulk complexes which all appear as coacervate phases, albeit differing in turbidity and fluidity, Figure 2-6.

2.4 Discussion

A well-established feature of the LbL process is charge overcompensation early in the deposition stages.[19,41] The odd-even effect seen in PAA/PDMAEMA at pH 3 can be rationalized by the high charge asymmetry of PEs at pH 3 where PDMAEMA is nearly fully charged whereas PAA is roughly 5% charged. However, charge asymmetry alone cannot explain exponential PEM growth of the PAA/PDMAEMA film at pH 3, Figure 2-3. Since charge overcompensation occurs within a few layers (i.e., roughly a Debye thickness) adjacent to the film-solution interface, one would expect the same increment to deposit at each step, resulting in linear growth rate with respect to number of deposited layers. Exponential growth requires that at least one of the polyelectrolytes

diffuse much deeper into the film than a Debye layer deep. Although the actual degree of protonation of weak polyanions is strongly affected by the presence of the polycation inside the film,[42-44] a charge fraction of 5% is in fact consistent with the ratio of PAA to PDMAEMA mass increments, Figure 2-3, assuming a fully charged PDMAEMA. The ratio of PAA and PDMAEMA mass increments (around 20 to 1 in Figure 2-3 for pH 3) indicates that the charge fraction of PAA chains adsorbing onto the interface is barely affected by PDMAEMA, at least in the vicinity of the interface. The charge regulation effect of PDMAEMA thus appears to be negligible for PAA/PDMAEMA. Assuming protonated AA units do not interact with PDMAEMA, electrostatic interactions are not sufficient to bring about bulk complexation, as a 5% charge fraction is tantamount to a mixing ratio of 1 AA charged unit for every 20 DMAEMA units. In fact, a general rule for PEC\P's stipulates that at mixing ratios smaller than ~1:6-1:9, PEC\P is suppressed[2] and is replaced by emergence of nano-sized wIPC's in bulk, which is not the case at pH 3, as seen in Figure 2-3. Even if charge regulation of PDMAEMA is presumed to be appreciable, the resulting bulk complexation driven by enhanced electrostatic interactions is in direct contradiction to some of our observations such as the weak susceptibility of PAA/PDMAEMA complexes to salinity at pH 3, mentioned in the previous section. Figure 2-A-2 in appendix 2.5.2 illustrates the effect of KCl on the physical form of PAA/PDMAEMA complexes at pH 3.

The likely weakness of electrostatic interactions between PAA/PDMAEMA at pH 3 underscores the importance of non-Coulombic interactions, hereafter referred to as secondary interactions, in driving bulk complexation seen in PAA/PDMAEMA at this pH. Although electrostatics is involved in all intermolecular interactions, we adopt the term "secondary" to distinguish them from primary Coulombic ion-ion forces that oppositely PEs experience in complexation. Even though a detailed description of such secondary interactions is beyond the scope of this study, it is useful to consider their possible source. Hydrogen bonding between even neutral polymers, for instance, has been amply reported to be strong enough to construct a PEM without requiring any electrostatic interactions at all.[45] In fact, a large fraction of protonated AA groups can form hydrogen bonds with water, other AA units, and also with the carbonyl groups on PDMAEMA at pH 3.

As noted earlier, PAA/PDADMAC has weaker electrostatic interaction of the two PE pairs. Following our earlier observations in the previous section, the strongest PAA/PDADMAC

interaction is present at pH 3 where electrostatic interaction is nearly absent. These findings underline both the existence and dominance of secondary interactions over electrostatic interactions for PAA/PDADMAC at pH 3. In fact, Alonso *et al*.[40] reported that complexation of PAA and PDADMAC is the most exothermic at pH 3 and becomes endothermic at basic pH, providing further evidence for the significance of secondary interactions. Litmanovich *et al*.[46] reported the complexation of PAA/PDADMAC at extremely acidic pH which was unanticipated given that PAA is barely charged and proposed that interactions of carbonyl groups with quaternary amine groups change from ion-dipole to ion-ion upon increase of pH. We observe that the PAA/PDADMAC complex phase is a precipitate at pH 3 while coacervation is visible at higher pH in the absence of salt. Since there is no hydrogen bonding of AA groups with PDADMAC, by inference, other type(s) of secondary interactions must be considerably stronger than electrostatic interactions, which are dominant at pH 7, to account for precipitation and higher critical salt concentration at pH 3 than at pH 7, despite the low charge density of PAA at pH 3.

Recent molecular dynamic simulations of Jha *et al*.[47] demonstrate that deprotonated AA repeat units are considerably more hydrated than protonated ones, thus making it harder for charged AA units to complex with polybase repeat units, despite the Coulombic interactions between them. Therefore, another possible contribution to the stronger net interaction at pH 3, relative to pH 7 for both PE pairs, is the extensive hydration of deprotonated AA units at pH 7, which weakens the electrostatically-induced complexation. 'Masking' of AA units at pH 7, combined with other types of pH-dependent secondary interactions, might render the overall interaction and thus complexation driving force weaker at pH 7 than at pH 3. Absence of strong hydration effects at lower pH, hydrogen bonding of AA units to polybase repeat units in the case of PDMAEMA, as well as other secondary interactions of AA units such as ion-dipole interactions in the case of PDADMAC, may promote formation of PEC/P's and make critical salt concentrations at low pH higher than they are at pH 7.

Stronger interaction, regardless of its nature, increases the lifetime of ionic, hydrogen bonding, or other physically reversible linkage points formed between the chains, thereby increasing the relaxation time and decreasing the chain center-of-mass (C.O.M) diffusivity. Therefore, if the overall interactions are sufficiently strong, the complex phase will be a precipitate, given that a

complex precipitate is a dynamically arrested state. At pH 7, dominant electrostatic interactions are continuously weakened via the charge screening effect of KCl, thereby decreasing the relaxation time and increasing the C.O.M diffusivity of the chains. This increase in diffusivity with salt concentration, or so-called "plasticization effect" of salt on the PE complex, has been previously demonstrated.[11,13] PAA/PDMAEMA and PAA/PDADMAC complexes formed in the absence of KCl at pH 7 are already a coacervate phase and therefore addition of KCl does not change the bulk behavior, as shown in Figures 2-5 and 2-6, which is consistent with the plasticization effect of KCl and thus faster dynamics in the presence of KCl.

The strength of interactions has a direct impact on the dynamics of chains both in the bulk complex phase as well as in a PEM assembly. As noted earlier, the exponential character of PEM growth depends on the extent to which PE chains can diffuse into the PEM. Chain diffusion in the PEM differs from the C.O.M diffusion in the bulk complex phase, in that the former is the displacement of a chain relative to the PEM driven by the potential gradients whereas the latter is brought about by thermal fluctuations that are present even in a homogeneous system. Nonetheless, the strength of interactions affects both of them in a somewhat similar fashion, as both are Arrhenius processes, albeit with disparate activation energies. In fact, analogous salt plasticization effects have been reported for chain diffusion into a PEM.[48] Moreover, an isothermal calorimetric study by Laugel *et al*.[49] demonstrated that conditions leading to linear film growth, as a result of small chain penetration into PEM, are more exothermic than ones exhibiting exponential growth, for which complexation can even be endothermic and driven entropically. Thus, the strength of interactions control not only phase behavior in the bulk, but also the kinetics of PEM growth. During the growth of a PAA/PDMAEMA film at pH 3, shown in Figure 2-3, there is a noticeable region of exponential growth preceding the transition towards linear growth at around deposition step 5, implying that incoming chains from the solution are able to explore the whole film thickness via diffusion during the first few deposition steps. Forming a complex coacervate at pH 3, chains in PAA/PDMAEMA complex have sufficient mobility, which allows for sufficient diffusion of chains during film growth in PAA/PDMAEMA, in agreement with the exponential growth kinetics at pH 3. At pH 5 and 6, the overall strength of interactions in PAA/PDMAEMA is so high, that precipitates appear in bulk in the absence of added salt. Therefore, it is plausible that the same strong interactions responsible for glassy dynamics of PAA/PDMAEMA complexes at pH 5 and 6 in the bulk

hinder chain diffusion during alternate deposition steps, thereby slowing down the growth kinetics and blunting its exponential character, relative to the behavior at pH 3. Yet, the growth of PAA/PDMAEMA films retains its exponential character, despite slowing, while the nature of complex phase changes as pH is raised from 3 to 6. Even if the interactions during PEM growth of PAA/PDMAEMA respond to pH in a similar fashion as in bulk, they need not lead to identically fast dynamics. Indeed, the interactions in bulk complexes of PAA/PDMAEMA at pH 5 and 6 are strong enough to arrest the dynamics and lead to precipitation while similar interactions at the same conditions are not enough to suppress chain diffusion during film growth enough to prevent films from growing exponentially. A similar mismatch between the dynamics in bulk and LbL growth behavior can be inferred for the PAA/PDADMAC system. For PAA/PDADMAC, the overall strength of interactions decreases continuously as pH is raised from 3 to 9, leading to progressively faster dynamics in bulk and formation of well-equilibrated coacervate phases, as indicated in Figure 1-1B. However, the non-monotonic LbL growth kinetics of PAA/PDADMAC as pH increases from 3 to 9 suggest that such a trend of faster dynamics in bulk with increased pH does not apply to LbL growth rates for PAA/PDADMAC. In fact, the LBL growth rate of PAA/PDADMAC slows and becomes linear as pH is shifted into the basic region; see Figure 2-4. Even though coacervation in bulk indicates fast dynamics, films assembled at corresponding conditions will not necessarily grow exponentially. Therefore, fast dynamics in bulk does not necessarily imply fast LbL film growth or vice versa.

The strength of predominantly electrostatic interactions at pH 7 decreases monotonically for both the PE pairs as the KCl concentration is increased, thereby accelerating the dynamics of both the bulk complex phase and the PEM growth. Interestingly, however, both PE pairs exhibit a non-monotonic variation of LbL growth rate with salt. In fact, for both pairs, increasing KCl concentration accelerates the LbL dynamics, resulting in faster growth rates with exponential character, or equivalently higher mass increment deposited per layer, Figure 2-7, up to 20-30% of the critical KCl concentration after which the growth rate decreases and tends to progressively lose its exponential character. Note that, in bulk, the faster dynamics resulting from the plasticization effect of KCl, leads to either a transition from precipitation to coacervation or to looser coacervates. A similar plasticization effect of salt on PEM dynamics, results in accelerated film growth at low KCl concentrations, which is followed by deceleration at high KCl concentrations. No clear correlation is found, however, between the transition between

precipitation and coacervation in the bulk complex phase and linear-to-exponential transition in the PEM growth kinetics.

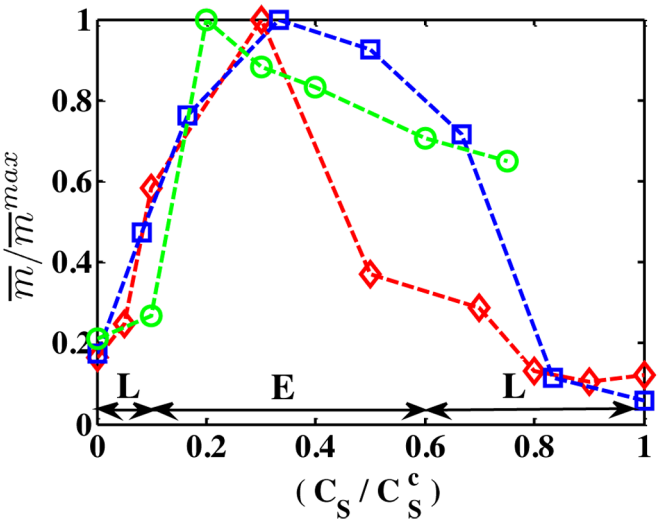

Figure 2-7: Mass density per layer of LbL assembled PEM films normalized by the maximum mass density versus KCl concentration normalized by the critical KCl concentration for each PE pair at pH 7 at room temperature. The red diamonds, blue squares and green dots represent PAA/PDMAEMA, PAA/PDADMAC and PAA/PAH, respectively. The letters L and E represent linear and exponential growth regimes, respectively.

The structures produced in bulk mixtures are different from those in LbL films, whose behavior is influenced by preparation history and by differences in composition. The actual composition of the PEM might deviate from the ratio of PEs in deposition solutions, i.e. equimolarity, which was used in the LbL study in this work. However, the precipitation-to-coacervation transition was shown to be totally insensitive to overall composition of mixtures, Figure 2-2. As a result, differences in composition of the PEM and the corresponding equimolar bulk mixture cannot completely explain the lack of correspondence between the trends in bulk and PEM assembly. While we expect some correspondence between structures of bulk phases and the corresponding LbLs, there is no necessity that trends will be identical or even well correlated.

The PE flux during a dipping step is generally controlled by the thermodynamic diffusion driving force weighted by a mutual diffusivity prefactor between the incoming PE chain and the network. In general, a stronger interaction of free chains with the PEM network both increases the driving force for diffusion and also lowers the diffusivity of PEs into the PEM network. It is the coupled effect of these two factors that determines the overall flux during LbL growth. Thus, it is understandable that the strength of interaction affects growth kinetics of the PEM non-monotonically, while monotonically speeding up the dynamics in bulk. The effect of increasing

KCl on LbL deposition is thus twofold, namely 1) an increase in diffusivity caused by film plasticization and 2) a reduction of thermodynamic diffusion driving force. The balance of these two effects manifests itself in the non-monotonic effect of KCl on growth kinetics as seen in all the three cases examined. We believe that this hypothesis helps explain the trends in the phase behavior and PEM growth kinetics.

Unlike salinity, variation of pH in the absence of KCl alters both the nature and strength of interactions in a complicated way. The simpler pattern is shown by PAA/PDADMAC, in which, as explained earlier, interactions weaken monotonically as pH increases with the strongest interactions at pH 3, producing a precipitate at this pH. So, for PAA/PDADMAC in the no salt limit studied here, for PEM growth, we expect the diffusion driving force to fall and diffusivity to increase monotonically with pH. At pH 5, weaker interactions allow for formation of a bulk coacervate phase. During PEM growth at pH 5, the boost to diffusivity exceeds the fall in diffusion driving force and the growth kinetics peaks at pH 5. A further increase in degree of ionization of PAA evidently decreases the driving force more than it increases diffusivity and we observe slower, linear, kinetics than at pH 5. The bulk dynamics, however, is unaffected by gradients in composition and the bulk remains a coacervate. C_S^c for PAA/PDMAEMA decreases continuously with pH while the precipitate-to-coacervate transition peaks at pH 4-6. Therefore, the PAA/PDMAEMA system shows a more complex dependence of phase behavior on pH, making it difficult to establish how strength of interactions varies with pH.

Despite the differences in chemistry, PEM film growth for both systems shows a similar "universal" non-monotonic dependence of normalized growth rate on normalized KCl concentration at pH 7, as shown in Figure 2-7. To further check the universality of the non-monotonicity in growth rate as a function of salt, we studied the effect of ionic strength on one more pair, PAA/PAH, details of which are outlined in the appendix 2.5.2. The PAA/PAH normalized growth kinetic data, when superposed on Figure 2-7 (green circles), show reasonable alignment with the behavior of the other two pairs, PAA/PDMAEMA and PAA/PDADMAC, thereby raising confidence in the universal effect of salinity on PEM growth at pH 7.

2.5 Appendix

2.5.1 Ellipsometry for PAA/PDMAEMA pair at pH 5 and pH 6

Ellipsometry was carried out to monitor the growth of salt-free PAA/PDMAEMA system at pH 5 and 6. Ellipsometric responses, Ψ and Δ, were acquired over a wavelength range from 600 to 1100 nm, simultaneously at a 75° angle of incidence over dry films using a Woolam (M2000V, NE, USA) ellipsometer. The films were grown on a silica wafer by submerging into alternate PAA and PDMAEMA solutions. The concentration and duration of deposition is identical to QCM experiments in the text. Ψ and Δ were recorded as a function of wavelength λ and were fitted to a two-layer model consisting of silica/PEM in order to extract the PEM properties which was taken to be a homogenous medium (Cauchy material) with a given height, d, and a wavelength dependent refractive index, $n_{PEM} = A_{PEM} + B_{PEM} / (\lambda / \mu m)^2$. d, A_{PEM}, B_{PEM} were simultaneously fitted by the software provided by the manufacturer. The results of ellipsometry are presented in Figure 2-A-1.

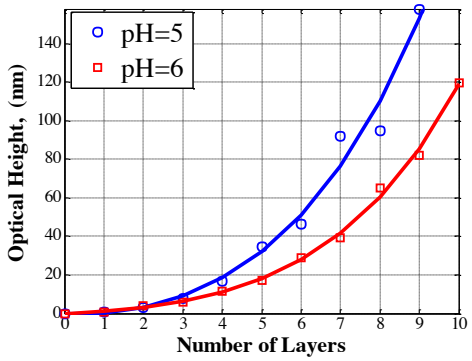

Figure 2-A-1: Ellipsometry measurements of film height for PAA/PDMAEMA LbL layers at room temperature in the absence of salt.

2.5.2 Effect of Ionic Strength at pH 7 for PAA/PAH pair

Interestingly, a similar non-monotonic response of the growth rate to salt concentration is observed for PAA/PAH as was observed for the other two PE pairs at pH 7. In fact, for PAA/PAH, precipitation occurs at salt concentrations of up to 200 mM KCl while the corresponding LbL growth is slow, but exponential; see Figure 2-A-4. For KCl concentrations above 200 mM, growth is faster and initially has an exponential character while the corresponding complex phases are coacervates with increasing fluidity and transparency with increased salt. At the highest salt concentrations, above 400 mM, growth begins to slow down, and loses its exponential character after multiple layers have deposited. Complexation is visible even in the presence of 2 M KCl, which indicates the strength of the electrostatic interactions between PAA and PAH due to PAH being a primary amine, as discussed earlier.

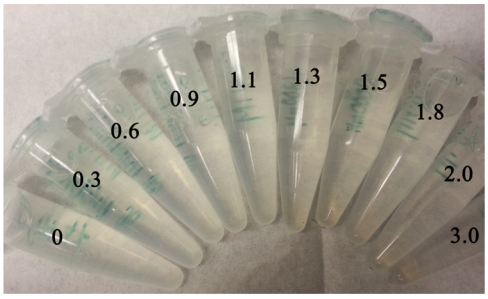

Figure 2-A-2: Phase behavior of PAA/PDMAEMA mixtures with equi-molar concentrations of monomers at pH 3 and room temperature. Numbers indicate the KCl concentration in moles, M.

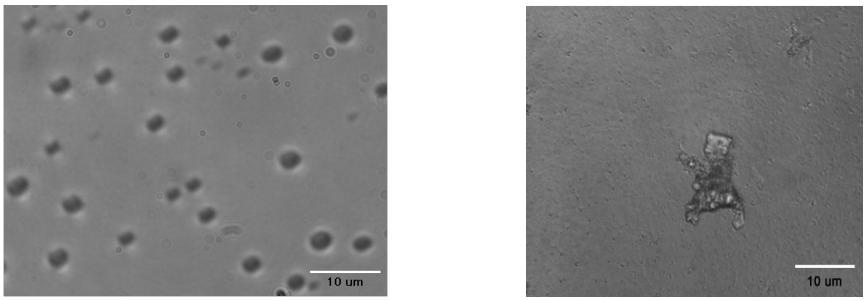

Figure 2-A-3: Typical optical micrographs used in distinguishing a coacervate phase from a precipitate phase for PAA/PDMAEMA at PH 7 at 900 mM KCl salt (left), and PAA/PDMAEMA at PH 5 at 300 mM KCl salt (right).

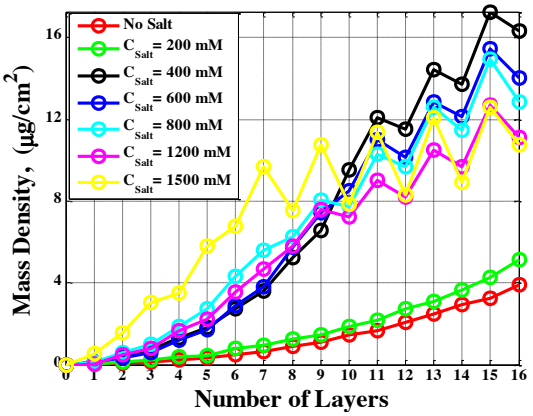

Figure 2-A-4: Effect of KCl concentration on PEM growth kinetics

2.6 References

[1] Overbeek, J.T.G; Voorn, M.J. *J. Cell. Compar. Physiol.* **1957**, 49, 7–22.

[2] Van der Gucht, J.; Spruijt, E.; Lemmers, M.; Cohen Stuart, M.A. *J. Coll. Int. Sci.* **2011**, 361, 407–422.

[3] Spruijt, E.; Westphal, A.H.; Borst, J.W.; Cohen Stuart, M.A.; Van der Gucht, J. *Macromolecules* **2010**, 43, 6476–4684.

[4] Kudlay, A.; Olvera de la Cruz, M. *J. Chem. Phys.* **2004**, 120, 404–412.

[5] Castelnovo, M.; Joanny, J.F. *Eur. Phys. J. E* **2001**, 6, 377–386.

[6] Chollakup, R.; Smitthipong, W.; Eisenbach, C.D.; Tirrell, M. *Macromolecules* **2010**, 43, 2518–2528.

[7] Chollakup, R.; Beck, B.J.; Dirnberger, K.; Tirrell, M.; Eisenbach, C.D. *Macromolecules* **2013**, 46, 2376–2390.

[8] Priftis, D.; Megley, K.; Laugel, N.; Tirrell, M. *J. Coll. Int. Sci.* **2013**, 398, 39–50.

[9] Priftis, D.; Tirrell, M. *Soft Matter* **2012**, 8, 9396–9405.

[10] Chen, Q.; Tudryn, G.J.; Colby, R.H. *J. Rheol.* **2013**, 57, 1441–1462.

[11] Spruijt, E.; Sprakel, J.; Lemmers, M.; Cohen Stuart, M.A.; van der Gucht, J. *Phys. Rev. Lett.* **2010**, 105, 208301.

[12] Colby, R.H.; Zheng, X.; Rafailovich, M.H.; Sokolov, J.; Peiffer, D.G.; Schwarz, S.A.; Strzhemechny, Y.; Nguyen, D. *Phys. Rev. Lett.* **1998**, 81, 3876–3879.

[13] Spruijt, E.; Cohen Stuart M.A.; van der Gucht, J. *Macromolecules* **2013**, 46, 1633–1641.

[14] Spruijt, E.; Leermakers, F.A.M.; Fokkink, R.; Schweins, R.; van Well, A.A.; Cohen Stuart M.A.; van der Gucht, J. *Macromolecules* **2013**, 46, 4596–4605.

[15] Baxandall, L.G. *Macromolecules* **1989**, 22, 1982–1988.

[16] Leibler, L.; Rubinstein, M.; Colby, R.H. *Macromolecules* **1991**, 24, 4701–4707.

[17] Kharlampieva, E.; Ankner, J.F.; Rubinstein, M.; Sukhishvili, S.A. *Phys. Rev. Lett.* **2008**, 100, 128303.

[18] Lavalle, Ph.; Picart, C,; Mutterer, J.; Gergely, C.; Reiss, H.; Voegel, J.C.; Senger, B.; Schaaf, P. *J. Phys. Chem. B* **2004**, 108, 635–648.

[19] Hoda, N.; Larson, R.G. *J. Phys. Chem. B.* **2009**, 113, 4233–4241.

[20] Haynie, D.T.; Cho, E.; Waduge, P. *Langmuir* **2011**, 27, 5700–5704.

[21] Schlenoff, J.B.; Dubas, S.T. *Macromolecules* **2001**, 34, 592–598.

[22] Bucur, C.B.; Sui, Z.; Schlenoff, J.B. *J. Am. Chem. Soc.* **2006**, 128, 13690–13691.

[23] Guzman, E.; Ritacco, H.; Ortega, F.; Svitova, T.; Radke, C.J. Rubio, R.G. *J. Phys. Chem. B* **2009**, 113, 7128–7137.

[24] Jaber, J.A.; Schlenoff, J.B. *J. Am. Chem. Soc.* **2006**, 128, 2940–2947.

[25] Lehaf, A.M.; Hariri, H.H.; Schlenoff, J.B. *Langmuir* **2012**, 28, 6348–6355.

[26] Xu, L.; Pristinski, D.; Zhuk, A.; Stoddart, C.; Ankner, J.F.; Sukhishvili, S.A. *Macromolecules* **2012**, 45, 3892–3901.

[27] Sukhishvili, S.A.; Kharlampieva, E.; Izumrudov, V. *Macromolecules* **2006**, 39, 8873–8881.

[28] Mjahed, H.; Voegel, J.C.; Chassepot, A.; Senger, B.; Schaaf, P.; Boulmedais, F.; Ball, V. *J. Coll. Int. Sci.* **2010**, 346, 163–171.

[29] Park, S.Y.; Barret, C.J.; Rubner, M.F.; Mayes, A.M. *Macromolecules* **2001**, 34, 3384–3388.

[30] Sauerbrey, G. *Z. Phys.* **1959**, 155, 206–222.

[31] Petrov, A.I.; Antipov, A.A.; Sukhorukov, G.B. *Macromolecules* **2003,** *36,* 10079-10086.

[32] Bieker, P.; Schonhoff, M. *Macromolecules* **2010**, 43, 5052–5059.

[33] Xu, L.; Ankner, J.F.; Sukhishvili, S.A. *Macromolecules* **2011**, 44, 6518–6524.

[34] Dubas, S.T.; Schlenoff, J.B. *Macromolecules* **2001**, 34, 3736–3740.

[35] Schoeler, B.; Kumaraswamy, G.; Caruso, F. *Macromolecules* **2002**, 35, 889–897.

[36] Sui, Z.; Saloum, D.; Schlenoff, J.B. *Langmuir* **2003**, 19, 2491–2495.

[37] Kovacevic, D.; van der Burgh, S.; de Keizer, A.; Cohen Stuart, M.A. *J. Phys. Chem. B.* **2003**, 107, 7998–8002.

[38] Kovacevic, D.; van der Burgh, S.; de Keizer, A.; Cohen Stuart, M.A. *Langmuir* **2002**, 18, 5607–5612.

[39] Ghostine, R.A.; Markarian, M.Z.; Schlenoff, J.B. *J. Am. Chem. Soc.* **2013**, 135, 7636–7646.

[40] Alonso, T.; Irigoyen, J.; Iturri, J.J.; Larena, I.L.; Moya, S.E. *Soft Matter* **2013**, 9, 1920–1928.

[41] Picart, C.; Lavalle, Ph.; Hubert, P.; Cuisinier, F. J. G.; Decher, G.; Schaaf, P.; Voegel, J.C. *Langmuir* **2001**, 17, 7414–7424.

[42] Xie, A.F.; Granick, S. *Macromolecules* **2002**, 35, 1805–1813.

[43] Rmaile, H.H.; Schlenoff, J.B. *Langmuir* **2002**, 18, 8263–8265.

[44] Petrov, A.I.; Antipov, A.A.; Sukhorukov, G.B. *Macromolecules* **2003**, 36, 10079–10086.

[45] Kharlampieva, E.; Kozlovskaya, V.; Ankner, J.F.; Sukhishvili, S.A. *Langmuir* **2008**, 24, 11346–11349.

[46] Litmanovich, E.A.; Chernikova, E.V.; Stoychev, G.V.; Zakharchenko, S.O. *Macromolecules* **2010**, 43, 6871–6876.

[47] Jha, P.K.; Desai, P.S.; Li, J.; Larson, R.G. *Polymers* **2014**, 6, 1414–1436.

[48] Zan, X.; Peng, B.; Hoagland, D.A.; Su, Z. *Polym. Chem.* **2011**, 2, 2581–2589.

[49] Laugel, N.; Betscha, C.; Winterhalter, M.; Voegel, J.C.; Schaaf, P.; Ball, V. *J. Phys. Chem. B.* **2006**, 110, 19443–19449.

Chapter 3: A Molecular Thermodynamic Model of Complex Coacervation*

3.1 Introduction

Despite the rapidly growing applications, modeling of PEC has been slow to keep up. This is in large part due to highly correlated nature of unlike charges in the complex as well as a significance of chemistry specificity, see chapter 2. In particular, functional groups along oppositely charged PEs can bind together to form inter-chain ionic cross-links or "ion-pairs," the strength of which is strongly dependent on the chemistry of the chains involved. Cross-chain ion-pairs, referred to as simply "ion-pairs" hereafter, impart viscoelasticity to complex coacervates with their viscosity and storage modulus shown to decrease steadily as ion-pairs diminish with addition of salt.[1–3] Counterion activity in single-PE solutions deviates strongly from ideal behavior[4] resulting from localization (condensation) of counterions along polymer chains,[5] lowering the effective chain charge density and mobility of counterions. "Counterion condensation" (CC) is chiefly controlled by a competition between loss of counterion translational entropy and monomer electrostatic repulsion[6] as well as gain in dipole polarization energy upon CC, the magnitude of which again depends on the physiochemistry of counterions and PE.[7] Throughout this work, the term "ion pairing" or "ion pair" (IP) refers to binding of charges on oppositely charged PEs, while "counterion condensation" (CC) refers to binding of a small salt ion to an oppositely charged PE.

In the framework of the classical Voorn-Overbeek (VO) model proposed in 1957,[8] complex coacervation is driven primarily by the small translational entropy of polymer chains and the reduction in electrostatic energy as described by the Debye-Hückel (DH) theory of simple electrolytes. The VO model neglects finite ion sizes, chain connectivity, and the highly

* This chapter is adapted from my publication in Macromolecules *49* (**2016**) pp. 9706-9719.

correlated nature of opposite charges at short length scales present in a complex coacervate, including CC and IP and thus much of the chemistry-specificity of the components involved cannot be accommodated. Furthermore, charge densities of either PE chain type remain constant in the VO model thus neglecting the charge regulation effects induced by the local environment especially in weakly dissociating PEs. Despite its clear shortcomings, the predictions of the VO model can be brought into good qualitative[9,10] and quantitative[11] agreement with experiments by the liberal use of adjustable parameters and a possible fortuitous cancellation of competing neglected effects the nature of which is poorly understood.[12]

We refer the reader to a recent review for a detailed discussion of the extensions to VO model and modern developments in theory of complex coacervation.[12] Chain connectivity effects missing in the VO model have been addressed utilizing the random phase approximation (RPA) for ideal chains, the accuracy of which is limited to weak and long-ranged fluctuations and low charge densities. Chain connectivity has been recently evaluated explicitly at the Gaussian level in the high wavevector limit and shown to alter the long-ranged electrostatics dramatically at low salt[13] compared to DH expression derived for simple salts, but CC, IP and charge regulation was not considered in this work. The short-range electrostatic correlations can be described by treating CC as a reversible chemical reaction. This has been done both for CC in single-PE solutions[14,15] and for IP in oppositely charged PE mixtures.[16−18] We note that in their model, Jha *et al*. accounted for the size mismatch between components as well as the salt-induced ionization of PEs.[19] They did so by using experimentally obtained acidity constants pK_A^*s treated as explicit functions of salinity. They, however, did not consider CC or IP.

The VO model and subsequent extensions discussed above are based on the assumption that PE complexation is driven by long ranged electrostatic field fluctuations of freely interacting charges. However, simulation and experimental studies[20, 21] explain PE complexation in terms of counterion release (CR) whereby PEs shed their bound counterions while forming IP's with the oppositely charged PE. Long ranged electrostatic fluctuations are largely irrelevant in the CR mechanism since bound charges are practically free charges removed from the system. Following the work of Semenov and Rubinstein on associative polymers,[22] a molecular thermodynamic model has been proposed[23] for cross-associating polymers such as oppositely charged PEs undergoing IP but this theory did not address long-ranged electrostatics, the effect

of salt counterions, CC and charge regulation. A unified theory of PE complex coacervation reconciling the two aforementioned views is still lacking. Moreover, both IP and CC as well as charge regulation have not been considered simultaneously in the context of PE complex coacervation, to the best of our knowledge.

Using liquid state (LS) integral theory, Perry and Sing recently demonstrated that coacervate formation is enhanced while CR intensifies as chains become more rigid, promoting strong correlations between oppositely charged groups.[24] Field-theoretic methods, LS integral equation methods, and their hybrid variants are sophisticated, yet they do not provide closed-form expressions for thermodynamic function explicitly in terms of macroscopic variables for free energy. Closed-form thermodynamic functions that are mathematically tractable are desirable for the development of advanced transport models of PE multilayer build-up, where derivatives of free energy needed to be calculated sufficiently fast to obtain driving forces.[25]

Inspired by a growing body of calorimetric and potentiometric titration studies on the complexation reaction in various systems,[26–28] we propose a molecular model yielding closed-form free energy expressions for a solvated mixture of PEs and ions, which incorporates short-ranged electrostatic interaction, namely CC, IP and, in case of weakly dissociating PEs, charge regulation effects on protonation. Not only do the preceding charge association phenomena need to be incorporated in a unified theory of complex coacervation to allow for consistency with thermodynamic measurements, we demonstrate in this work that they provide a picture of PE complex coacervation that can be driven entirely by CR, i.e. a competition between IP and CC. This chapter is organized as follows: in the second section, we lay out the model. In the third, we first demonstrate that our model captures the charge regulation effects observed experimentally in potentiometric titration of single-phase systems. Later, we consider phase separation of both strongly and weakly dissociating oppositely charged PEs and compare our model predictions to experimental phase diagrams available for two such systems. Finally, in the fourth section, we summarize and draw conclusions.

3.2 Theory

We consider here a system comprising polycation and polyanion chains denoted by "*C*" and "*A*", respectively, counterions accompanying the chains, coions introduced by added salt and the water molecules, represented by "*W*." For simplicity, we assume counterions and coions of like

charge are of the same chemical identity so that we refer to them collectively as counterions hereafter. All ions are monovalent and the positive and negative simple ions are designated by "+" and "−" symbols. Further, we take both PEs to be weakly dissociating and monoprotic. We shall demonstrate that strong dissociation is a limiting case of weakly dissociating PEs and we thus proceed assuming the latter for generality. We consider four additive contributions to the normalized Helmholtz free energy density *f*, each of which is described separately:

$$f \equiv \frac{l^3 F}{V k_B T} = f^{EVO} + f^C + f^{\infty} + f^B \tag{3-1}$$

Here l denotes the cubic root of the volume of water molecules ~ 0.31 nm taken as the reference length scale and V is the solution volume. The first contribution is here called the 'extended VO' (EVO) free energy density f^{EVO}, given by eqn. 3-2 below. It includes the translational entropy of components and long-ranged *electrostatic* field fluctuations (electrostatic screening) contained in the original VO theory,[8] although the electrostatic term is slightly improved from the lowest order expression of Voorn and Overbeek, as suggested by by Jha et al.[19] In addition, the EVO free energy includes the short-ranged van der Waals (VdW) interactions suggested by Veis[29] and Spruijt et al.[9] Following Jha et al.[19] the translational entropy of component '*i*' given in terms of volume fractions, ϕ_i is inversely weighted by ω_i, the ratio of the corresponding molecular volume to that of solvent.

$$f^{EVO} = f^T + f^{\chi} + f^{DH} = \sum_{i=A,C,W,\pm,OH,H_3O} \frac{\phi_i ln \phi_i}{N_i \omega_i} + \sum_{ij} \chi_{ij} \phi_i \phi_j - \frac{1}{4\pi\bar{\omega}} \left[\ln(1+\bar{\kappa}) - \bar{\kappa} + \frac{\bar{\kappa}^2}{2} \right] \tag{3-2}$$

N_i represents the polymerization index of i in eqn. (3-2) and is taken to be unity for all non-polymeric components; ω_i for a polymeric species is thus the ratio of the volume of the monomer to the volume of a water molecule. Short-ranged VdW interactions f^{χ} are quantified by Flory-type interaction parameter χ_{ij} between species. The third term in eqn. (3-2) f^{DH} is the extended DH free energy expression employed by Jha *et al*.[19] that captures electrostatic field fluctuations for a constellation of charges with a mean volume of $\bar{\omega} l^3$ where any explicit consideration of the connectivity effects is neglected. We simply retain the DH expression for long-ranged (screening) electrostatic free energy in the EVO model. (Connectivity can be encompassed implicitly in our model, however, through fits of standard state free energies or equilibrium constants, as will become apparent in what follows.) The non-dimensional reciprocal Debye length denoted by $\bar{\kappa}$ is given below:

$$\bar{\kappa}^2 \equiv \kappa^2 l^2 \bar{\omega}^{2/3} = \frac{4\pi \ell_B \bar{\omega}^{2/3}}{l} \sum_{i=A,C,\pm,OH,H_3O} \frac{\sigma_i \phi_i}{\omega_i} \quad (3\text{-}3)$$

The charge density σ_i of each ionic species is unity except for the PE monomers, where σ_i is the fraction of monomers that carry an unpaired charge, and is controlled by the extent of ionization (which is $1 - \alpha_{AH}$ for polyanions or α_{CH} for polycations), and by CC, as well by as the fraction of bare charges paired with PE charges of opposite sign, given by eqns. (3-4) and (3-5).

$$\sigma_A = f_A(1 - \beta_A) = (1 - \alpha_{AH})\,(1 - \alpha_{A+})(1 - \beta_A) \quad (3\text{-}4)$$

$$\sigma_C = f_C(1 - \beta_C) = \alpha_{CH}\,(1 - \alpha_{CH-})(1 - \beta_C) \quad (3\text{-}5)$$

Here f_i denotes the overall fraction of repeat units of i available for IP. At equilibrium, a portion of the simple ions condense along PEs, losing their translational entropy in the process. Only free simple ions are active in electrostatic screening and thus contribute to the reciprocal Debye length. When chains become sufficiently charged, short-ranged electrostatic effects become important and a portion of the simple ions as well as the PE charges become highly localized along chains of opposite charge to form electrostatic dipoles and multipoles. We assume that all the bare charges, condensed simple ions, as well as ion-pairs follow an annealed distribution along the chains such that they break up and reform in a dynamic equilibrium; see Figure 3-1. Therefore, any given polyanion site could be protonated with probability α_{AH}, which is the fraction of polyanion sites that are protonated. A deprotonated PE group could be carrying a condensed counterion; the probability that a PE site is both deprotonated and carrying a counterion is thus $(1 - \alpha_{AH})\,\alpha_{A+}$. Also, there is a probability β_A that a bare deprotonated polyanion group forms an ion-pair with a polycation monomer. Similarly, there is a probability α_{CH} that a given polycation site is protonated and thus charged while the probability of finding a site that is both protonated and carrying a condensed counterion is $\alpha_{CH}\alpha_{CH-}$. Note that in this subscript notation, the "–" stands for the negatively charged condensed ion, and does not indicate a charge on the polymer. The subscript "*CH*" means that a proton is bound to the neutral cationic monomer "*C*". In this notation, we truncate the "+" from the "H+", since we use the symbol "+" to designate the cationic salt ion. Lastly, there is a probability β_C that a bare protonated polycation group forms an ion-pair. Association and complexation are illustrated schematically in Figure 3-1.

In general, the charge densities σ_i's, given by eqns. (3-4) and (3-5) in our model, are functions of pH, salinity and oppositely charged PE. The charge density of PEs in our model are not known a priori and need to be obtained self-consistently as explained later in this section. This stands in sharp contrast to the original VO model where the charge densities need to be prescribed. Jha et al.[19] treated PE charge densities as explicit functions of salinity and pH but ignored CC and role of oppositely charged PE (IP). Conservation of total ions yields two relations between the total volume fraction of the counterions, which are the parameters in eqns. (3-6) and (3-7) superscripted with "*o*", and the free and bounds ions.

$$\phi_+^o = \phi_+ + \phi_A(1-\alpha_{AH})\alpha_{A+}\left(\frac{\omega_+}{\omega_A}\right) \tag{3-6}$$

$$\phi_-^o = \phi_- + \phi_C\alpha_{CH}\alpha_{CH-}\left(\frac{\omega_-}{\omega_C}\right) \tag{3-7}$$

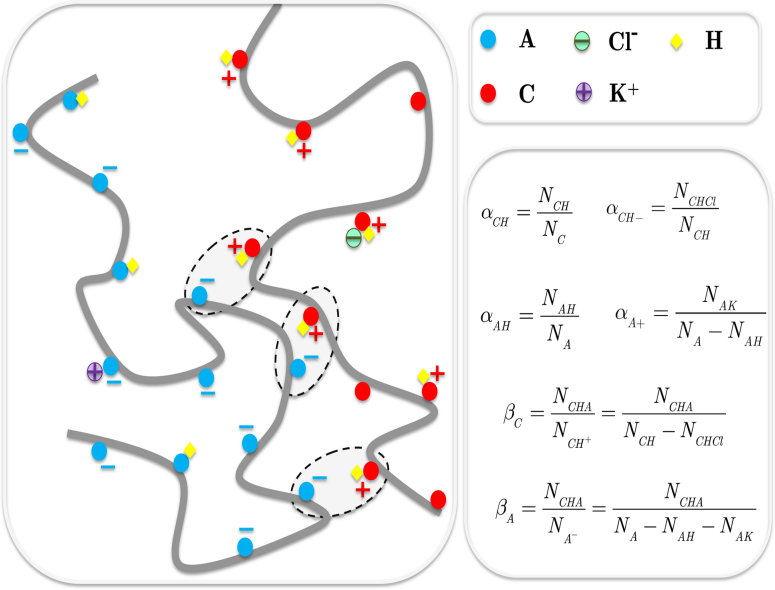

Figure 3-1: Definitions of extents of protonation of repeat units, CC (with counterions chosen to be potassium and chloride only for demonstration) and IP for two representative chains. Not shown are freely floating counterions, hydroxyl and hydronium ions and water. The dashed ellipses represent ion-pairs. N_A and N_C denote the total number of repeat units.

Here we assume a 1:1 stoichiometry in IP, which is plausible for most systems,[26] even though deviations from a 1:1 stoichiometry have been observed in calorimetric measurements.[28,30] The 1:1 stoichiometry of ion-pair formation between two oppositely charged PEs affords the following constraint, relating the extents of association/dissociation.

$$\phi_C\alpha_{CH}(1-\alpha_{CH-})\beta_C\omega_A = \phi_A(1-\alpha_{AH})(1-\alpha_{A+})\beta_A\omega_C \tag{3-8}$$

The remaining contributions in eqn. (3-1), which we append to the EVO model, are respectively, I) the combinatorial entropy associated with the distribution of ion-pairs and condensed simple ions along the chains deriving from the short-ranged electrostatic correlations, II) changes in free energy due to association/dissociation phenomena modeled here as reversible chemical reactions arising from strong short-ranged electrostatic correlations with the exception of water self-dissociation and III) Born (solvation) free energy of ions. Note that we have also included the hydronium and hydroxyl ions volumes in eqn. (3-2), the sizes of which are taken to be equal to that of water. These species are included to allow for charge regulation effects. The chemical identity of functional groups and counterions change upon association/dissociation of ions, described by six linearly independent reversible reactions: protonation/deprotonation of each PE eqns. (3-9) and (3-10), CC on each PE eqns. (3-11) and (3-12) IP eqn. (3-13) and water self-dissociation eqn. (3-14), which is needed for completeness.

$$AH + H_2O \overset{\Delta G^{\infty}_{AH}}{\Longleftrightarrow} H_3O + A \tag{3-9}$$

$$C + H_2O \overset{\Delta G^{\infty}_{CH}}{\Longleftrightarrow} OH + CH \tag{3-10}$$

$$(A+) \overset{\Delta G^{\infty}_{A+}}{\Longleftrightarrow} A + (+) \tag{3-11}$$

$$(CH-) \overset{\Delta G^{\infty}_{CH-}}{\Longleftrightarrow} CH + (-) \tag{3-12}$$

$$A + CH \overset{\Delta G^{\infty}_{ip}}{\Longleftrightarrow} CHA \tag{3-13}$$

$$2H_2O \overset{\Delta G^{\infty}_{w}}{\Longleftrightarrow} H_3O + OH \tag{3-14}$$

Note that the symbols used for the charged reactants and products in eqns. (3-9) through (3-14) do not indicate the charge that they may possess; for instance, a bare deprotonated PE repeat unit, denoted by "*A*", carries a negative charge while a protonated polycation monomer, denoted "*CH*", is positively charged, despite the lack of any explicit indication of their charges on these symbols. As remarked earlier, the simple salt cations and anions are represented simply by "+" and "–", respectively. Oppositely charged counterions or PE groups can neutralize the bare charged groups along the chains, thus forming monomer-simple ion dipoles, $(A+)$ and $(CH-)$ (which are neutral), or neutral monomer-monomer ion-pairs *CHA*. The quantities appearing over

the double-sided arrows in eqns. (3-9) through (3-14) denote the standard free energy change in k_BT unit associated with the corresponding reactions. The standard free energies of all reactions are specified at a temperature T and in the infinite dilution limit, i.e. in the limit of $\phi_w \to 1$, and hence are denoted by the superscript '∞' hereafter. In the latter limit, ions are solvated by pure water and the dielectric constant and Bjerrum length tend to ϵ_r^w and ℓ_B^w, respectively. The contribution to free energy due to chemical reactions, f^∞ is the sum of the standard free energies of the association/dissociation equilibria each weighted by the appropriate reaction extents and the normalized concentrations as below:

$$f^\infty = \left(\phi_{H_3O} + \frac{\alpha_{AH}\phi_A}{\omega_A}\right)\Delta G_w^\infty + \frac{\alpha_{CH}\phi_C}{\omega_C}\Delta G_{CH}^\infty - \frac{\alpha_{AH}\phi_A}{\omega_A}\Delta G_{AH}^\infty - \frac{\alpha_{CH}\alpha_{CH-}\phi_C}{\omega_C}\Delta G_{CH-}^\infty - \frac{(1-\alpha_{AH})\alpha_{A+}\phi_A}{\omega_A}\Delta G_{A+}^\infty + \frac{\alpha_{CH}(1-\alpha_{CH-})\beta_C\phi_C}{\omega_C}\Delta G_{ip}^\infty \quad (3\text{-}15)$$

Note that the standard free energies do not include the translational entropy of reactants and products as they have already been accounted for in f^{EVO}. The standard free energies in the infinite dilution limit used above are conceptually equivalent to bond energy and dielectric mismatch parameters introduced by Semenov and Rubinstein[22] and Muthukumar,[31] respectively. They should be in principle independent of composition, provided that the model captures all other contributions to the total free energy adequately. However, they can very well depend on the extents of association/dissociation equilibria due to the mean-field treatment employed here wherein all monomers are treated as if disconnected. (The effect of the connectivity could be captured phenomenologically in the standard free energies by allowing them to depend on polymer molecular weight, for example). In appendix 3.4.3, we demonstrate that the front factor in the first term of eqn. (3-15) may be written equivalently in terms of hydroxyl volume fraction and α_{CH}, using electroneutrality and incompressibility conditions.

The combinatorial entropy associated with the short-ranged correlations along PE chain are treated in a mean-field fashion wherein the connectivity of the chains is neglected, following the earlier works on self-associating[22] and cross-associating polymers.[23] In appendix 3.4.2, we demonstrate that short-ranged free energy f^C is obtained as the sum of five contributions each associated with one of the five association/dissociation equilibria represented by eqns. (3-9) through (3-13), given by eqn. (3-16)

$$f^C = -\frac{l^3 \ln Z}{V} = f_{AH} + f_{CH} + f_{A+} + f_{CH-} + f_{ip} \tag{3-16}$$

The first two terms on the right side of eqn. (3-16) are entropic contributions of protonation /deprotonation equilibria, eqns. (3-9) and (3-10), given by eqns. (3-17) and (3-18).

$$f_{AH} = \frac{\phi_A}{\omega_A}[\alpha_{AH}\, ln\, \alpha_{AH} + (1-\alpha_{AH})\, ln(1-\alpha_{AH})] \tag{3-17}$$

$$f_{CH} = \frac{\phi_C}{\omega_C}[\alpha_{CH}\, ln\, \alpha_{CH} + (1-\alpha_{CH})\, ln(1-\alpha_{CH})] \tag{3-18}$$

The third and fourth terms on the right hand side of eqn. (3-16) arise from entropic free energy associated with the CC equilibria along polyanions and polycation chains, respectively, represented by eqns. (3-19) and (3-20).

$$f_{A+} = \frac{\phi_A}{\omega_A}(1-\alpha_{AH})[\alpha_{A+}\, ln\, \alpha_{A+} + (1-\alpha_{A+})\, ln(1-\alpha_{A+})] \tag{3-19}$$

$$f_{CH-} = \frac{\phi_C \alpha_{CH}}{\omega_C}[\alpha_{CH-}\, ln\, \alpha_{CH-} + (1-\alpha_{CH-})\, ln(1-\alpha_{CH-})] \tag{3-20}$$

The last contribution in Eq. (3-16) derives from the distribution of ion-pairs along chains of both types, given by eqn. (3-21), where the last of the three terms, the one with a negative sign, derives from the IP bond probability (see appendix 3.4.2) favoring phase separation. (Note that the stoichiometric constraint, Eq. 3-8, would also allow Eq. (3-21) to be written in terms of the concentration of anion ϕ_A rather than cation ϕ_C.)

$$f_{ip} = (1-\alpha_{AH})(1-\alpha_{A+})[\,\beta_A \ln\,\beta_A + (1-\,\beta_A)\ln(1-\,\beta_A)] + \frac{\phi_C \alpha_{CH}}{\omega_C}(1-\alpha_{CH-})[\,\beta_C \ln\,\beta_C + (1-\,\beta_C)\ln(1-\,\beta_C)] - \frac{\phi_C \alpha_{CH}}{\omega_C}(1-\alpha_{CH-})\,\beta_C \ln\left[\phi_C \alpha_{CH}(1-\alpha_{CH-})\,\beta_C \left(\frac{\omega_A+\omega_C}{\omega_C}\right)\right] \tag{3-21}$$

The Born (self- or solvation) energy[32] of all ions f^B is simply the sum of the individual contributions of each ionic species. However, only the deviations of Born energy from that in the infinite-dilution limit need to be considered here. Again, the condensed counterions do not contribute to f^B as given by eqn. (3-22).

$$f^B = \frac{\ell_B - \ell_B^W}{2l} \sum_{i=A,C,\pm,OH,H_3O} \frac{\sigma_i \phi_i}{\omega_i^{4/3}} \tag{3-22}$$

The effective Bjerrum length, $\ell_B \equiv (e^2/4\pi\epsilon_r\epsilon_o k_B\, T)$ is lower in the polymer-rich phase, thus increasing the propensity of counterions to adsorb onto oppositely charged sites along the

chains.[31,33] Here e is the elementary charge, k_B the Boltzmann constant, T is the absolute temperature and ϵ_o is the vacuum permittivity. Both PEs are assumed to have similar dielectric constants $\epsilon_r^P = 3$ and that the relative dielectric constant of all other components is equal to that of water $\epsilon_r^w = 78$, and we further use a linear volume-averaged to evaluate the effective dielectric constant in each phase, eqn. (3-23) for simplicity.

$$\epsilon_r = \epsilon_r^w + (\epsilon_r^P - \epsilon_r^w)(\phi_A + \phi_C) \tag{3-23}$$

Note that eqn. (3-23) is only intended to capture the composition-dependence of the dielectric constant qualitatively. The remaining six equations needed to close the model mathematically are obtained by setting to zero the variation of Helmholtz free energy at constant volume with respect to 6 independent degrees of freedom, namely $\phi_{H_3O}, \alpha_{AH}, \alpha_{CH}, \alpha_{A+}, \alpha_{CH-}, \beta_C$, subject to the constraints introduced by eqns. (3-6)-(3-8), and electroneutrality and incompressibility given respectively by eqn. (3-24) and (3-25). The resulting six laws of mass action (LMA) are listed in Appendix. Electroneutrality allows us to eliminate the hydroxyl volume fraction throughout.

$$0 = \phi_{H_3O} - \phi_{OH} + \frac{\alpha_{CH}\phi_C}{\omega_C} - \frac{(1-\alpha_{AH})\phi_A}{\omega_A} + \frac{\phi_+^o}{\omega_+} - \frac{\phi_-^o}{\omega_-} \tag{3-24}$$

$$1 = \sum_i \phi_i = \phi_W + \phi_+^o\left(\frac{\omega_+ + 1}{\omega_+}\right) + \phi_-^o\left(\frac{\omega_- - 1}{\omega_-}\right) + \phi_A\left(\frac{\omega_A + \alpha_{AH} - 1}{\omega_A}\right) + \phi_C\left(\frac{\omega_C + \alpha_{CH}}{\omega_C}\right) + 2\phi_{H_3O} \tag{3-25}$$

The composition of free counterions appears in the LMA equations corresponding to CC equilibria, given in the Appendix 3.4.1 as eqns. (3-A-4) and (3-A-5), and is related to the total counterion composition introduced through the conservation constraints, eqns. (3-6) and (3-7). It can be readily verified that in the limiting case of a strongly dissociating polyanion, for sufficiently large K_A in eqn. (3-A-2), α_{AH} tends to zero asymptotically such that f_{AH} vanishes and the term proportional to ΔG_{AH}^{∞} in eqn. (3-15) becomes linear in composition and hence thermodynamically inconsequential. A similar argument can be made for a strongly dissociating polycation. Therefore, our model applies to both weakly and strongly dissociating PEs.

Since the main thrust of our model is the role of short-ranged electrostatics in driving complex coacervation, we have adopted the DH expression for long-ranged (screening) electrostatic free energy. Indeed, if CC and IP are proven to be the primary driving force for complex coacervation in some systems, a majority of charges could be neutralized by an opposite charge and thus do not contribute to long ranged electrostatic fluctuations whether or not connectivity is considered.

In our model, variations in conformational entropy of chains upon complex coacervation are not considered. This might be reasonable given that experimental SANS observations have confirmed that complex coacervation does not lead to a drastic stiffening or collapse of the chains, which continue to adopt nearly ideal Gaussian conformations over a range of molecular weight even in the coacervate phase.[34,35] we have also neglected the dipole-dipole electrostatic interactions as they can be somewhat captured through VdW interactions by using appropriate FH parameters in f^{χ}. In fact, Muthukumar demonstrated that interactions of freely rotating dipoles mainly in single-PE solutions act to lower the effective short-ranged excluded volume interaction parameter.[31] Lastly, our model does not accommodate inter-polyelectrolyte colloidal particles that can be formed in supernatant phases.

3.3 Results and Discussion

As a direct consequence of the incompressibility assumption, eqn. (3-25), the partial molar volume of each species is a constant and is equal to the corresponding molecular volume. Therefore, the molar concentration C_i is related to volume fractions according to eqn. (3-26).

$$\phi_i = \frac{C_i \omega_i l^3 N_{Avo}}{10^{24}} \tag{3-26}$$

where N_{Avo} is Avogadro's number and the characteristic length l = 0.31 nm. For convenience, we employ the p[.] function commonly used in analytical chemistry to quantify protonation and CC equilibrium constants of PEs expressed in (mol/liter), as below:

$$p[\cdot] \equiv -log_{10}\left(\frac{10^{24}}{l^3 N_{Avo}}[\cdot]\right) \tag{3-27}$$

The term $\frac{10^{24}}{l^3 N_{Avo}} \sim$ 55.56 (mol/L) in the logarithm converts the non-dimensional equilibrium constants in our model into ones expressed in (mol/L). Here N_{Avo} is Avogadro's number and the factor 10^{24} is the conversion factor from nm^3 into liter. Instead of standard free energies, the equilibrium constants of protonation/deprotonation equilibria as well as CC reactions in the infinite dilution limit are chosen as the main parameters and expressed using the p[.] function in this section. This choice of parameter representation is intended to connect the model parameters to the conventional terminology for reporting the ionization equilibria of weak PEs. Conversion between free energies and equilibrium constants at the infinite-dilution limit can be accomplished unambiguously using eqns. (3-A-1) through (3-A-6) in the Appendix 3.4.1.

We first demonstrate that charge regulation, missing from all earlier models, follows naturally from our model by solving LMA equations even in single-phase PE mixtures such as multilayer films or vesicles. Moreover, the next section serves as an illustration of how equilibrium constants of weak PE employed in our model could be extracted from fairly straightforward potentiometric titration of weak PEs and subsequently used in phase behavior predictions.

3.3.1 Charge Regulation in Single-Phase Mixtures

Unlike the corresponding low molecular weight monomers, PE chains become progressively harder to ionize as the extent of ionization increases,[36–38] such that acidity/basicity of sufficiently long PEs cannot be characterized by a single ionization constant, K_A for a polyanion chain, e.g. poly(acrylic acid) PAA, or K_C for polycations, e.g. poly(2-dimethylamino ethyl methacrylate) PDMAEMA. Experiments and theoretical studies have demonstrated that the apparent ionization constant for PAA and other weakly dissociating PEs in solution increase almost linearly as the extent of ionization of the chain increases, eqn. (3-28), implying that the chains become increasingly harder to ionize as charge fraction increases, relative to what is predicted by the Henderson-Haselbalch (HH) theory. The mean apparent ionization constant, denoted by the overbar in eqn. (3-28), can be simply taken as the pH at the halfway equivalence point, i.e., the point at which half the charges on the chain are neutralized.

$$pK_A^{\infty} = \overline{pK_A} + A(\gamma_A - 0.5) \tag{3-28}$$

The variable γ_A is here equal to the polyanion ionization fraction f_A in PE. (For other cases discussed later, we take it to be the net fraction σ_A of unpaired charges on the polyanion.) The prefactor A in eqn. (3-28) is generally a function of salinity and decreases at higher salt. The preceding equation is valid if no other PE is present. However, it is plausible to expect a similar effect of ionization on the effective infinite dilution *pK*'s in the presence of oppositely charged PEs. A crude and yet intuitive approach to capture the aforementioned effect involves setting $\gamma_A = \sigma_A$, as discussed shortly.

Figure 3-2A compares our simulation results for a single-phase system to experimentally obtained titration results for a stoichiometric mixture of PAA/poly(diallyldimethylammonium chloride) PDADMAC. The experimental results, given by symbols in Figure 3-2A, measured the deprotonation degree of PAA in multilayer films[39] and in capsules as well as in inter-PE

complexes[40] exposed to a salt-free pH-adjusted bath. In the limit of zero ion-pairing constant, our result coincides with the experimental result for salt-free pure PAA films and complexes, given by open symbols in Figure 3-2A and 3-2C. These clearly do not conform to the dashed curve in Figure 3-2A, i.e. the prediction of the classical HH formula with a constant $pK_A^\infty = \overline{pK_A} = 6.5$ corresponding to the pH at the halfway equivalence point. Since the systems studied in Figure 3-2 are salt-free, we have neglected electrostatic screening effects. Also, we have absorbed the Born solvation contribution, i.e. the third term in the argument of the exponential function in eqn. (3-A-2), with dissociation free energy of PAA ΔG_{AH}^∞, amounting to using a constant pK_A^∞ so that the Born free energy term is not explicitly considered, since the composition, and hence the dielectric constant, can be taken to be a constant in a single phase.

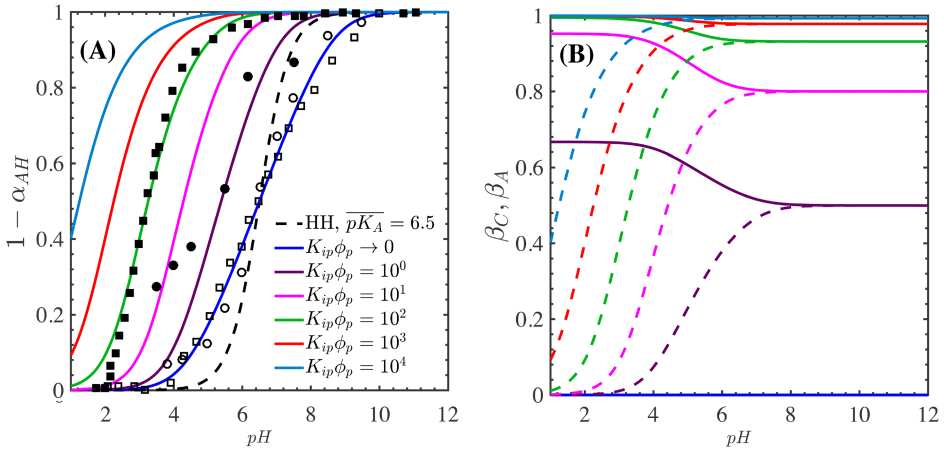

Figure 3-2: Comparison of model predictions at various ion-pairing constants for (A) deprotonation degree and (B) extents of ion-pairing of PAA (solid lines) and PDADMAC (dashed lines), in potentiometric titration of equimolar PAA/PDADMAC with experimental data reported by Choi and Rubner[39] (both open and filled circles) and Petrov et al.[40] (both open and filled squares). Open symbols correspond to pure PAA and filled symbols to PAA/PDADMAC. The effective protonation constant of PAA was evaluated using eqn. (3-28) with $\gamma_A = \sigma_A$.

PDADMAC is a strong polycation with $\alpha_{CH} = 1$ irrespective of pH. The prefactor A = 2.5 and $\overline{pK_A} = 6.5$ in conjunction with eqns. (3-28) was found to provide the best fit in our predictions, given by the blue lines in Figures 3-2A and reproduced in 3-2B, to the titration profile of salt-free PAA system with two molecular weights, given by the open symbols in Figures 3-2A and 3-2B. (Note that for pure PAA, there is no IP and hence there is no difference between f_A and σ_A.)

The presence of polycations shifts the apparent deprotonation constant of PAA by 1-3 units relative to pure PAA, depending on the chain's molecular weight and experimental conditions. A systematic variation of the IP constant weighted by polymer volume fraction in conjunction with

eqn. (3-28) for PAA with $\gamma_A = \sigma_A$ demonstrates that IP between PAA and the oppositely charged PDAMDAC semi-quantitatively predicts the observed experimental shifts, as shown by Figure 3-2A. Even though the prefactors used with pure PEs may not necessarily be the same as those for mixed polyanion/polycation systems and the crude approach taken to generalize eqn. (3-28) from pure PEs to mixed PEs may be inaccurate, our predictions should at least prompt more quantitative work to assess the protonation constants of weak PEs in the presence of oppositely charged chains.

As $K_{ip}\phi_p$ increases, the extent of ion-pairing of the deprotonated carboxylic groups increases accordingly, as shown by the solid lines in Figure 3-2B. For sufficiently high IP constant, β_A approaches unity, effectively removing bare carboxylate groups with which protons can interact, and thus inducing more protonated groups to dissociate in order to maintain equilibrium, according to the Le Châtelier's principle. As pH increases, more PAA repeat units become deprotonated and thus available for ion-pair formation with fully ionized PDAMDAC groups resulting in an increase of β_C, as shown by the dashed lines in Figure 3-2B. Beyond pH ~ 6, extents of ion-pairing for both polymers reach a plateau which increases at higher values of the ion-pairing constant, Figure 3-2B. Application of Le Châtelier's principle to eqns. (3-9), (3-10) and (3-13) suggests that ion-pairs remove the bare charged functional groups, thus inducing further chain ionization to maintain equilibrium. In fact, a similar concept based on ion-pair formation has been used to explain pH shifts in PAA solutions in response to addition of another chain type capable of forming ionic or hydrogen bonds with PAA.[41, 42]

For PAA/PDADMAC at pH = 7, $K_{ip}\phi_p$ ~ 5 can be inferred from experimental ITC measurements.[30] Although this deviates from the values providing best fits to the experimental data in Figures 3-2A, namely $K_{ip}\phi_p$ = 10-100, the proposed model captures the significant shifts in pK_A of PAA qualitatively well, given that the experimental titration data evidently depend on molecular weight, as well as our assumption of a pH-independent ion-pairing equilibrium constant. The latter quantity has been shown to be sensitive to pH variations and even a 10-fold increase in response to pH variation can be expected.[28]

Charge regulation in a weak polyanion such as PAA is also predicted in the presence of a weak polycation such as poly(allylammonium hydrochloride) PAH; see appendix 3.4.5. The proposed model can also capture the main features of potentiometric titration of non-equimolar mixtures,

as demonstrated for PSS/PDMAEMA system appendix 3.4.6; see Figure 3-A-4. A similar observation has been reported for PDMAEMA in the presence of strongly charged poly(styrene sulfonate) PSS.[38] In appendix 3.4.7, consistent with experimental trends, salt counterions are also shown to induce further deprotonation (protonation) in PAA (PDMAEMA) and that the potentiometric titrations of single-type PE solutions can be used to obtain CC equilibrium constants, used in section 3.3.2.2. Having demonstrated the capacity of the proposed model to capture the charge regulation effects in weakly dissociating PEs induced by simple salts and oppositely charged PE, we proceed to illustrate the effect of CC and IP on predicted binodal diagrams. We focus on monovalent PE mixtures prepared at stoichiometric conditions for simplicity, hereafter.

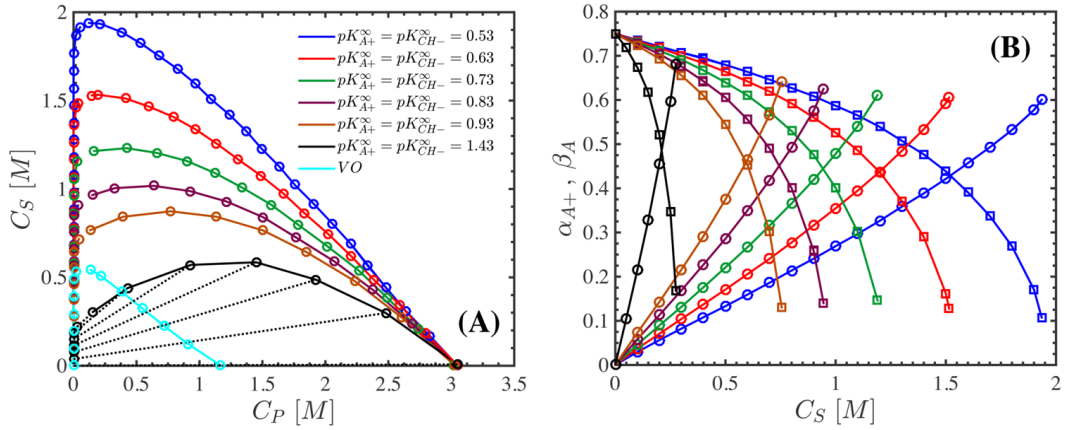

Figure 3-3: Effect of CC equilibrium constant on A) binodal diagrams for an equimolar symmetric mixture of two strongly charged PEs at a fixed IP constant of 120.8 in the infinite dilution limit, where the concentration C_S is the molar concentration of salt (moles/volume of either salt ion) and C_P is the molar concentration of monomers of either PE. Due to symmetry and equimolarity, concentrations of both PEs are identical and so are the total concentrations of either counterion. Open circles on either side of the diagrams mark the end-points of consecutive tie-lines corresponding to increasing salt concentrations. For clarity, only the dotted tie-lines for the black curve in (A) is presented here. B) Extents of IP for polyanions (open squares) and extents of CC along polyanions chains (open circles), in the dense phase as a function of bulk salt concentration. The extents of IP and CC for the positively charged chain are identical to corresponding values of the polyanion chain due to symmetry. $\omega_+ = \omega_- = \bar{\omega} = 1$, $\omega_A = \omega_C = 2.4$, $T = 298$ K and $f^{\chi} = 0$.

3.3.2 Binodal Diagrams

3.3.2.1 Strong Polyelectrolytes

While the protonation degree of a strong PE is insensitive to pH, its effective charge density is determined by the PE, salt and the oppositely charged PE concentrations through CC and IP, which lower the effective charge density. The charge density σ_i of a strong PE in VO-based models remains constant (usually unity) regardless. In our model, however, the charge density is

evaluated self-consistently upon free energy minimization. Figure 3-3A depicts the binodal curves for an equimolar and symmetric system of strongly dissociating PEs such as the well-studied PSS/PDADMAC strongly dissociating system ($\alpha_{AH} = 0, \alpha_{CH} = 1$), at a fixed IP equilibrium constant $K_{ip}^{\infty} = 120.8$ for various infinite-dilution CC constants; note that the effective constants are deteremined by eqns. (3-A-4) through (3-A-6) in the Appendix 3.4.1. As both PEs are insensitive to pH, water self-dissociation has been neglected and the concentrations of hydronium and hydroxyl ions have been neglected, simplifying the model for this system. Note the definitions of molar concentrations give in the caption to Figure 3-3, which we use throughout.

The binodal diagrams predicted for the system considered in Figure 3-3A exhibit richer features than those derived from the extended VO model that accounts for different components sizes. Note that in a symmetric system with identical CC parameters used for both PE-counterion pairs, the extents of CC and IP in a symmetric equimolar mixture are identical for both PEs. Also, the total concentration of negatively charged counterions in the single phase prior to coacervation is equal to the total concentration of positively charged counterions, and the concentration of either is denoted by C_S. Similarly, the total concentrations of oppositely charged PEs are equal to each other and the concentration of each is denoted by C_P. Our model clearly predicts an associative phase separation with a dense polymer-rich phase consisting of equal amounts of each PE and a supernatant phase almost devoid of polymers.

At sufficiently low salt concentrations, there is an abundance of charged PE repeat units and a dearth of counterions, resulting in much ion-pairing and little CC in the dense phase irrespective of the strength of counterion-PE local electrostatic interactions; see the circles in Figure 3-3B. Upon formation of each ion-pair for the system at hand in the infinite dilution limit, the total free energy (excluding the entropy of mixing) is lowered by $\sim 3.8 k_B T$. The free energy thus attains a minimum as more and more ion-pairs are formed. PEs try to form as many ion-pairs as possible through phase separation into a dense phase where the probability of polyanion-polycation encounters is significantly higher. As evidenced by eqn. (3-A-6), the extent of IP increases in denser systems such that f_{ip} tends to densify the coacervate as much as possible, expelling water. However, the substantial entropy of water opposes excessive densification of the gel phase. At the same molar concentration and IP constant, the PE with the lower monomer volume occupies

less volume in the dense phase and thus face less resistance from entropy of water. Therefore, the two-phase region of the phase diagram, expressed in terms of molarities, shrinks down for complex coacervation of oppositely charged PEs with bulky repeat units.

A comparison with predictions of the EVO model with the charge density of both PEs set to unity proves that the main driving force for complex coacervation in this system is the favorable IP which is increasingly counteracted as CC intensifies, i.e. at higher pK^{∞}_{A+} and pK^{∞}_{CH-}. This is a major departure from the classical VO model where complex coacervation is attributed solely to a gain in long-ranged electrostatic interactions. In fact, ~ 75% of the repeat units in the dense phase at low salt concentrations in our model, Figure 3-3B, are neutralized by an oppositely charged group increasing the Debye length, significantly diminishing the contribution of the long-ranged fluctuation energy to PEC.

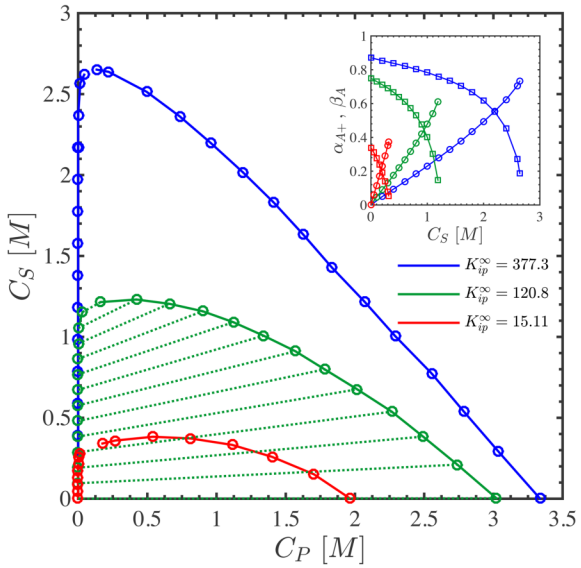

Figure 3-4: Similar to Figure 3-3 except with constant CC parameters $pK^{\infty}_{A+} = pK^{\infty}_{CH-} = 0.73$ at three IP constants. The dotted tie-lines only for the intermediate IP strength are presented here, for clarity. Inset illustrates the extents of IP for polyanions (open squares) and extents of CC along polyanions chains (open circles), in the dense phase as a function of overall salt concentration. The extents of IP and CC for the positively charged chain are identical to the corresponding values of the polyanion chain.

As more salt is introduced, a competition between IP formation and CC controls the shape and curvature of the branch of binodal diagram corresponding to the coacervate phase. At high salt concentrations, CC is enhanced, causing some polymer-polymer ion-pairs to break up, which in turn translates into a lower mechanical gel modulus for the coacervate phase. The so-called salt-induced plasticization of PE complexes is well understood qualitatively.[1, 43] Consistent with

molecular simulations and experimental observations on PSS/PDADMAC complexes and multilayers,[44–46] the extent of IP (intrinsic charge compensation) decreases monotonically as salt concentration responsible for extrinsic compensation increases; see Figure 3-3B. As the strength of short-ranged counterion-PE interactions increases, represented by higher $pK^{\infty}_{A+} = pK^{\infty}_{CH-}$, more ion-pairs are broken up in the dense phase at any given salt concentration, leading to a lower critical salt concentration. Note in Figure 3-3B that for any value of $pK^{\infty}_{A+} = pK^{\infty}_{CH-}$, at the critical salt concentration, the extent of IP reaches a critical minimum of ~ 0.1 for the set of parameters employed in Figure 3-3B, while the CC extent reaches a maximum of ~ 0.65. In fact, all the curves in Figure 3-3B could be collapsed onto a single universal plot upon normalization of C_S by the corresponding critical salt concentration.

Perry and Sing[24] applied LS theory to strongly and oppositely charged PEs of segment size either similar to, or smaller than, that of counterions and demonstrated that LS predicts a significantly *lower* counterion concentration in the dense phase than in the supernatant, which at least for the case of PSS/PDADMA/KBr system does not seem to be valid.[3] In the limit where both IP and CC are weak, our model for strongly charged PEs reduces to the EVO model modified to account for Born energy effects. Our proposed model predicts the counterion release (CR) from a chemical standpoint. Upon adding eqns. (3-11) through (3-13) we arrive at another form of complexation reaction generally envisaged in CR view of complex coacervation.

$$(A+) + (CH-) \xleftrightarrow{\Delta G^{\infty}_{ip} + \Delta G^{\infty}_{A+} + \Delta G^{\infty}_{CH-}} CHA + (+) + (-) \tag{3-29}$$

Eqn. (3-29) makes clear that increasing the salt concentration pushes the equilibrium in the backward direction causing the ion pairs (condensed counterions) to decrease (increase). At any given overall polymer and salt concentration greater than zero within the binodal envelope, the CC (IP) extent is lower (greater) in a dense phase than it would be if the system remained in a single phase. In other words, chains release their associated counterions to form ion-pairs with oppositely charged chains upon complex coacervation.

According to eqn. (3-29), a higher IP constant increases the extent of IP at fixed salt and PE concentrations. Figure 3-4 demonstrates the role of the IP constant on binodal diagrams. Unlike the salt concentration that primarily sets the critical condition for phase separation, the IP constant alters the phase behavior in a more drastic way. At no-salt conditions, the tendency of

oppositely charged PEs to form ion pairs is in large part balanced by the entropy of water. As the extent of IP increases - see the squares in the inset of Figure 3-4 - the extent of CC decreases at any given salt concentration.

It should be noted that there exists a maximum PE volume fraction in the dense phase, which is achieved in the no-salt conditions in equimolar mixtures (where $\alpha_P = \alpha_{A+} = \alpha_{CH-} = 0$) and in the limit $K_{ip}^{\infty} \to \infty$, i.e. $\beta \to 1$. Such a maximum is obtained by setting the osmotic pressure of the water to zero for infinitely long, strongly dissociating PEs in the aforementioned limit. For the parameter set in Figure 3-4, the maximum total PE concentration in the dense phase for a symmetric PE mixture predicted by our model – which is a function of $\omega_P = \omega_A = \omega_C$ and FH parameter in water, is found to be ~ 3.75 M as $K_{ip}^{\infty} \to \infty$; see appendix 3.4.9 for further detail.

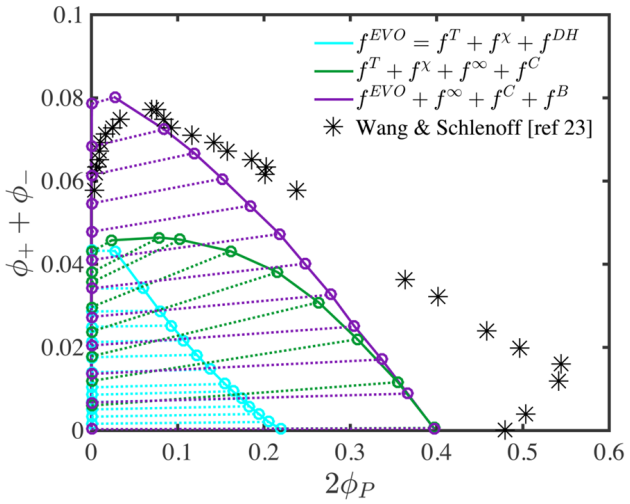

Figure 3-5: Binodal diagram of PSS/PDADMAC/KBr system predicted by EVO (cyan lines), and by our model with (violet lines) and without (green lines) the Debye-Hückel (DH) free energy. The volume fraction of either repeat unit is denoted by ϕ_P while the total KBr volume fraction is given on the vertical axis. Black stars represent the experimental data demarcating the binodal boundary.[3] The open circles mark the KBr and PE volume fractions in coexisting phases connected by the tie-lines, which are dotted lines. The relevant parameters are listed in Table 3-1.

Figure 3-5 illustrates the comparison of our model predictions with and without DH free energy contribution to the binodal diagrams inferred from the phase diagram reported by Wang and Schlenoff for equimolar mixtures of PSS (N_A ~ 2000)/PDADMAC (N_C ~ 1000) in the presence of KBr.[3] Their reported polymer weight fractions in coexisting phases were converted to volume fractions using the mass densities of pure KBr (2.75 g/cm^3) water and polymer (1.13 g/cm^3). Molar concentrations and weight fractions of PEs and KBr in coacervate phases reported by Wang and Schlenoff,[3] $\omega_P = \omega_A = \omega_C = 6.5$ and $\omega_+ = \omega_- = 1$ can be inferred according to eqn.

(3-26). Table 3-1 summarizes the parameters used in Figure 3-5. We have taken the CC constants and FH parameters for both PSS and PDADMAC repeat units to be identical to limit the parameter space.

Even though neutral and sufficiently long chains for which the Flory-Huggins (FH) χ parameter in water exceeds ~ 0.5 are poorly soluble in water, a single-component PE can tolerate χ parameters up to unity and still remain soluble in water owing to the huge loss of translational entropy of the counterions that would occur if the polyions were to phase separate, as demonstrated in more detail in appendix 3.4.9. However, if both chains of both charges are present at equimolarity, these chains phase separate at any salt concentration when both chains have χ values with respect to water that exceed 0.5. The critical χ in this case is not higher than this because the oppositely charged chains can achieve charge neutrality phase without carrying their counterions with them as they phase separate, and thus there is no entropic cost that might raise the critical value of χ above 0.5, as there is when only chains of a single charge phase separate. The same is true of the EVO model and we believe all models with a constant FH χ parameter between water and PEs. The effective χ parameter of PSS/PDADMA multilayers where the repeat units are expected to be highly ion-paired has been reported to be ~ 0.85.[47] For the maximum constant χ parameter that has a critical salt concentration above which there is no phase separation, namely χ = 0.5, the maximum PE volume fraction predicted in our model is ~ 0.4, considerably underestimating the experimentally observed value of ~ 0.55 in Figure 3-5. Nonetheless, our model clearly outperforms the EVO model in Figure 3-5. Figure 3-5 also shows the prediction of our model without the DH term, thereby illustrating that IP and CC alone term can predict complex coacervation and critical behavior at high salinity with the DH term influencing the predictions only at elevated salinity in our model.

Table 3-1: The parameters employed in obtaining the binodal diagram in Figure 3-5.

pK_{A+}^{∞}	pK_{CH-}^{∞}	K_{ip}^{∞}	$\chi_{AW} = \chi_{CW}$	$\omega_A = \omega_C$	$\omega_+ = \omega_-$
2.58	2.58	347300	0.5	6.5	1.0

Any higher IP constant beyond that reported in Table 3-1 could be used in conjunction with correspondingly higher pK_{A+}^{∞} and pK_{CH-}^{∞} to provide a similar fit to the experimental data in

Figure 3-5. This suggests that the underlying equilibrium free energy in this system with strong IP is that of counterion release (CR), whose net free energy change is given by eqn. (3-29). This gives $\Delta G_{ip}^{\infty} + \Delta G_{A+}^{\infty} + \Delta G_{CH-}^{\infty} \sim 6.2 k_B T$ for the IP and CC parameters used in Table 3-1, which agrees reasonably well with the experimental range of values (4.7-7.9) $k_B T$ reported for "doping equilibria" of PSS/PDADMA with simple salts.[45, 48] Upon measurement of two of the CC and/or IP equilibrium constants for this system (which is equivalent to measuring ΔG_{A+}^{∞}, ΔG_{CH-}^{∞}, or ΔG_{ip}^{∞}), the third free energy contribution could be inferred unambiguously.

Near the critical salt concentration in Figure 3-5, the measured polymer concentration in the supernatant becomes appreciable, as can be observed in the asterisks near the top of the phase diagram. However, due to the high polymerization index used in the work of Wang and Schlenoff,[3] our theory as well as VO-based models predict a vanishingly small PE concentration in the supernatant phase, since neither accounts for inter-polyelectrolyte complexes that presumably exist as colloidal particles in the supernatant phase. In appendix 3.4.9, we demonstrate that allowing χ parameters to increase linearly beyond 0.5 as a function of IP extent, we can improve our model predictions, especially in the low salt limit. Additionally, the supernatant phase in this case can contain a sizeable amount of both PEs at the critical point. Lastly, experimentally, it is evident in Figure 3-5 that, at low salt concentration, addition of KBr raises the PE concentration in the dense phase, a behavior that has yet to be captured by any theory. Even though it is possible to suggest remedies such as the aforementioned composition-dependent χ parameters for such a shortcoming, we defer such refinements to future work until more systematic investigations become available.

3.3.2.2 Weak Polyelectrolytes

In a mixture of two weakly dissociating chains in the presence of added salt, protons, counterions and oppositely charged repeat units compete to bind to PEs. This competition is determined by the free energies associated with eqns. (3-9) through (3-13). Unlike in a mixture of strongly dissociating PEs, with weak PEs water self-dissociation eqn. (3-14) cannot be ignored. In controlled experiments, the pH and salinity are commonly adjusted prior to mixing the stock solutions containing either PE individually. Upon mixing, the pH is subject to change even if the system does not phase separate. Given that either buffer solutions or strong acid/bases are commonly used to adjust the pH of the stock solutions, here assumed to be the same for both

starting PE solutions and designated hereafter by pH°, the concentrations of simple ions and PEs depend on the particular mixing and pH-adjustment protocol and thus can not be varied independently. In previous models, the pH is typically specified for the final *mixed solution*, which ignores changes in pH resulting from charge regulation effect upon mixing of stock solutions.

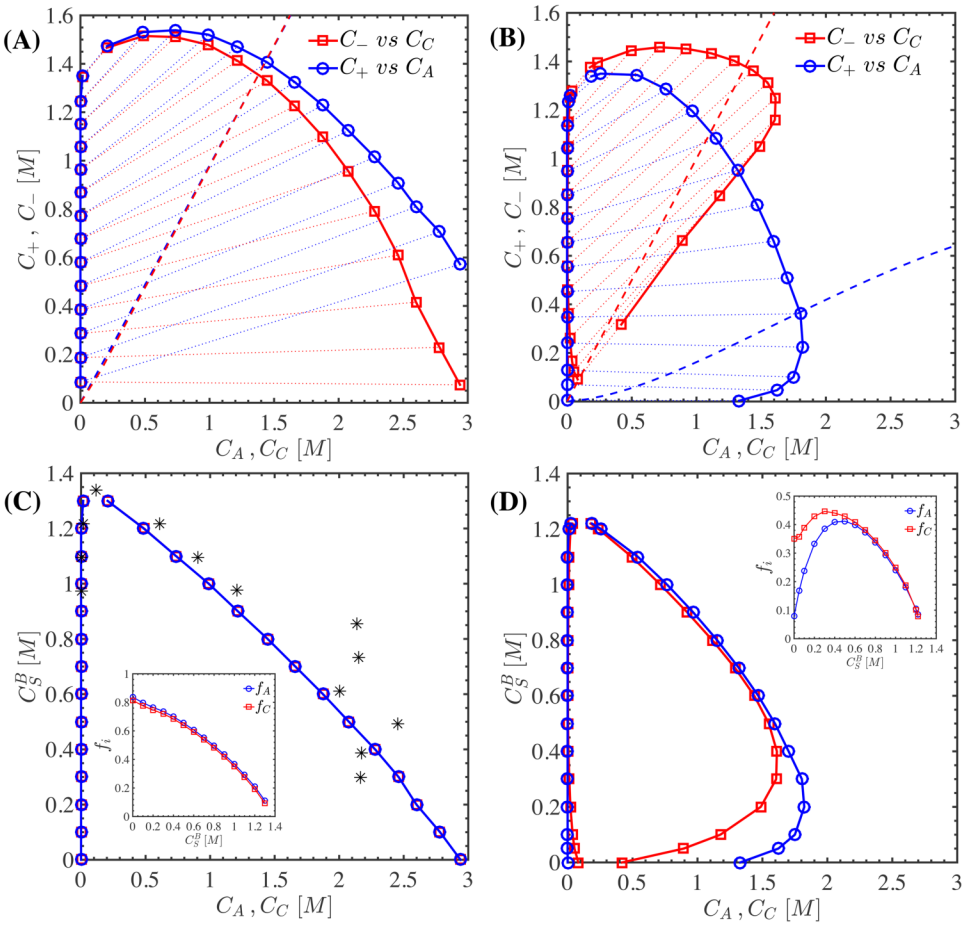

Figure 3-6: Binodal diagram illustrating the concentrations of two weakly dissociating PEs in coexisting phases versus their corresponding counterion concentrations for an aqueous equimolar system at A) pH° = 7 B) pH° = 5. The dashed blue and red lines (which nearly superimpose in A) mark the salt-polymer concentrations below which the pH of either stock solution cannot be adjusted to the specified value, pH°. C and D correspond to the binodal diagrams in A and B, respectively, where the bulk salt concentration in the stock solutions (assumed to be the same in each) is plotted against the PE concentrations in coexisting phases. Note that circles and squares in C are almost indistinguishable. The PE concentration in both stock solutions is fixed at 0.11 M. Experimental binodal data[9] for PAA/PDMAEMA system at pH = 6.5 are represented by asterisks in C. (This is slightly different from the value pH° = 7 used in our calculations.) The insets show the dependence of the fraction of PE units in the dense phase that are charged and therefore available for IP.

In the remainder of this section, we denote the molar concentration of added salt (moles of either ion per unit volume of added salt, beyond any ions introduced through the acid or base used for pH regulation) in each of the stock PE solutions by C_S^B and follow a computational sequence

mimicking the typical experimental procedure whereby the pH of each PE stock solution is adjusted by a strong inorganic acid or base sharing the counterions corresponding to the salt used. For instance, if the added salt is chosen to be KCl, as is the case in the remainder of this section, enough HCl or KOH is added to the stock solutions to adjust the pH to the desired pH^o at a given bulk salt concentration. As a result, the concentrations of the counterion from the acid or base (Cl^- or K^+) can be significantly different depending upon the prescribed pH^o. The red and blue dashed lines in Figure 3-6A and 3-6B depict the minimum counterion concentration introduced at an initially no-salt condition through the addition of enough KOH or HCl to achieve the designated pH values in each stock solution of PAA and PDMAEMA for a given polymer concentration. To adjust the pH to $pH^o = 7$, almost equal amounts of KOH and HCl are required, while to achieve $pH^o = 5$, considerably more HCl should be added to the PDMAEMA solution than the amount of KOH that needs to be added to PAA.

Table 3-2: The association/dissociation equilibrium constants at the infinite dilution limit employed in Figure 3-6.

pK_A^∞	pK_C^∞	pK_{A+}^∞	pK_{CH-}^∞	K_{ip}^∞	pK_w^∞
6.65	8	1.89	2.29	43800	14

A survey of experimental studies indicates a dearth of systematic studies on binodal compositions of weak polyelectrolyte coacervates. We here use the experimentally obtained binodal diagrams[9] of the PAA/PDMAEMA/KCl system (both chains with a polymerization index ~ 500) at pH = 6.5± 0.2, as a reference in the following calculations. Spruijt *et al.*[9] assumed that the KCl concentration was the same in both phases and that within each phase the PAA and PDMAEMA concentrations were equal to each other. We explain in appendix 3.4.7 how the protonation and CC constants for both PEs in the infinite dilution limit can be extracted from the potentiometric titration data for PAA and PDMAEMA measured at various salinities; see Figure 3-A-5 in appendix 3.4.7. Note that we do not consider any dependence of protonation constants on protonation extents here since the titration data for these polymers conform reasonably well to the Henderson-Haselbalch (HH) model at the no-salt condition. Given the scatter in the experimental data, the ion-pairing equilibrium constant was adjusted to provide a reasonable fit to the experimental coacervate phase concentrations, shown in Figure 3-6C. The value so obtained along with other parameters tabulated in Table 3-2 were consistently employed to predict the binodal diagram at $pH^o = 5$; see Figures 3-6B and 3-6D. Unlike the

PSS/PDADMA/KBr system where the IP and CC could not be uniquely determined, the corresponding values in PAA/PDMAEMA/KCl system are uniquely determined as the extents of CC were independently obtained using the potentiometric titration data discussed in the appendix 3.4.7.

The sizes of the PAA and PDMAEMA repeat units are taken to be equal to each other and determined from the reported water content of the coacervate at no salt-conditions, i.e., ~ 72% by weight,[9] using eqn. (3-28), ($\omega_A = \omega_C = 2.4$) while the effective sizes of potassium and chloride ions are both assumed to be equal to that of the water molecule. Molecular simulations have demonstrated that the VdW interactions of protonated and deprotonated PAA repeat units with water are different enough to justify neglecting the χ parameter for the deprotonated monomer against water and thus $f^{\chi} = \chi_{AHW}\alpha_{AH}\phi_A\phi_W$. Thus we take $f^{\chi} = 0.45\alpha_{AH}\phi_A\phi_W$ where $\chi_{AHW} = 0.45$ is the FH χ parameter of protonated PAA repeat units in water, which was taken from the literature,[49] consistent with the calculations in Figure 3-A-5 in appendix 3.4.7 used to obtain the protonation and CC parameters. For PDMAEMA, repeat units were shown not to differ significantly upon protonation.[19] Here, for simplicity, we simply neglect any FH χ parameter for PDMAEMA, or any other pairs of species, keeping only the χ parameter for protonated PAA in water.

IP between PEs upon mixing perturbs the pH. As a result, PAA chains at $pH^o = 5$ in the stock solution undergo further deprotonation upon mixing at low salt conditions, leading to a pH of ~ 2.55 and 3.3 in the supernatant and coacervate phases, respectively. For $pH^o = 7$, the pH in both phases after mixing is ~ 7.85. This result cautions against the use of the pH measured in the supernatant as the local pH inside the coacervate phase, as is often assumed in the VO model and other models.[50] We reiterate here that none of the existing models of complex coacervation account for charge regulation effects.

At $pH^o = 5$, there is an excess of chloride ions introduced by HCl, as evidenced by the minimum chloride and potassium concentration required to adjust pH in stock solutions, represented by the red and blue dashed lines in Figure 3-6B. The high protonation degree of the PAA chain at low salt at $pH^o = 5$ cannot be completely overcome by the propensity of the repeat units to form IPs; this leads to a higher concentration of PAA units in the coacervate phase to provide sufficient PAA units to ion-pair with PDMAEMA groups. Given that PDMAEMA chains are predicted to

be 35 % ionized at the no-salt condition while PAA groups are merely 10 % ionized (see Figure 3-A-5 in appendix 3.4.7) the resultant coacervate is nearly three and a half times more concentrated in PAA monomers than it is in PDMAEMA repeat units.

Unlike the PSS/PDADMAC system discussed in Figure 3-5, in the experiments, the supernatant phase in PAA/PDMAEMA system remains almost fully depleted of either PE at neutral pH; see Figure 3-6C, indicating the absence of inter-polyelectrolyte complex particles in the supernatant for this system. In appendix 3.4.10, we have compared our predictions to those of the EVO model with an empirical expression to account for charge regulation by Jha *et al*.[19] for weak PEs for this system using identical parameters as those used in Table 3-2. Using these parameters, which are much more realistic than the fitting parameters used by Jha et al., the model of Jha et al. significantly underestimates the experimental binodal diagrams at $pH^o = 7$.

As demonstrated in section 3.3.2.1, the predicted binodal diagrams are most sensitive to the IP standard free energy; see Figure 3-4. Similarly, the phase behavior of weak PEs is highly sensitive to IP strength. In Figure 3-A-6 in appendix 3.4.8, the critical KCl concentration of PAA/PDMAEMA system at $pH^o = 3$ is shown to increase over 30-fold (from ~ 0.12 M to 4 M) when the pK_{ip}^{∞} is decreased by 1 unit - equivalent to a 10-fold increase in K_{ip}^{∞}. Note that PAA/PDMAEMA at $pH^o = 3$ and 5 with the bulk concentrations used in Figure 3-6 undergoes phase separation at salinities as high as 3 M KCl, see chapter 2, suggesting the necessity for considering the a pH- dependence of K_{ip}^{∞} to capture the critical salt concentration at different pH values. Our treatment of IP and CC in eqns. (3-11) through (3-13) is a simplified picture wherein the water structure around individual participants is neglected. However, the release of hydration water molecules has been shown to play a significant role in PE complexation in multilayers.[51] The number of hydrating water molecules forming H-bonds to deprotonated PAA units was shown to decrease at low pH, causing a reduction of around ~1 k_BT in the complexation enthalpy of PAA/PDADMAC as pH was lowered from 10 to 3.[52] Similarly, the IP equilibrium constant for poly(L-ornithine hydrobromide)/poly(L-glutamic acid) was found to increase over 13-fold as the pH was raised form 7 to 8.8.[28] Once relevant experimental and simulation data become available, the IP and CC free energies and even FH χ parameters can be made functions of composition, pH, IP and CC extents etc. to reflect the chemistry-specific details missing in VO-based models and LS theories.

3.4 Appendices

3.4.1 Laws of Mass Action

Here we present six law-of-mass-action (LMA) equations that follow from minimization of total Helmholtz free energy with respect to six degrees of freedom.

$$\frac{\phi_{H_3O}\phi_{OH}}{\phi_w^2} = K_w \equiv exp\left[-\Delta G_w^{\infty} + \frac{\kappa\ell_B}{1+\overline{\kappa}} + \frac{\ell_B - \ell_B^w}{l} - \left.\frac{\partial f^{\chi}}{\partial \phi_{H_3O}}\right|_{T,V}\right] \tag{3-A-1}$$

$$\frac{(1-\beta_A)(1-\alpha_{A+})(1-\alpha_{AH})\,\phi_{H_3O}}{\alpha_{AH}\,\phi_w} = K_A \equiv exp\left[-\Delta G_{AH}^{\infty} + \frac{\kappa\ell_B}{1+\overline{\kappa}} + \frac{\ell_B - \ell_B^w}{2l}\left(\omega_A^{-1/3} + 1\right) - \left.\frac{\partial f^{\chi}}{\partial \alpha_{AH}}\right|_{T,V}\right] \tag{3-A-2}$$

$$\frac{(1-\beta_C)(1-\alpha_{CH-})\,\alpha_{CH}\,\phi_{OH}}{(1-\alpha_{CH})\,\phi_w} = K_C \equiv exp\left[-\Delta G_{CH}^{\infty} + \frac{\kappa\ell_B}{1+\overline{\kappa}} + \frac{\ell_B - \ell_B^w}{2l}\left(\omega_C^{-1/3} + 1\right) - \left.\frac{\partial f^{\chi}}{\partial \alpha_{CH}}\right|_{T,V}\right] \tag{3-A-3}$$

$$\frac{(1-\beta_A)(1-\alpha_{A+})\,\phi_+}{\alpha_{A+}} = K_{A+} \equiv exp\left[-\Delta G_{A+}^{\infty} + \frac{\kappa\ell_B}{1+\overline{\kappa}} + \frac{\ell_B - \ell_B^w}{2l}\left(\omega_A^{-1/3} + \omega_+^{-1/3}\right) - \left.\frac{\partial f^{\chi}}{\partial \alpha_{A+}}\right|_{T,V} - 1\right] \tag{3-A-4}$$

$$\frac{(1-\beta_C)(1-\alpha_{CH-})\,\phi_-}{\alpha_{CH-}} = K_{CH-} \equiv exp\left[-\Delta G_{CH-}^{\infty} + \frac{\kappa\ell_B}{1+\overline{\kappa}} + \frac{\ell_B - \ell_B^w}{2l}\left(\omega_C^{-1/3} + \omega_-^{-1/3}\right) - \left.\frac{\partial f^{\chi}}{\partial \alpha_{CH-}}\right|_{T,V} - 1\right] \tag{3-A-5}$$

$$\frac{\beta_A\omega_C}{(1-\beta_C)(1-\beta_A)\phi_C\alpha_{CH}(1-\alpha_{CH-})(\omega_C+\omega_A)} = K_{ip} \equiv exp\left[-\Delta G_{ip}^{\infty} - \frac{\kappa\ell_B}{1+\overline{\kappa}} - \frac{\ell_B - \ell_B^w}{2l}\left(\omega_C^{-1/3} + \omega_A^{-1/3}\right) - \left.\frac{\partial f^{\chi}}{\partial \beta_C}\right|_{T,V} + 1\right] \tag{3-A-6}$$

3.4.2 Combinatorial Free Energy

Here, we treat the combinatorial entropy associated with the short-ranged correlations along polyion chain in a mean-field fashion wherein the connectivity of the chains is neglected. Let n_A and n_C be the total numbers of negatively and positively charged polyion repeat units, respectively. The partition function corresponding to the distribution of counterions, ion-pairs and protons, is given following earlier work on self-associating[43] and cross-associating polymers.[44]

$$Z = \Omega_A\Omega_C\Omega_{ip}\Lambda \tag{3-A-7}$$

Note that the free energies associated with various association/dissociation equilibria and cooperativity effects are already accounted for in f^{∞} - see eqn. (3-15) - so that all the permutations of arrangements of the four binding states of monomers along each chain, namely

uncharged, charged but unpaired, charged and paired to a small ion (i.e., by counterion condensation), and charged and ion-paired with a charged monomer of opposite charge, for fixed fractions of each state (i.e., fixed values of the α's and β's) are assumed to be isoenergetic. The total number of permutations of functional groups in four possible states along polyanions and polycations are denoted by Ω_A, Ω_C respectively and are given in eqns. (3-A-8) and (3-A-9).

$$\Omega_A = \left[\frac{n_A!}{(n_A\alpha_{AH})!(n_A[1-\alpha_{AH}]\alpha_{A+})!(n_A[1-\alpha_{AH}][1-\alpha_{A+}][1-\beta_A])!(n_A[1-\alpha_{AH}][1-\alpha_{A+}]\beta_A)!}\right] \quad (3\text{-A-8})$$

$$\Omega_C = \left[\frac{n_C!}{(n_C[1-\alpha_{CH}])!(n_C\alpha_{CH}\alpha_{CH-})!(n_C\alpha_{CH}[1-\alpha_{CH-}][1-\beta_C])!(n_C\alpha_{CH}[1-\alpha_{CH-}]\beta_C)!}\right] \quad (3\text{-A-9})$$

Note that we assume that all the repeat units in any of the 4 possible states are completely indistinguishable in this mean-field treatment. The total number of ways to create $N_{CHA} = (n_C\alpha_{CH}[1-\alpha_{CH-}]\beta_C)$ ion-pairs is given below:

$$\Omega_{ip} = (n_C\alpha_{CH}[1-\alpha_{CH-}]\beta_C)! \quad (3\text{-A-10})$$

The bonding probability Λ in eqn. (3-A-7) is the probability of having N_{CHA} ion-pairs each within an effective bond volume $v_B = (\omega_A + \omega_C)l^3$ in a total volume V. In addition to the energy level, the bonding probability alters the overall probability associated with each permutation. As the concentration of polymers increases, the likelihood of a given repeat unit encountering an oppositely charged group increases according to eqn. (3-A-11).

$$\Lambda = \left(\frac{v_B}{V}\right)^{N_{CHA}} \quad (3\text{-A-11})$$

Upon substitution of eqns. (3-A-8) through (3-A-11) into (3-A-7), using Stirling's approximation and mathematical manipulations, the short-ranged free energy f^C is obtained as the sum of five contributions each associated with one of the five association/dissociation equilibria represented by eqns. (3-9) through (3-13), given by eqn. (3-16).

3.4.3 Water Self-Dissociation

Instead of hydronium, hydroxyl volume fraction could be equivalently used as the indicator of water dissociation extent, in which case the hydroxyl ions produced by the protonation of polycation need to be subtracted out. The equivalence of either choice is readily confirmed by means of the electroneutrality condition eqn. (3-A-12)

$$0 = \phi_{H_3O} - \phi_{OH} + \frac{\alpha_{CH}\phi_C}{\omega_C} - \frac{(1-\alpha_{AH})\phi_A}{\omega_A} + \frac{\phi_+^o}{\omega_+} - \frac{\phi_-^o}{\omega_-} \quad \text{(3-A-12)}$$

The bracketed term in front of ΔG_w^{∞} in eqn. (3-15) may be replaced by hydroxyl volume fraction and the extent of protonation of polycations upon rearranging eqn. (3-A-13) as below:

$$\phi_{H_3O} + \frac{\alpha_{AH}\phi_A}{\omega_A} = \phi_{OH} - \frac{\alpha_{CH}\phi_C}{\omega_C} - \frac{\phi_+^o}{\omega_+} + \frac{\phi_-^o}{\omega_-} + \frac{\phi_A}{\omega_A} \quad \text{(3-A-13)}$$

The three last terms on the r.h.s of eqn. (3-A-13) can be dropped upon substitution of the r.h.s into eqn. (3-15), for any given composition of counterions and PEs, since they generate terms that are only linear in composition and thus of no thermodynamic relevance.

3.4.4 Nonlinearity of Laws of Mass Action

Here we suggest a change of variables that significantly reduces the non-linearity of laws of mass action (LMA) arising from the minimization of free energy at constant volume and temperature with respect to the volume fraction of hydronium (or pH equivalently) and extents of reversible reactions, constituting 6 unknown degrees of freedom overall, see eqns. (3-A-1) through (3-A-6) in the Appendix. For any given set of standard free energies associated with the LMA equations, temperature, ω_i's, polymer dielectric constant, bulk polymer and salt concentrations denoted by superscript '°' and, in case of weakly dissociation polyions, pH^o, there are four composition variables over which the free energy minimization is performed in order to locate the binodal boundaries. The minimization involves many free energy density evaluations, which involves finding all the unknown degrees of freedoms as well as volume fraction of water and hydroxyl ions using electroneutrality and incompressibility conditions. As a result, a robust algorithm guaranteeing convergence to a solution of LMA equation for any given set of trial compositions in either of two phases is desired.

Solution of the highly nonlinear set of LMA equations employing the Newton-Raphson (NR) method can be quite challenging for certain compositions in either phase. While extents of protonation, counterion condensation and ion-pairing range anywhere between 0 and 1 (exclusive), in practice, only pH values ranging from 0 to 14 are of interest in the experimental studies involving polyelectrolyte complexation, corresponding to a hydronium volume fraction of 0.02 or less. Let:

$$PH \equiv ln\left(\phi_{H_3O}\right),\ POH \equiv ln(\phi_{OH}),\ PW = ln(\phi_w) \quad \text{(3-A-14)}$$

$$x_A \equiv ln\left(\frac{\alpha_{AH}}{1-\alpha_{AH}}\right),\ x_C \equiv ln\left(\frac{\alpha_{CH}}{1-\alpha_{CH}}\right) \tag{3-A-15}$$

$$x_{A+} \equiv ln\left(\frac{\alpha_{A+}}{1-\alpha_{A+}}\right),\ x_{CH-} \equiv ln\left(\frac{\alpha_{CH-}}{1-\alpha_{CH-}}\right) \tag{3-A-16}$$

$$y_A \equiv ln\left(\frac{\beta_A}{1-\beta_A}\right),\ y_C \equiv ln\left(\frac{\beta_C}{1-\beta_C}\right) \tag{3-A-17}$$

The non-linearity of the set of LMA equations can then be tempered by taking the natural logarithm of both sides of eqns. (3-A-1) through (3-A-6), and rewriting eqn. (3-8), (3-24) and (3-25) in terms of a redefined set of unknowns defined in eqns. (3-A-14) through (3-A-17). In the following we neglect the van der Waals contribution to equilibrium constants listed in 3.4.1.

$$PH + POH - 2PW = -\Delta G_w^{\infty} + \frac{\kappa\ell_B}{1+\bar{\kappa}} + \frac{\ell_B - \ell_B^w}{l} \tag{3-A-18}$$

$$-x_A + PH - PW - ln(1+e^{x_{A+}}) - ln(1+e^{y_A}) = -\Delta G_{AH}^{\infty} + \frac{\kappa\ell_B}{1+\bar{\kappa}} + \frac{\ell_B - \ell_B^w}{2l}\left(\frac{1}{\omega_A^{1/3}} + 1\right) \tag{3-A-19}$$

$$x_C + POH - PW - ln(1+e^{x_{CH-}}) - ln(1+e^{y_C}) = -\Delta G_{CH-}^{\infty} + \frac{\kappa\ell_B}{1+\bar{\kappa}} + \frac{\ell_B - \ell_B^w}{2l}\left(\frac{1}{\omega_C^{1/3}} + 1\right) \tag{3-A-20}$$

$$-x_{A+} + ln\phi_+ - ln(1+e^{y_A}) = -\Delta G_{A+}^{\infty} + \frac{\kappa\ell_B}{1+\bar{\kappa}} + \frac{\ell_B - \ell_B^w}{2l}\left(\frac{1}{\omega_A^{1/3}} + \frac{1}{\omega_+^{1/3}}\right) - 1 \tag{3-A-21}$$

$$-x_{CH-} + ln\phi_- - ln(1+e^{y_C}) = -\Delta G_{CH-}^{\infty} + \frac{\kappa\ell_B}{1+\bar{\kappa}} + \frac{\ell_B - \ell_B^w}{2l}\left(\frac{1}{\omega_C^{1/3}} + \frac{1}{\omega_-^{1/3}}\right) - 1 \tag{3-A-22}$$

$$y_A - x_C + ln(1+e^{x_C}) + ln(1+e^{x_{CH-}}) + ln(1+e^{y_C}) = -\Delta G_{ip}^{\infty} - \frac{\kappa\ell_B}{1+\bar{\kappa}} - \frac{\ell_B - \ell_B^w}{2l}\left(\frac{1}{\omega_C^{1/3}} + \frac{1}{\omega_A^{1/3}}\right) + 1 \tag{3-A-23}$$

$$e^{POH} - e^{PH} - \frac{\phi_C^o}{\omega_C}\left(\frac{e^{x_C}}{1+e^{x_C}}\right) + \frac{\phi_A^o}{\omega_A}\left(\frac{1}{1+e^{x_A}}\right) - \frac{\phi_+}{\omega_+} + \frac{\phi_-}{\omega_-} = 0 \tag{3-A-24}$$

$$\frac{\phi_C^o}{\omega_C}\left(\frac{e^{x_C}}{1+e^{x_C}}\right)\left(\frac{1}{1+e^{x_{CH-}}}\right)\left(\frac{e^{y_C}}{1+e^{y_C}}\right) - \frac{\phi_A^o}{\omega_A}\left(\frac{1}{1+e^{x_A}}\right)\left(\frac{1}{1+e^{x_{A+}}}\right)\left(\frac{e^{y_A}}{1+e^{y_A}}\right) = 0 \tag{3-A-25}$$

$$\phi_+^o = \phi_+ + \phi_A^o\left(\frac{1}{1+e^{x_A}}\right)\left(\frac{e^{x_{A+}}}{1+e^{x_{A+}}}\right)\left(\frac{\omega_+}{\omega_A}\right) \tag{3-A-26}$$

$$\phi_-^o = \phi_- + \phi_C^o\left(\frac{e^{x_C}}{1+e^{x_C}}\right)\left(\frac{e^{x_{CH-}}}{1+e^{x_{CH-}}}\right)\left(\frac{\omega_-}{\omega_C}\right) \tag{3-A-27}$$

Even though these equations are longer and more complicated, they remain well defined over a wide range of the nine renormalized parameters involved, making application of nonlinear solvers more likely to converge to the solution, given a judiciously picked initial guess. The initial guess can be obtained through estimation of extents of protonation of both polyions

according to pH^o and pK_A^∞ and pK_C^∞ using Henderson-Hasselbalch (HH) equation. The extents of protonation thus obtained can be converted to x_A and x_C. Having the preceding parameters, one can proceed to calculate x_{A+}, x_{CH^-}, y_A and y_C if the Born and DH free energy contributions to the LMA equations are ignored and setting

$$\phi_-^o \sim \phi_- \tag{3-A-28}$$

$$\phi_+^o \sim \phi_+ \tag{3-A-29}$$

$$\phi_w \sim 1 - \phi_-^o - \phi_+^o - \phi_C^o - \phi_A^o \tag{3-A-30}$$

The last equation essentially neglects the volume fraction of hydroxyl and hydronium ions in comparison with that of water, which turns out to be a nearly perfect assumption. Even though hydronium and hydroxyl do not play a substantial role in determining the volume fraction of water, they do affect protonation extents of weakly dissociating polyions strongly. Finally, the water self-dissociation along with two protonation equilibria affords three expressions to determine the two remaining unknowns, namely PH and POH. Even though the system of three equations involving two unknowns is over-determined, we observe that using the self-dissociation and one of the arbitrarily chosen protonation equilibria along with the parameters estimated earlier provides a suitable initial guess. The procedure described here can be coded in a subroutine that allows for a robust solution of recast laws of mass action (LMAs) each time free energy density is to be evaluated in either phase. The procedure can be simplified for strongly dissociating polyions where PH, POH and renormalized protonation extents x_A and x_C need not be considered. A sample MATLAB® script to compute binodal boundaries is available upon request.

To obtain phase behavior, the total free energy of the system is minimized with respect to five degrees of freedom, namely PE and counterion volume fractions as well as the volume fraction of the coacervate phase, subject to the constraints laid out in previous section in both coexisting phases. Additionally, the overall mass balance on PEs and simple salt affords auxiliary relations necessary in the free energy minimization. Once an overall salt and PE concentration are specified $\{\phi_i^o\}$, a flash calculation involving the minimization of overall free energy with respect to the composition and volume fraction of the coacervate phase yields the salt and PE concentrations in coexisting phases at either end of a tie-line. For a mixture of strong and

oppositely charged PEs, hydroxyl and hydronium ions can be neglected in which case the number of degrees of freedom reduces to four, namely volume fractions of PEs, water in either dense phase or supernatant and the coacervate volume fraction defined as the ratio of volume of coacervate and the total system volume. We only consider equimolar mixtures of PEs and start off with a flash calculation at the no-salt condition at a trial bulk PE concentration chosen in the two-phase region of binodal diagram. Salinity is increased step-wise until we reach the binodal boundary at the trial PE concentration after which we repeat the process in an ad hoc fashion at a different bulk PE concentrations until the binodal boundaries are satisfactorily delineated. We have followed a somewhat similar numerical approach to that employed by Jha et al.[19] except that in general five association/dissociation extents as well as pH need to be computed in each evaluation of free energy density by solving the nonlinear set of eqns. (3-A-1) through (3-A-6).

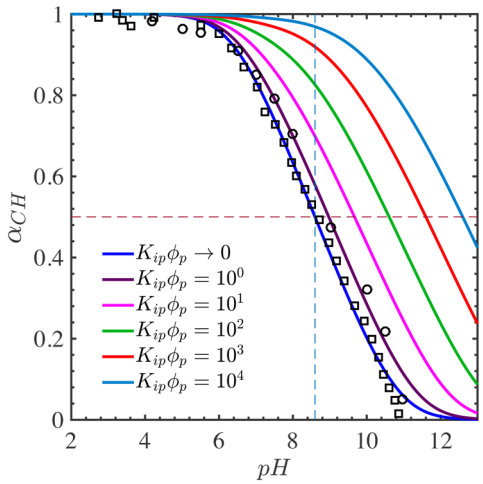

Figure 3-A-1: Protonation degree of PAH for an equimolar PAA/PAH with $\gamma_A = f_A$ and A = 2.5 for PAA in eqn. (3-28) and $\gamma_C = f_C$ and B = 2.7 for PAH in eqn. (3-A-31). Open circles are reported by Choi and Rubner[39] for pure PAH and the open squares are reported by Petrov *et al.*[40] Refer to the text for model parameters.

3.4.5 Potentiometric Titration in PAA/PAH System

B = 2.7 and $\overline{pK_C}$ = 5.4 in eqn. (3-A-31) provide a good fit to potentiometric titration profile of pure PAH; see the dark blue curve and empty symbols in Figure 3-A-1.

$$pK_C^{\infty} = \overline{pK_C} + B(\gamma_C - 0.5) \qquad \text{(3-A-31)}$$

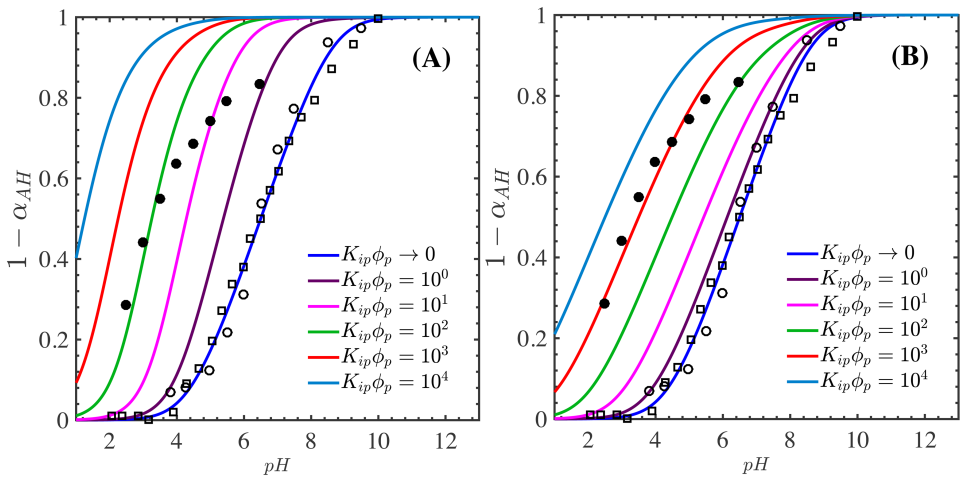

Figure 3-A-2: Protonation degree of PAA in an equimolar PAA/PAH system for PAH with (A) $\gamma_A = \sigma_A$ and $\gamma_C = \sigma_C$ (B) $\gamma_A = f_A$ and $\gamma_C = f_C$ with A = 2.5 and B = 2.7 in eqn. (3-28) and (3-A-31), respectively. Open symbols pertain to pure PAA and filled circles in from the data reported by Choi and Rubner.[39]

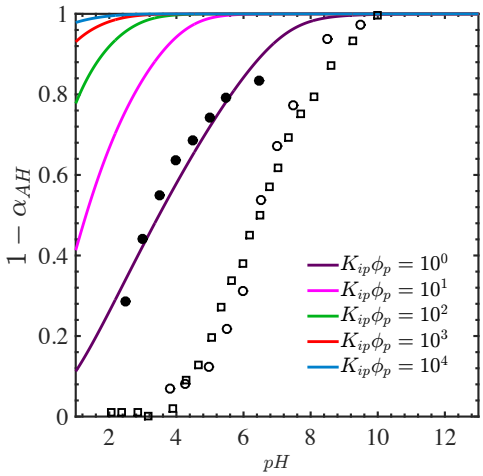

Figure 3-A-3: Protonation degree of PAA for an equimolar PAA/PAH system with $\gamma_A = \sigma_A$ and A = 9 for PAA and $\gamma_C = \sigma_C$ and B = 9 for PAH in eqns. (3-28) and (3-A-31). Open symbols pertain to pure PAA reproduced from Fig. 3-A-2 and filled circles are from the data reported by Choi and Rubner.[39]

The predictions using eqns. (3-28) for PAA again use A = 2.5 with $\gamma_A = \sigma_A$ and (3-A-31) for PAH again with B = 2.7 with $\gamma_C = \sigma_C$, fails to provide an acceptable fit to the experimental titration data of PAA for the system given by the filled circles in Figure 3-A-2, over a wide range of ion-pairing constants. However, model predictions using eqn. (3-28) and (3-A-31) with $\gamma_A = f_A$ for PAA and $\gamma_C = f_C$ for PAH - i.e. neglecting the effect of IP on charge density- match the experiments fairly well at $K_{ip}\phi_p$= 1000; see the red curve in Figure 3-A-2B. This anomaly may be due to using the same A and B for pure PAA and PAH as used in mixed PAA/PAH systems. In fact, using A = B = 9 for PAA and PAH in PAA/PAH with $\gamma_A = \sigma_A$ and $\gamma_C = \sigma_C$ eqn. (3-28)

and (3-A-31) respectively with all remaining parameters held fixed also fits the experimental data, filled circles in 3-A-3, fairly well.

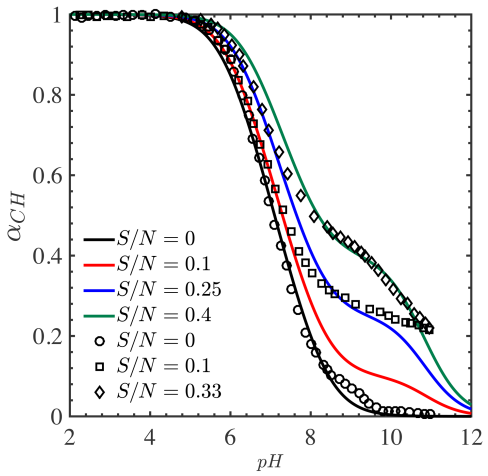

Figure 3-A-4: Protonation extent of PDMAEMA in the presence of PSS at various *S/N* ratios. Solid lines represent the model predictions based on the assumption of 1:1 stoichiometry for ion-pair formation, eqn. (3-8). Experimental data were adapted from reference 38 and are designated by open symbols.

3.4.6 Stoichiometry of Ion Pairing

The assumption of 1:1 stoichiometry of the ion pairs employed in eqn. (3-8) is tested by comparing the model predictions with titration profiles of PDMAEMA solutions in the presence of PSS, Figure 3-A-4, with different mixing ratios, as measured by the ratios of sulfur to nitrogen (S/N) reported in ref. 38. The apparent dissociation constant of pure PDAMEMA used in Figure 3-A-4 is given by eqn. (3-A-31) with $\gamma_C = \sigma_C$, B = 1.0 and $\overline{pK_C}$ = 6.9 obtained as the halfway equivalence point corresponding to α_{CH} = 0.5 in the titration profile of pure PDMAEMA. We use a single value $K_{ip}\phi_C$ = 1000 adjusted in Figure 3-A-4 to provide the best fit to the experiments, assuming a 1:1 ion-pairing stoichiometry. In non-equimolar mixtures of PDMAEMA/PSS, the titration data deviate from predictions of our model based upon a 1:1 ion-pairing stoichiometry, with the greatest deviation for S/N = 0.1. We might surmise from this that each PSS repeat unit interacts with more than one PDMAEMA repeat unit. To illustrate the possible influence of deviations from 1:1 stoichiometry, in Figure S4 we adjust the S/N ratios in the theory to give the best-fit predictions for the experimental curves with S/N = 0.1 and 0.33; the best-fit theoretical values are 0.25 and 0.4, respectively. Regardless of the reason for the deviation, the general trends of the predicted titration curves agree reasonably well with those of the experiments for PDMAEMA/PSS mixtures using a single adjusted parameter.

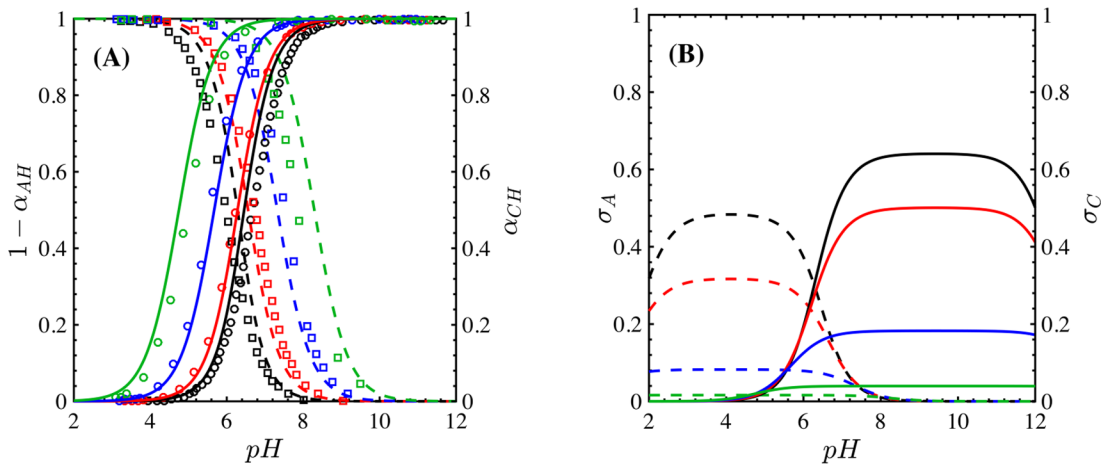

Figure 3-A-5: (A) Salt-induced charge regulation in potentiometric titration of PAA and PDMAEMA. Solid lines and open circles represent our model predictions and experimentally obtained titration data for PAA, respectively.[1] Dashed lines and open squares represent similar information for PDMAEMA.[1] (B) The simulated effective charge density of PAA and PDMAEMA corresponding to the theoretical results in (A) with the same color code. Colors correspond to different salt concentrations; black represents the salt-free systems while red, blue and green designate 10 mM, 100 mM, 1000 mM KCl, respectively. Polymer concentrations and the temperature in simulations are matched to experimental values. Potassium and chloride ions are both taken to be of identical size to a water molecule. pK_w^{∞} = 14 is taken from the literature while infinite dilution pK's for CC, pK_{A+}^{∞} = 1.89, pK_{CH-}^{∞} = 2.29, are adjusted parameters that can be converted to values of ΔG_{A+}^{∞}~ 7.36 and ΔG_{CH-}^{∞} ~ 8.28. Note that "+" and "–" in the subscripts refer to potassium and chloride counterions, respectively.

3.4.7 Potentiometric Titration of PAA and PDMAEMA

Salinity has been demonstrated to substantially affect the protonation behavior of weakly dissociating PEs.[36,53] Spruijt et al.[1] demonstrated that the apparent deprotonation constant pK_A of PAA ($\bar{M}_n$ ~ 36 Kg/mol) decreases by two units as KCl concentration is increased from 0 to 1 M. This apparent increase in acidity of PAA has been attributed to stabilization of deprotonated carboxylic groups and hydronium ions by the salt-induced electrostatic screening. An assessment of eqn. (3-A-2) in the Appendix 3.4.1, however, indicates that in the high-salt limit, its right side reduces to around 2.3, implying that the screening effects as captured by the Debye-Hückel (DH) model only account for roughly a single unit of shift in pK_A in this limit. A similar shift in the effective pK_C of PDMAEMA has been reported.[1,38] This deficiency of the DH model could be tackled by incorporation of empirical constants in the original DH expression.[19, 36] However, this treatment does not consider CC at high salt concentrations. Experimental studies on *salt-free* Na-PAA solutions at basic conditions have indicated that ~ 60-90% of all accompanying counterions are localized along the chains, depending on the Na-PAA concentration.[54, 55] Condensed counterions neutralize deprotonated carboxyl groups, thus reducing the chain's effective charge

density. Therefore, overlooking CC in titration experiments could significantly overestimate the effective chain charge density. In the study of binodal compositions of PAA/PDMAEMA complex coacervates at pH = 6.5, Spruijt et al.[1] took PAA (PDMAEMA) chains to be nearly fully deprotonated (protonated) and thus nearly fully *charged* over the range of salt concentrations 0-1 M KCl,[9] even though PAA (PDMAEMA) chains at salt-free conditions are merely ~ 35% deprotonated (protonated); see the symbols in Figure 3-A-5, where the theoretical predictions are compared to the titration experiments on PAA/PDMAEMA reported by Spruijt et al.[1] Here, we use their reported potentiometric titration data to estimate condensation equilibrium constants of potassium and chloride ions along PAA and PDMAEMA chains used in the study, which is subsequently used here to predict the PAA/PDMAEMA phase behavior.

Note that we take the CC parameters as absolute constants in Figure 3-A-5 for simplicity, since the main purpose here is to illustrate how the proposed phase behavior model parameters can be obtained through single-phase experiments. In fact, the two-zone Oosawa model of CC[56] which contains both short- and long-range charge-charge correlations, leads to an LMA equation yielding the extent of CC set by an equilibrium constant that scales as the cube-root inverse of the extent of CC.[57] To simulate a titration experiment in Figure 3-A-5, the pH was varied from 2 to 12 and eqns. (3-A-1) through (3-A-5) were solved under the electroneutrality condition for polymer concentrations and temperature reported by Spruijt et al.[1] Note that in single-PE simulations, phase separation and (polymer-polymer) ion-pairing equilibria need not be considered. CC parameters were adjusted to provide the best fit to the experimental data. Based on the celebrated Henderson-Hasselbach (HH) equation, the values of the pK's for protonation/deprotonation, i.e., $pK_A^\infty = 6.65, pK_C^\infty = 8$, are equal to the pH and pOH at the halfway equivalence points in the experimental results in salt-free solutions corresponding to black symbols in Figure 3-A-5. As enough KOH and HCl are titrated into the PE solutions to effect the pH change, even in the salt-free systems, our simulations deviate moderately from experimental data as potassium and chloride ions interact with PAA and PDMAEMA, suggesting that the HH formula should be modified for the more complicated system of reactions in our model. Additionally, both pK_A^∞ and pK_C^∞ are assumed to be constants while the measured apparent deprotonation constants are generally monotonically increasing functions of degree of deprotonation.[36, 37] In principle, all four equilibrium constants for protonation and CC should be treated as adjustable parameters but we use the pH and pOH halfway equivalence points to

estimate pK_A^∞ and pK_C^∞, in the interest of simplicity. Deprotonated PAA units have been shown to be more hydrophilic than protonated ones[19] while the hydrophobicity of PDMAEMA repeat units whose amine functional groups are hanging to the backbone at the end of a long aliphatic arm, are relatively insensitive to protonation. In view of this, we account for variations in hydrophilicity of PAA through a protonation-dependent short-ranged van der Waals expression, as follows:

$$f^{\chi} = \chi_{AHW}\alpha_{AH}\phi_w\phi_A \qquad \text{(3-A-32)}$$

We use χ_{AHW} = 0.45 as the FH χ parameter of protonated PAA repeat units in water, reported in the literature[49] and we neglect the van der Waals interactions between deprotonated PAA repeat units; i.e., we take χ_{AW} = 0. As the added KCl concentration increases, CC intensifies, lowering the effective charge density of PEs as depicted in Figure 3-A-5. However, potentiometric titration does not distinguish a bare ionized group from one carrying a bound counterion. As more counterions localize along chains, Le Châtelier's principle applied to eqns. (3-9) and (3-11) implies that more carboxylic acid groups need to become deprotonated to compensate for the bare carboxylate repeat units that disappear as they are neutralized with potassium ions. A similar argument can be made for cationic PDMAEMA chains and chloride ions. In other words, CC induces further deprotonation in PAA and protonation in PDMAEMA as salinity increases.

The effective charge density of PEs predicted here, accounting for the loss of charges due to counterion condensation, differs significantly from α_{CH} and $1 - \alpha_{AH}$, which are typically taken respectively as the charge density of polycations and polyanions. At 1 M KCl, our simulations overestimate the experimental data showing an effective charge density of ~ 5% at pH > 8 for PAA and a mere ~ 2% for PDMAEMA at pH < 4, see the green curves in Figure 3-A-5B. As noted earlier, the high degree of CC is not unreasonable at such high salt concentrations, given the experimental observations for salt-free systems.[54] Also, using a constant value for the CC LMA equilibrium constant is another reason for the high extent of condensation in our simulations. As more counterions bind to the chains, the mean distance between nearest charges along a chain increases and eventually equals the system Bjerrum length beyond which the driving force for CC begins to diminish substantially.

3.4.8 Effect of Ion Pairing Equilibrium Constant on Complex Coacervation

Experimental work demonstrates that the critical KCl concentration in an equimolar PAA/PDMAEMA solution is a strong function of pH with the highest critical points observed at acidic pH values, see Figure 2-1 in chapter 2. However, our model predicts a monotonically decreasing critical salt concentration, as the pH is lowered, assuming a fixed standard IP free energy. In fact, the critical KCl concentration at pH^o = 3 is less than 150 mM, Figure 3-A-6, whereas the system is observed experimentally to undergo coacervation at as high a KCl concentration as 3000 mM. Jha et al.[19] explained this observation by considering the hydrophobicity of protonated acrylic acid repeat units using a similar f^{χ} as used here, eqn. (3-A-32). They used a rather large $\chi_{AHW} = 0.75$, rendering water a poor solvent for 'protonated' PAA repeat units. Even though deprotonated PAA repeat units are decidedly more hydrophilic than protonated ones,[19] experimental results do not bear out the insolubility of PAA at pH = 3 implied by the c value assumed by Jha *et al*.[19] The van der Waals interactions of all deprotonated groups are already neglected thus making $\chi_{AHW} = 0.45$ a conservative choice for f^{χ}.

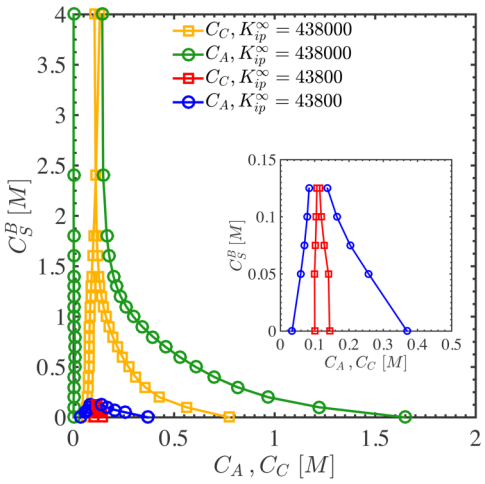

Figure 3-A-6: Binodal diagrams for PAA/PDMAEMA/KCl at pH^o = 3 at two ion-pairing equilibrium constants in the infinite dilution limit. The remaining parameters are the same as in Figure 3-6. The inset is a zoomed-in view of the binodal diagram corresponding to the lower equilibrium constant.

Instead of an excessively large c parameter between protonated PAA repeat units and water, we believe that the observed stability of PAA/PDMAEMA coacervate at pH^o = 3 could be explained by a stronger IP between PAA and PDMAEMA repeat units. We have examined the sensitivity of the phase behavior to the ion-pairing constant in Figure S6. Upon a 10-fold increase in K_{ip}^{∞} relative to the value used earlier (i.e., $K_{ip}^{\infty} \sim 43800$) at pH^o = 3, the critical point is not reached

even at a KCl concentration as high as ~ 4 M. Nonetheless, under these conditions there is a noticeable asymmetry predicted for PE concentrations in the coacervate where the PAA repeat units are more concentrated than are the PDMAEMA counterparts, which are fully protonated at pH^{o} = 3. The higher tendency of PDMAEMA units to form ion pairs with PAA leads to its higher concentration in the coacervate relative to the coacervation at K_{ip}^{∞} ~ 43800 where PDAMEMA is almost evenly partitioned between coexisting phases; see the inset in Figure 3-A-6.

3.4.9 Osmotic Pressure and Maximum Polymer Volume Fraction at No-Salt Condition

VdW interactions in oppositely charged polyelectrolyte systems represented by f^{χ} are likely to be a complicated function of IP and CC extents. For an equimolar mixture of polyions where $\phi_P = \phi_A = \phi_C$, f^{χ} is given by eqn. (3-A-33).

$$f^{\chi} = 2\phi_W\phi_P\chi_P = 2(1-2\phi_P)\phi_P\chi_P \qquad (3\text{-A-}33)$$

We propose here to use an effective FH parameter of either PE given by eqn. (3-A-34) that can exceed the constant critical value of χ_{PW} ~ 0.5 above which system remains single phase regardless of salt concentration.

$$\chi_P = \chi_{PW} + (1-\alpha_P)\beta\Delta\chi^{ip} \qquad (3\text{-A-}34)$$

Here ϕ_P, χ_P and ω_P (P: A, C) are taken to be the same for both PE, we take $\alpha_P = \alpha_{A+} = \alpha_{CH-}$, and we use $\Delta\chi^{ip}$ as a phenomenological constant, which allow for the fact that water solvency for PEs decreases as PE functional groups typically lose their hydration water upon IP.[51] The maximum PE volume fraction is attained in the limit of in the no-salt limit for an equimolar mixture of infinitely long PEs and for infinite IP constant and thus $\beta \to 1$, i.e. in the limit $\phi_+ = \phi_- \to 0 \Rightarrow \alpha_P = \alpha_{A+} = \alpha_{CH-} \to 0$. The osmotic pressure Π[58] in the latter limit is given by eqn. (3-A-35) where both f^{B} and f^{DH} tend to zero as PE free charges become fully paired. Note that $f(\phi_P = 0) = 0$.

$$\lim_{\phi_+ = \phi_- \to 0, K_{ip}^{\infty} \to \infty} \left(\frac{\Pi l^3}{k_B T}\right) = 2\frac{\partial f}{\partial \phi_P} - f - f(\phi_P = 0) = -ln(1-2\phi_P) - 2\phi_P - 4\left(\chi_{PW} + \Delta\chi^{ip}\right)\phi_P^2 - \frac{\phi_P}{\omega_P} \qquad (3\text{-A-}35)$$

The maximum equilibrium volume fraction of total PE, $2\phi_P^{max}$ is found by solving $\Pi = 0$, assuming a fully depleted supernatant phase, which is an accurate assumption for infinitely long chains. As IP constant increases the extent of IP tends to unity and the maximum PE volume

fraction for any given χ_{PW} and ω_P is achieved; see Figure 3-A-7. As the size of PE repeat units increases, the complexation becomes harder and the oppositely charged repeat units pack less compactly in the dense phase which becomes increasingly more hydrated. As expected, the dense phase becomes less hydrated as PEs become more hydrophobic corresponding to higher χ_P.

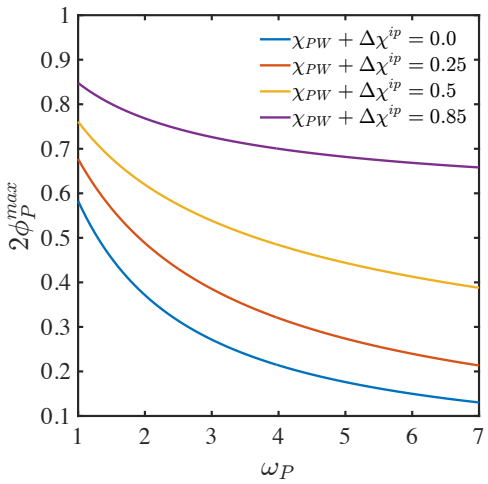

Figure 3-A-7: Maximum total PE volume fraction in the dense phase versus the ratio of monomer volume to that of water for an equimolar mixture of infinitely long PEs obtained by evaluating the roots of eqn. (3-A-35) for various effective FH parameters in water.

Figure 3-A-8 illustrates the binodal diagrams of PSS/PDADMA/KBr system for constant and IP-dependent f^{χ} given by eqn. (3-A-33) predicted by our model and by the extended Voorn-Overbeek (EVO) model, see eqn. (3-2). Using an IP-dependent FH parameter improves the fit to the experimental data at low salt concentration. Note that if a constant $\chi_P > 0.5$ were used, no critical point would be observed and counterions would not suppress complex coacervation regardless of salt concentration. As can be inferred from Figure 3-A-8, making χ_P IP dependent appreciably increases the PE volume fraction at the critical point, as shown by the two arrows in Figure 3-A-8, indicating the change in critical polymer concentration. Additionally, using a slightly smaller $\omega_P = 5$ results with a constant $\chi_P = 0.5$ in results in a better fit quality, given by the purple curve Figure 3-A-8, indicating how ω_P could be adjusted to provide seemingly better predictions despite not being accurate. ($\omega_P = 6.5$ is the acceptable value based on the weight fraction and concentrations of polyions reported by Wang and Schlenoff,[3] assuming incompressibility)

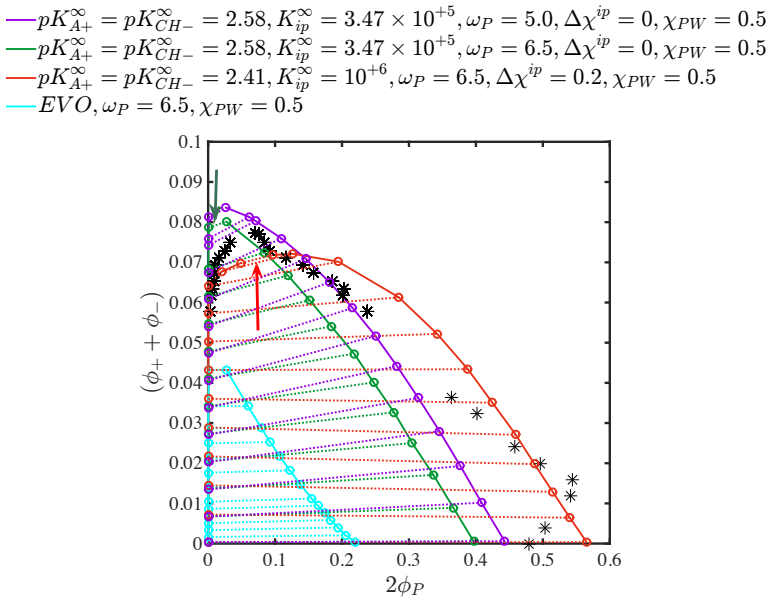

Figure 3-A-8: Binodal diagrams for PSS/PDADMA/KBr system obtained by our model for constant and IP-dependent χ_P given by eqn. (3-A-34), and for the EVO model. The black asterisks represent experimental data reported by Wang and Schlenoff.[3] Open circles and dotted lines indicate the tie lines obtained using flash calculations. The red curve represents our model predictions with IP-dependent FH parameter. For definition of FH parameters in the legend, see eqn. (3-A-34). The red and green arrows point to the critical point for the binodal curves predicted for constant and IP-dependent FH parameters, respectively. The cyan curve represents the binodal diagram predicted by EVO model. The purple curve is included to show the sensitivity of our predictions to monomer sizes, ω_P.

3.4.10 Binodal Diagram for PAA/PDMAEMA/KCl

In Figure 3-A-9, we compare the prediction of our predicted binodal diagram for PAA/PDMAEMA/KCl at room temperature at pH^o = 5 and 7 reproduced from Figure 3-6C and 3-6D to that by the VO model extended by Jha *et al.*[19] which accounts for salt-induced protonation in weak polyelectrolytes by using an experimentally obtained acidity and basicity of PAA/PDMAEMA as a function of KCl concentration. For prediction of the EVO model in Figure 3-A-9, we used identical FH χ parameters, monomer and counterion size and acidity and basicity as those used in the predictions for our new theory, all listed in Table 3-2.

As can be seen in Figure 3-A-9, the EVO model underestimates the experimental data available at pH^o = 7 by roughly 70%. Note that monomer and counterion sizes and FH χ parameters can be adjusted to improve the predictions of EVO model. However, such liberal use of these parameters is not justified given that concentration and weight fraction allows for a direct calculation of the ω_i's using eqn. (3-26). Furthermore, isothermal calorimetric measurements

constrain the values of FH χ parameters. Our model accommodates calorimetric measurements of counterion condensation and ion pairing by construct.

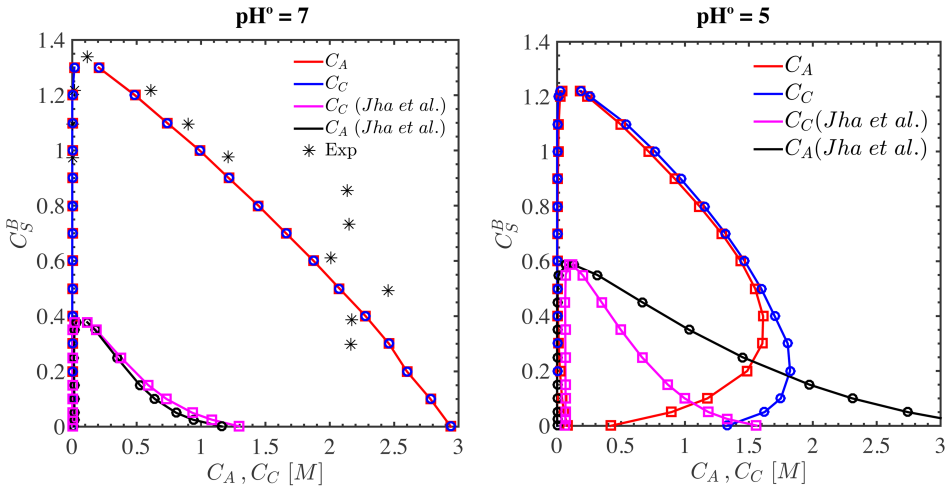

Figure 3-A-9: Binodal diagrams for PAA/PDMAEMA/KCl with C_S^B being the added KCl molar concentration predicted by our model and an EVO model proposed by Jha *et al*., with an empirical charge regulation model[19] (black and magenta curves) for weak polyions using the same parameters listed in Table 3-2. Binodal diagram predicted by our model and experimental data, dark stars, are reproduced from Figure 3-6.

3.5 References

[1] Spruijt, E.; Cohen Stuart, M. A.; van der Gucht, J. *Macromolecules* **2013,** *46,* 1633-1641.

[2] Tekaat, M.; Bütergerds, D.; Schönhoff, M.; Fery, A.; Cramer, C. *Phys. Chem. Chem. Phys.* **2015,** *17,* 22552-22556.

[3] Wang, Q.; Schlenoff, J. B. *Macromolecules* **2014,** *47,* 3108-3116.

[4] Wandrey, C.; Hunkeler, D.; Wendler, U.; Jaeger, W. *Macromolecules* **2000,** *33,* 7136-7143.

[5] Dobrynin, A. V.; Rubinstein, M. *Prog. Polym. Sci.* **2005,** *30,* 1049-1118.

[6] Brilliantov, N. V.; Kuznetsov, D. V.; Klein, R. *Phys. Rev. Lett.* **1998,** *81,* 1433-1436.

[7] Muthukumar, M.; Hua, J.; Kundagrami, A. *J. Chem. Phys.* **2010,** *132,* 84901-84910.

[8] Overbeek, J. T. G.; Voorn, M. J. *J. Cellular Comparative Physiology* **1957,** *49,* 7-26.

[9] Spruijt, E.; Westphal, A. H.; Borst, J. W.; Cohen Stuart, M. A.; van der Gucht, J. *Macromolecules* **2010,** *43,* 6476-6484.

[10] Boustta, M.; Leclercq, L.; Vert, M.; Vasilevskaya, V. V. *Macromolecules* **2014,** *47,* 3574-3581.

[11] Qin, J.; Prifitis, D.; Farina, R.; Perry, S. L.; Leon, L.; Whitmer, J.; Hoffmann, K.; Tirrell, M.; de Pablo, J. J. *ACS Macro Lett.* **2014,** *3,* 565-568.

[12] Sing, C. E. *Adv. Colloid Interface Sci.* **2017**, 239, 2-16.

[13] Qin, J.; de Pablo, J. J. *Macromolecules* **2016**, 49, 8789-8800.

[14] Ermoshkin, A. V.; Olvera de la Cruz, M. A *Macromolecules* **2003,** *36,* 7824-7832.

[15] Donley, J. P.; Heine, D. R.; Wu, D. T. *Macromolecules* **2005,** *38,* 1007-1020.

[16] Kudlay, A.; Ermoshkin, A. V.; Olvera de la Cruz, M. *Macromolecules* **2004,** *37,* 9231-9241.

[17] Kudlay, A.; Olvera de la Cruz, M. *J. Chem. Phys.* **2004,** *120,* 404-412.

[18] Castelnovo, M.; Joanny, J.-F. *Eur. Phys. J. E* **2001,** *6,* 377-386.

[19] Jha, P. K.; Desai, P. S.; Li, J.; Larson, R. G. *Polymers* **2014,** *6,* 1414-1436.

[20] Ou, Z.; Muthukumar, M. *J. Phys. Chem.* **2006**, *124,* 154902-154913.

[21] Xu, X.; Kanduč, M.; Wu, J.; Dzubiella, J. *J. Chem. Phys.* **2016**, *145*, 034901-034911.

[22] Semenov, A. N.; Rubinstein, M. *Macromolecules* **1998,** *31,* 1373-1385.

[23] Tcyrulnikov, S.; Victorov, A. I. *Macromolecules* **2013,** *46,* 46-4715.

[24] Perry, S. L.; Sing, C. E. *Macromolecules* **2015,** *48,* 5040-5053.

[25] Hoda, N.; Larson, R. G. *J. Phys. Chem. B* **2009,** *113,* 4232-4241.

[26] Petrauskas, V.; Maximowitsch, E.; Matulis, D. *J. Phys. Chem. B* **2015,** *119,* 12164-12171.

[27] Ma, P. L.; Lavertu, M.; Winnik, F. M.; Buschmann, M. D. *Biomacromolecules* **2009,** *10,* 1490-1499.

[28] Priftis, D.; Laugel, N.; Tirrell, M. *Langmuir* **2012,** *28,* 15947-15957.

[29] Veis, A. *J. Phys. Chem.* **1961,** *65,* 1798-1803.

[30] Vitorazi, L.; Ould-Moussa, N.; Sekar, S.; Fresnais, J.; Loh, W.; Chapel, J.-P.; Berret, J.-F. *Soft Matter* **2014,** *10,* 9496-9505.

[31] Muthukumar, M. *J. Chem. Phys.* **2004,** *120,* 9343-9350.

[32] Israelachvili, J. N. *Intermolecular and Surface Forces,* 3rd ed.; Academic Press: San Diego, 2011.

[33] Manning, G. S. *Physica A* **1996,** *231,* 236-253.

[34] Spruijt, E.; Leermakers, F. A. M.; Fokkink, R.; Schweins, R.; van Well, A. A.; M.A., C. S.; van der Gucht, J. *Macromolecules* **2013,** *46,* 4596-4605.

[35] Markarian, M. Z.; Hariri, H. H.; Reisch, A.; Urban, V. S.; Schlenoff, J. B. *Macromolecules* **2012,** *45,* 1016-1024.

[36] Sadeghpour, A.; Vaccaro, A.; Rentsch, S.; Borkovec, M. *Polymer* **2009,** *50,* 3950-3954.

[37] Bohinc, K.; Kovačević, D.; Požar, J. *Phys. Chem. Chem. Phys.* **2013,** *15,* 7210-7219.

[38] Lee, H.; Son, S. H.; Sharma, R.; Won, Y. Y. *J. Phys. Chem. B* **2011,** *115,* 844-860.

[39] Choi, J.; Rubner, M. F. *Macromolecules* **2005,** *38,* 116-124.

[40] Petrov, A. I.; Antipov, A. A. *Macromolecules* **2003,** *36,* 10079-10086.

[41] Ahn, H. J.; Kang, E. C.; Jang, C. H.; Song, K. W.; Lee, J. O. *J. Macro. Sci. Part A* **2000,** *37,* 573-590.

[42] Vasheghani, B.; Rajabi, F. H.; Ahmadi, M. H. *Polymer Bulletin* **2006,** *58,* 553-563.

[43] Shamoun, R. F.; Hariri, H. H.; Ghostine, R. A.; Schlenoff, J. B. *Macromolecules* **2012,** *45,* 9759-9767.

[44] Fu, J.; Schlenoff, J. B. *J. Am. Chem. Soc.* **2016,** *138,* 980-990.

[45] Bucur, C. B.; Sui, Z.; Schlenoff, J. B. *J. Am. Chem. Soc.* **2006,** *128,* 13690-13691.

[46] Qiao, B.; Cerdà, J. J.; Holm, C. *Macromolecules* **2010,** *43,* 7828-7838.

[47] Köhler, R.; Dönch, I.; Ott, P.; Laschewsky, A.; Fery, A.; Krastev, R. *Langmuir* **2009**, *25*, 11576-11585.

[48] Dubas, S.T.; Schlenoff, J.B. *Langmuir* **2001**, *17*, 7725-7727.

[49] Mehrdad, A.; Samadiani, N.; Poormoosa, L. *J. Mol. Liq.* **2013,** *187,* 177-182.

[50] Biesheuvel, P. M.; Cohen Stuart, M. A. *Langmuir* **2004,** *20,* 4764-4770.

[51] Schlenoff, J. B.; Rmaile, A. H.; Bucur, C. B. *J. Am. Chem. Soc.* **2008,** *130,* 13589-13597.

[52] Alonso, T.; Irigoyen, J.; Iturri, J. J.; Iarena, I. L.; Moya, S. E. *Soft Matter* **2013,** *9,* 1920-1928.

[53] Carnal, F.; Ulrich, S.; Stoll, S. *Macromolecules* **2010,** *43,* 2544-2553.

[54] Truzzolillo, D.; Bordi, F.; Cametti, C.; Sennato, S. *Phys. Rev. E* **2009,** *79,* 11804-11813.

[55] Bordi, F.; Colby, R. H.; Cametti, C.; De Lorenzo, L.; Gili, T. *J. Phys. Chem. B* **2002,** *106,* 6887-6893.

[56] Oosawa, F. *Polyeletrolytes;* Marcel Dekker: New York, 1971.

[57] Dobrynin, A. V.; Rubinstein, M. *Macromolecules* **2001,** *34,* 1964-1972.

[58] Doi, M.; Soft Matter Physics, Oxford University Press, 2013.

Chapter 4: A Multicomponent Stress-Diffusion Coupling Model of Drug Release From Polymer-Matrix Tablets*

4.1 Introduction

One of the early models is due to Lustig and Peppas[1] who developed a 1D description of solute transport using Fick's second law of diffusion with Fujita-type diffusivities. While Lustig and Peppas transformed their spatial coordinates globally to track the overall thickness of the polymer film as it swelled with solvent, they did not transform their equations locally into a proper Lagrangian polymer-fixed frame. Ju *et al*.[2] and Narasimhan and Peppas[3] incorporated matrix re-dissolution by appending a polymer diffusion boundary layer to the tablet-solvent interface where chain disentanglement dynamics dictates the polymer erosion rate. Siepmann and coworkers[4,5] solved 2D axisymmetric diffusion equations without advection terms in cylindrical coordinates (r and z) coupled to Fujita-type pseudo binary flux laws and accounted for swelling by following the overall content of individual area elements and zeroth order matrix re-dissolution kinetics. Borgquist *et al*.[6] also employed Fick's flux law but included the swelling-induced convective terms in their finite volume simulations explicitly. Hariharan and Peppas[7] and Brazel and Peppas[8] incorporated the matrix stress relaxation in penetrant transport equation via a prescribed convective term that controls diffusion of drug molecules implicitly. Combining Darcy's law and a diffusion-advection equation for water and drug respectively, Xu *et al*.[9] predicted the drug release and swelling kinetics of linearly elastic cross-linked hydrogels with low initial drug loading. They did not consider matrix viscoelasticity. Recent 2D finite element simulations of Kaunisto *et al*.[10,11] using a generalized Fick's law and Caccavo *et al*.[12] employed pseudo-binary flux law and dynamic re-meshing to keep track of the matrix re-dissolution and swelling-induced deformation of the computational domain using the Arbitrary Lagrangian-

* This chapter has been adapted from my publication in the Journal of Controlled Release *224* (**2016**) pp. 43-58.

Eulerian (ALE) method. While mathematically elegant, the matrix viscoelasticity and thermodynamic non-idealities were lacking in both of the last studies.

Solution of conventional models utilizing the pseudo binary Fick's law leads to Fickian drug release and penetrant sorption kinetics both characterized by a square root of time dependence. Numerous experimental investigations have long established that in addition to Fickian release, anomalous, linear (Case II) and even super linear (Sigmoidal or Super Case II) drug release profiles, collectively referred to as non-Fickian behavior hereafter, can also occur under certain conditions.[13,14] Non-Fickian diffusion has been originally investigated in the context of the closely related area of penetrant sorption into glassy polymers. A number of theories have been particularly proposed to elucidate Case II transport in glassy polymers that account for a sharp glassy-rubbery (swelling) front moving inwards, either explicitly by including a convective term into the penetrant conservation equation[8,15] or implicitly by coupling the glassy-rubbery transition kinetics to the conservation equations.[16-18] Both of the foregoing approaches require a prior knowledge of the experimentally-determined moving front velocity or empirical parameters describing kinetics of swelling.

Although there is an alternative explanation based on free volume theory,[19] Case II diffusion is now widely attributed to a coupling between the viscoelastic stress response of the polymer matrix and Fickian diffusion as penetrant ingress and drug release lead to matrix deformation. In fact, a broadly accepted criterion for non-Fickian transport is that, in Case II diffusion, there is a steep moving composition front at which the diffusional Deborah number = $O(1)$ implying that at the moving front the chain relaxation time is comparable to the characteristic time for diffusion of solvent over the width of front region.[20] Coupling the polymer constitutive equation for stress with mass conservation and incorporating a history-dependent contribution of matrix deformation to the total free energy of mixing, Durning and Tabor[21] developed a model that obviated the need to know *a priori* the experimental front velocity or swelling dynamics at glassy-rubbery front. Peppas and coworkers[22,23] introduced polymer surface dissolution to the model of Durning and Tabor[21] but neglected the time dependence of the surface boundary conditions and deformation tensor in their Lagrangian[22] and Eulerian[23] approaches.

Despite the foregoing advances, some points have been largely overlooked in the literature. The time dependencies of boundary conditions at tablet outermost interface have either been

completely neglected or included through a phenomenological exponential function whose rate is set by the chain relaxation time.[8] Due to sensitivity of water and API diffusivities to water concentration, use of static boundary conditions on water is not generally an accurate assumption.

More importantly, Fujita-type *pseudo-binary* flux laws are prevalent choices for transport of drug and penetrant molecules. The pseudo-binary flux law is accurate only for tablets with very low drug loading, since it does not account for diffusional friction between penetrant and drug molecules. Additionally, pseudo binary Fickian fluxes, being defined with respect to a reference velocity, do not properly account for diffusion-induced convection and therefore fail to satisfy Galilean invariance, a basic physical principle. Use of pseudo-binary flux laws in different reference frames can also render mutual diffusivities, a basic material property, frame-dependent. Lastly, in systems with more than three constituents, even a matrix-fixed frame may not be adequate except in very special cases. A more detailed comparison between ESM and pseudo-binary fluxes is provided in appendix 4.4.1.

In what follows, we offer an extension of the two-component model of Durning and Tabor[21] to multi-component systems by employing frame-invariant ESM flux laws that explicitly account for diffusional drag between water and drug, thereby allowing arbitrary initial drug loading, and allowing simultaneous drug release and solvent sorption. Moreover, ESM flux laws establish a physically meaningful link between molecular scale simulations and continuum level transport models. In the subsequent sections, we first put forth a detailed description of our model followed by illustrative simulation results and discussion to demonstrate the salient features of the model.

4.2 Model Development

4.2.1 Assumptions

We have made a number of fundamental assumptions listed below. We shall explain the rationale for these later in this section.

1. Upon exposure to a release medium, taken to be pure water hereafter, a matrix tablet is a ternary system composed of water, API (drug) and polymer matrix (excipient) denoted by W, D and E, respectively. (A detailed notation list is furnished at the end for quick reference.)

2. Ideal mixing. The excess volume of the system is identically zero irrespective of composition. In other words, partial molar volumes of all species are equal to those of respective pure components at the same pressure and temperature.

3. Polymer chains remain chemically stable in water throughout the duration of dissolution. This assumption applies to a broad range of hydrophilic polymers.

4. Tablet ingredients constitute a single continuous phase, i.e. tablet bulk porosity is not considered here.

5. Initially, ingredients are uniformly distributed across the tablet.

6. Phase change; i.e., crystallization or crystal dissolution, is not explicitly considered.

7. There is no resistance to mass transfer in the release medium up to the interface with the tablet. Consequently, a thermodynamic equilibrium between the tablet's outermost surface and bulk release medium is established instantaneously.

4.2.2 Governing Equations

We restrict ourselves to one dimension in a planar geometry so as to underscore the main features as well as departures from previous models more readily. Generalization to higher dimensions and different coordinate systems will be straightforward, albeit with more computational and algebraic complexity. To begin with, consider a large slab of polymer matrix, two dimensions of which are vastly larger than the third one, taken as *x*-axis. A 1D treatment is particularly relevant in *in vitro* API release studies of powders of high-aspect-ratio cylindrical particles and microspheres. The tablet contains an initially known drug loading and is immersed in physiological buffer comprising water and typically a host of ions. We take the release medium to be pure water according to the first assumption even though the gastrointestinal fluids are complex buffer solutions. This assumption is not restrictive as many polymeric excipients are marginally sensitive to salinity and pH. For ionizable polymers in physiological buffers, however, we shall explain how the present model could accommodate ion transport and pH effects. The mass conservation of species *i*: *W, D* is expressed as the following general equations in which use had been made of the second assumption to convert the molar concentration and flux of species *i* into volume fraction ϕ_i and volumetric flux $\hat{N}_i$, eqn. (4-1).

$$\frac{\partial \phi_i}{\partial t} = -\nabla \hat{N}_i + R_i \tag{4-1}$$

Following our 6th assumption there is no distinction between dissolved or crystalline API and thus the reaction term in eqn. (4-1) R_i is set to zero for both water and API. For a system comprised of m distinct components, only $m - 1$ of the conservation equations are linearly independent so that the following incompressibility condition, eqn. (4-2), must be enforced to obtain the local excipient composition.

$$\phi_E = 1 - \phi_W - \phi_D \tag{4-2}$$

The pseudo binary flux law has been the most popular choice to relate the molar flux of a given component solely to its own diffusion driving force. Even though this approach could be plausible for low drug loading, the diffusion-induced advection of a given component due to friction with other components should not be disregarded *a priori*. One thus needs to use the generalized Stefan-Maxwell (GSM) flux law, eqn. (4-3), to take into account the diffusional frictions of any given species with all other components present in an isothermal system in the absence of body forces.

$$CRTd_i = C_i \nabla \mu_i \Big|_{P,T} + (\phi_i - w_i)\nabla P = RT \sum_{j \neq i} \frac{y_i N_j - y_j N_i}{D_{ij}} \tag{4-3}$$

Here C is the total molar concentration, C_i is the molar concentration and w_i the mass fraction of species i. R and T are gas constant and absolute temperature. Gradients of chemical potential of species i, μ_i and total pressure P contribute to diffusion, albeit with different significance, as discussed shortly. Note that the GSM flux relates the total diffusion driving force to the mole fraction y_i and molar flux N_i of species i. Accordingly GSM mutual diffusivities D_{ij} are defined on a molar basis. A GSM flux law is essentially a force balance between total friction force and the total diffusion driving force per unit volume d_i exerted on species i.

The sum of total diffusion driving forces of all species adds up to zero, due to the principle of equal and opposite reaction and the Gibbs-Duhem thermodynamic constraint. Eqn. (4-3) in terms of molar quantities and mole fractions was historically developed for gas mixtures and simple fluids where collision frequencies are proportional to the *number* of molecules, which is not the case with starkly different-sized components. Given that mole fraction of excipient is also ill

defined in a gel, it is more appropriate to recast eqn. (4-3) in terms of volume fractions. Straightforward as it may seem, conversion of GSM flux laws into a form using component volume fractions while ensuring that both the Onsager reciprocity principle[24] and the Gibbs-Duhem relation are satisfied has been a challenge over the past decade. We here adopt the approach proposed by Fornasiero *et al*.[25] who simply modified the collision frequency of components by introducing a reference molar volume υ, akin to the one employed in the Flory-Huggins (FH) lattice formalism. Consequently, no molecular weight or concentration for the excipient need be specified and thus transport coefficients can be measured experimentally without confusion. Hereafter, we refer to the extension of GSM proposed by Fornasiero *et al*.[25] as the *extended* Stefan-Maxwell flux law, eqn. (4-4), where the hatted variables are species fluxes on a volumetric basis. For simplicity, we use the same notation for ESM diffusivities in eqn. (4-4) as those used in GSM flux law, eqn. (4-3).

$$d_i = \left(\frac{\upsilon}{\upsilon_i}\right)\phi_i \nabla\left(\frac{\mu_i}{RT}\right)_{P,T} + \frac{\upsilon(\phi_i - w_i)}{RT}\nabla P = \sum_{j\neq i}\frac{\phi_i \hat{N}_j - \phi_j \hat{N}_i}{D_{ij}} \tag{4-4}$$

The reference volume υ is chosen to be that of the smallest component in the system, typically that of the water, υ_W. The FH mixing free energy functional at the reference pressure per lattice site includes entropic and enthalpic interactions contributed by all three components and admits the following form if υ is set to υ_W, eqn. (5).

$$\frac{\upsilon \Delta F_{mix}^{FH}}{V k_B T} = \phi_W \ln \phi_W + \left(\frac{\upsilon_W}{\upsilon_D}\right)\left[\phi_D \ln \phi_D + \chi_{DE}\phi_D\phi_E\right] + \chi_{WD}\phi_D\phi_W + \chi_{WE}\phi_W\phi_E \tag{4-5}$$

Here χ_{ij} denotes the FH interaction parameter between *i* and *j* and k_B is the Boltzmann constant. Implicit in eqn. (4-5) is the negligible entropic contribution of the excipient as a typical polymer chain is immensely larger than water or API molecules. Note that the chemical potential contribution to the total driving force has to take into account the monomer connectivity and the actual size ratio of the components. Even so, no molecular weight has to be specified for excipient to evaluate driving forces of eqn. (4-4) given that free energy functional, eqn. (4-5), is expressed in terms of component volume fractions and the size ratio of water and drug molecules.

Taking the *yz*-plane passing through the origin as the symmetry plane, all fluxes must vanish at the tablet mid-plane. The volume-averaged velocity, v^*, will be solenoidal, i.e. have a zero

divergence, according to our second assumption. Note that the second assumption is consistent with the inherent incompressibility in the FH formalism. Combining the latter fact with zero flux condition at mid-plane, we arrive at an auxiliary equation to be coupled with ESM flux laws, eqn. (4-6)

$$\nabla \cdot \mathrm{v}^* = \frac{\partial \mathrm{v}^*_x}{\partial x} = 0 \Rightarrow \mathrm{v}^*_x = \sum_i \phi_i \mathrm{v}^*_{i,x} = \sum_i \hat{N}_{i,x} = 0 \tag{4-6}$$

Eqn. (4-6) allows the flux-implicit ESM flux laws, eqn. (4-4) to be inverted to flux-explicit laws, where the fluxes are expressed explicitly in terms of the driving forces d_i, thereby allowing equations to be solved conveniently. Neglecting inertia and body forces, the momentum balance equation is given by eqn. (4-7).

$$\frac{\partial}{\partial x}\left[\sigma^E_{xx} - P\right] = 0 \tag{4-7}$$

Here the superscript indicates that only the excipient deviatoric stress $\sigma_{xx}^{\ E}$ is considered, as solvent and API deviatoric stresses are negligible compared to the deviatoric stress generated in the matrix. Once a constitutive model for polymer matrix is chosen, the pressure gradient may be eliminated from eqns. (4-3) and (4-7). According to eqn. (4-7), the pressure gradient in the absence of body forces balances gradient of the *xx* component of the matrix stress. This has led some authors[22,26] to argue that matrix contributes to total driving force d_i through the pressure gradient term in eqn. (4-3). However, the density of most polymers does not differ much from that of water and therefore the difference between the mass fraction and the volume fraction (ϕ_i – w_i) in eqn. (4-3) is negligible for such mixtures. Indeed, the pressure gradient contribution to diffusion vanishes entirely for components with identical mass density.

It is now well understood that the matrix stress contribution to d_i should be incorporated into the free energy or equivalently into species chemical potentials.[21,27] Put another way, the total free energy of systems in which excipient interacts physiochemically with the rest of system can be conceived of as consisting of two contributions, namely one from the ordinary mixing free energy and another history-dependent contribution due to matrix elasticity arising from nonrandom chain orientations due to water influx. Hence, the chemical potential of species *i* can be written as the sum of the two aforementioned contributions.

$$d\mu_i\Big|_{P,T} = d\mu_i^{mix}\Big|_{P,T} + d\mu_i^{s}\Big|_{P,T} \tag{4-8}$$

The superscript '*s*' is added to signify the matrix stress response for which an expression in terms of matrix stress tensor is derived in appendix 4.4.2 and is given by eqn. (4-9). Only the *xx* element of the excipient stress tensor in our model has a non-zero contribution to the trace and thus to the internal energy.

$$d\mu_i^s\Big|_{P,T} = \frac{N_o \upsilon_i}{2} d\sigma_{xx}^E\Big|_{P,T} \tag{4-9}$$

Here N_o refers to the Avogadro's number. Note that the reference state is defined as the stress-free matrix at the reference pressure and temperature. Even for components with constant and identical mass densities where the pressure gradient has zero net contribution to diffusion, one can readily verify that the matrix will continue to contribute to the diffusion driving force d_i through the chemical potential gradient term as long as there is elastic energy stored in the matrix. The choice of the constitutive equation depends on the polymer characteristics and is of a secondary importance in our model. We here adopt the upper convected Maxwell (UCM) model, which is an appropriate constitutive equation for entangled Gaussian chains for small to moderate deformations and follows from transient network theory.[35] The *xx* element of stress in the original UCM model can be simplified to eqn. (4-10) as below:

$$\frac{\partial \sigma_{xx}^E}{\partial t} + \frac{\sigma_{xx}^E}{\tau} = 2(G + \sigma_{xx}^E)\Gamma_{xx}^E \tag{4-10}$$

Note that partial time derivative in eqn. (4-10) will need to be replaced by the substantial time derivative when there is a spatial dependence of stress and strain rate. The denominator of the second term in eqn. (4-10) is the matrix relaxation time τ and is known to be a function of composition. For infinitely large τ, UCM predicts a perfectly elastic response. If not, any stress generated in the material is predicted to decay completely at a rate set by τ. The latter prediction is consistent with entangled polymers. However, a different constitutive equation such as the Kelvin-Voigt model should be employed for cross-linked polymers that behave as solid-viscoelastic materials, such as cross-linked hydrogels based on alginate. The *xx* element of the matrix strain rate tensor, Γ_{xx}^E is defined as the derivative of the excipient velocity in the *x* direction:

$$\Gamma_{xx}^E = \frac{\partial \mathrm{v}_x^E}{\partial x} \tag{4-11}$$

Note that only deformation of the excipient is considered in eqn. (4-11). The *xx* elements of the velocity gradient and deformation tensor, λ_x referred to as the stretch ratio hereafter, are related according to eqn. (4-12).

$$\frac{\partial \lambda_x}{\partial t} = \lambda_x \frac{\partial v_x^E}{\partial x} \tag{4-12}$$

The matrix modulus in transient network theory is directly proportional to the number of network strands per unit volume[28] and in the typical derivation of the UCM it is taken to be constant since only volume-preserving deformations are ordinarily considered. However, uniaxial extension of excipient in response to water influx and drug release is not volume preserving and thus the network strand density is subject to change. If we assume that network junctions remain intact during matrix swelling, and since swelling is one-dimensional in the *x* direction with no matrix contraction in the lateral dimensions, the matrix modulus should be inversely proportional to stretch ratio according to eqn. (4-13).

$$G = \frac{G^o}{\lambda_x} \tag{4-13}$$

The superscript ^{o} refers to the reference, or undeformed, state, which we take as the excipient in dry tablet. We note here that if the "network junctions" are physical entanglements, and if some of these entanglements are lost during the swelling, and not just diluted by solvent, then the modulus could drop more steeply with swelling than indicated by eqn. (4-13). Assuming only dilution of strand density, the form of the UCM used here, in contrast to the original UCM model, is derived in appendix 4.4.3. Also, the constitutive equations describe polymer material points, which are free to move along the *x*-axis in our model. Thus, the time derivatives in the constitutive equation must be replaced with substantial derivatives. Finally, the *xx* element of the modified UCM is given by eqn. (4-14).

$$\frac{D\sigma_{xx}^E}{Dt} + \frac{\sigma_{xx}^E}{\tau} = \left(\frac{2G^o}{\lambda_x^2} + \frac{\sigma_{xx}^E}{\lambda_x} \right) \frac{D\lambda_x}{Dt} \tag{4-14}$$

Utilizing conservation of excipient and eqn. (4-11), the local stretch ratio can be expressed in terms of local excipient volume fraction according to eqn. (4-15).

$$\lambda_x = \frac{\phi_E^o}{\phi_E} \tag{4-15}$$

All derivations thus far have been in a spatially fixed frame. It has been customary in the literature on solvent sorption in glassy polymers to adopt a Lagrangian polymer-fixed frame wherein the polymer velocity is identically zero across the tablet. In the presence of polymer re-dissolution, however, an Eulerian front-tracking approach is the logical choice. In order to address the moving interface between the release medium and tablet, we introduce a dimensionless position, $\xi \in [0,\ 1]$ that renders the computational domain stationary via the following Landau [29] transformation.

$$\xi \equiv \frac{x}{L(t)} \tag{4-16}$$

In eqn. (4-16), L is the instantaneous half thickness of the tablet. In accordance with the Landau transformation of eqn. (4-16), all temporal and spatial derivatives in the fixed spatial frame (x,t) should be replaced with their corresponding derivatives in the deforming frame, (ξ ,t).

$$\left.\frac{\partial}{\partial x}\right|_t = \left.\frac{\partial}{L\,\partial \xi}\right|_t \tag{4-17}$$

$$\left.\frac{\partial}{\partial t}\right|_x = \left.\frac{\partial}{\partial t}\right|_\xi + \left.\frac{\partial \xi}{\partial t}\right|_x \left.\frac{\partial}{\partial \xi}\right|_t = \left.\frac{\partial}{\partial t}\right|_\xi - \left(\frac{\xi}{L}\right)\frac{dL}{dt}\left.\frac{\partial}{\partial \xi}\right|_t \tag{4-18}$$

Having established the matrix stress contribution to species chemical potentials, ESM flux laws can be inverted to yield species fluxes explicitly in terms of gradients of composition and stress. Applying the chain rules of eqn. (4-17) and (4-18) to conservation equations in the fixed frame, eqn. (4-1), final closed forms of water and drug conservation equations in the deforming frame are given by the following.

$$L^2\frac{\partial \phi_W}{\partial t} = \frac{\partial}{\partial \xi}\left(A_W\frac{\partial \phi_W}{\partial \xi}\right) + L\xi\left(\frac{dL}{dt}\right)\frac{\partial \phi_W}{\partial \xi} + \frac{\partial}{\partial \xi}\left(A_D\frac{\partial \phi_D}{\partial \xi}\right) + \frac{\partial}{\partial \xi}\left(A_E\frac{\partial \phi_E}{\partial \xi} + A_\sigma\frac{\partial \sigma^E_{xx}}{\partial \xi}\right) \tag{4-19}$$

$$L^2\frac{\partial \phi_D}{\partial t} = \frac{\partial}{\partial \xi}\left(B_D\frac{\partial \phi_D}{\partial \xi}\right) + L\xi\left(\frac{dL}{dt}\right)\frac{\partial \phi_D}{\partial \xi} + \frac{\partial}{\partial \xi}\left(B_W\frac{\partial \phi_W}{\partial \xi}\right) + \frac{\partial}{\partial \xi}\left(B_E\frac{\partial \phi_E}{\partial \xi} + B_\sigma\frac{\partial \sigma^E_{xx}}{\partial \xi}\right) \tag{4-20}$$

All the coefficients in eqns. (4-19) and (4-20) are algebraic functions of ESM mutual diffusivities and composition and closed form expressions are provided in in appendix 4.4.4. The first terms on the left in eqns. (4-19) and (4-20) should be interpreted as the conventional diffusive terms based on pseudo binary flux laws. The second terms in the two equations stem

from the Landau transformations and represent a pseudo advective term arising from relocation of grid points in the fixed frame relative to the deforming frame. The third terms embody diffusion-induced advection of water and drug caused by their counter-current movement during water sorption and drug release. The fourth terms represent the advection generated through excipient stress response as well as thermodynamic interactions of excipient with water and drug. In deriving eqns. (4-19) and (4-20), we took the mass densities of all species to be identical so that the pressure gradient contribution to total diffusion in eqn. (4-5) becomes identically zero. This assumption is not crucial in developing our model and is hardly restrictive, given that the density of most polymeric materials does not deviate substantially from that of water. All the coefficients in eqns. (4-19) and (4-20) combine both thermodynamic non-idealities arising from FH model and kinetic factors in the ESM flux laws. A_W and B_D would reduce to D_{WE} and D_{DE}, respectively, and the remaining terms in r.h.s of eqn. (4-19) and (4-20) would vanish, only if all thermodynamic non-idealities were neglected, D_{WD} were set to infinity and, instead of the moving frame, a polymer-fixed reference frame were adopted.

The Landau transformation introduced in eqn. (4-16) is advantageous in as much as it maintains the computational domain fixed over time even with matrix swelling and surface erosion. As is standard in all moving boundary problems, an auxiliary equation, called the Stefan condition, should be derived in order to keep track of the half thickness over time, $L(t)$. Interfacial mass balance on excipient serves the purpose.

$$\frac{dL}{dt} = \left. \frac{\hat{N}_{E,x} - \mathrm{v}_{er}}{\phi_E} \right|_{\xi=1} \tag{4-21}$$

The quantity v_{er} is referred to as the erosion velocity and denotes the volumetric flux of excipient eroded per unit area and can be both measured experimentally and estimated theoretically by the chain reptation model. Alternatively, eqn. (4-21) can be derived by differentiation of the total volume of the slab per unit area given by eqn. (4-22) with respect to time and applying the Leibniz integral rule, as shown below

$$L(t) = \int_o^L \left(\sum_{i \neq E} \phi_i \right) dx + \left(L_E^o - \int_o^t \mathrm{v}_{er}(t')\, dt' \right) \Rightarrow \frac{dL}{dt} = \int_o^L \left(\sum_{i \neq E} \frac{\partial \phi_i}{\partial t} \right) dx - \mathrm{v}_{er}(t) \tag{4-22}$$

Here L_E^o designates the excipient contribution to the initial half thickness of the slab. That is, if the initial slab half thickness is L^o, and the initial excipient volume fraction is 0.7 (the rest being API), then $L_E^o = 0.7\ L^o$. Substituting the time derivatives of the species volume fractions using eqn. (4-1), and recognizing that matrix erosion is assumed to occur only at the outermost surface of the matrix and that all generation rates sum up to zero, eqn. (4-21) is re-derived. Discussion of erosion velocity and material functions is deferred until the next section.

4.2.3 Boundary Conditions

In deriving eqn. (4-6), we have already introduced a symmetry argument at the tablet mid-plane whereby all species fluxes and gradients of all field variables vanish there. This assumption may be formally described by eqns. (4-23) and (4-24).

$$\hat{N}_{W,x}\Big|_{\xi=0} = \hat{N}_{D,x}\Big|_{\xi=0} = \hat{N}_{E,x}\Big|_{\xi=0} = 0 \tag{4-23}$$

$$\left.\frac{\partial \sigma_{xx}^{E}}{\partial \xi}\right|_{\xi=0} = \left.\frac{\partial P}{\partial \xi}\right|_{\xi=0} = 0 \tag{4-24}$$

As for the boundary condition at the tablet interface with the release medium, it is plausible to presume instantaneous continuity of chemical potentials there, as specified in our 7th assumption. In many experimental studies, the release medium is well stirred and it acts as an instantaneous sink, relative to the slow transport of mass through the tablet, which justifies neglecting mass transfer resistance outside the tablet. Therefore, the tablet interface is kept at equilibrium with the bulk of the release medium throughout the simulation. The preceding argument results in a trivial boundary condition on drug composition at the interface, namely

$$\phi_D(t,\xi=1)=0 \tag{4-25}$$

Applying the continuity of chemical potential of water, eqn. (4-26), reveals the time-dependent nature of the boundary condition on water composition as well as polymer stress at the interface.

$$\mu_W(t,1)=\mu_W^{mix}+\mu_W^{s}=0 \Rightarrow ln\,\phi_W^{BC}+(1-\phi_W^{BC})+\chi_{WE}(1-\phi_W^{BC})^2+\frac{\upsilon_W}{2k_BT}\sigma_{xx}^{E}=0 \tag{4-26}$$

where the chemical potential of water has been evaluated using the FH free energy density, eqn. (4-5) in which the drug volume fraction at the interface is set to zero. The superscript *BC* denotes the parameters evaluated at the outer boundary. Some studies have employed Flory-Rehner theory to calculate the boundary condition on water concentration,[3] which is only valid if the

excipient is permanently cross-linked in which case eqn. (4-26) predicts a static boundary condition.

Constitutive eqn. (4-14) combined with eqns. (4-15) and (4-26) constitute an initial value problem (IVP), the solution of which yields the time-dependent boundary conditions on volume fraction of water and excipient stress at the interface. Immediately after exposure of the tablet to the release medium, water molecules will rush into the interface eliciting an infinitely fast and thus *elastic* mechanical response from the excipient, curbing further water ingress into the interface. Therefore, the initial condition necessary to solve the IVP at the interface is obtained by solving eqn. (4-26) in which the excipient stress is replaced with elastic response, see eqn. (4-A-31) derived in appendix 4.4.3. Solution of eqn. (4-27) will thus establish an initial value of the water concentration for the IVP, describing boundary conditions at the interface.

$$ln\,\phi_W^{BC}\Big|_{t=0}+\left[1-\phi_W^{BC}\Big|_{t=0}\right]+\chi_{WE}\left[1-\phi_W^{BC}\Big|_{t=0}\right]^2+\frac{\upsilon_W G^o}{2k_B T}\left(\frac{1-\phi_D^o}{1-\phi_W^{BC}\Big|_{t=0}}-\frac{1-\phi_W^{BC}\Big|_{t=0}}{1-\phi_D^o}\right)=0 \qquad (4\text{-}27)$$

For finite relaxation time, the steady-state solution of the IVP, eqn. (4-26) combined with eqns. (4-14) and (4-15), is that of a stress-free excipient saturated with water. The boundary concentration of water tends to move towards this steady-state solution at long times, but is not attained at short times unless the excipient relaxation time is zero. The saturation, or steady-state, composition, corresponding to the stress-free tablet, is thus set only by the FH interaction parameter of water and excipient and is computed by setting the excipient stress in eqn. (4-26) to zero. Mechanical equilibrium at the interface, even before the mechanical stress relaxes, yields the boundary condition on pressure, eqn. (4-28).

$$\sigma_{xx}^E(t,\xi=1)-P(t,\xi=1)=-P_{ref} \qquad (4\text{-}28)$$

Here the reference pressure P_{ref} is set to atmospheric pressure. As bulk densities of all components are taken as equal, pressure decouples from the rest of equations and remains only as a response function. Drug release and swelling rates are directly dependent upon species fluxes at the interface. Hence, any model of drug release should be able to provide accurate estimation of interfacial fluxes. Admittedly, variable interfacial boundary conditions add to the mathematical complexity of our model. Nonetheless, accurate determination of interfacial fluxes is not possible without due attention to the time evolution of boundary conditions. Moreover, the treatment presented here will ensure that the interfacial boundary conditions approach the time

independent limits expected for fully elastic or inelastic viscous excipients. Indeed, both the initial jump in volume fraction and the subsequent time evolution at the interface have long been reported experimentally and demonstrated to lead to anomalous sorption behavior.[30,31]

4.2.4 Material Functions

4.2.4.1 Relaxation Time

The glassy-rubbery transition, marked by dramatic changes in dynamic behavior of the polymeric excipients, is strongly affected by composition. Therefore, the choice of material functions, while not affecting the model formulation directly, has far-reaching implications for such simulation outputs as drug release profile and tablet size versus time. Given that the present work does not focus on any particular drug/excipient chemistry, material functions are chosen here only to capture their expected behavior qualitatively.

A chain in the proximity of a tablet outermost surface can disentangle itself, or release itself from physical bonds to the rest of the matrix, upon sufficient dilution by water. As a result, the erosion velocity, eqn. (4-21), is dictated by the chain relaxation time at the interface. Chain mobility and cooperative segment rearrangements characteristic of relaxation, though absent in the glassy state, are increasingly facilitated in the presence of solvent. Consistently, the chain relaxation time in binary polymer-solvent systems is known to be a strong function of composition. In particular, the relaxation time in the entangled rubbery regime scales with polymer volume fraction with exponents ranging from 1.85 to 7/3.[32] In addition, free volume theory in glassy binary systems predicts strong composition dependence for self-diffusion coefficients, inversely correlated with relaxation time.[33] Chain mobility in ternary systems is also affected by the nature of drug-excipient interaction. Hence, chain relaxation time is a function of both drug and water volume fractions.

Assuming that the API has no plasticization (or anti-plasticization) effect on the excipient, we posit that the relaxation time in water and drug varies with water volume fraction in much the same way as it would in a binary mixture with water except that ratio of local water and excipient volume fractions, $r\,(\zeta, t) \equiv \phi_W/\phi_E$ in the ternary case controls the relaxation time. Korsmeyer *et al*.[34] demonstrated that an exponential function in terms of penetrant mass fraction can be fitted onto the self-diffusion coefficient and relaxation time predicted by free volume

theory.[33] We propose to generalize this idea to a ternary mixture by replacing water volume fraction with r, as in eqn. (4-29).

$$\tau = \tau_o \, exp\left(-\frac{r}{ar+b}\right) \tag{4-29}$$

The parameters in eqn. (4-29) can be estimated using the specific volume of components extrapolated to absolute zero temperature in addition to other structural parameters within the context of free volume theory. Given that volume fraction of drug has been excluded explicitly from eqn. (4-29), all parameters should be treated as being implicit functions of drug concentration. One must also note that polymers typically are polydisperse and thus have a relaxation time spectrum. As a result, the relaxation time used in our model should be interpreted as an average value. In general, the relaxation spectrum of the polymer matrix can be measured and used to develop a multi-mode constitutive model for polymer relaxation, which can replace the simple one-mode model used here. Obviously, our theory can readily be adjusted to account for other functional forms for the dependence of relaxation time on water and drug concentrations.

4.2.4.2 ESM Diffusivities

Increased mobility of chains in response to water ingress also manifests itself in composition dependence of mutual diffusivities. Vrentas *et al*.[35] have demonstrated that Fickian diffusivity in binary polymer/solvent systems is directly proportional to solvent and polymer self-diffusivities and thus inversely correlated with relaxation time. ESM diffusivities are generally complicated functions of composition and are directly related to Onsager coefficients, which can, in principle, be computed via molecular simulations.[36,37] As noted earlier, Fujita-type pseudo-binary diffusivities are commonly utilized in the literature. With the aim of representing the trends, the following Fujita-type forms for ESM diffusivities are adopted here.

$$D_{WE} = D_{WE}^{o} \, exp\left(\frac{\beta_W r}{1+r}\right) \tag{4-30}$$

$$D_{DE} = D_{DE}^{o} \, exp\left(\frac{\beta_D r}{1+r}\right) \tag{4-31}$$

The ESM diffusivity of water with respect to drug D_{WD} is taken to be a weak function of composition as compared to the other two involving the excipient and thus taken to be a constant throughout individual simulations.

4.2.4.3 Erosion Velocity

Erosion of polymer chains can be conceived of as a surface reaction analogous to electrochemical deplating of metals, albeit with a different mechanism, and as such, prior knowledge of its kinetic description is necessary for closing our model development. Erosion velocity can be defined as the ratio of a length roughly the size of a chain, e.g. the radius of gyration, and the time a representative chain takes to slide that length out of the entangled matrix. Chains with sufficient mobility thus detach themselves from the tablet at a rate controlled by the chain's relaxation time. Some authors have treated the erosion velocity as a constant fitting parameter.[12] However, water concentration at the interface increases gradually, which further speeds up chain relaxation; see eqn. (4-29), and thus the disentanglement rate. Assuming that interfacial chain dissolution is governed by reptation dynamics in the bulk, the erosion velocity has been suggested to be the ratio of the chain radius of gyration to the reptation time in bulk.[23] However, the environment adjacent to the tablet interface is different from the bulk and chain thermodynamic affinity for water alters the dissolution velocity. For instance, a water-excipient FH interaction parameter greater than 0.5 implies that water is a poor solvent for polymer chains, which then prefer to remain in the tablet bulk rather than leave it for the water phase. Here, the prefactor τ_o in eqn. (4-29), the chain unperturbed radius of gyration R_g and a thermodynamic factor, accounting for chain affinity for water relative to bulk, are all lumped into a single proportionality factor in the following expression for erosion velocity, eqn. (4-32).

$$\mathrm{v}_{er} \propto \frac{R_g^o \, exp\left(-\frac{\Delta F_{mix}}{k_B T}\right)}{\tau} = k_{er} \, exp\left(\frac{r}{ar+b}\right) \tag{4-32}$$

The numerator of the first exponential factor in eqn. (4-32) is the free energy difference between a single chain residing in water and that in the matrix.

4.3 Results and Discussion

The aim in this section is to illustrate how the main aspects of our model and parameters employed therein translate into quantities of interest in controlled drug delivery such as API release profile, tablet size, polymer re-dissolution etc. The relative magnitudes of the three dominant processes in our model, namely diffusion, relaxation and surface erosion, control the final characteristics of the aforementioned functions. For the ensuing discussion, we turn our focus to the kinetic parameters. To this end, all thermodynamic parameters are held constant throughout this section. It is worth noting that during its passage through the GI tract, tablet experiences different pH levels, which affect transport of drug and water if either the excipient or the drug is ionizable. For instance, excipients with carboxylic functional groups undergo deswelling if the pH is lowered significantly. However, the ionizable excipients are not the main focus of this work even though deswelling can be artificially captured in our model by abruptly lowering the solvent-excipient FH parameter in the course of simulation. We thus assume that the conditions in the release medium are held constant during the simulation, which is typically the case in *in vitro* studies.

The initial API loading is held constant among all the following simulations at 30% by volume. The excipients are generally hydrophilic polymers for which water can be taken as a good solvent. Without loss of generality, FH interaction parameters of drug-excipient and water-drug are both set to zero for the following simulations. As shown by Milner *et al.*,[38] there is a generic contribution to the FH interaction parameter of about 0.3 for many polymers in good solvents arising from difference in affinity of chain repeat units and solvent for free volume. Accordingly, we have adopted 0.3 for the FH interaction parameter of water and excipient. The molecular weight of API is taken to be 252 (*g/mol*) corresponding to phenytoin. For simplicity, the mass density of all three components is taken to be 1 (g/cm^3). All simulations were performed at 300 K. Finally, an initial tablet thickness of 0.5 *mm* is chosen in all the results presented here. In the following simulations, cumulative %API released is defined by eqn. (4-33).

$$\%API\ Rel. = \left(1 - \frac{L}{\phi_D^o L^o}\int_o^1 \phi_D\, d\xi\right) \times 100\% \tag{4-33}$$

All equations in this work were solved using a time-explicit finite difference method with a forward Euler's method that is first-order in time. A down-winding predictor-corrector scheme is

used to evaluate the spatial gradients of water and API volume fractions in the pseudo-advective terms of eqns. (4-19) and (4-20), respectively, where compositions at time step p with a first-order forward difference is used when velocity of the interface (dL/dt) is positive and vice versa. Once a new estimate of compositions in the next time is obtained, they are used to estimate the composition gradients at time step $p+1$. The arithmetic mean of the gradients evaluated at time steps p and $p+1$ is then used to evaluate the water and API composition gradients in the pseudo-advective terms in eqns. (4-19) and (4-20). The down-winding scheme proved beneficial to the stability of finite difference method inasmuch as a higher time step could be used to obtain stable results, compared with using either only forward or backward composition gradients throughout the simulation to evaluate the pseudo-advective terms in eqns. (4-19) and (4-20). A similar down-winding scheme is used to evaluate spatial gradients of both excipient stress and stretch ratio arising in eqn. (4-14) after implementing the Landau transformation, eqn. (4-18).

Instead of discretizing the second order spatial derivatives on the r.h.s of eqns. (4-19) and (4-20), backward differencing of the gradients of fluxes are directly employed. The latter is combined with forward differencing of the spatial gradients in diffusion driving force eqn. (4-3) in terms of which water and API fluxes can be expressed. Even though the water and API flux gradients are explicitly broken down to four different contributions in eqns. (4-19) and (4-20) to underscore the interplay of diffusional frictions of different components, direct discretization of flux spatial gradients requires appreciably fewer algebraic evaluations due to the non-linearity of water and API fluxes. The Stefan condition of eqn. (4-21) is integrated using explicit Euler's method. The trapezoid rule is utilized to evaluate the cumulative API release eqn. (4-33) numerically. In the following simulations 100-150 grid points with time increments ranging from 5×10^{-4} to 10^{-2} seconds have been used, ensuring the insensitivity of obtained results to grid size and further temporal and spatial discretization.

We start by focusing on how the ESM flux law affects diffusion by neglecting surface erosion and excipient stress relaxation for the moment. In perfectly elastic excipients, chain relaxation and surface erosion are absent. As a result, the drug release is solely controlled by diffusion of drug into and water out of the tablet. The foregoing argument holds for systems involving long chains or cross-linking where relaxation and surface erosion are vastly slower than diffusion of water. Such cases correspond to infinitely large Deborah numbers for which Fickian transport is expected. Our simulations in the elastic limit conform to the anticipated Fickian behavior. For a

series of ESM diffusivities, both API release and tablet size exhibit Fickian behavior, Figure 4-1. In fact, all curves in Figure 4-1 at least at short time could be fitted with power law functions with exponent 0.5, characteristic of Fickian transport. Referring to eqn. (4-21), the tangent to the half thickness curves in the absence of erosion is directly proportional to the excipient flux at the tablet-water interface, which in turn is the negative sum of water and API fluxes. Similarly, the slope of the water sorption versus time in the absence of erosion can be readily demonstrated to be a linear combination of API and water fluxes at the interface. The water sorption profile thus mirror the tablet size variation versus time, which is dominated by the water uptake rate given the relatively low API loading of 30 %vol used throughout the following simulations. Therefore, identical information can be inferred from water sorption and tablet size versus time curves and only the latter is thus presented here.

Given that water and API move in opposite directions, diffusional friction between them, inversely related to water-API ESM diffusivity, is expected to hinder API release and water sorption. Consistently, both API release and tablet size dominated by water sorption slow down as water-excipient diffusivity D_{WD} decreases from infinity, corresponding to frictionless collisions of water and API molecules, to finite values that are comparable to water-excipient D_{WE} and API-excipient D_{DE} ESM diffusivities, Figure 4-1A and 4-1B. The same dynamic slow-down is observed for other values of D^o_{WE} and D^o_{DE} as water-excipient diffusivity is lowered.

D^o_{WE} and D^o_{DE} could be taken as pseudo-binary diffusivities of water and API, respectively, provided that water exerts negligible friction on API and that an excipient-tracking frame of reference is employed; see appendix 4.4.1. As evident in Figures 4-1A and 4-1B, a priori neglect of API-water diffusional friction would lead to major errors in theoretical predictions, unless $D_{WD} > 10^{-9}$ (m^2/s). Similarly, any attempt to extract the pseudo-binary diffusivities based on pseudo-binary curve fitting of experimental API release profiles, is potentially prone to significant errors. Pseudo binary fluxes ignore an inherent degree of freedom and thus make it unreliable to compare diffusivities obtained from macroscopic studies with those obtained via molecular-scale simulations. Use of counterpart of pseudo-binary flux laws in electrochemical systems, namely Nernst-Planck equations, is long recognized to lead to major inconsistencies that can only be resolved if friction between ions is considered. Even though water and API concentrations are not as strongly correlated as oppositely charged ions are, it will be imperative to adopt ESM flux

laws in order to fit the experimental results if the ESM diffusivities are to be determined unambiguously and if they are to be compared to diffusivities computed at molecular scale.

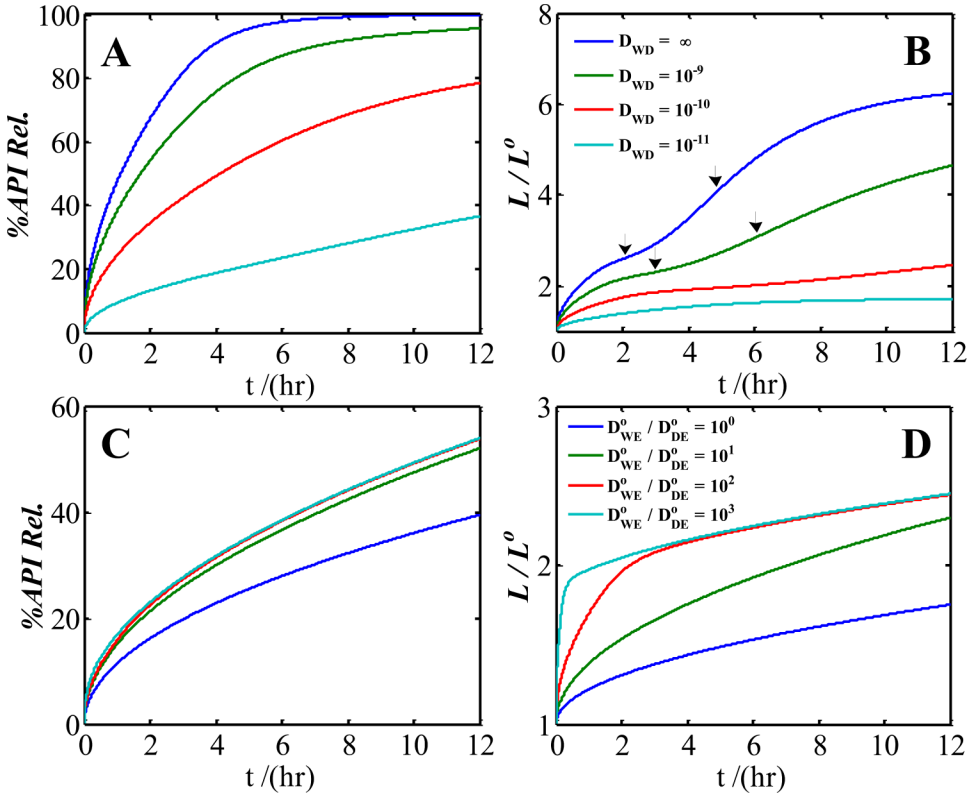

Figure 4-1: Effect of water-API ESM diffusivity in (m^2/s) on API release (A) and normalized half thickness (B) versus time for D^o_{WE} = 10 D^o_{DE} = 10^{-12} (m^2/s). API release (C) and normalized half thickness (D) versus time at three water-excipient to API-excipient ESM diffusivity ratios for D^o_{DE} = 10^{-14} (m^2/s) and an infinitely large water-API ESM diffusivity. Black arrows point to the location of inflexion points. Excipient is taken to be fully elastic with no surface erosion. A modulus at the unreformed state G^o of $50RT$ (Pa), where the initial density of elastic network strands is taken to be ν^o = 5 (mol/m^3), and identical Fujita parameters of 10 have been used for both water and API in all of the plots. For the rest of simulation parameters, refer to the text.

The two-stage behavior observed for the highest D_{WD} values employed in Figure 4-1B results from the counter current fluxes of API and water as well as the negligible volume of mixing. As noted earlier, the tangent to the half thickness curves in the absence of erosion is the negative sum of water and API fluxes. At early stages, the negative curvature of the half thickness is dominated by the monotonic decrease of water influx. When the absolute value of the derivative of API flux exceeds that of water flux at the interface, the curvature of half thickness curve switches sign, creating the first inflexion point indicated by the black arrows at intermediate stages of the blue and green curves in Figure 4-1B. As the API close to the interface nears depletion, the API flux asymptotically tends toward zero faster than water does and the

monotonically decreasing water influx again dictates the curvature of the half thickness profiles in the latter part of the simulations leading to the emergence of the second inflexion points indicated by black arrows for the blue and green curves in Figure 4-1B.

The two-stage behavior is most pronounced for large D_{WD} where both water and API fluxes are higher. A ten-fold decrease in both API and water ESM diffusivity through the excipient from the blue curve in Figure 4-1B to the green curve in 1D suppresses the two-stage behavior in the simulation time studied here, pushing the first inflexion point to ~ 30 hours (data not shown here). Furthermore, two-stage expansion of tablet thickness versus time is more likely to emerge in tablets with high API loading as the contribution of API release to the overall size is accordingly high. In contrast, API release profiles are only controlled by API flux at the tablet interface. Since in the fully elastic limit, the interfacial API flux will be a monotonically decreasing function of time, no inflexion point is predicted in the API release profile (Figure 4-1A) in this limit, despite the presence of inflexion points in the thickness profiles (Figure 4-1B).

The coupling between API and water transport can be readily inferred from the API release and half thickness profiles in simulations at fixed D_{WD} and D^{o}_{DE} represented in Figures 4-1C and 4-1D. As the ratio of D^{o}_{WE} to D^{o}_{DE} increases, API release and thickness increases at any given instant of time. However, the boost in transport of API becomes progressively smaller as D^{o}_{WE}/D^{o}_{DE} exceeds 10, Figure 1C. (Note that since the same Fujita parameters are used here for all diffusivities, that D_{WE}/D_{DE} is identical at all times to D^{o}_{WE}/D^{o}_{DE}.) Since D_{DE} is implicitly influenced by water concentration through the Fujita-type expression eqn. (4-31), an increase in D^{o}_{WE} should give rise to higher water concentrations in the tablet and a correspondingly higher D_{DE} that should eventually facilitate API release. However, water concentration in the immediate vicinity of the tablet interface with water does not vary substantially as D^{o}_{WE}/D^{o}_{DE} increases; see Figure 4-2. In fact, the water volume fraction at the interface remains constant at ~ 0.9, see Figure 4-2, throughout the simulation time regardless of the ESM diffusivities in Figures 4-1C and 4-1D, excluding water plasticization and higher D_{DE} as the reason for the boost in API release observed in Figure 4-1C.

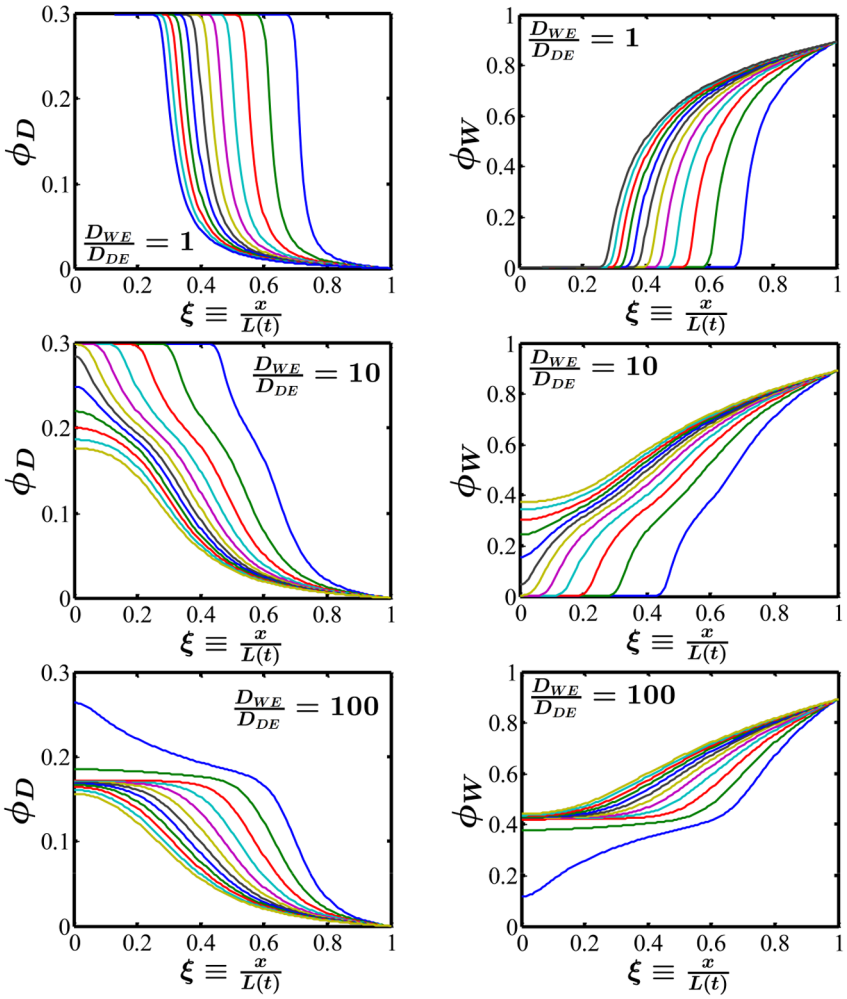

Figure 4-2: Effect of the ratio of water-excipient to API-excipient ESM diffusivity on the API (left) and water volume fraction profiles (right) for $D_{DE}^{o} = 10^{-14}$ (m^2/s) and an infinitely large water-API ESM diffusivity with otherwise identical parameters as those used in Figure 1. Note that since the same Fujita parameters are used here for all diffusivities, that D_{WE}/D_{DE} is identical at all times to D_{WE}^{o}/D_{DE}^{o}. Composition profiles are evenly spaced in 1-hour intervals over 12 hours.

In order for API molecules to escape the tablet, they need to have a net migration relative to the matrix, which, in the absence of friction with water, is set by the API-excipient ESM diffusivity. If water influx is slower than the outward movement of API relative to excipient, API release will be limited by water diffusion, which is the case for $0 < D^{o}_{WE}/D^{o}_{DE} < 1$. For $1 < D^{o}_{WE}/D^{o}_{DE} <$ 10 the rates of water inward flux and API outward velocity relative to excipient are comparable. The swelling front thus moves toward the tablet core faster, hydrating more of the tablet core and exposing more of the API content that will then be transported outward through the swollen layer. As a result, API flux in the swollen layer increases, enhancing the overall API release. Beyond this limit, i.e. for $(D^{o}_{WE}/D^{o}_{DE}) >> 1$, the tablet will be nearly saturated with water and

API release will be limited by the diffusion of API relative to the excipient. In other words, even though water in this limit diffuses rapidly, API mobility through the swollen layer is no longer enough to allow velocity of API diffusion to keep up with the inward velocity of swelling front controlled by water influx and API release approaches its upper limit, the red curve in Figure 1C. The trends in Figures 4-1C and 4-1D holds as long as D_{WD} is sufficiently greater than the API and water ESM diffusivities through the excipient.

Table 4-1: Parameters employed in all simulations results presented in Figure 4-3 as well as the subsequent figures, unless otherwise specified.

G^o [GPa]	β_D	β_W	D_{WD}	$D^o{}_{WE}$ [m^2/s]	$D^o{}_{DE}$ [m^2/s]
0.123	15	15	∞	10^{-14}	10^{-15}

We now turn to the effect of viscoelastic diffusion, still in the absence of erosion, where the mechanical response of the polymer profoundly alters the transport process in the tablet. In principle, the relaxation time of the excipient is a strong function of composition with nearly elastic behavior at low water concentration and viscous behavior prevailing at higher water concentrations. It is worth considering a simple relaxation function that approximates eqn. (4-29) by means of two parameters chosen such that excipient is fully elastic below a threshold r_o with the relaxation time being finite and insensitive to concentration beyond it, as in eqn. (4-34).

$$\tau = \frac{\tau_R}{H\left[r - r_o\right]} \tag{4-34}$$

Here H [·] denotes the Heaviside step function. The numerator in eqn. (4-34) can be considered an average relaxation time above the threshold concentration. For a set of kinetic parameters, listed in Table 4-1, the effect of the average relaxation time on API release and half thickness kinetics is shown in Figures 4-3A and 4-3B respectively.

API release and half thickness evolve faster for all simulations with finite average relaxation than in the fully elastic limit, given by the black curves in Figure 4-3. The water sorption curves for the corresponding simulations of Figure 4-2A and 4-2B are provided in Figure 4-3C. As expected, Fickian water sorption is observed in the fully elastic limit. At the higher end of average relaxation times, namely the purple and cyan curves in Figure 4-3A, transport remains Fickian at short times. The half thickness increases over the simulation time in power law fashion with the power law exponents increasing as the average relaxation time decreases in

Figure 4-3B. API release profiles, on the other hand, become nearly linear in time as the average relaxation time decreases and at the lowest average relaxation time studied here, 200 seconds, the blue curve in Figure 4-3A, API release exhibits anomalous transport that can be fitted with a power law equation with an exponent of ~ 0.82.

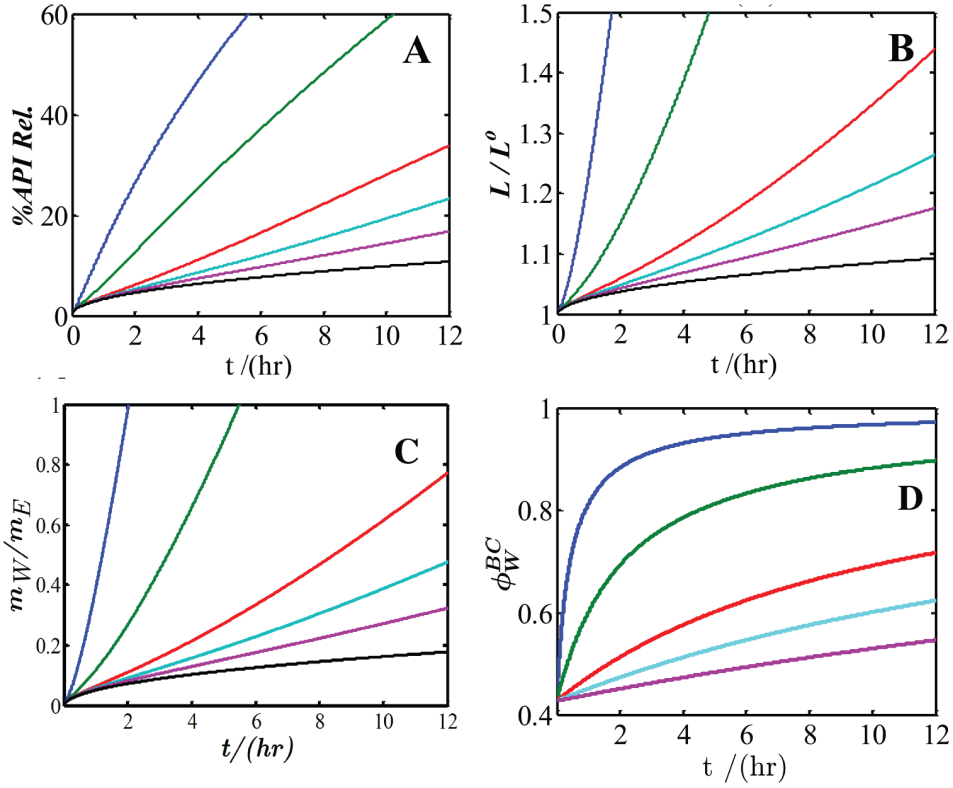

Figure 4-3: Effect of average chain relaxation time on API release (A) and normalized half thickness (B) water sorption profiles normalized by the excipient mass (C) and water volume fraction at tablet interface with release medium (D) versus time. The blue, green red, cyan and purple curves respectively correspond to simulations with r_o = 0.09 and τ_R = 200, 1000, 5000, 10000, 20000 seconds, respectively. The black curves represent fully elastic behavior limit. For definitions and the remaining kinetic parameters, refer to the text and Table 4-1.

The role of excipient viscoelasticity is more clearly elucidated when the effect it has on the water concentration boundary condition at the tablet-water interface is considered, Figure 4-3D. The water volume fraction at the tablet's outermost surface remains constant at ~ 0.43 in the fully elastic limit while for the viscoelastic matrices its deviation from a volume fraction of unity decays exponentially at a rate directly set by the average relaxation time. Diffusion driving forces are related to compositional and stress gradients that monotonically decrease in time when the boundary conditions remain fixed in time, i.e., for the elastic limit. As a result, static boundary conditions result in the classical Fickian behavior observed at short times in Figure 4-1 and for the fully elastic result, the black curves in Figure 4-3A through C. However, for a

viscoelastic excipient the stress decreases continuously at the interface at a fixed water volume fraction, and this in turn allows it to accommodate more water according to eqn. (4-26). The water concentration thus is predicted to increase monotonically and asymptotically approach the equilibrium value of unity. Predictions of interfacial water volume fraction versus time are consistent with observations of Long and Richman in polymer-solvent systems.[30] Given that water and API ESM diffusivities through the excipient are both exponentially increasing functions of water concentration, according to eqn. (4-30) and (4-31), the rise in water concentration at the boundary increases the apparent diffusivity of both API and water, A_W and B_D in eqns. (4-19) and eqn. (4-20), partially and even fully offsetting the decline in API diffusion driving force. This leads to a nearly constant excipient flux at the interface and almost linear API release profiles, shown by the red and green curves in Figure 4-3A.

As is evident from Figure 4-3A, a viscous behavior of the excipient facilitates API and water transport through the tablet. However, the simulation performed with the lowest average relaxation time, given by the blue curve in Figure 4-3A, deviates discernibly from the linear release observed at moderate values and demonstrates anomalous behavior. Although simulations with even lower average relaxation times were not performed due to the increasingly long computational time required, the API release is expected to approach the Fickian limit as the average relaxation time tends toward zero, corresponding to the limit of a zero diffusional Deborah number. In this limit, the water volume fraction at the tablet outer boundary reaches within 10 % of the final value very early in the simulation, as shown by the blue curve in Figure 4-3D, and tends to increase ever so slowly afterwards. As a result, the API flux reaches a very high value early on but decreases slowly as time passes, giving rise to a negative curvature and anomalous API release, as shown by the blue curve in Figure 4-3A.

While a linear API release at moderate average relaxation time transitions to anomalous behavior at sufficiently short relaxation times, the half thickness versus time curves, controlled predominantly by water uptake, transitions from Fickian behavior at long relaxation times to quasi-parabolic curves with power law behavior with exponents greater than 1, at short relaxation times. This behavior represents the so-called super Case II transport. Unlike the API flux, the water influx increases over simulation time, despite the identical dependence of API-excipient and water-excipient ESM diffusivity on composition. The increasing water influx at the

interface can be explained by the nature of API and water volume fraction boundary conditions. The API volume fraction at the interface remains fixed at 0 throughout the simulation according to our 7th assumption whereas the water volume fraction increases monotonically from 0.43 toward unity at the rate set by average relaxation time, keeping the gradients from declining as fast as they do in the fully elastic limit.

In any set of experimental conditions, there exists a critical excipient concentration above which chains cannot withstand the shear stresses exerted by thermodynamic and mechanical stresses exerted by the surrounding solvent. This critical excipient volume fraction could be roughly estimated as the onset of chain entanglement and generally ranges from 0.01 to 0.1 depending on chain molecular weight and flexibility. Therefore, the results for late times for an average relaxation time of 200 seconds, given by blue curves in Figure 4-3, are subject to correction due to the effect of erosion. Excipient erosion at the surface of the tablet will be discussed later in this section, but as will be demonstrated shortly, it tends to curb the rapid rise in the surface water volume fraction. Nonetheless, the transition of API release from Fickian behavior to Case II and anomalous transport is in harmony with the concept of diffusion Deborah number that has been used for years to describe the flow behavior of viscoelastic fluids.[39,40] Fickian behavior is observed at either end of the Deborah number range while anomalous and Case II transport is dominant at $O(1)$ Deborah numbers, according to our simulations.

The excipient volume fraction and stress profiles offer further insight into the mechanism by which stress relaxation alters transport. For the two lowest average relaxation times studied in Figure 4-3, excipient volume fraction and stress normalized by G^o, the modulus of the unswollen reference state, are shown in Figure 4-4. In both simulations, a rather sharp swelling front develops within the tablet that divides the swollen layer behind from the glassy core in front of the moving front. The swelling front travels inwards as water steadily attacks the dry and API-rich excipient core. At the front position, the stress profile exhibits a sharp peak that travels inward. The sharp stress peaks, resulting from matrix resistance against swelling induced by water uptake, impede further movement of the swelling front towards the tablet core. For longer relaxation times, the peak heights increase and become smeared and spread.

In light of the preceding argument, the swelling front velocity should be inversely correlated with the relaxation time. Our predictions of swollen layer thickness versus time are consistent

with this; see Figure 4-5. In fact, swollen layer thickness for the simulation with τ_R = 200 seconds increases linearly with time with a slope of ~ 0.275 (*mm/hr*). For longer average relaxation times, the swollen layer thickness varies with time as a power law with exponents ~ 0.8 and 0.7 for τ_R = 1000 and 5000 seconds, respectively. The classical Fickian description predicts a linear dependence of swollen layer thickness on the square root of time. The swollen layer thickness predicted by simulations, Figure 4-5, with the three lowest average relaxation times studied here departs from Fickian behavior in accordance with the observed anomalous API and water transport in those cases; see Figures 4-3A and 4-3B.

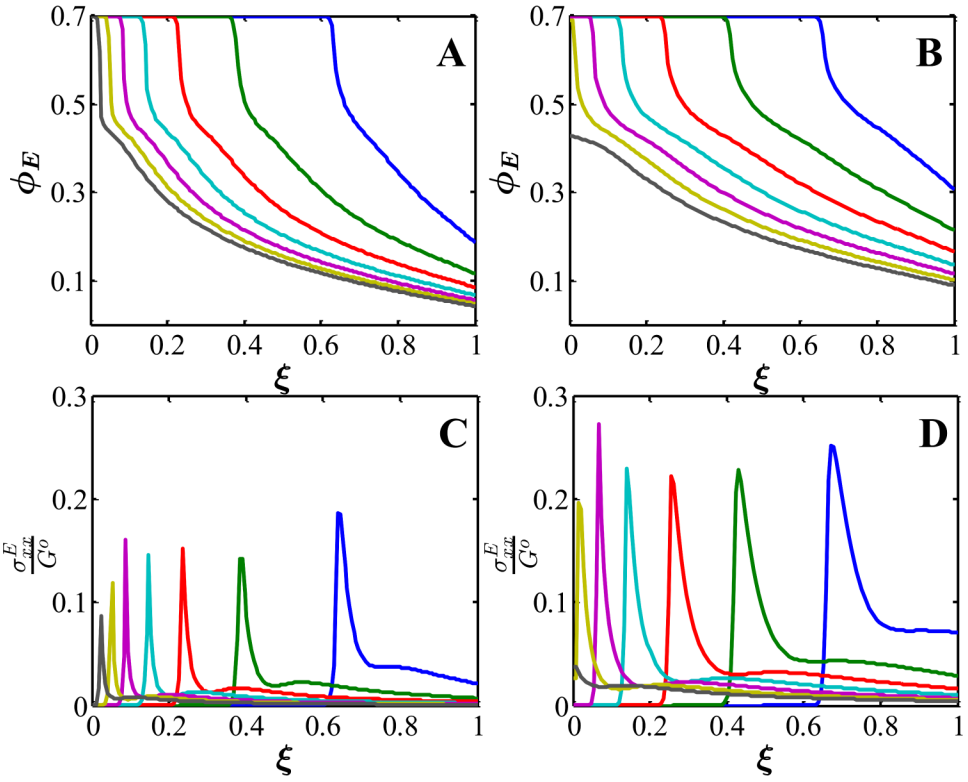

Figure 4-4: Excipient volume fraction and normalized stress distribution versus normalized position for parameters in Table 4-1 and r_o= 0.09 at two average relaxation times; τ_R = 200 s (A) and (C) and τ_R = 1000 s (B) and (D). All curves are equally spaced in time with one-hour intervals.

As noted in the preceding sections, traditional models of anomalous and Case II transport in drug delivery[7,8] commonly presuppose an experimentally determined swelling front velocity that enters the solvent balance laws as a pseudo convective term. The need to impose this velocity by hand of course detracts from the predictive power of the theory. Moreover, numerous experimental reports have established that the swelling front velocity, i.e. the slope of swollen layer thickness versus time, is not necessarily constant in systems with anomalous API

release.[18,41,42] Another common approach considers a glassy-rubbery transition at the swelling front that introduces adjustable parameters and is applicable when the solvent cannot diffuse at all into the glassy region. The latter hypothesis of course is not generally observed experimentally, as evidenced by existence of partially swollen glassy region in some systems.[43] The present work obviates the need for any prescribed front velocities, as the diffusional frictions and resistances due to excipient stress automatically give rise to induced advective fluxes in the API and water balance equations, i.e. through the last three terms on the right side of eqns. (4-19) and (4-20).

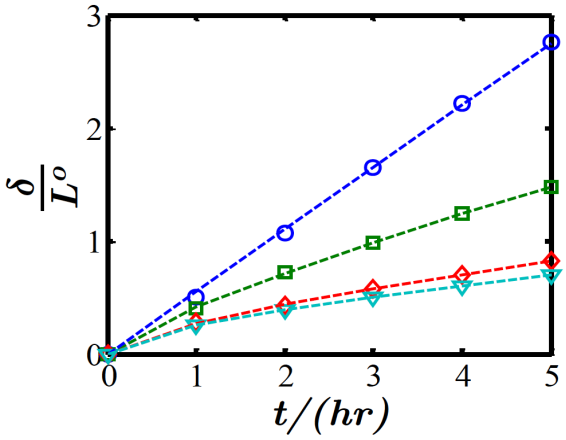

Figure 4-5: Swollen layer thickness δ normalized by the initial dry half thickness, L^o, versus time for four average relaxation times corresponding to the corresponding simulations in Figures 4-3 using the same color code. Dashed blue line represents a linear fit to simulation predictions depicted by the blue circles while the other dashed lines are power law fits to their corresponding simulation predictions.

Using eqn. (4-34) to approximate the composition dependence of the relaxation time, eqn. (4-29), we have explained the main features of relaxation-controlled transport. However, the excipient relaxation time generally exhibits moderate to strong composition dependence even at moderate water concentration, depending on the chain length and chemistry. As we explain at the end of this section, material functions can also be affected by API composition. Furthermore, one cannot overlook excipient dissolution at the tablet outermost surface when the water concentration there is close to the disentanglement threshold. Illustrated in Figure 4-6 are API release and tablet size versus time for a system with mild composition dependence of relaxation time at moderate to high water concentrations with the erosion mechanism active at various erosion parameters, k_{er} in eqn. (4-32).

As quantified by eqn. (4-21), two opposing processes, namely excipient erosion and excipient swelling induced by influx of water and API release, control the tablet thickness. Depending on the relative strength of these, the tablet could expand or shrink over time. As erosion intensifies, the expansion of the tablet slows down and is eventually replaced by ever faster shrinkage, Figure 4-6B. At moderate erosion parameters, swelling-induced expansion of the tablet is offset by chain re-dissolution that causes the tablet to decrease in size ever so slowly, as given by the red curve in Figure 4-6B.

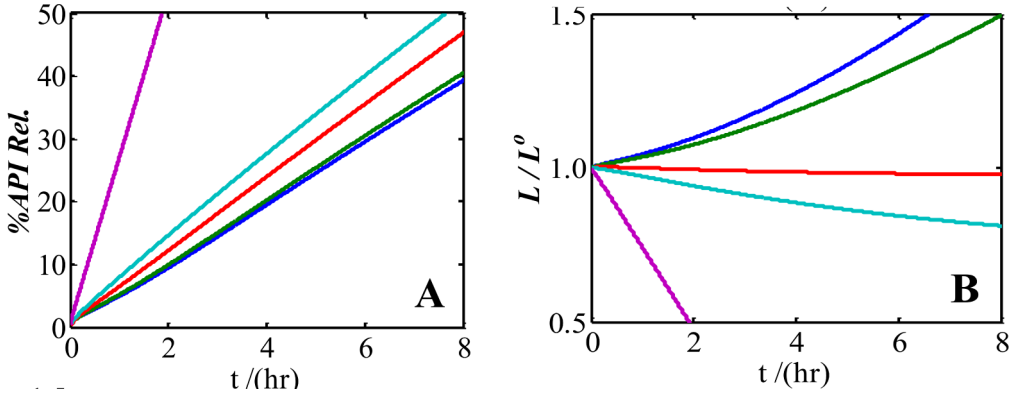

Figure 4-6: API release profiles (A) and normalized half thickness (B) versus time for various surface erosion parameters for relaxation function given by eqn. (4-29) with $a = 0.022$, $b = 10^{-4}$ and $\tau_o = 6\times10^{+22}$ (s). The blue, green, red, cyan and purple curve respectively correspond to $k_{er}\tau_o$ = 0, 1, 5, 10 and 50 μm. The remaining simulation parameters are listed in Table 4-1.

Concomitant with the steep rate at which the tablet shrinks for the highest erosion parameter, given by the purple curve in Figure 4-6B, a rapid and linear API release profile is observed, in the purple curve in Figure 4-6A. Since API molecules are dispersed in the excipient, they detach from the tablet along with the excipient chains close to the interface that are sloughed off. As the erosion parameter increases, the contribution of excipient erosion to API release increases accordingly, as shown in Figure 4-6A. In simulations with $k_{er}\tau_o$ = 1, 5, 10 (μm) in Figure 4-6A, the API release profile deviates gradually from the result in the no-erosion limit while a steep linear profile results from the highest erosion parameter, $k_{er}\tau_o = 50$ (μm).

For both sets of relaxation parameters, a crossover from swelling-controlled release to erosion-limited API release is observed as the erosion parameter increases. However, one should note that erosion and swelling in our model affect one another reciprocally. Chain erosion at the surface exposes new tablet material in the vicinity of the original surface. Since the only location in the tablet at equilibrium with outer solution is the outermost surface, the newly exposed

surfaces are temporarily out of equilibrium with the outer solution. Because of the instantaneous equilibrium following from our 7th assumption, the newly exposed surface equilibrates instantly with the bulk release medium as water and API chemical potentials there must maintain equality with those in the bulk solution, according to eqns. (4-25) and eqn. (4-26), in much the same way as they do at the very beginning of the simulation at $t = 0$. We also account for the non-zero stress at the newly exposed surface when solving eqn. (4-26). Therefore, chain detachment at the surface and subsequent re-equilibration with the surrounding medium hinder the relaxation process, maintaining higher levels of stress and lower capacity for water uptake at the interface. Accordingly, the ESM diffusivities decrease as erosion intensifies, adversely affecting the diffusion of API through the hydrated layer. On the other hand, continuous erosion thins out the swollen region across which API molecules must diffuse to escape the tablet. It can be thus concluded that matrix erosion at the surface has a non-trivial, self-correcting effect on the diffusional contribution to overall API release.

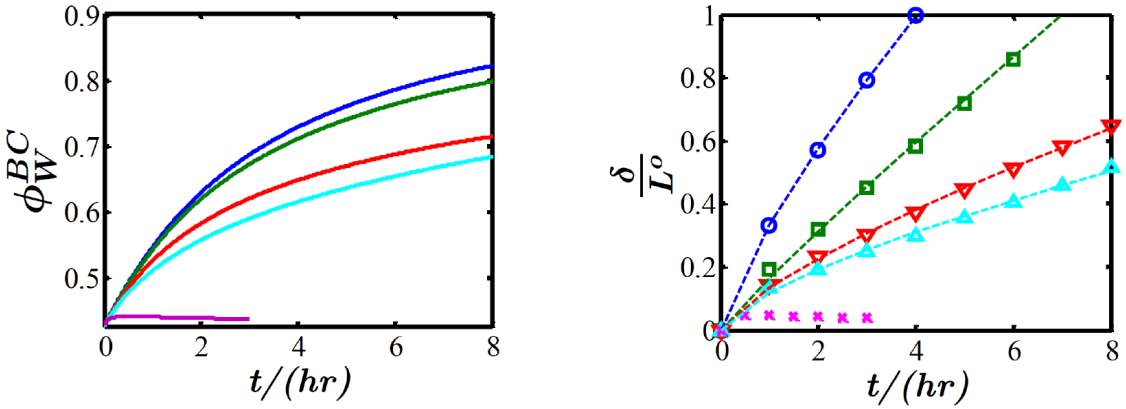

Figure 4-7: Water volume fraction at tablet interface with release medium (left) and swollen layer thickness δ normalized by the initial dry half thickness, L^o (right) versus time. The blue, green, red, cyan and purple curves respectively correspond to simulations with relaxation function given by eqn. (4-29) with $a = 0.022$, $b = 10^{-4}$ and $\tau_o = 6 \times 10^{22}$ (s) at various erosion intensity parameters. The curves correspond to the curves of identical color in Figure 4-6. For definitions and the remaining kinetic parameters, refer to the text and Table 4-1.

Corroborating the preceding argument are the corresponding water concentrations at the interface as well as swollen layer thickness profiles versus time, Figure 4-7. Except for the highest erosion parameters used in Figure 4-7, the swollen layer increases in thickness over the time scale studied here. Increasing swollen layer thickness even in systems with overall tablet shrinkage has been observed experimentally in front tracking studies.[42,44] Since the erosion velocity is inversely correlated with the relaxation time at the tablet's outermost surface at any

instant in time, the hindrance to relaxation resulting from chain detachment ultimately slows down the erosion rate itself allowing for the relaxation process to proceed. The convoluted interplay between relaxation and erosion makes it hard to resolve their individual contribution to overall transport. This is a major reason why it is important to allow swelling, viscoelastic relaxation, and erosion all to emerge self consistently, rather than imposing a priori velocities of migration of a stress front or of an erosion front.

Except for the highest erosion parameters employed in simulations depicted in Figure 4-6, the departure of API release curves with erosion from that of erosion-free case is not as remarkable as those of corresponding thickness curves versus time. This observation indicates that the contributions of surface erosion and of swelling-controlled API diffusion should be comparable in these cases. An increase in the erosion contribution to transport is offset by the loss of API diffusion, although the former increasingly overcompensates the loss of API diffusion at higher erosion parameters. For the highest erosion parameters studied here, namely the purple and red curves in Figure 4-6, API release is dominated by surface erosion. Compared to erosion-free simulations, the swollen layer thickness is significantly decreased for the highest erosion parameter, $k_{er}\tau_o$ = 50 (μm), while the water composition at the interface is pinned down at markedly lower values, indicating that erosion strongly interferes with relaxation at the highest erosion parameter; see the Figure 4-7. Given the value of the Fujita parameter, β_D = 15, the decrease in water concentration for the highest erosion produces a three orders-of-magnitude drop in API-excipient diffusivity whereas the swollen layer exhibits an order of magnitude decrease in thickness. Hence, the diffusion contribution to the API release rate is expected to decline by two orders of magnitude as compared to erosion-free simulations. Despite the tremendous drop in API diffusion rate, API release is the fastest for the highest erosion parameter in Figure 4-5, $k_{er}\tau_o$ = 50 (μm), indicative of huge contribution of surface erosion to API release at these conditions.

A close examination of water and API spatial distributions reveals yet another aspect of erosion-controlled transport. The time evolution of API and water profiles corresponding to the two highest erosion parameters in Figure 4-6 are presented in Figure 4-8. The most noticeable feature of both Figures 4-8C and 4-8D is the slow inward progression of water and API composition profiles toward the core despite a considerably thinner tablet at $k_{er}\tau_o$ = 50 (μm). Inside the

swollen layer in Figure 4-8B, water profiles are almost linear implying that the time scale for water diffusion at $k_{er}\tau_o = 10$ (μm) is comparable to that of excipient relaxation time.

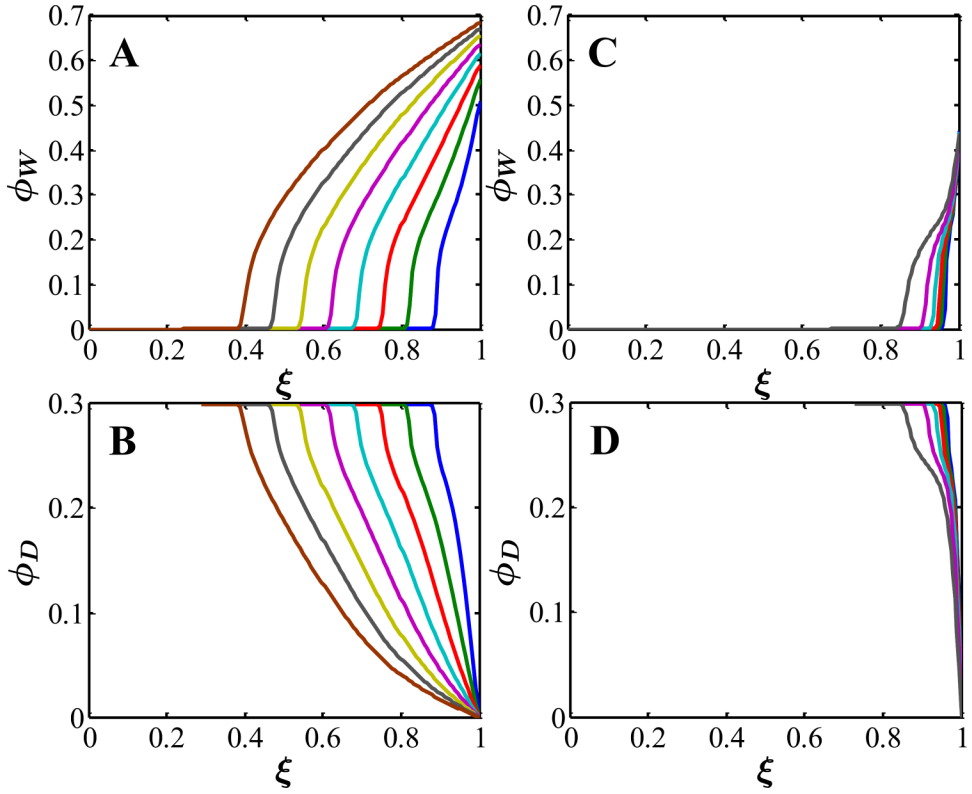

Figure 4-8: Water and API volume fraction distribution profiles versus normalized position respectively at $k_{er}\tau_o = 10\ \mu m$ (A) and (B) and at $k_{er}\tau_o = 50\ \mu m$ (C) and (D). In all simulations, the relaxation function eqn. (4-29) with $a = 0.022$, $b = 10^{-4}$ and $\tau_o = 6 \times 10^{+22}$ (s) has been used. The remaining simulation parameters are listed in Table 4-1. Curves in (A) and (B) are equally spaced in time with 1 hour intervals while those in (C) and (D) are evenly spaced with half-hour intervals.

4.4 Appendices

4.4.1 Problems with Pseudo-Binary Flux Laws

Consider a hypothetical case where solute molecules adhere strongly to the matrix, implying zero relative velocity between drug and matrix. Use of a pseudo binary Fick's law, with a low diffusion coefficient assigned to the drug to account for its lack of diffusion relative to the matrix, would leave the drug almost entirely frozen in place, and for appreciably swelling matrices, would not account for the dragging of the drug molecules with the matrix as the matrix expands. This failure is a direct result of pseudo binary fluxes not being invariant with respect to choice of reference velocity.

In certain conditions, ESM diffusivities reduce to pseudo binary ones with proper choice of reference velocity and pseudo binary diffusivities. This approach, however, is only valid as long as the resulting pseudo-binary diffusivities are of similar magnitude. Otherwise, it results in pseudo binary diffusivities that depend on reference velocity. In the example case where drug is strongly bound to the matrix, one could switch to a matrix-fixed frame whereupon all pseudo-binary fluxes should be specified relative to the matrix velocity. Due to substantial friction between drug and matrix in this case, the pseudo binary diffusivity of drug through the matrix can be assigned a zero value and consequently matrix and drug would be both correctly predicted to remain stationery in a matrix-fixed frame. As we explain shortly in this section, however, the zero-valued drug pseudo binary diffusivity through the matrix cannot imply a zero-valued drug diffusivity relative to mass, mole or volume averaged velocities, rendering this basic material property frame-dependent.

Although a reference velocity needs to be specified regardless of flux constitutive laws in order to render any set of flux-force equations invertible, ESM fluxes, unlike pseudo binary counterparts, are invariant with the choice of reference velocity or reference frame. Even though the ensuing arguments exploit volume-averaged velocity, the conclusions are equally valid for mass and mole averaged velocities as well. Using the volume-averaged velocity v^* of a system as the reference velocity has the advantage of having zero divergence provided the system excess volume is negligible, a condition typically met in typical tablet formulations. Consider a binary system in which Fick's excess flux relative to the volume-averaged velocity J_1^* is given by eqn. (4-A-1).

$$-\phi_1 D_{12} \nabla \left(\frac{\mu_1}{k_B T} \right) = \phi_1 (\mathrm{v}_1 - \mathrm{v}^*) \tag{4-A-1}$$

Upon moving to a frame that tracks species 2, excess flux of 1 relative to velocity of species 2 should be evaluated. Using the definition of volume-averaged velocity, eqn. (4-A-2) one can easily demonstrate that the excess flux of 1 relative to 2, J_1^2, is simply related to that relative to volume-averaged velocity according to eqn. (4-A-3).

$$\mathrm{v}^* \equiv \sum_{i=1,2} \phi_i \mathrm{v}_i \tag{4-A-2}$$

$$J_1^2 = \frac{J_1^*}{\phi_2} \tag{4-A-3}$$

Substituting for the numerator in eqn. (4-A-3) with eqn. (4-A-1), the desired excess flux relative to velocity of species 2 is given as below.

$$J_1^2 = -\frac{\phi_1 D_{12}}{\phi_2}\nabla\left(\frac{\mu_1}{k_B T}\right) \tag{4-A-4}$$

Therefore, diffusivity can be determined unambiguously irrespective of reference velocity and frame. Of course, one can readily verify that ESM flux law eqn. (4-4) applied to a binary system will identically reduce to eqn. (4-A-4). Pseudo binary flux equations generalize the Fick's law to multicomponent systems with *m* components by stipulating that movement of *m* – 1 components (solutes) are solely limited by a preponderant m^{th} component (solvent, *m*) at any composition. In other words, mutual diffusional frictions among all solutes are neglected. This assumption could be valid, for instance, when a host of solutes, especially neutral ones, diffuse in a solvent that is in vast excess, rendering solute-solute encounters rare. In that case, it is plausible to adopt the solvent velocity as the reference, in which case the excess fluxes relative to solvent J_i^m would be of the following form

$$J_i^m \equiv \phi_i(\mathrm{v}_i - \mathrm{v}_m) = -\frac{\phi_i D_{im}}{\phi_m}\nabla\left(\frac{\mu_i}{k_B T}\right) \quad (i \neq m) \tag{4-A-5}$$

The above equation is a generalization of eqn. (4-A-4) to multicomponent systems. The set of ESM flux equations follows from eqn. (4) as below:

$$\phi_i \nabla\left(\frac{\mu_i}{k_B T}\right) = \sum_{j\neq i,m}\frac{\phi_i\phi_j}{\widehat{D}_{ij}}[\mathrm{v}_j - \mathrm{v}_i] + \frac{\phi_i\phi_m}{\widehat{D}_{im}}[\mathrm{v}_m - \mathrm{v}_i] \quad (i \neq m) \tag{4-A-6}$$

In the limit of zero friction, i.e. infinitely large ESM diffusivity, between solute *i* and all other solutes, the summands in the summations will vanish entirely and eqn. (4-A-6) reduces to (4-A-5) upon recognition of the following identity.

$$D_{im} = \widehat{D}_{im} \tag{4-A-7}$$

The set of excess fluxes relative to solvent and those relative to the volume-averaged velocity are related using a linear transformation.

$$\underline{\underline{J}}^m = \underline{\underline{Q}} \bullet \underline{\underline{J}}^* \tag{4-A-8}$$

where the superscript "*m*" denotes a flux relative to the solvent velocity and the asterisk means it is relative to the volumetric velocity. Using the Kronecker delta notation, the elements of non-singular (*m*–1) by (*m*–1) matrix $\underline{\underline{Q}}$ is given as follows.

$$Q_{ij} = \delta_{ij} + \frac{\phi_i}{\phi_m} \tag{4-A-9}$$

In a ternary system composed of water *W* and drug *D* as solutes and matrix *E* as the solvent, eqn. (4-A-8) simplifies to the following form.

$$J_W^E = \left(1 + \frac{\phi_W}{\phi_E}\right) J_W^* + \frac{\phi_W}{\phi_E} J_D^* \tag{4-A-10A}$$

$$J_D^E = \frac{\phi_D}{\phi_E} J_W^* + \left(1 + \frac{\phi_D}{\phi_E}\right) J_D^* \tag{4-A-10B}$$

If drug molecules adhere strongly to the matrix, both pseudo-binary and ESM diffusivity between drug and matrix will be zero, implying a zero drug flux relative to the matrix. As a result, eqn. (4-A-10B) rearranges to the following.

$$J_D^* = -\left(\frac{\phi_D}{1-\phi_W}\right) J_W^* \tag{4-A-11}$$

Given that water flux cannot be zero unless at the steady state, drug flux relative to volume-averaged velocity, shown to be zero in our model, would be invariably non-zero according to eqn. (4-A-11). Similar to eqn. (4-A-1), another pseudo binary diffusivity based on volume-average velocity could be defined as the following.

$$J_D^* = -\phi_D D_{DE}^* \nabla\left(\frac{\mu_D}{k_B T}\right) \tag{4-A-12}$$

Since J_D^* in eqn. (4-A-11) was shown to be nonzero, D_{DE}^* cannot be zero, either. Hence, pseudo binary diffusivities cannot be unambiguously determined in multicomponent systems, particularly when water and drug experience markedly different resistances in diffusing through the matrix. Note that in a truly binary system the mutual diffusivity is unique, irrespective of the reference velocity; see eqns. (4-A-1) and (4-A-4). Lastly, simulations in matrix-fixed frames, especially in three-dimensions where matrix deformations can become anisotropic, requires

careful implementation as the matrix becomes locally diluted causing the mesh to become highly distorted.

4.4.2 Elastic Contribution to Chemical Potential

The total change in internal energy of a system dU is the sum of heat exchanges and various flavors of work including recoverable straining work, dU^s.

$$dU = TdS - pdV + \sum_i \mu_i^{mix} dn_i + dU^s \tag{4-A-13}$$

where the chemical potential only includes the entropic and energetic contributions from the conventional mixing free energy, ΔF_{mix}. Using Euler's homogeneous function theorem, eqn. B-1 can be integrated:

$$U = -pV + TS + \sum_i n_i \mu_i^{mix} + U^s \tag{4-A-14}$$

For a collection of Gaussian strands the endpoints of which deform affinely, the stored elastic energy per unit volume is proportional to the trace of stress tensor.[32]

$$\frac{U^s}{V} = \frac{tr(\underline{\underline{\sigma}}^E)}{2} \Rightarrow U^s = \frac{V\sigma_{xx}^E}{2} \tag{4-A-15}$$

Here elongation only in the x-axis is considered. The work applied for an infinitesimal deformation during which the volume is not conserved is thus given by eqn. 4-A-16.

$$\delta W^s = dU^s = \frac{\sigma_{xx}^E dV}{2} \tag{4-A-16}$$

Substituting the last term in eqn. 4-A-14 with the r.h.s of eqn. 4-A-15, after differentiating and subtraction of eqn. 4-A-13 from the result, one obtains eqn. 4-A-17.

$$VdP - SdT = \sum_i n_i d\mu_i^{mix} + \frac{Vd\sigma_{xx}^E}{2} \tag{4-A-17}$$

Introducing the equation of state at constant temperature and pressure, eqn. 4-A-17 can be written as below

$$0 = \sum_i n_i \left(\frac{\upsilon_i}{2} d\sigma_{xx}^E + d\mu_i^{mix}\Big|_{P,T} \right) \tag{4-A-18}$$

Comparison of eqn. 4-A-18 to the well-celebrated Gibbs-Duhem equation suggests that the matrix contribution to total chemical potential of species "*i*", μ_i^s is given by eqn. 4-A-19.

$$d\mu_i^s = \frac{\upsilon_i}{2} d\sigma_{xx}^E \Rightarrow \mu_i^s = \frac{\upsilon_i}{2} \sigma_{xx}^E \tag{4-A-19}$$

An expression for stress in the fully elastic limit has been derived in appendix 4.4.3, which can be plugged into eqn. 4-A-19 to yield the fully elastic limit for species chemical potentials.

$$lim_{\tau \to \infty} \ \mu_i^s = \frac{\upsilon_i G^o}{2} \left(\lambda_x - \lambda_x^{-1} \right) = \frac{\upsilon_i G}{2} \left(\lambda_x^2 - 1 \right) \tag{4-A-20}$$

4.4.3 Constitutive Equation for Matrix Stress

We here present a modification of original UCM model to accommodate swelling and volume change. For a collection of Gaussian chains the endpoints of which deform affinely, the stress is directly proportional to second moment of end-to-end distance probability distribution function [32], eqn. (4-A-21).

$$\underline{\underline{s}} = 2\nu k_B T \beta^2 \left\langle \underline{\underline{RR}} \right\rangle = 2\beta^2 G \left\langle \underline{\underline{RR}} \right\rangle \tag{4-A-21}$$

In the original derivation, use has been made of the fact that strand density ν remains constant as the deformations were assumed to preserve the volume. Since the foregoing is no longer valid in unidirectional swelling, strand density and modulus are inversely proportional to determinant of deformation tensor, which is a measure of change in volume, eqn. (4-A-22).

$$\nu = \frac{\nu^o}{det(F)} \Rightarrow G = \frac{G^o}{det(F)} \tag{4-A-22}$$

Smoluchowski's equation allows for calculation of the second moment of probability distribution function, eqn. (4-A-23).

$$\frac{d\left\langle \underline{\underline{RR}} \right\rangle}{dt} - \nabla \mathrm{v}^T \cdot \left\langle \underline{\underline{RR}} \right\rangle - \left\langle \underline{\underline{RR}} \right\rangle \cdot \nabla \mathrm{v} + \frac{8k_B T \beta^2}{\varsigma} \left\langle \underline{\underline{RR}} \right\rangle - \frac{4k_B T}{\varsigma} \underline{\underline{I}} = 0 \tag{4-A-23}$$

where I denotes the identity matrix. Let:

$$\tau \equiv \frac{8k_B T\beta^2}{\varsigma} \tag{4-A-24}$$

Substituting the second moment in eqn. (4-A-23) using eqn. (4-A-21), (4-A-22), we arrive at the following form:

$$\frac{d\underline{\underline{s}}}{dt} - \nabla \mathrm{v}^T \cdot \underline{\underline{s}} - \underline{\underline{s}} \cdot \nabla \mathrm{v} + \frac{1}{\tau}\left(\underline{\underline{s}} - G\underline{\underline{I}}\right) + \frac{d\,ln\left[det(F)\right]}{dt}\underline{\underline{s}} = 0 \tag{4-A-25}$$

The above equation can be written in a compact form, using upper convected time derivative of stress tensor, eqn. (4-A-26).

$$\overset{\nabla}{\underline{\underline{s}}} \equiv \frac{d\underline{\underline{s}}}{dt} - \nabla \mathrm{v}^T \cdot \underline{\underline{s}} - \underline{\underline{s}} \cdot \nabla \mathrm{v} \tag{4-A-26}$$

Since subtracting an isotropic term from the stress tensor does not change the state of stress in eqn. (4-A-25), let us define a new stress tensor according to eqn. (4-A-27).

$$\underline{\underline{\sigma}} = \underline{\underline{s}} - G\underline{\underline{I}} \tag{4-A-27}$$

Upon introducing the new stress tensor, eqn. (4-A-27) into eqn. (4-A-25) and utilizing the upper convected time derivative notation, eqn. (4-A-26), the final form of modified UCM constitutive model is given by eqn. (4-A-28), in which strain rate tensor, Γ, has been introduced.

$$\overset{\nabla}{\underline{\underline{\sigma}}} + \frac{\underline{\underline{\sigma}}}{\tau} = 2G\underline{\underline{\Gamma}} - \frac{d\,ln\left[det(F)\right]}{dt}\underline{\underline{\sigma}} \tag{4-A-28}$$

It can be readily verified that eqn. (4-A-28) reduces to the ordinary UCM model for volume preserving deformations. In deriving eqn. (4-A-28), the following identity has been used, the accuracy of which may be checked by applying chain rule to eqn. (4-A-22).

$$\frac{dG}{dt} + G\frac{d\,ln\left[det(F)\right]}{dt} = 0 \tag{4-A-29}$$

The case of interest in this work is unidirectional swelling in the *x*-axis for which eqn. (4-A-28) can be simplified to the following expression giving the *xx* element of the stress tensor, eqn. (4-A-30).

$$\frac{d\sigma_{xx}}{dt} + \frac{\sigma_{xx}}{\tau} = (2G + \sigma_{xx})\frac{d\,ln(\lambda_x)}{dt} = \left(\frac{2G^o}{\lambda_x^2} + \frac{\sigma_{xx}}{\lambda_x}\right)\frac{d\lambda_x}{dt} \tag{4-A-30}$$

The fully elastic limit of eqn. (4-A-30) can be solved for by neglecting the relaxation term, assuming zero stress in the absence of deformation.

$$lim_{\tau\to\infty}\ \sigma_{xx} = G^o\left(\lambda_x - \lambda_x^{-1}\right) = G\left(\lambda_x^2 - 1\right) \tag{4-A-31}$$

Consistently, elastic stress in response to swelling is smaller in magnitude than in volume preserving deformations. The result has been plugged in eqn. (4-A-19) to yield eqn. (4-A-20).

4.4.4 Thermodynamic and Kinetic Factors

The following dimensionless six thermodynamic factors arise in the derivation of the chemical potential gradients in diffusion driving forces, eqn. (4-3), using the FH mixing free energy model, eqn. (4-5).

$$d_{WW} = 1 - \phi_W - \chi_{WD}\phi_W\phi_D - \chi_{WE}\phi_W\phi_E \tag{4-A-32}$$

$$d_{WD} = (1-\phi_W)\chi_{WD} - \left(\frac{\upsilon_W}{\upsilon_D}\right)(\chi_{DE}\phi_E - 1) \tag{4-A-33}$$

$$d_{WE} = (1-\phi_W)\chi_{WE} + \left(\frac{\upsilon_W}{\upsilon_D}\right)\chi_{DE}\phi_D \tag{4-A-34}$$

$$d_{DD} = 1 - \phi_D - \chi_{WD}\phi_W\phi_D\left(\frac{\upsilon_D}{\upsilon_W}\right) - \chi_{DE}\phi_D\phi_E \tag{4-A-35}$$

$$d_{DW} = \left(\frac{\upsilon_D}{\upsilon_W}\right)\left[(1-\phi_D)\chi_{WD} - \chi_{WE}\phi_E - 1\right] \tag{4-A-36}$$

$$d_{DE} = (1-\phi_D)\chi_{DE} - \chi_{WE}\phi_W\left(\frac{\upsilon_D}{\upsilon_W}\right) \tag{4-A-37}$$

In deriving eqns. (4-A-32) to (4-A-37), the pressure gradient is neglected in eqn. (4-3). The following kinetic factors arise upon inversion of ESM flux laws for water and drug, eqn. (4-4), coupled with no compressibility condition imposed by eqn. (4-6).

$$W_W = \left[\frac{\phi_W D_{DE} + (1-\phi_W)D_{WD}}{\phi_D D_{WE} + \phi_W D_{DE} + \phi_E D_{WD}}\right] D_{WE} \tag{4-A-38}$$

$$W_D = \left[\frac{D_{WD} - D_{WE}}{\phi_D D_{WE} + \phi_W D_{DE} + \phi_E D_{WD}}\right] D_{DE} \tag{4-A-39}$$

$$D_D = \left[\frac{\phi_D D_{WE} + (1-\phi_D)D_{WD}}{\phi_D D_{WE} + \phi_W D_{DE} + \phi_E D_{WD}}\right] D_{DE} \tag{4-A-40}$$

$$D_W = \left[\frac{D_{WD} - D_{DE}}{\phi_D D_{WE} + \phi_W D_{DE} + \phi_E D_{WD}}\right] D_{WE} \tag{4-A-41}$$

Water and drug fluxes are linear combinations of total diffusion forces with the foregoing terms as coefficients. Eight different coefficients, all functions of composition and ESM diffusivities, were introduced in eqn. (4-19) and (4-20). Ultimately, the following equations give those coefficients in terms of combinations of kinetic and thermodynamic factors.

$$A_W = W_W d_{WW} - W_D d_{DW} \phi_W \phi_D \quad (4\text{-A-}42)$$

$$A_D = \phi_W (W_W d_{WD} - W_D d_{DD}) \quad (4\text{-A-}43)$$

$$A_E = \phi_W (W_W d_{WE} - W_D d_{DE} \phi_D) \quad (4\text{-A-}44)$$

$$A_\sigma = -\frac{\upsilon_W \phi_W}{2 k_B T} \quad (4\text{-A-}45)$$

$$B_D = D_D d_{DD} - D_W d_{WD} \phi_W \phi_D \quad (4\text{-A-}46)$$

$$B_W = \phi_D (D_D d_{DW} - D_W d_{WW}) \quad (4\text{-A-}47)$$

$$B_E = \phi_D (D_D d_{DE} - D_W d_{WE} \phi_W) \quad (4\text{-A-}48)$$

$$B_\sigma = -\frac{\upsilon_D \phi_D}{2 k_B T} \quad (4\text{-A-}49)$$

4.5 References

[1] S.R. Lustig, N.A. Peppas, *J. Appl. Polym. Sci.* 33 (**1987**) 533-549.

[2] R.T.C. Ju, P.R. Nixon, M.V. Patel, D.M. Tong, *J. Pharm. Sci.* 84 (**1995**) 1464-1477.

[3] B. Narasimhan, N.A. Peppas, *J. Pharm. Sci.* 86 (**1997**) 297-304.
[4] J. Siepmann, H. Kranz, R. Bodmeier, N.A. Peppas, *Pharm. Res.* 16 (**1999**) 1748-1756.

[5] J. Siepmann, Y. Karrout, M. Gehrke, F.K. Penz, F. Siepmann, *Int. J. Pharm.* 441 (**2013**) 826-834.

[6] P. Borgquist, A. Körner, L. Piculell, A. Larsson, A. Axelsson, *J. Control. Release* 113 (**2006**) 216-225.

[7] D. Hariharan, N.A. Peppas, *J. Control. Release* 23 (**1993**) 123-136.

[8] C.S. Brazel, N.A. Peppas, *Eur. J. Pharm. Biopharm.* 49 (**2000**) 47-58.

[9] Y. Xu, Y. Jia, Z. Wang, Z. Wang, *J. Pharm. Sci.* 102 (**2013**) 1532-1543.

[10] E. Kaunisto, F. Tajarobi, S. Abrahmsen-Alami, A. Larsson, B. Nilsson, A. Axelsson, *Eur. J. Pharm. Sci.* 48 (**2013**) 698-708.

[11] E. Kaunisto, S. Abrahmsen-Alami, P. Borgquist, A. Larsson, B. Nilsson, A. Axelsson, *J. Control. Release* 147 (**2010**) 232-241.

[12] D. Caccavo, S. Cascone, G. Lamberti, A.A. Barba, *Mol. Pharmaceutics* 12 (**2015**) 474-483.

[13] P. Costa, J.M.S. Lobo, *Eur. J. Pharm. Sci.* 13 (**2001**) 123-133.

[14] Y. Ji, R. Paus, A. Prudic, C. Lübbert, G. Sadowski, *Pharm. Res.* 32 (**2015**) 2559-2578.

[15] H.L. Frisch, T.T. Wang, T.K. Kwei, *J. Polym. Sci.* A2 7 (**1969**) 879-887.

[16] G. Astaluta, G.C. Sarti, *Polym. Eng. Sci.* 18 (**1978**) 388-395.

[17] A. Pedacchia, A. Adrover, *Chem. Eng. Comm.* 202 (**2015**) 876-884.

[18] J. Klier, N.A. Peppas, *J. Control. Release* 7 (**1988**) 61-68.

[19] J.S. Vrentas, C.M. Vrentas, *Chem. Eng. Sci.* 53 (**1998**) 629-638.

[20] J.S. Vrentas, J.L. Duda, *J. Polym. Sci. Polym. Phys. Ed.* 15 (**1977**) 441-453.

[21] C.J. Durning, M. Tabor, *Macromolecules* 19 (**1986**) 2220-2232.

[22] N.A. Peppas, J.C. Wu, E.D. von Meerwall, *Macromolecules* 27 (**1994**) 5626-5638.

[23] B. Narasimhan, N.A. Peppas, *Macromolecules* 29 (**1996**) 3283-3291.

[24] L. Onsager, *Phys. Rev.* 37 (**1931**) 405-426.

[25] F. Fornasiero, J.M. Prasunitz, C.J. Radke, *Macromolecules* 38 (**2005**) 1364-1370.

[26] J.C. Wu, N.A. Peppas, *J. Polym. Sci. B Polym. Phys.* 31 (**1993**) 1503-1518.

[27] M.F. Herman, S.F. Edwards, *Macromolecules* 23 (**1990**) 3662-3671.

[28] R.G. Larson, Constitutive Equations for Polymer Melts and Solutions, Butterworth Publishers, MA, **1988**.

[29] H.G. Landau, *Quart. Appl. Math.* 8 (**1950**) 81-94.

[30] F.A. Long, D. Richman, *J. Am. Chem. Soc.* 82 (**1960**) 513-519.

[31] J. Crank, Mathematics of Diffusion, Oxford Press, London, **1956**.

[32] M. Rubinstein, R.H. Colby, Polymer Physics, Oxford university press, New York, **2003**.

[33] J.S. Vrentas, J.L. Duda, *J. Polym. Sci. Polym. Phys. Ed.* 15 (**1977**) 403-416.

[34] R.W. Korsmeyer, E. von Meerwall, N.A. Peppas, *J. Polym. Sci. B Polym. Phys.* 24 (**1986**) 409-434.

[35] J.S. Vrentas, C.M. Vrentas, *Macromolecules* 26 (**1993**) 6129-6131.

[36] X. Liu, S.K. Schnell, J.M. Simon, P. Krüger, D. Bedeaux, S. Kjelstrup, A. Bardow, T.J.H. Vlugt, *Int. J. Thermophys.* 34 (**2013**) 1169-1196.

[37] D.R. Wheeler, J. Newman, *J. Phys. Chem. B* 108 (**2004**) 18353-18367.

[38] S.T. Milner, M-D Lacasse, W.W. Graessley, *Macromolecules* 42 (**2009**) 876-886.

[39] G.W.R. Davidson III, N.A. Peppas, S, *J. Control. Release* 3 (**1986**) 259-271.

[40] J.S. Vrentas, C.M. Jarzebski, J.L. Duda, *AIChE J.* 21 (**1975**) 894-901.

[41] P. Colombo, R. Bettini, P. Santi, A. De Ascentiis, N.A. Peppas, *J. Control. Release* 39 (**1996**) 231-237.

[42] C. Ferrero, D. Massuelle, E. Doelker, *J. Control. Release* 141 (**2010**) 223-233.

[43] M. Kojima, S. Ando, K. Kataoka, T. Hirota, K. Aoyagi, H. Nakagami, *Chem. Pharm. Bull.* 46 (**1998**) 324-328.

[44] A.T. Pham, P.I. Lee, *Pharm. Res.* 11 (**1994**) 1379-1384.

Chapter 5: Electro-Stress-Diffusion Coupling Model of Polyelectrolyte LbL Assembly

5.1 Introduction

Despite the plethora of experimental work on the Layer-by-Layer (LbL) deposition process, only a handful of modeling works have been reported to date, see chapter 2. Diffusion of either PEs into the PEM is now widely held to be responsible for the exponential growth,[1,2] in spite of other phenomenological models.[3,4] Chain relaxation at the film surface was shown to lead to erosion of polymers from tablets in the last chapter. Similarly, instability of LbL assembled multilayers in high salinity occurs when ion-pairs are broken up by salt leading to chain relaxation and eventual dissolution in the surrounding solution; see section 2.3.3. In fact, stress relaxation in mixtures of oppositely charged polyelectrolytes is intricately correlated with mutual diffusion through the ion-pair break and formation time scales and number density. Recalling that self and mutual diffusivity is inversely correlated with chain relaxation time, it is thus not surprising that chain mutual diffusivity in LbL films and the relaxation time increase and decrease respectively in response to increase in salinity.[5,6] The time and length scales involved in a typical LbL process, namely 10-1000 sec, and 1-1000 nm respectively, put modeling of it well beyond the scope of typical atomistic simulations, which, when applied to LbL, remain restricted to small system sizes with only a few hundred polymer chains, at most.[7-9] These simulations are also typically restricted to coarse-grained meso-scale models, which do not capture the important chemo-specificity of chains manifest in charge regulation, ion-pairing and counterion condensation processes, discussed in chapter 3. Thus, molecular simulations are not able to capture crucial features of LbL process.

Not surprisingly, the majority of the relevant theoretical studies have focused on continuum modeling of LbL process at the expense of some molecular details. Even understanding LbL at a

continuum level has proved a major challenge so far, as there are many phenomena that need to be taken into account, some of which involve disparate time scales. Previous continuum models of LbL fall under two categories: (1) sequential *diffusion* models that track the time-dependent diffusion of only the polymer that is incoming during each LbL step and hold fixed the composition profiles of polymers adsorbed in preceding steps, [1,2] and (2) *sequential equilibrium* ones that treat the LbL process as a sequence of equilibrated, yet irreversible, adsorption steps,[10-13] and overlooks the diffusion dynamics within a single step altogether. The latter, sequential equilibrium, type of model simply generalizes self-consistent field theoretic (SCFT) treatment of polyelectrolyte adsorption on charged substrates to multi-step processes. [14,15] In both types of model, during each dipping step, the accumulated composition profile from preceding dipping steps is imposed as a frozen constraint. But in sequential equilibrium models, within a each step, an SCFT equilibrium calculation is carried out that determines the equilibrium composition profile of the invading polyion subject to the frozen profile of previous material. This calculation also determines the new electrostatic potential distribution resulting from that LbL step. These sequential equilibrium models, also collectively referred to as 'sequential adsorption models', are able to predict surface charge overcompensation, a process by which the electrostatic potential (and charge) at the film surface reverses sign due to adsorption of oppositely charged polyions during exposure of an LbL film to a dipping solution. However, the lack of dynamics in sequential adsorption models limits their accuracy to time scales over which chain diffusion into the film is comparable with, or less than, the macroscopic dipping time. Additionally, chain loss and film re-dissolution can only be added through a phenomenologically modeled "rinsing" process, given that network stress, which is essential to allow swelling without complete dissolution, does not come into play in these sequential equilibrium models. Short-ranged (nonlinear) electrostatic effects described in chapter 3 have been entirely left out of SCFT treatments in sequential equilibrium models to date. In principle, ion pairing and charge regulation etc. could be incorporated into a SCFT framework but the appropriate free energy model to capture all such effects had not been available until the work described in chapter 3 was recently published.

Following the pioneering work of Lavalle *et al*.[1] which confirmed that vertical chain diffusion across a portion, or all of the LbL film can occur depending on dipping conditions, Hoda and Larson[2] proposed a sequential diffusion transport model, that introduced time-dependent chain

diffusion to predict exponential growth of an LbL assembled film and a transition to linear growth as films became thicker. In their work, only one of the polyions, chosen to be the polycation, was assumed to have enough mobility for diffusion deep into the film. Unlike the sequential equilibrium model described above, in the model of Hoda and Larson the electrostatic potential profile was assumed to remain unchanged by the dipping step. Additionally, the bound charge distribution inside the film was not explicitly accounted for, but instead was accounted for approximately by imposing a time-invariant electrostatic charge density as a boundary condition at the solution-film interface at any given step. Neither the sequential equilibrium nor the sequential diffusion models consider the stress relaxation of polyions comprising the LbL assembled film and thus cannot predict the re-dissolution of LbL films and the saw-toothed growth-shrinkage profiles observed in chapter 2; see e.g. Figure 2-6.

In addition to solvent imbibition, the modulus of a mixture of oppositely charged polyions such as that in an LbL assembled film can change due to ion pair formation and break-up. While the Upper-Convected Maxwell (UCM) model for an electroneutral polymer was modified to account for solvent imbibition in section 4.4.3, a constitutive equation for time-dependent network stress capturing the effects of simultaneous solvent imbibition and ion pairing has yet to be developed.

Thus, even though the two modeling strategies described above are valid within certain rather severe limits, a rigorous dynamic framework to incorporate crucial features of LbL assembly, namely chain interdiffusion, stress relaxation, nonlinear electrostatic interactions and charge regulation is still lacking. In the present work, we develop a general model for transport in mixtures of multiple charged polymers and small ions that includes chemical potentials, electric fields, and mechanical stresses, using a unified framework based on free energy and dissipation rate of change. The two previous modeling strategies, sequential equilibrium and sequential diffusion, then become special cases of our proposed model. We additionally, propose an appropriate constitutive equation for stress of a mixture of two oppositely charged polyelectrolytes.

5.2 Model

5.2.1 General Formulation

The general conservation equation in a non-reactive system of water *(W)*, simple ions ('+' and '–') in addition to two polyion chain types of opposite charge (*A*: polyanion, *C*: polycation) is given by eqn. (5-1).

$$\rho \frac{\partial w_i}{\partial t} = -\boldsymbol{\nabla} \cdot (\rho_i \boldsymbol{v}_i) \tag{5-1}$$

The mass fraction and mass density of species 'i' are denoted by w_i and ρ_i, respectively while ρ represents the total system density. Each species velocity vector $\boldsymbol{v}_i$ is determined from a flux law representing a balance of the friction and diffusion driving forces exerted on individual species. For a multicomponent mixture of simple fluids, these 'flux laws' take the form of Stefan-Maxwell equations; see chapter 4, in which the diffusion driving forces are related to species velocities through a mobility matrix involving Onsager coefficients. However, Stefan-Maxwell equations do not make readily clear how the diffusion driving force should incorporate elastic stresses and electrostatic fields subject to the incompressibility constraint. Thus, rather than use the Stefan-Maxwell equations, we derive the relevant flux laws in a self-consistent manner using the Rayleighian R of the system, eqn. (5-2), following the multi-fluid model of Doi and Onuki.[16] The variational derivative of R with respect to each component velocity yields consistent dynamic equations that govern the system. Consequently, the dynamics of any non-inertial system is described through minimization of R with respect to species velocities comprising the system.

$$R \equiv \frac{\dot{S}}{2} + \dot{F} \tag{5-2}$$

The overdots above imply the time derivatives of the terms on the right side where S and F denote the system total dissipation and free energy. Acceleration could also be included in R by adding a net momentum flux and momentum rate of change with time. However, inertial effects can be safely left out of the equations for sluggish motions of polyions over the time scales of interest to us. Assuming a constant total density ρ set to 1 g/cm^3 and a zero net excess volume of mixing, the incompressibility constraint is imposed. Thus, eqn. (5-1) can be recast in terms of volume fractions ϕ_i:

$$\frac{\partial \phi_i}{\partial t} = -\boldsymbol{\nabla} \cdot (\phi_i \boldsymbol{v}_i) \tag{5-3}$$

The incompressibility constraint further implies that the volume fractions of species add up to unity, as given in eqn. (5-4), and the volume-averaged velocity $\boldsymbol{v} \equiv \sum \phi_i \boldsymbol{v}_i$ is then solenoidal.

$$1 = \phi_A + \phi_C + \phi_w + \phi_+ + \phi_- \rightarrow \boldsymbol{\nabla} \cdot \boldsymbol{v} = 0 \tag{5-4}$$

Introducing a Lagrange multiplier p, the incompressibility constraint is enforced in the Rayleighian, eqn. (5-5) where $\boldsymbol{r}$ denotes the position vector. In addition to minimizing with respect to the species velocities, the Rayleighian now also needs to be minimized with respect to p.

$$R \equiv \frac{\dot{S}}{2} + \dot{F} - \int d\boldsymbol{r}\, p\, \boldsymbol{\nabla} \cdot \boldsymbol{v} \tag{5-5}$$

The rate of mutual frictional dissipation between two species is proportional to the square of their relative velocity. Another source of energy dissipation originates from deformation gradients of purely viscous small molecules, particularly of the solvent, characterized by a Newtonian viscosity η. We model polymers as typical bead-spring chains, in which stretching of the spring due to velocity gradients leads to elastic stress arising from the conformational entropy which thus should be incorporated in the free energy functional. Here we take these springs, as usual, to be instantaneously elastic, so that polymer dissipation occurs only through frictional motion of their beads past surrounding molecules. However, deformation gradients only dissipate energy through instantaneously viscous components, characterized by viscosity η_i, which do not include the polyions. With this exclusion, $\dot{S}$ from the two dissipative processes is given by eqn. (5-6).

$$\dot{S} = \int d\boldsymbol{r} \left[{}^1\!/_2 \sum_i \sum_{i>j} \zeta_{ij}\, (\boldsymbol{v}_i - \boldsymbol{v}_j)^2 + \sum_{i \neq A,C} \eta_i \boldsymbol{\nabla} \boldsymbol{v}_i : \boldsymbol{\nabla} \boldsymbol{v}_i \right] \tag{5-6}$$

The mutual friction coefficient between i and j denoted by ζ_{ij}, is inversely proportional to the mutual diffusivity according to eqn. (5-7).

$$\zeta_{ij} = \frac{k_B T \phi_i \phi_j}{D_{ij} v_i} \tag{5-7}$$

where v_i is the molar volume of species i. Note that the values of ζ_{ij} or D_{ij} might also depend on molecular weight and solvent quality, and in general depend on temperature.

The free energy of systems involving polyelectrolytes, in particular of oppositely charged polyelectrolytes, is an emerging area of research in molecular thermodynamics and a definitive

continuum, i.e. closed form, free energy functional does not exist as yet, as discussed in chapter 3. The complexities of deriving a general free energy expression for multi-component polyelectrolytes arise from the highly correlated nature of charges that could lead to phase separation. Here we represent the free energy functional as a combination of a mean-field contribution that encompasses electrostatic field and non-local effects, an elastic free energy stored in polymer chains, as well as a non-mean-field contribution from correlated electrostatic fluctuations.

$$F = \int d\boldsymbol{r}\,(f_{MF} + f_{Corr}) + F_{elas} \tag{5-8}$$

The mean-field free energy, in turn, encompasses the conventional Flory-Huggins (FH) mixing energy, electrostatic, and non-local free energy contributions. Taking the time derivative of F, we arrive at the following form.

$$\dot{F} = \int d\boldsymbol{r}\,\sum_i \left(\frac{\delta F}{\delta \phi_i}\right)\left(\frac{\partial \phi_i}{\partial t}\right) + \dot{F}_{elas} \tag{5-9}$$

For the sake of brevity in notation, we leave off the subscripts conventionally used to indicate which variables are held fixed in the variational and partial derivatives in eqn. (5-9); instead, we note here that all variables, except for the one with respect to which the derivative is taken, are held fixed. In the generalized version of Brochard's theory for mutual diffusion in the presence of elastic stress gradients,[17] the two polymers whose degrees of polymerization exceed the entanglement threshold form a network that carries a total "network stress" given by a tensor $\boldsymbol{\sigma}$, a portion of which is borne by each polymer type according to an effective friction in the network ζ_{iN}; here *i*: *A* & *C*, denoted polycation and polyanion and the subscript "N" denotes the network that they together form. Note that the friction coefficient between the two polyions ζ_{AC} is shown in the above work to be the harmonic average of ζ_{AN} and ζ_{CN}.[16] The network stress is generated by the gradient of an effective network velocity $\boldsymbol{v}_N$, which is determined by the requirement that the frictional forces acting on the network should balance according to eqn. (5-10).

$$\zeta_{AN}(\boldsymbol{v}_A - \boldsymbol{v}_N) + \zeta_{CN}(\boldsymbol{v}_C - \boldsymbol{v}_N) = 0 \Rightarrow \boldsymbol{v}_N = \frac{\zeta_{AN}\boldsymbol{v}_A + \zeta_{CN}\boldsymbol{v}_C}{\zeta_{AN}+\zeta_{CN}} = \alpha_A \boldsymbol{v}_A + \alpha_C \boldsymbol{v}_C \tag{5-10}$$

Here, $\alpha_i \equiv \frac{\zeta_{iN}}{\zeta_{AN}+\zeta_{CN}}$ for *i: A, C*. In the special case in which the monomeric friction coefficients and degrees of polymerization of the two chain types are identical, then α_i is simply given by the

fraction of chain type i in the network. The time derivative of the elastic free energy is now expressed as:[16]

$$\dot{F}_{elas} = \int d\boldsymbol{r}\, (\boldsymbol{\sigma} : \boldsymbol{\nabla} \boldsymbol{v_N}) \tag{5-11}$$

Defining electrochemical potentials $\psi_i \equiv \left(\frac{\delta F}{\delta \phi_i}\right)$ and substituting for the time derivatives of volume fractions in eqn. (5-9) using the species conservation eqn. (5-3), the time derivative of free energy is now given by eqn. (5-12).

$$\dot{F} = \int d\boldsymbol{r}\, [\boldsymbol{\sigma} : \boldsymbol{\nabla} \boldsymbol{v_N} - \textstyle\sum_i \psi_i \boldsymbol{\nabla} \cdot (\phi_i \boldsymbol{v_i})] \tag{5-12}$$

The electrostatic potential, mixing free energy, and non-local effects all contribute to the electrochemical potentials ψ_i in eqn. (5-12). Explicit forms of the electrochemical potential will be derived in the subsequent sections. The variational derivative of R with respect to velocities yields the force balance on each component in the absence of inertia.

$$\left(\frac{\delta R}{\delta \boldsymbol{v}_i}\right) = 0 = \textstyle\sum_{j \neq i} \zeta_{ij} \left(\boldsymbol{v}_i - \boldsymbol{v}_j\right) + \phi_i \boldsymbol{\nabla} \psi_i + \phi_i \boldsymbol{\nabla} p - \boldsymbol{\nabla} \cdot \boldsymbol{\sigma}_i \tag{5-13}$$

The Onsager reciprocal principle stipulates that $\zeta_{ij} = \zeta_{ji}$. The last term in eqn. (5-13) is the stress-gradient diffusion driving force, and is given by eqn. (5-14a) for the solvent and salt molecules while those of the polymeric species are related to the network stress according to eqns. (5-14 b & c).

$$\boldsymbol{\nabla} \cdot \boldsymbol{\sigma}_i = \eta_i \boldsymbol{\nabla}^2 \boldsymbol{v}_i \qquad (i: W, +, -) \tag{5-14a}$$

$$\boldsymbol{\nabla} \cdot \boldsymbol{\sigma}_A = \alpha_A \ \boldsymbol{\nabla} \cdot \boldsymbol{\sigma} \tag{5-14b}$$

$$\boldsymbol{\nabla} \cdot \boldsymbol{\sigma}_C = \alpha_C \ \boldsymbol{\nabla} \cdot \boldsymbol{\sigma} \tag{5-14c}$$

In eqn. (5-14a), η_i for each salt ion and for water should be equal to each other, and taken to be the viscosity of the salt-in-water solution that constitutes the non-polymeric species in our model. (This assumption is of no consequence here, since we will end up neglecting the viscous stresses from these three species.) Note that α_A & α_C are both dependent on the volume fractions of polyanion and polycation chains and thus the prefactors of $\boldsymbol{\nabla} \cdot \boldsymbol{\sigma}$ in eqn. (5-14 b & c) may not be moved inside the divergence operator and merged into re-defined stresses. Note also that inertial effects, if needed, can be accounted for simply by appending the term $\rho_i \frac{D\boldsymbol{v}_i}{Dt}$ to the end of eqn. (5-13). The final dynamic equations involving the two polyelectrolytes are similar to those derived

by Doi and Onuki in their two-fluid model,[16] with the exception that they did not consider electrostatics and restricted their discussion to binary systems; i.e., a polymer and a solvent, or two polymers. Extension of the two-fluid model to a multi-component system is straightforward, however, and has been proposed for a system of solvent/non-solvent/neutral polymer where the polymer viscoelasticity was ignored.[18] The current development is thus a generalization of the two-fluid model to charged-multi-component systems involving more than one polymeric species that also allows for stress relaxation. For an M-component system, there are M+1 unknowns, namely M velocities and the Lagrange multiplier p. The incompressibility condition, eqn. (5-4), along with eqn. (5-12) applied to each component, affords the requisite M+1 equations, once an appropriate constitutive equation for stress and a free energy density are chosen. The mean-field electrostatic field Φ is obtained by minimizing R or equivalently F with respect to Φ, which, as we demonstrate in the next section, gives the Poisson equation if electrostatic correlations are ignored.

$$\frac{\delta R}{\delta \Phi} = 0 \tag{5-15}$$

Before applying the simplifying assumptions relevant to LbL deposition, we note that a constitutive equation for the network stress must account for two important features, namely network junction formation due to complexation between oppositely charged segments, as well as dilution of elastic strand density resulting from solvent imbibition, both of which result in a time dependence of both shear and osmotic bulk moduli. However, such a constitutive equation has not previously been derived, to the best of our knowledge. In the next section, we therefore develop a constitutive equation that includes the aforementioned key features.

5.2.2 Constitutive Equation for Elastic Stress

In this section, we seek to develop a constitutive equation that is appropriate to a mixture of oppositely charged polyelectrolytes, which accounts for solvent imbibition and complexation. However, the present work is not meant to provide a rigorous treatment of this topic which would require dealing with thermodynamic non-idealities and electrostatic potential inhomogeneities, in addition to multi-mode polymer relaxation dynamics. Here we will focus on developing a single-mode constitutive equation for elastic stress relaxation that accounts for changes in modulus due to swelling by solvent and time-dependent changes in polyelectrolyte

concentration. We consider a network of strands of opposite charge, temporarily bound to each other by ion pairing, which can break and reform, ultimately giving rise to relaxation of polymer configurations and therefore of stress. In the absence of composition gradients, this would give rise, in the simplest case, to an ordinary upper-convected Maxwell (UCM) equation for the stress. However, there are two polymeric species (polycation and polyanion) that are inter-diffusing, which leads to gradients of the density of ion pairs, and therefore variations in the modulus. In addition, there is swelling of the network by solvent, leading to dilution of the modulus. The dependence of modulus on network junction concentration produced by affine network swelling differs from that produced by diffusion of polyelectrolyte, and hence care must be taken in generalizing the UCM model to account, even qualitatively, for these effects. For this reason, we need to re-derive the constitutive equation from a starting point that is general enough to account for both deformation and spatial variations in network density. To develop a suitable starting point, we will combine the theory of spatially inhomogeneous dumbbells of Bhave *et al*.[19] with the network theory of Yamamoto *et al*.,[20-22] to produce a one-mode theory of stress relaxation in inhomogeneous networks of strands, where the dumbbells of Bhave *et al*.[19] will be re-interpreted as mean-field network strands in our theory. A more complete theory would involve multiple relaxation modes, and employ the "sticky diffusion" concept of Rubinstein[23] to link the breakage time of an ion pair to the distribution of relaxation times of the molecules and of the network.

In the kinetic theory of a dilute inhomogeneous solution of Hookean dumbbells, Bhave *et al*.[19] developed the Smoluchowski equation, eqn. (5-16), governing the evolution of the grand configuration density function $\Psi(\boldsymbol{r},\boldsymbol{Q},t)$ as a function of spatial coordinates $\boldsymbol{r}$, end-to-end dumbbell vector $\boldsymbol{Q}$ and time. $\Psi(\boldsymbol{r},\boldsymbol{Q},t)$ is the product of a local configurational distribution function $\psi(\boldsymbol{r},\boldsymbol{Q},t)$, which is normalized to unity when integrated over $\boldsymbol{Q}$ at each position $\boldsymbol{r}$, and a local number density of dumbbells $n(\boldsymbol{r},t)$. The subscripted nabla operator $\boldsymbol{\nabla}_Q$ in eqn. (5-16) denotes the gradient in conformation space while $\boldsymbol{\nabla}$ denotes the conventional spatial gradient in $\boldsymbol{r}$.

$$\frac{\partial\Psi}{\partial t} = -\boldsymbol{\nabla}\cdot\left[\left(\boldsymbol{v}(\boldsymbol{r}) - \frac{k_BT}{2\zeta}\boldsymbol{\nabla}\ln(\Psi)\right)\Psi\right] - \boldsymbol{\nabla}_Q\cdot\left[\left(\boldsymbol{Q}\cdot\boldsymbol{\nabla}\boldsymbol{v} - \frac{2k_BT}{\zeta}\boldsymbol{\nabla}_Q\ln(\Psi) - \frac{2H}{\zeta}\boldsymbol{Q}\right)\Psi\right] \quad (5\text{-}16)$$

Bhave *et al*.[19] derived the following constitutive equation by taking the second moment of eqn. (5-16) in configurational space $\boldsymbol{Q}$. Their result is reproduced below up to the second order given by eqn. (5-17) where the subscript "(1)" denotes the upper-convected derivative defined in eqn. (5-18) for an arbitrary tensor $\boldsymbol{B}$.

$$\Rightarrow \boldsymbol{\sigma}_{(1)} + \frac{1}{\tau}\boldsymbol{\sigma} = 2nk_BT\boldsymbol{D} + D(\boldsymbol{\nabla}^2\boldsymbol{\sigma} + \boldsymbol{\nabla}\boldsymbol{\nabla}\colon\boldsymbol{\sigma}\boldsymbol{\delta}) \tag{5-17}$$

$$\boldsymbol{B}_{(1)} \equiv \frac{\partial[\boldsymbol{B}]}{\partial t} + \boldsymbol{v}\cdot\boldsymbol{\nabla}\boldsymbol{B} - (\boldsymbol{\nabla}\boldsymbol{v})^{\boldsymbol{t}}\cdot\boldsymbol{B} - \boldsymbol{B}\cdot(\boldsymbol{\nabla}\boldsymbol{v}) \tag{5-18}$$

where the superscript "t" denotes the transpose of the tensor. The dumbbell translational diffusivity in the solvent D is given by $\frac{k_BT}{2\zeta}$, where ζ is the drag coefficient of a dumbbell bead. The dumbbell spring constant is denoted by H and $\tau = \frac{\zeta}{4H}$ is the relaxation time in this single-mode description of a dumbbell. The strain rate tensor $\boldsymbol{D}$ is given by $2\boldsymbol{D} = \boldsymbol{\nabla}\boldsymbol{v}+(\boldsymbol{\nabla}\boldsymbol{v})^{\boldsymbol{t}}$. The number density of dumbbells n whose centers of mass are located at position $\boldsymbol{r}$ is obtained by integration of the probability distribution function Ψ over $\boldsymbol{Q}$ space, eqn. (5-19).

$$n(\boldsymbol{r},t) = \int \Psi(\boldsymbol{r},\boldsymbol{Q},t)d\boldsymbol{Q} \tag{5-19}$$

The velocity $\boldsymbol{v}(\boldsymbol{r},t)$ in eqn. (5-16) in the work of Bhave *et al*.[19] is the mass-averaged velocity and the fluid, which is taken to be a simple solvent, was taken to be incompressible. Here, the relevant velocity that determines the deformations of the polymer is the network velocity $\boldsymbol{v_N}$ defined earlier by eqn. (5-10) for which $\boldsymbol{\nabla}\cdot\boldsymbol{v_N} \neq 0$ since solvent imbibition causes the dilution of strands and a decrease in network modulus; see the appendix 4.4.3 of chapter 4. Hereafter, we replace $\boldsymbol{v}$ with $\boldsymbol{v_N}$ in all equations including the upper-convected derivative given by eqn. (5-18). Next, we recognize a few distinctions between the dilute polymer solutions, for which the last three equations were derived, and a mixture of oppositely charged polyelectrolytes that form a network. Firstly, the network strands in the latter are composed of two types of polyions that form a network through entanglements and ion-pairs. Here, we will regard the dynamics of these differing strands as intimately connected to each other through their ion pairing junctions, so that we only consider the relaxation dynamics of one kind of "average" strand, which is set by the rate of formation and breakage of network junctions. Secondly, LbL assembled polyelectrolyte films are generally not dilute, and therefore the terms $\ln(\Psi)$ in eqn. (5-16) needs to be replaced

by a generalized thermodynamic potential function to account for non-idealities and the electrostatic field. However, for simplicity, we leave the ln(Ψ) in eqn. (5-16) intact.

Lastly, elastic strands can be created and destroyed through the formation and break-up of ion pairs between oppositely charged segments. Therefore, we need to include a reaction term in our modified probability density distribution equation to account for strand formation and disappearance. To do so, we borrow from Yamamoto's network model,[20-22,24] which can be written for a homogeneous network, with no spatial variations, as

$$\frac{\partial \psi}{\partial t} = -\boldsymbol{\nabla}_Q \cdot [(\boldsymbol{Q} \cdot \boldsymbol{\nabla} \boldsymbol{v_N})\psi] + \left[k\psi_o - \frac{\psi}{\tau_o}\right] \tag{5-20}$$

The final two terms of this equation are, respectively, the rate of creation of new network strands, which have configurations of the equilibrium (no-stress) ensemble, ψ_o, while the last term is the destruction rate, set by the time required for junction breakage τ_o. The above equation assumes that strands deform affinely until a junction breaks, after which the strand takes on an equilibrium configuration. Detailed balance, in which strands can relax, but are not destroyed or created, implies that $k = 1/\tau_o$. The Yamamoto model is most applicable to simple telechelic polymer networks with network-forming stickers confined to the two ends of the polymer molecule, where breakage of a single junction allows the connected strands to quickly relax completely, on a time scale of τ_o. For a polyelectrolyte network, however, with multiple stickers per molecule, loss of a single junction permits only partial relaxation. To relax the stress completely, even within a single strand, the entire molecule must relax, on a time scale much longer than the sticker lifetime τ_o. The chain as a whole relaxes according to Rouse or reptation diffusion dynamics, with diffusion rate set by the time constant τ_o, a process known as "sticky diffusion." Theories for sticky diffusion are able to relate τ_o to a much longer time scale τ for relaxation of the entire chain, and hence of the stress. To generate a one-mode model for relaxation of stress governed by breakage of ion pairs, in a spatially inhomogeneous network, we append a modified strand creation term and a destruction term to the diffusion equation of Bhave *et al*.[19] given by eqn. (5-16):

$$\frac{\partial \Psi}{\partial t} = -\boldsymbol{\nabla} \cdot \left[\left(\boldsymbol{v}_N(\boldsymbol{r}) - D\boldsymbol{\nabla}\ln(\Psi)\right)\Psi\right] - \boldsymbol{\nabla}_Q \cdot \left[\left(\boldsymbol{Q} \cdot \boldsymbol{\nabla}\boldsymbol{v}_N - 4D\boldsymbol{\nabla}_Q \ln(\Psi) - \frac{2H}{\zeta}\boldsymbol{Q}\right)\Psi\right] +$$

$$\left[k\left[\alpha\psi_o + (1-\alpha)\psi\right] - \frac{\Psi}{\tau_o}\right] \tag{5-21}$$

Again, the normalized probability distribution function ψ reverts at equilibrium to ψ_o and both of distribution functions integrate to unity in $\boldsymbol{Q}$ space. In eqn. (5-21), k is the rate of network formation per unit volume, which in turn depends on the local composition of the network. Note that we no longer allow breakage of a network junction to completely relax the strand, since it is strongly constrained by the remaining junctions along the chain. Thus, we introduce the coefficient α as a microscopic parameter that controls the portion of the orientation that a freed strand relaxes before forming a new ion pair. The parameter α is clearly a function of chain microstructure, chain length, and cooperativity of complexation, which could be determined by e.g. molecular simulations. We have also replaced the dumbbell diffusion coefficient in the equation of Bhave *et al.*[19] with D, the polymer network diffusivity. Integrating eqn. (5-21) over $\boldsymbol{Q}$ space yields the strand conservation equation up to second order gradient terms.

$$\frac{\mathrm{D}n}{\mathrm{D}t} + n(\boldsymbol{\nabla}\cdot\boldsymbol{v}_N) = D\boldsymbol{\nabla}^2 n - \frac{D}{k_B T}\boldsymbol{\nabla}\boldsymbol{\nabla}\colon\boldsymbol{\sigma} + k - \frac{n}{\tau_o} \tag{5-22}$$

In the limit in which the exchange rate between newly formed ion pairs and the ones breaking up is much faster than the transport of the strands (which would be the case if there are many ion pairs per chain), the reaction term in eqn. (5-22) dominates and we can write:

$$k - \frac{n}{\tau_o} = 0 \Rightarrow k = \frac{n}{\tau_o} \tag{5-23}$$

The network stress $\boldsymbol{\sigma}$ is related to the second moment of the probability distribution function $\langle\boldsymbol{QQ}\rangle$ according to eqn. (5-24). At equilibrium, $\Psi = \Psi_o$ is a Gaussian function and the polymer stress vanishes. Accordingly, $\langle\boldsymbol{QQ}\rangle$ becomes isotropic at equilibrium and equal to $\frac{nk_BT}{H}\boldsymbol{\delta}$.

$$Hn\langle\boldsymbol{QQ}\rangle = H\int d\boldsymbol{Q}\Psi\boldsymbol{QQ} = \boldsymbol{\sigma} + nk_BT\boldsymbol{\delta} \tag{5-24}$$

Taking the second moment of the configuration probability distribution equation (5-21), we arrive at an expression for the evolution of the second moment given below.

$$[n\langle\boldsymbol{QQ}\rangle]_{(1)} + (\boldsymbol{\nabla}\cdot\boldsymbol{v}_N)n\langle\boldsymbol{QQ}\rangle = D\boldsymbol{\nabla}^2[n\langle\boldsymbol{QQ}\rangle] + 8nD\boldsymbol{\delta} - \frac{4Hn}{\zeta}\langle\boldsymbol{QQ}\rangle + k\left[\alpha\frac{k_BT}{H}\boldsymbol{\delta} + (1-\alpha)\langle\boldsymbol{QQ}\rangle\right] - \frac{n\langle\boldsymbol{QQ}\rangle}{\tau_o} \tag{5-25}$$

Substituting for $n\langle\boldsymbol{QQ}\rangle$ and k in eqn. (5-25) using eqn. (5-23) and (5-24), we arrive at the following constitutive equation with the third and higher order gradient terms dropped.

$$\boldsymbol{\sigma}_{(1)} + \left(\frac{\mathrm{D}n}{\mathrm{D}t} + n\boldsymbol{\nabla}\cdot\boldsymbol{v}_N - D\boldsymbol{\nabla}^2 n\right)k_BT\boldsymbol{\delta} - 2nk_BT\boldsymbol{D} + (\boldsymbol{\nabla}\cdot\boldsymbol{v}_N)\boldsymbol{\sigma} = D\boldsymbol{\nabla}^2\boldsymbol{\sigma} - \left(\frac{4H}{\zeta} + \frac{\alpha}{\tau_o}\right)\boldsymbol{\sigma} \tag{5-26}$$

The second term on the left side of eqn. (5-26) can be substituted out with the strand conservation eqn. (5-22). We notice that the microscopic details embodied in the parameter α can be absorbed into an effective single-mode relaxation time $\tau_{eff} \equiv \left(\frac{4H}{\zeta} + \frac{\alpha}{\tau_o}\right)^{-1}$. Since the lowest order network stress is zero, at least the first order terms in the constitutive equation need to be retained, and given as below after some rearrangement.

$$\boldsymbol{\sigma}_{(1)} + \frac{\boldsymbol{\sigma}}{\tau_{eff}} + (\boldsymbol{\nabla} \cdot \boldsymbol{v}_N)\boldsymbol{\sigma} = 2nk_BT\boldsymbol{D} + D(\boldsymbol{\nabla}^2\boldsymbol{\sigma} + \boldsymbol{\nabla}\boldsymbol{\nabla}\colon\boldsymbol{\sigma}\boldsymbol{\delta}) \tag{5-27}$$

Due to solvent imbibition and consequent swelling of the network, eqn. (5-27) has an additional term $(\boldsymbol{\nabla} \cdot \boldsymbol{v}_N)\boldsymbol{\sigma}$ not present in eqn. (5-17) which accounts for the decrease in modulus $G = nk_BT$ as the network takes up more solvent. For the purpose of transport in the LbL assembled films, the first order terms in the constitutive equation suffice, particularly given that the thermodynamic non-idealities and electrostatic potential were left out of the probability distribution eqn. (5-21) to begin with. The second order terms would be strictly accurate anyway only in the dilute regime for neutral polymer solutions. Dropping the second order terms in eqn. (5-27), we arrive at the desired constitutive equation appropriate to ion-pair forming polyelectrolyte mixtures subject to swelling/de-swelling. The result at the first order level resembles the conventional upper-convected Maxwell model and in fact reduces to it if the deformations are volume preserving and network reaction is absent.

$$\boldsymbol{\sigma}_{(1)} + \frac{\boldsymbol{\sigma}}{\tau_{eff}} + (\boldsymbol{\nabla} \cdot \boldsymbol{v}_N)\boldsymbol{\sigma} = 2G\boldsymbol{D} \tag{5-28}$$

While the above may seem to be a rather trivial modification from the ordinary UCM equation, it contains two significant differences, both related to the modulus $G = nk_BT$, which is a function of time, through its dependence on the network density n. Both diffusive motion of the two polyelectrolytes and swelling make the modulus time dependent, captured, for example, by setting G proportional to $\phi_A\phi_C$. However, modulus change due to swelling is accompanied by deformation, and this is captured by the upper convected derivative, modified by the volume-change term $(\boldsymbol{\nabla} \cdot \boldsymbol{v}_N)\boldsymbol{\sigma}$. Correct development of these terms required starting from the general Smoluchowski probability equation, along with the network creation/destruction terms. In our model, we only consider the z-element of the network velocity $\boldsymbol{v}_{N,z} = v_N$, uniaxial deformations,

and thus only the zz-component of the polymer stress, $\boldsymbol{\sigma}_{zz} = \sigma$. Thus the working constitutive equation for our model reduces to the following form after some rearrangement.

$$\frac{\partial \sigma}{\partial t} + \frac{\sigma}{\tau_{eff}} = (2G + \sigma)\nabla_z v_N \tag{5-29}$$

The result is identical to that derived in chapter 4, eqn. (4-A-30) once $\nabla_z v_N$ in (5-29) is expressed in terms of local stretch ratio λ and the dilution of the modulus as $G \propto \phi_A \phi_C \propto 1/\lambda^2$ is accounted for. In general, the modulus G is proportional to the number density of ion pairs, which is assumed to be proportional to strand density $G = nk_BT$. This can be affected by the instantaneous equilibrium between ion pair formation and break-up reactions, which produces changes in G additional to that produced by network dilation. The equilibrium ion-pair and thus the strand density in a mixture of two oppositely charged polyelectrolytes has been shown to be a highly nonlinear function of individual polyion composition as well as of the salinity, dielectric constant etc.; see chapter 3. However, in the weak ion pairing limit where the fraction of polyions binding with oppositely charged repeat units is much smaller than unity, then $n \propto K_{ip}\phi_A\phi_C$ where K_{ip} is the thermodynamic equilibrium constant of the ion pairing reaction. Therefore, we can set $G = G^o\phi_A\phi_C k_BT$ in this limit, which allows for the variation of modulus due to complexation reaction, as well as due to swelling and de-swelling in our model.

5.2.3 Model Reduction

In this section, we introduce a few simplifying assumptions and narrow our focus to certain limits, with the recognition that all of them can be relaxed in the general framework laid out in the previous section.

To begin with, we note that the thicknesses of LbL-assembled PEM films range from 50 nm to a few microns. Given that LbL assembled films are typically much wider than they are thick, a one-dimensional description, say in the z direction, is adequate. Therefore, all bold-faced quantities in the above, designating tensors and vectors, can be replaced with the z component, i.e. $v_C \equiv \boldsymbol{v}_C^z$, etc., and we only retain the zz component of the network stress denoted by σ. Furthermore, we consider the low-salt regime where the size of simple ions is negligible and thus they can be approximated as point charges. (This and other restrictions can readily be relaxed, if desired.) We only consider monovalent salts and polyion monomers. Accurate description of the

free energy of simple electrolyte solutions at high salinity requires numerical approaches such as liquid state integral theory that lack closed-form expressions requisite in our transport framework. Additionally, the point-charge assumption greatly reduces the computational complexity of the numerical solutions.

Yet another simplification comes about from the disparate time scales associated with diffusion of polymers and small molecules. The mutual diffusivity of a polymer chain through another polymer is, depending on the molecular weight, typically many orders of magnitude slower than that of small molecules. This decoupling of diffusivities and thus of diffusion time scales allows for considering the dynamic equations for polyions only while small-molecule components instantaneously equilibrate across the film. Consequently, this constraint allows for considerably larger time steps in numerical schemes than would be otherwise permissible. As a result, the only friction coefficient that needs to be retained in the analysis henceforth is that between the two polyion types ζ_{AC}.

Solvent imbibition by the polymers generates mechanical stress that opposes further solvent ingress. Polymer stresses tend to be much larger than the solvent viscous stress. Therefore, the latter is neglected compared to frictions with polymer and polymer stress. Applying our simplifying assumptions and using $\nabla_z \equiv \frac{\partial}{\partial z}$ as shorthand, we can rewrite the equations in the general framework starting with the incompressibility condition, eqn. (5-4)

$$1 = \phi_A + \phi_C + \phi_w \tag{5-30}$$

Approximating salt ions as point charges as well as the rapid equilibration assumption decouple them from dynamic equations simply because they pose no friction when moving in the system. In fact, as we shall see, the salt ion concentrations become enslaved to the electrostatic potential distribution. The force balance on water and simple ions denoted collectively by '$\pm$' by shorthand notation, eqn. (5-13) applied to $i = W, \pm$ reduces to the simple forms below where the friction forces other than those involving polymer-polymer friction, as well as the viscous stress terms, have been dropped.

$$0 = \phi_w \nabla_z (\psi_w + p) \tag{5-31}$$

$$0 = \nabla_z \psi_{\pm} \tag{5-32}$$

Note that the Lagrange multiplier p does not apply to point charges anymore, as they occupy no volume. Retaining the friction term between the two polymer types in eqn. (5-13) applied to $i = A, C$, the force balance for them simplifies to the following:

$$0 = \zeta_{AC}(v_C - v_A) + \phi_C \nabla_z \psi_C + \phi_C \nabla_z p - \alpha_C \nabla_z \sigma \tag{5-33}$$

$$0 = \zeta_{CA}(v_A - v_C) + \phi_A \nabla_z \psi_A + \phi_A \nabla_z p - \alpha_A \nabla_z \sigma \tag{5-34}$$

As can be seen from the last two equations, the velocity v_W of the solvent decouples from the dynamic equations explicitly so that, of the conservation equations, eqn. (5-3), we only need to consider those for the two polymers. The Lagrange multiplier p in eqns. (5-33) and (5-34) is a response function that can be determined by solving for the composition profiles. Eliminating p and introducing exchange electrochemical potentials as $\psi_{iw} \equiv \psi_i - \psi_W$, eqns. (5-33) and (5-34) are rewritten below:

$$0 = \zeta_{AC}(v_C - v_A) + \phi_C \nabla_z \psi_{CW} - \alpha_C \nabla_z \sigma \Rightarrow \zeta_{AC}(v_C - v_A) = -\phi_C \nabla_z \psi_{CW} + \alpha_C \nabla_z \sigma \equiv d_C$$

$$0 = \zeta_{CA}(v_A - v_C) + \phi_A \nabla_z \psi_{AW} - \alpha_A \nabla_z \sigma \Rightarrow \zeta_{CA}(v_A - v_C) = -\phi_A \nabla_z \psi_{AW} + \alpha_A \nabla_z \sigma \equiv d_A$$

(5-35 a & b)

Here we have defined the net diffusion driving force d_i for each polyion type, i = A, C. Given a free energy density to evaluate exchange electrochemical potentials and a constitutive equation for σ, the two polymer conservation equations, eqn. (5-3) for $i = A, C$ coupled with eqns. (5-33) and (5-34) seemingly provide four independent equations to solve for the four field variables of interest, namely ϕ_C, ϕ_A, v_C, v_A. However, it is only possible to derive explicit expressions for relative polymer velocities using eqns. (5-33) and (5-34). This is a direct consequence of requiring rapid equilibration of water and salt ions, which leave the relative velocity of the polymer chains as the only dynamically relevant term. The next equation is obtained by summing the last two equations, yielding the overall force balance in the system, eqn. (5-36).

$$d_C + d_A = 0 \rightarrow \phi_C \nabla_z \psi_{CW} + \phi_A \nabla_z \psi_{AW} = \nabla_z \sigma \tag{5-36}$$

We will return to eqn. (5-36) later and recast it in a more familiar form. We next turn our attention to the exchange electrochemical potentials by choosing explicit free energy densities in F. We point out that the choice of free energy model here does not alter the general dynamic framework. In general, a definitive theory of correlation free energy of oppositely charged polyelectrolytes is still an emerging area and, despite recent progress, see chapter 3, rigorous

closed-form expressions requisite for a transport model are still lacking. Therefore, we focus only on the mean-field contributions to the free energy in order to reduce the complexities arising from charge regulation, complexation etc. The first contribution to the mean-field free energy is the Flory-Huggins (FH) theory includes the van der Waals (VdW) interactions between species i and j characterized by χ_{ij} and the translational entropy of each component weighted inversely by N_i the ratio of the molecule size and the volume of a lattice site l^3 taken to be volume of a water molecule $\sim 30^3$ Å^3. All parameters with an overlying tilde are non-dimensional, hereafter.

$$\tilde{f}_{FH} \equiv \frac{l^3 F_{FH}}{V k_B T} = \sum_{i=A,C,W} \frac{\phi_i \, ln \, \phi_i}{N_i} + (C_+ l^3) \, ln(\, C_+ l^3) + (C_- l^3) \, ln(\, C_- l^3) + \sum_i \sum_{i>j} \chi_{ij} \phi_i \phi_j \quad (5\text{-}37)$$

In eqn. (5-37), k_B, T and V represent the Boltzmann constant, temperature and volume, respectively. The mean-field electrostatic free energy of a molecule of component i with a charge valence of z_i in an electrostatic potential Φ is simply $z_i\Phi$. Additionally, the energy stored in an electrostatic field is proportional to square of the gradient of the electrostatic potential. Therefore the normalized mean-field electrostatic free energy $\tilde{f}_{ele}$ is given as:

$$\tilde{f}_{elec} \equiv \frac{l^3 F_{elec}}{V k_B T} = \tilde{\Phi}(C_+ l^3 - C_- l^3 + \sum_{i \neq \pm} z_i \phi_i) + \frac{2\pi l^3}{\ell_B} \left(\nabla_z \tilde{\Phi}\right)^2 \quad (5\text{-}38)$$

The charge valence of polyions, even strong ones, is generally a function of composition, i.e. there is charge regulation. However, here, for simplicity, charge valencies are taken to be insensitive to composition and electrostatic potential given that correlation free energies are not considered here. As a result, we take all polymer repeat units hereafter to be monovalent and fully ionized, i.e. $z_C = -z_A = 1$. Note that we have developed a free energy expression that includes charge regulation and electrostatic fluctuations, which could be used in our general framework, see chapter 3, but to keep the equations from becoming overly complex, we here leave out these free energy terms. They could be included, however, in future work. The electrostatic potential in eqn. (5-38) is made non-dimensional according to $\tilde{\Phi} \equiv \frac{e_o \Phi}{k_B T}$ where e_o denotes the elementary charge. Note that we have used the number concentration of the salt ions, rather than their volume fractions, as they do not occupy any volume. We have also defined the Bjerrum length, $\ell_B \equiv \frac{e_o^2}{4\pi\varepsilon k_B T}$ which quantifies the relative importance of electrostatic and thermal energies.

The non-local (gradient) free energy F_{Gr} penalizes concentration non-homogeneities and leads to smoothly varying composition profiles across interfaces. The non-local free energy is proportional to the sum of the square gradients weighted by their respective stiffness coefficients $\kappa_{ij} = \kappa_{ji}$.

$$\tilde{f}_{Gr} \equiv \frac{l^3 F_{Gr}}{V k_B T} = \frac{1}{2} \sum_{i=A,C} \sum_{j=A,C} \kappa_{ij} \left| \nabla_z \phi_i \cdot \nabla_z \phi_j \right| \tag{5-39}$$

The square gradient terms for non-polymeric components are not considered here. The normalized mean-field free energy is thus given by $\tilde{f}_{MF} = \tilde{f}_{FH} + \tilde{f}_{elec} + \tilde{f}_{Gr}$. Minimization of R with respect to electrostatic potential in eqn. (5-5) can now be carried out leading to the Poisson equation as below.

$$\frac{\delta R}{\delta \tilde{\Phi}} = \left(\frac{\partial \tilde{f}_{elec}}{\partial \tilde{\Phi}} \right) - \nabla_z \left(\frac{\partial \tilde{f}_{elec}}{\partial \nabla_z \tilde{\Phi}} \right) = 0$$

$$\Rightarrow \nabla_z \left(\varepsilon \nabla_z \tilde{\Phi} \right) = - \frac{e_o^2}{k_B T l^3} \left(C_+ l^3 - C_- l^3 + \sum_{i=A,C} z_i \phi_i \right) \tag{5-40}$$

The electrochemical potential ψ_i can be evaluated by taking the variational derivative of the free energy functional with respect to component volume fractions.

$$\tilde{\psi}_i \equiv \frac{\psi_i l^3}{k_B T} = \frac{l^3}{k_B T} \left(\frac{\delta F}{\delta \phi_i} \right) = \tilde{\mu}_i + z_i \tilde{\Phi} \tag{5-41}$$

The dimensionless chemical potential $\tilde{\mu}_i \equiv \frac{\mu_i l^3}{k_B T}$ encompasses all contributions to free energy except the electrostatic potential and is evaluated as following.

$$\tilde{\mu}_i = \left(\frac{\partial \tilde{f}_{FH}}{\partial \phi_i} \right) - \nabla_z \left(\frac{\partial \tilde{f}_{Gr}}{\partial \nabla_z \phi_i} \right) \tag{5-42}$$

The electrochemical potentials in the overall force balance eqn. (5-36) can be replaced with eqn. (5-41) resulting in the nondimensionalized form given below where $\tilde{\sigma} \equiv \frac{\sigma l^3}{k_B T}$.

$$\phi_C \nabla_z \tilde{\psi}_{CW} + \phi_A \nabla_z \tilde{\psi}_{AW} = \nabla_z \tilde{\sigma} \tag{5-43}$$

Enforcing the rapid equilibration of simple salt ions by setting the variation of the free energy functional with respect to their concentration to zero, eqn. resulting in (5-32), yields the Boltzmann concentration distribution as demonstrated below, given that the volumes of simple

salt ions are taken to be negligible and the only contribution of simple salts to free energy is through their translational entropy and electrostatic energy.

$$0 = \nabla_z \tilde{\psi}_{\pm} = \nabla_z \left(\frac{\delta F}{\delta C_{\pm}}\right) = \nabla_z \left(\tilde{\mu}_{\pm} \pm \tilde{\Phi}\right) = \nabla_z \left(ln\, C_{\pm} l^3 + 1 \pm \tilde{\Phi}\right) \Rightarrow C_{\pm} = C_{\pm}^{\infty} e^{\mp \tilde{\Phi}} \tag{5-44}$$

In the last equation, we have introduced the bulk salt concentrations, i.e. infinitely far from the film, $C_{\pm}^{\infty}$ where we take the reference electrostatic potential Φ^{∞} to be zero. We can recast eqn. (5-43) by introducing the osmotic pressure tensor defined as below.

$$\boldsymbol{\Pi} \equiv \phi_A \left(\frac{\delta F}{\delta \phi_A}\right)_{\Phi,\, \phi_W} + \phi_C \left(\frac{\delta F}{\delta \phi_C}\right)_{\Phi,\, \phi_W} + C_{\pm} \left(\frac{\delta F}{\delta C_{\pm}}\right)_{\Phi,\, \phi_W} - f \tag{5-45}$$

Due to the linear dependence of mean-field electrostatic free energy f_{ele} on composition, eqn. (5-38), Φ does not contribute to the osmotic pressure and thus the variational derivatives can be replaced with exchange chemical potentials for the two polyions, $\mu_{AW} \equiv (\mu_A - \mu_W), \mu_{CW} \equiv (\mu_C - \mu_W)$ and the regular chemical potentials for simple point-like ions, $\mu_{\pm}$. Additionally, $f = f_{MF}$ is the only contribution to the free energy density in the absence of correlation terms. Due to the one-dimensional nature of our model, we only consider the zz-component of the osmotic pressure tensor in the non-dimensional form $\tilde{\Pi} = \frac{\Pi_{zz} l^3}{k_B T}$. In this case, taking the divergence of the osmotic pressure tensor simplifies to taking the gradient of $\tilde{\Pi}$, which allows us to convert eq. (5-45) to the following expression in the non-dimensional form where we have used the non-dimensional chemical potentials defined earlier.

$$\nabla_z \tilde{\Pi} = \phi_A \nabla_z \tilde{\mu}_{AW} + \phi_C \nabla_z \tilde{\mu}_{CW} + C_{\pm} l^3 \nabla_z \tilde{\mu}_{\pm} \tag{5-46}$$

In the above, we have used the Gibbs-Duhem relation given by eqn. (5-47) to obtain eqn. (5-46) by substituting for the volume fraction of the water using the incompressibility constraint.

$$\nabla_z f = \sum_{i=A,C,W} \mu_i \nabla_z \phi_i + \mu_{\pm} \nabla_z C_{\pm} = (\mu_A - \mu_W) \nabla_z \phi_A + (\mu_C - \mu_W) \nabla_z \phi_C + \mu_{\pm} \nabla_z C_{\pm} \tag{5-47}$$

We can now substitute for the chemical potentials gradients into eqn. (5-47) with their electrochemical counterparts using eqn. (5-41) and the Boltzmann distribution of simple ions, eqn. (5-44) where $\nabla_z \tilde{\mu}_{\pm} = \mp \nabla_z \tilde{\Phi}$.

$$\nabla_z \tilde{\Pi} + (C_{\pm} l^3 - \phi_A + \phi_C) \nabla_z \tilde{\Phi} = \phi_A \nabla_z \tilde{\psi}_{AW} + \phi_C \nabla_z \tilde{\psi}_{CW} \tag{5-48}$$

The right-hand-side of eqn. (5-48) can now be eliminated using the overall force balance eqn. (5-43).

$$\nabla_z \widetilde{\Pi} + (C_{\pm} l^3 - \phi_A + \phi_C)\nabla_z \widetilde{\Phi} = \nabla_z \tilde{\sigma} \tag{5-49}$$

We can further simplify the result by substituting out the terms in the brackets in eqn. (5-49) using the Poisson equation (5-40) as following.

$$\Rightarrow \nabla_z \widetilde{\Pi} - \frac{k_B T l^3}{e_o^2} \nabla_z \left(\varepsilon \nabla_z \widetilde{\Phi}\right) \nabla_z \widetilde{\Phi} - \nabla_z \tilde{\sigma} = 0 \tag{5-50}$$

A further simplification is possible if ε is taken to be constant, implying that the Bjerrum length ℓ_B is also constant throughout in which case eqn. (5-50) can be recast in a form that is readily integrated to yield the following.

$$\nabla_z \widetilde{\Pi} - \left(\frac{4\pi l^3}{\ell_B}\right) \nabla_z^2 \widetilde{\Phi}\, \nabla_z \widetilde{\Phi} - \nabla_z \tilde{\sigma} \Rightarrow \nabla_z \left(\widetilde{\Pi} - \tilde{\sigma}_E - \tilde{\sigma}\right) = 0 \Rightarrow \widetilde{\Pi} - \tilde{\sigma}_E - \tilde{\sigma} = \widetilde{\Pi}^{\infty} \tag{5-51}$$

Here, there appears the non-dimensional zz-component of the Maxwell electrostatic stress given by $\tilde{\sigma}_E = \frac{l^3}{8\pi \ell_B} \left(\nabla_z \widetilde{\Phi}\right)^2$. The last equation follows from the overall force balance, eqn. (5-43) and is one that is easily recognizable in the context of swelling of hydrogels with buffer, with the exception that the electrostatic stresses at the interfaces is insignificant at a macroscopic level. However, we need to retain $\tilde{\sigma}_E$ in eqn. (5-51) owing to the presence of sharp interfaces between the film and the solution and at the substrate. Throughout the system, the difference between the local osmotic pressure and the bulk $\widetilde{\Pi}^{\infty}$ is given by the sum of the Maxwell electrostatic and elastic stresses. Our one-dimensional model, eqn. (5-51) could be easily extended to multi-dimensional problems, for example involving solvent imbibition, in which case the zz-components on the left-hand-side can be replaced by their full tonsorial form with the right-hand-side of eqn. (5-51) multiplying the identity tensor.

5.3 Results and Discussion

5.3.1 Equilibrium Predictions

Water and simple salt always adopt the equilibrium distribution as discussed in section 5.2. Additionally, despite the dynamic nature of LbL assembly arising from slow mutual chain diffusion, an equilibrium distribution of polyions is often achieved in early stages between the deposited film, whose thickness does not exceed a few radii of the incoming chain, and the

solution with which it is brought into contact in a well-stirred solution. Polyelectrolyte films are highly responsive to external stimuli such as changes in the bulk pH or salinity due to the redistribution of water and salt ions. In fact, every deposition step is typically accompanied by a change in bulk salinity and occasionally the pH, causing an instantaneous film shrinkage/swelling that precedes the diffusion of the polyions in and out of the film. In the next two sections, we focus on equilibrium prediction of the proposed model for two cases, namely equilibrium adsorption and instantaneous swelling. We further demonstrate the limits in which the present model reduces to the sequential adsorption SCFT model of Wang.[12]

5.3.1.1 Chain Adsorption

In this section, we demonstrate that our dynamic model is capable of predicting equilibrium adsorption of polyelectrolytes onto a flat solid surface, which has been extensively studied using SCFT.[14,15] Additionally, we show that the proposed model in the equilibrium limit using appropriate parameters reduces to the sequential equilibrium model of LbL discussed earlier.[12] In the very first step of LbL assembly, polyions from the solution adsorb onto the bare oppositely charged substrate. Due to the absence of the oppositely charged polymer in the very first step and presence of adsorbing chains in close proximity of the substrate, equilibrium is achieved within the duration of a typical deposition step. Instantaneous chain adsorption is not limited to the first step. In the subsequent deposition steps, incoming polyions are assumed to equilibrate instantly in the well-stirred solution all the way up to and possibly including the solution-film interface prior to their gradual diffusion into the film. Under favorable conditions, equilibrium adsorption leads to overcompensation of bound surface charges, which is argued to be a crucial feature of stable LbL assembly.

We here consider equilibrium adsorption of fully charged monovalent polyanion chains from a solution of bulk concentration C_A^∞ (corresponding to a volume fraction ϕ_A^∞) and a bulk salt concentration of $C_\pm^\infty$ onto a positively charged surface of known surface charge density q_S. Note that the following analysis is also valid for adsorption of polycations onto a negatively charged substrate except for the obvious sign reversal. In the absence of polycations in the solution, the overall force balance at equilibrium reduces to the following form:

$$d_A = 0 \longrightarrow \phi_A \nabla_z \tilde{\psi}_{AW} = \nabla_z \tilde{\sigma} \longrightarrow \tilde{\psi}_{AW} = \tilde{\psi}_{AW}^\infty \tag{5-52}$$

Here, we have set mechanical stress to zero, $\sigma = 0$, since chains adsorb in a relaxed state. The force balance therefore implies the uniformity of the electrochemical potential of polyanions in this case. Replacing the electrochemical potentials with regular chemical and electrostatic potentials from eqn. (5-41) and deriving the mean-field chemical potential according to eqn. (5-42), eqn. (5-52) is recast as follows.

$$-\kappa_{AA}\nabla_z^2\phi_A + \frac{1}{N_A}ln(\phi_A/\phi_A^\infty) - ln(\phi_W/\phi_W^\infty) + 2\chi_{AW}(\phi_A^\infty - \phi_A) - \tilde{\Phi} = 0 \tag{5-53}$$

Note that we have treated κ_{AA} as a constant in eqn. (5-53). The boundary conditions in the far field, $z \to \infty$ $\phi_A = \phi_A^\infty$ and $\tilde{\Phi} = 0$ have already been imposed. We have also used the incompressibility, $\phi_W + \phi_A = 1$ to simplify the last equation. Assuming a constant dielectric constant, the Poisson equation can be rewritten in the following non-dimensional form.

$$l^2\nabla_z^2\tilde{\Phi} = 4\pi\left({\ell_B}/{l}\right)\left[\,2C_\pm^\infty l^3 sinh\left(\tilde{\Phi}\right) - C_A^\infty l^3 e^{-\tilde{\Phi}} + \phi_A - C_P l^3\right] \tag{5-54}$$

Here, $C_P(z > 0)$ includes the net bound charge concentration of previously deposited polyions, and $C_P = 0$ for the deposition of the very first layer. The boundary conditions at the substrate $z = 0$ are given below.

$$\nabla_z\Phi = -\frac{q_S}{\varepsilon} \longrightarrow \nabla_z\tilde{\Phi} = -q^S\left(\frac{4\pi\ell_B}{e_o}\right) \equiv -E_S \tag{5-55}$$

$$\nabla_z\phi_A = r_A^{-1} \tag{5-56}$$

Here E_S defined in eqn. (5-55) is proportional to areal substrate charge density q_S where e_o is the elementary charge as usual. E_S = 1 nm^{-1} in water at 300 K corresponds to $q_S \sim 0.018$ Cm^{-2}. In eqn. (5-56), r_A is the characteristic length scale for decay of all non-electrostatic interactions of the chain type (A) and the substrate and is widely used as a boundary condition in SCFT models. For the so-called indifferent substrate, $r_A = \infty$ (assumed to be the case hereafter), while negative (positive) values indicate attractive (repulsive) non-electrostatic forces. A cutoff value of $z = L^\infty$ was chosen such that the $|\Phi|_{z=L^\infty} < 10^{-10}$ corresponding to approximately zero electrostatic field at $z = L^\infty$. The computational domain along the z direction is discretized with a non-uniform grid with a fine mesh close to the substrate with a minimum grid size of $\Delta z \sim \frac{l}{60}$ nm that ensures that the results in Figure 5-1 are insensitive to further grid refinement. We used an error relaxation

method based on a damped Newton-Raphson method for solving the nonlinear discretized eqns. (5-53) and (5-54) subject to boundary conditions (5-55) and (5-56) and far-field conditions.

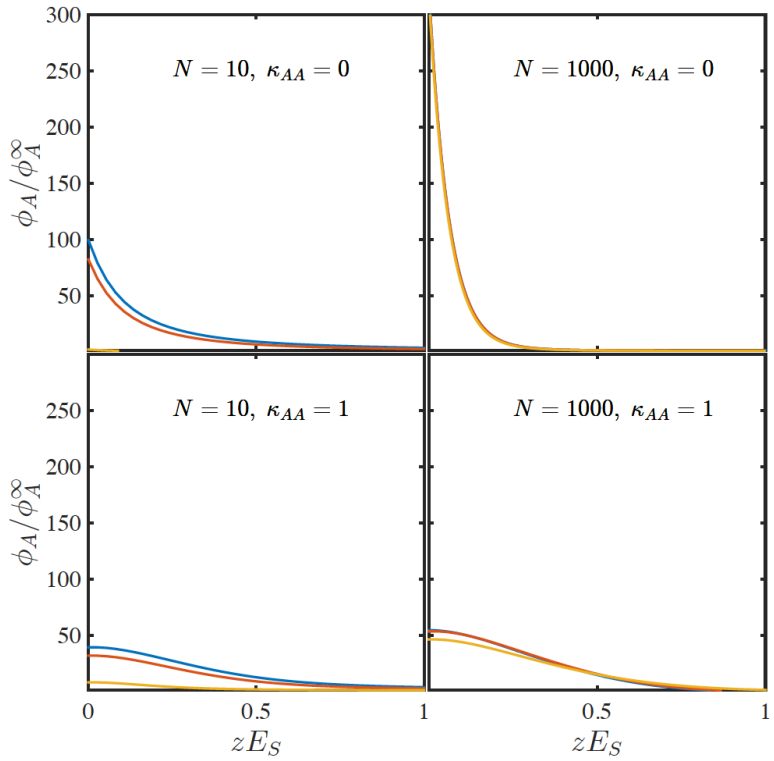

Figure 5-1: Normalized polyanion composition profiles on a positively charged substrate as a function of normalized position at bulk salinities $C_{\pm}^{\infty} = 10,\ 100,\ 1000$ mM represented by the blue, red and yellow curves, respectively, for two different polymerization indices N and stiffness coefficients κ_{AA}. In the upper right panel all three curves coincide.

Figure 5-1 depicts representative polymer segment density profiles normalized by ϕ_A^{∞} for three salt concentrations. Regardless of salinity, higher molecular weight chains adsorb more readily due to their lower translational entropy thus allowing for small counterions that would otherwise congregate in the double layer to be released into the bulk, and thereby pay a substantially lower entropic penalty than would be the case in the absence of polymer adsorption. Both with and without non-local terms, chain adsorption increases with the degree of polymerization N. For $\kappa_{AA} \neq 0$, the non-local term $-\kappa_{AA}\nabla_z^2\phi_A$ in eqn. (5-53) penalizes the non-uniform polymer composition profiles, and accordingly, the chain adsorption for the same N decreases substantially for $\kappa_{AA} = 1$ relative to that for $\kappa_{AA} = 0$. The adsorption of oppositely charged chains is accompanied by a reduction in the magnitude of the electrostatic potential field established by the surface charge relative to that in the vicinity of the substrate in a polymer-free solution.

Accordingly, the higher the chain adsorption, the lower the corresponding magnitude of the electrostatic potential at any given location, see Figure 5-2.

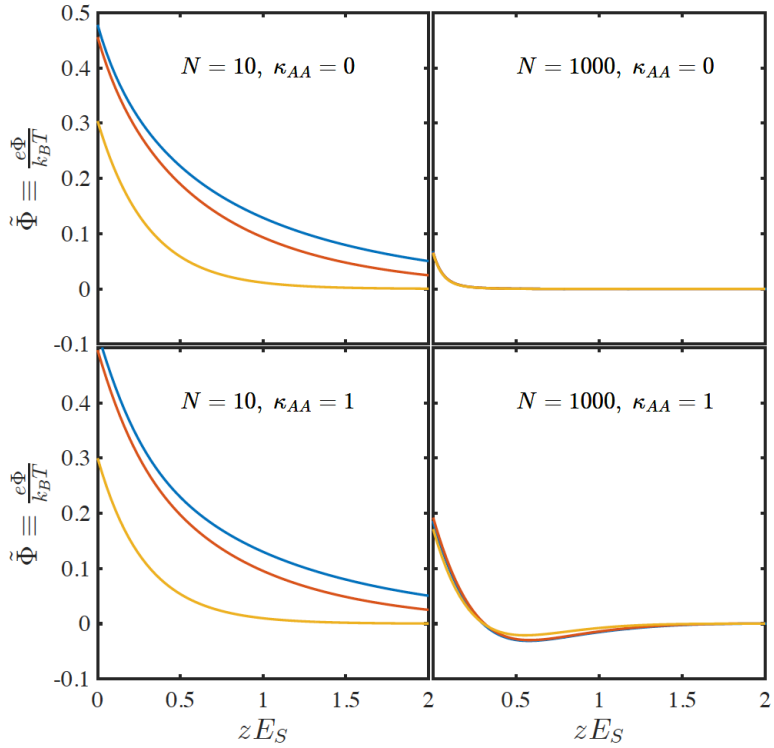

Figure 5-2: Spatial variation of the electrostatic potential corresponding to composition profiles in Figure 5-1.

A strongly bound base layer as well as sufficient ion pairing between polyions in the film generates and at least partially maintains the network elastic stress upon water and salt imbibition and is thus a prerequisite of a stable film growth. Otherwise, equilibration at early stages leads to a partial or complete dissolution of the film for instance at high salinity; see chapter 2. If the film thickness growth is slow enough over the first few deposition steps such that the film thickness does not exceed a few radii of gyration of the incoming chains, absorption of oppositely charged polyions proceeds to near equilibrium due to the short diffusion path of incoming chains through the film, contingent on the adequate stability of the film during this process.

If κ_{AA} is set to $\frac{l^2}{12\phi_A}$, which is valid for binary polymer-solvent systems and is also derived from a random phase approximation (RPA)[26] for $\phi_A \ll 1$ in the large wave vector limit, we recover the self-consistent-field theory (SCFT) result of Wang[12] in the ground state dominance limit for deposition of the first (base) layer at equilibrium. Now if the base layer is frozen so that its composition profile is not allowed to change when oppositely charged polymer invades, the

overall force balance eqn. (5-51) becomes redundant. If we then solve eqns. (5-53)* through (5-56) and thereby set the stress $\sigma = 0$ for each subsequent deposition step at equilibrium and include the bound charges arising from the previously deposited base layer as a frozen charge distribution in the Poisson equation, we can recover the sequential equilibrium adsorption model of LbL assembly, discussed earlier.[12]

5.3.1.2 Swelling

Equilibrium swelling of macroscopic ionizable gels where non-local and interfacial effects are absent is well established.[27] However, the interfacial and non-local effects cannot generally be ignored in thin LbL films. Nonetheless, the LbL models to date do not consider the film swelling/deswelling process. Here, we demonstrate that our dynamic framework in the equilibrium limit can capture the swelling/deswelling of ultra-thin films with interfacial effects.

In this section, we consider a case study of the first bilayer deposited in a typical LbL experiment adjacent to a substrate to demonstrate the equilibrium predictions of our model when there is a sudden change of the solution with which the multilayer is in contact, for instance when a rinsing step in pure buffer follows a step of dipping in a polyion solution. Despite the fact that the chains adsorb in the stress-free state, it is imperative that the chain segments of the base layer form practically irreversible bonds to the substrate, relative to the time scale of the subsequent chain deposition. If they do not, film growth is thwarted, as equilibration with buffer during the rinsing step would wash the film entirely off the substrate. Accordingly, here, the first layer is taken to behave as an elastic polymer adsorbed layer, the modulus of which is set by the areal number density of such bonds of polymer to the substrate. In this section, to demonstrate the applicability of our equilibrium predictions of our model. we consider an initially dry bilayer of arbitrary and non-uniform composition, see dotted lines in Figures 5-3A and 5-4A, that swell instantaneously in pure buffer.

We have thus far not considered the network stress in our analyses, since holding fixed the chain compositions of previously adsorbed polymer layers renders the tracking of network stress unnecessary. When swelling is allowed, however, the equilibrium conditions in our model need

* The first term in eqn. (5-53) should be replaced with $-\frac{l^2\nabla_z^2\sqrt{\phi_C}}{6\sqrt{\phi_C}}$ if $\kappa_{AA} = \frac{l^2}{6\phi_A}$ is used in deriving the chemical potentials according to eqn. (5-42).

to be imposed by solving the overall force balance eqn. (5-51) along with the Poisson equations. For simplicity, we choose an initial coordinate z_i corresponding to the bilayer prior to swelling, and another final coordinate after swelling, z_f, with the transformation between the two, $\lambda(z_i)$, which also denotes the local stretch ratio:

$$\frac{dz_f}{dz_i} \equiv \lambda(z_i) = \frac{\phi_A^i}{\phi_A^f} = \frac{\phi_C^i}{\phi_C^f} = \frac{\phi_A^i+\phi_C^i}{\phi_A^f+\phi_C^f} \tag{5-57}$$

Here 'i' and 'f' denote the initial (reference) state and final (equilibrium) state, respectively. An elastic response implies that both chain types are stretched to the same extent and there is no relative motion between them, as would be expected if the ion pairing interactions remain intact during swelling. Mutual diffusion of one polymer with respect to the other commences immediately after the initial equilibration with buffer and is driven by the sudden change in the buffer. The Poisson equation in the final state is now recast into the reference coordinate system as below.

$$l^2\nabla_{z_f}^2\tilde{\Phi} = \lambda(z_i)^{-2}\, l^2\nabla_{z_i}^2\tilde{\Phi} = 4\pi\left({}^{\ell_B}/_{l}\right)\left[\, 2C_{\pm}^{\infty} l^3 sinh\left(\tilde{\Phi}\right) + \lambda(z_i)^{-2}\left(\phi_A^i - \phi_C^i\right)\right] \tag{5-58}$$

The Poisson equation needs to be coupled with the overall force balance equation (5-51). Therefore, we need an expression for the bilayer modulus, which is proportional to the number density of elastic strands that is in turn proportional to the density of network junction points. In the first bilayer, polyanions are anchored to both the substrate and to the polycation chains via ion pairs. While the density of ion-pairs decreases upon swelling due to dilution of strands, the number of anchor points on the substrate is assumed here to remain unaffected by solvent ingress. We can thus take the dimensionless bilayer modulus $\tilde{G}$ to be the sum of two contributions.

$$\frac{Gl^3}{k_BT} \equiv \tilde{G} = \tilde{G}^o + \tilde{G}_{ip}^o \phi_A^f \phi_C^f \tag{5-59}$$

where G^o and G_{ip}^o have in the above been rendered dimensionless in the same way as G itself. The former contribution, G^o, is proportional to the areal density of anchor points on the substrate while the latter, $\tilde{G}_{ip}^o$, is a prefactor that is proportional to the equilibrium constant of an ion pairing reaction. The network stress σ is obtained by setting the relaxation time in the constitutive equation (5-29) to infinity in the elastic limit and substituting the modulus with the

proposed expression, eqn. (5-59). The result derived in the appendix 5.4 is given below in the non-dimensional form.

$$\tilde{\sigma} = 2\tilde{G}^{o}(\lambda - 1) + \frac{2}{3}\tilde{G}^{o}_{ip}(\lambda - \lambda^{-2}) \tag{5-60}$$

The mean-field osmotic pressure $\tilde{\Pi} = \tilde{\Pi}^{\mathrm{FH}} - \tilde{\Pi}^{\mathrm{Gr}}$ is the sum of a FH contribution, eqn. (5-61a), and one originating from non-local terms in $\tilde{f}_{Gr}$ given by eqn. (5-61b),

$$\tilde{\Pi}^{\mathrm{FH}} = -ln(1-\phi_A-\phi_C) - \phi_A - \phi_C + \left(\frac{\phi_C}{N_C} + \frac{\phi_A}{N_A} + C_{+}l^3 + C_{-}l^3\right) - (\chi_{AW}\phi_A + \chi_{CW}\phi_C) + \chi_{CW}\phi_C\phi_A \tag{5-61a}$$

$$\tilde{\Pi}^{\mathrm{Gr}} = \kappa_{CC}\left(\phi_C\nabla_z^2\phi_C - \frac{1}{2}(\nabla_z\phi_C)^2\right) + \kappa_{AA}\left(\phi_A\nabla_z^2\phi_A - \frac{1}{2}(\nabla_z\phi_A)^2\right) + \kappa_{AC}(\phi_C\nabla_z^2\phi_A + \phi_A\nabla_z^2\phi_C - \nabla_z\phi_C\nabla_z\phi_A) \tag{5-61b}$$

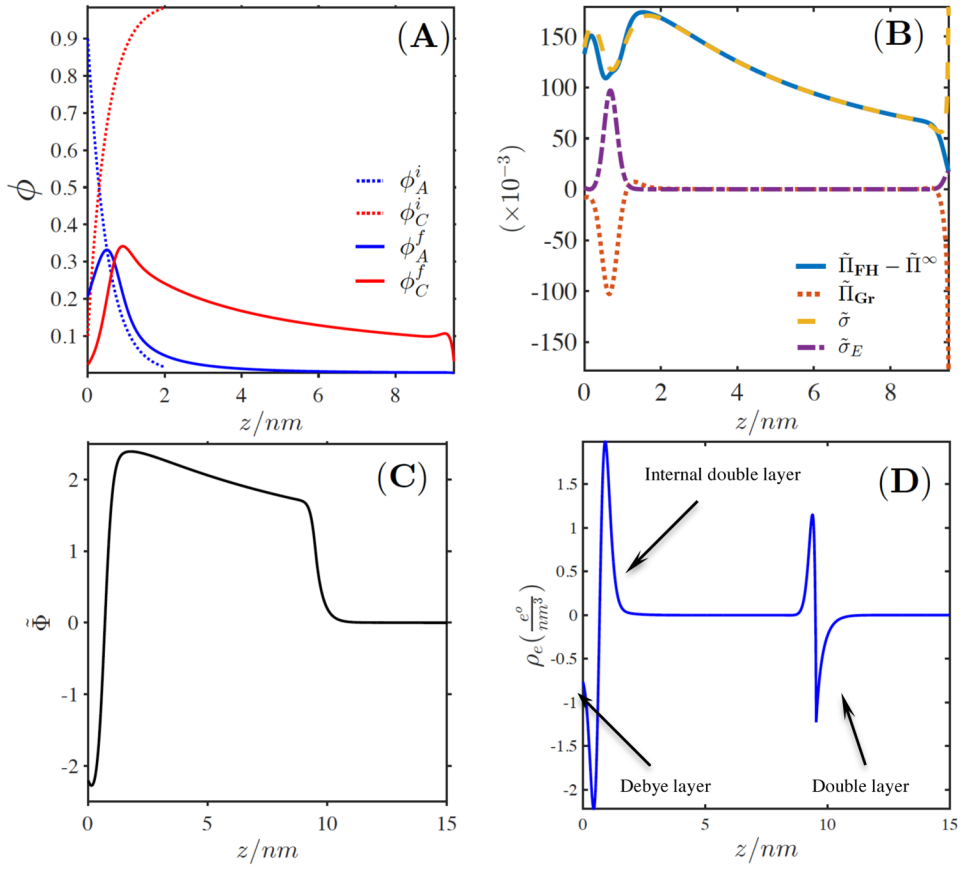

Figure 5-3: Equilibrium response of a dry bilayer composed of two strongly and fully charged polyions with an arbitrarily chosen structure after exposure to a buffer solution of $C_{\pm}^{\infty}$ = 1M. (A) Volume fraction profiles with dotted and solid curves representing initial and final states (B) non-dimensional osmotic pressure, elastic and electrostatic stress distributions in the final state at equilibrium(C) non-dimensional electrostatic potential in the final state at equilibrium, and (D) total charge density, including those of counterions). $\kappa_{CC} = \kappa_{AA}$ = 0.1 (nm^2). Other simulation parameters are listed in Table 5-1.

Table 5-1: Common numerical parameters used in both figures 5-3 and 5-4.

$N_A = N_C$	κ_{AC}	$\chi_{CW} = \chi_{AW}$	χ_{CA}	E_S	ℓ_B	T	G^o	G^o_{ip}
1000	0	0.5	-0.5	+1 nm^{-1}	0.71 nm	300 K	5000 Pa	10^8 Pa

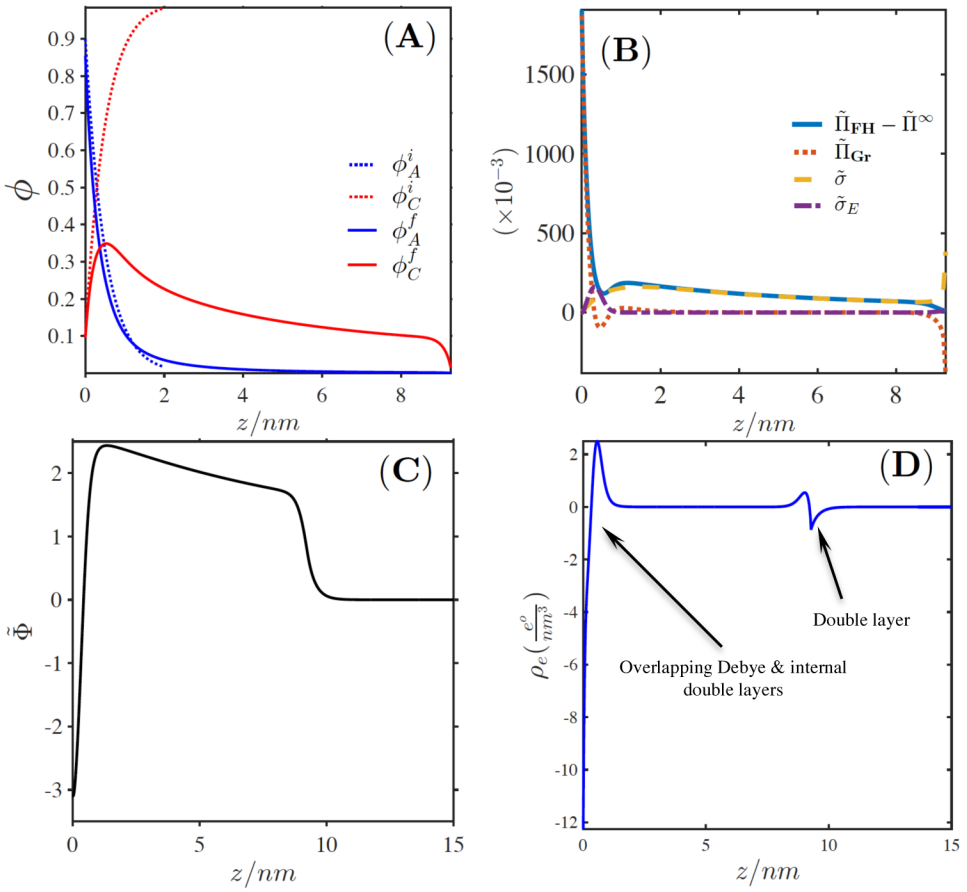

Figure 5-4: Same as Figure 5-3 but with $\kappa_{CC} = \kappa_{AA} = 1.0$ (nm^2). Other simulation parameters are identical to those used in Figure 5-3 and listed in Table 5-1.

The first term on the right side of eqn. (5-60) is the contribution of fixed anchor points of the adsorbed polyanion layer to the substrate. This contribution, without which the film will be washed off, would, in a more realistic model, be replaced by applying a boundary condition on polyanion composition such as eqn. (5-56) and solving eqn. (5-51), including the gradient free energy terms subject to the requirement that the total mass of the layer should be conserved in swelling. The gradient terms accounts more rigorously for chain connectivity, and keeps the adsorbed polymer concentration from dropping discontinuously from a finite surface concentration to zero in the nearby bulk. However, this approach would be numerically challenging and thus for simplicity we capture the anchoring of polyanion onto solid substrate and chain connectivity during swelling by using a constant, uniform, modulus G^o. This simple

approach accounts for the elastic resistance to swelling of adsorbed chains that are anchored to the substrate, preventing their arbitrary swelling, even when they are not in a network with oppositely charged polymers. In Figure 5-3A and 5-4A, the equilibrium structure, i.e. the final state denoted by (*f*), as well as the initial dry state denoted by (*i*) is depicted for two sets of stiffness parameters. The final state is a complicated balance of different forces in the bilayer, namely osmotic pressure, electrostatic and elastic stresses, the distribution of each of which is plotted in 5-3B and 5-4B. As expected, higher stiffness parameter used in Figure 5-4 penalizes sharp variations in curvature of composition profiles and results in a smoother profile in Figure 5-4A compared with that 5-3A. This is also evident in the magnitude of non-dimensional non-local osmotic pressure $\widetilde{\Pi}_{\mathrm{Gr}}$ in the vicinity of the substrate; see Figures 5-3B and 5-4B at $z\rightarrow 0$.

Chain stiffness is characterized by κ_{CC} & κ_{AA} which are proportional to the square of the persistence length. As a result, the initially high concentration of the polyanion segments near the substrate does not drop quite as drastically in Figure 5-4A as it does in 5-3A. Correspondingly, the negative-valued electrostatic potential near the wall is higher in magnitude in Figure 5-4C than it is in 5-3C. As expected, the total charge density ρ_e stored near the substrate is significantly greater in Figure 5-4D than in 5-3D. However the sum of the total charge stored in the film and in the solution per unit area in Figure 5-4D is identical to that in 5-3D, and opposite in sign to that on the surface, regardless of chain distribution. Thus, the charge in the film and solution balances the areal surface charge density set by the $E_S/4\pi\ell_B \sim 0.112$ nm^{-2}. In the vicinity of the solid substrate (z~0) and of the interface between the film and solution ($z \sim 9$ nm), a "Debye layer" and a "double layer" storing electrical charge are established, respectively, as seen in both Figures 5-3D and 5-4D. Note that here we distinguish what we here call the "Debye layer" as the layer of fluid at the wall, whose charge density does not change sign, from the "double layer" which we here take to be that within the film, whose charge density does change sign. An internal double layer overlapping with the substrate Debye layer in Figures 5-3D and 5-4D emerges around $z \sim 1$ nm where a change of the sign of net charge arising from both polyions occurs, which is due to the structure of the initially dry bilayer that is selected here.

5.3.2 Dynamic Predictions

In this section, we consider transient processes that can be predicted by the general model developed earlier in section (5-2). Dynamics enter the model through two mechanisms; namely

1) the mutual diffusion between polyions governed by eqn. (5-35) and 2) network stress relaxation set by the effective relaxation time of the network, τ_{eff}. Substituting the mutual friction coefficient between two polyions ζ_{AC}, given by eqn. (5-7), into either eqn. (5-35a) or (5-35b) and recognizing $J_i \equiv \phi_i v_i$ as the z-component of the species volumetric flux vector, we arrive at the pseudo-binary flux law, eqn. (5-62), governing the polyion diffusion process.

$$\tilde{\zeta}_{AC}(v_C - v_A) = \frac{\phi_A \phi_C (v_C - v_A)}{D_{AC}} = -\phi_C \nabla_z \tilde{\psi}_{CW} + \alpha_C \nabla_z \tilde{\sigma} \equiv \tilde{d}_C \tag{5-62}$$

Here, we have introduced the non-dimensional diffusion driving force for polycation migration $\tilde{d}_C \equiv \frac{d_C l^3}{k_B T}$ and the dimensionless friction coefficient $\tilde{\zeta}_{AC} \equiv \frac{\zeta_{AC} l^3}{k_B T}$. Note that an equivalent and dependent diffusion equation for polyions could be written based on the polyanion diffusion driving force, given below.

$$\tilde{\zeta}_{CA}(v_A - v_C) = -\phi_A \nabla_z \tilde{\psi}_{AW} + \alpha_A \nabla_z \tilde{\sigma} \equiv \tilde{d}_A \tag{5-63}$$

Recalling that $\tilde{\zeta}_{CA} = \tilde{\zeta}_{AC}$ and that eqn. (5-36) implies that $\tilde{d}_C + \tilde{d}_A = 0$, it is readily verified that eqns. (5-62) and (5-63) are linearly dependent. Because small molecules and ions exert negligible friction on either polyion, the total force exerted on each polyion type is exactly counterbalanced by the force on the other. It should be noted that water and salt counterions are free to move only in response to the slow diffusion of polyions. Salt counterion distribution is set by the electrostatic potential distribution; see eqn. (5-44). The overall force balance equation (5-51), incompressibility and Poisson equations set the water distribution.

The flux law, either eqn. (5-62) or (5-63) coupled with Poisson eqn. (5-40), overall force balance, eqn. (5-51), the constitutive equation for elastic stress, eqn. (5-29), and the polyion conservation equations (5-3) provide the required framework for predicting two sequentially and cyclically occurring steps in LbL assembly, namely rinsing with buffer and dipping in polyion solution. The equations comprising the proposed LbL dynamic framework are summarized in Figure 5-5 for quick reference. The final outcome of this chapter is a nonlinear and intricately coupled set of equations. It needs to accommodate the two-phase nature of the LbL experiments where a diffuse interphase between film and solution exists through which polyions can cross into and out of the film. Far away from the film, the system is either devoid of (in case of rinsing step) or very dilute in (in case of dipping step) either polyion. Any polymer outside of the film is of one type and thus, outside of the film, mutual diffusion of two polyions for which eqn. (5-63)

was developed should be replaced by polymer diffusion in water. However, it is numerically challenging to solve a system of equation in which the type and number of equations that need to be solved at a given grid point is subject to change.

- Incompressibility, eqn. (5-30) $$\sum_{i=A,C,W} \phi_i = 1$$
- Mass conservation, eqn. (5-3) $$\frac{\partial \phi_i}{\partial t} = -\nabla_z(\phi_i \, v_i) \quad [\, i : A, C \,]$$
- Poisson Eqn. (5-54) $$\nabla_z^2 \tilde{\Phi} = -\frac{4\pi \ell_B}{l^3}\Big(\sum_{i=A,C} z_i \phi_i + 2\, C_{\pm}^{\infty} l^3 \, sinh\, \tilde{\Phi}\Big)$$
- Flux law, eqn. (5-62) $$\frac{\phi_A \phi_C (v_C - v_A)}{D_{AC}} = -\phi_C \nabla_z \, \tilde{\psi}_{CW} \; + \alpha_C \nabla_z \, \tilde{\sigma}$$
- Solvent Equilibration, eqn. (5-51) $$\tilde{\Pi} - \frac{l^3}{8\pi \ell_B} |\nabla \tilde{\Phi}|^2 - \tilde{\sigma} = \tilde{\Pi}^{\infty}$$
- Elastic stress, eqn. (5-29) $$\frac{D\tilde{\sigma}}{Dt} + \frac{\tilde{\sigma}}{\tau_{eff}} = (2\tilde{G} + \tilde{\sigma}) \, \nabla_z (\alpha_A v_A + \alpha_C v_C)$$
- Boundary conditions eqns. (5-55) & (5-56) $$@z = 0 \rightarrow \; \nabla_z \tilde{\Phi} = -E_S, \; v_C = \; v_A = 0, \; \nabla_z \phi_A = r_A^{-1}, \; \nabla_z \phi_C = r_C^{-1}$$ $$@z = \infty \rightarrow \; \nabla_z \tilde{\Phi} = 0 = \tilde{\Phi}, \; \phi_C = \phi_C^{\infty}, \; \phi_A = \phi_A^{\infty}, \; \nabla_z \phi_A = 0, \; \nabla_z \phi_A = 0$$

Figure 5-5: Summary of coupled system of equations governing LbL dynamics proposed here.

The rapid equilibration constraint on small ions and water significantly accelerates the simulation time by tracking only the slowest diffusion and relaxation process in the film, but it breaks down outside of the film, if one attempts to solve the same set of equations consistently over the whole domain $0 < z < \infty$, because of the absence of either polyion (rinsing step) or negligible mutual diffusion between the two (dipping step). During the dipping steps, the dilute concentrations used in the dipping solution bath and presence of only a single polyelectrolyte imply negligible ion pairing and vanishingly small relaxation time, so that solving the same equations over the whole domain would require a small time step that would significantly slow down the simulation. To avoid such difficulties, we therefore treat our model as a moving boundary problem wherein polyion conservation, the elastic stress constitutive equation as well as the flux law for polyion mutual diffusion are solved for only in the film, and are terminated by introducing a jump condition at the film-solution 'interface' while the Poisson equation and the overall force balance, eqn. (5-51) are still to be solved over the entire domain $0 < z < \infty$. While this method speeds the simulation, jump conditions in polymer composition across the interface pose numerical challenges, especially if the non-local terms in free energy are included.

In the next two subsections, two simplified test cases are presented that allow us to reduce the nonlinearity of our framework by freezing one of the polyions at the substrate and introducing a jump boundary condition on the mobile polyion composition during rinsing and dipping steps. Development of a rigorous and efficient numerical strategy for solving the model summarized in Figure 5 will be pursued in future work and we outline possible strategies to achieve this end in the closing chapter.

5.3.2.1 Rinsing Step

Consider a polyanion layer of uniform composition 0.5 (50% hydration level by volume) with a constant thickness *L* of 10 nm. We take this polyanion layer to be firmly tethered to the substrate and its compositional profile to be frozen in place at all times such that the corresponding volume fraction profile for the polyanion is imposed as below.

$$\phi_A(z,t) = 0.5\, Heaviside(10 - z) \Rightarrow v_A(z,t) = 0 \tag{5-64}$$

To this strongly and fully charged polyanion adsorbed layer, we equilibrate a solution with $C_{\pm}^{\infty}$ = 100mM and C_C^{∞}= 10 mM by monomer of strongly and fully charged polycations of three different polymerization indices; namely 10, 100, 1000. The equilibrium polycation volume fraction distribution inside the film just before the beginning of the rinsing with pure buffer of $C_{\pm}^{\infty}$ = 100mM in each case is used as the initial condition; see the top panels in Figure 5-6. We assume that the ion-pairs formed between polyions are so short-lived that polycations can move in a stress-free state, i.e., we take $\alpha_C \sim 0$ in eqn. (5-62) during the time scale in which they diffuse out of the polyanion adsorbed layer while that layer remains firmly anchored to the substrate. In this case, the overall force balance, eqn. (5-51) can be used to derive the local stress $\tilde{\sigma}$, which is now treated as response function. Since the velocity of polyanion is set to zero, the flux of polycation can now be derived explicitly from eqn. (5-62) and is given by eqn. (5-65).

$$J_C = -\frac{D_{AC}\phi_C}{\phi_A}\nabla_z\left(\tilde{\mu}_{CW} + z_C\tilde{\Phi}\right) \tag{5-65}$$

Here, the polycation volumetric flux J_C reduces to a simple pseudo-binary (Fickian) flux expression with a generalized driving force. Eqn. (5-65) is essentially similar to the flux expression derived by Hoda and Larson[2] except that they used the regular (not the exchange) chemical potential of the polycation μ_C. A notable difference between the model of Hoda and

Larson[2] and the present work is the absence in our work of any imposed electrostatic boundary condition in our model at the film-solution interface, i.e. $z = L$, which implies that the Poisson equation needs to be solved dynamically in conjunction with conservation eqn. (5-3) and the simplified polycation flux equation, eqn. (5-65), throughout the simulation and thus extending into the solution. (Hoda and Larson[2] did not consider the evolution of the electrostatic potential during a given LbL step.) We take the solution side to be well mixed and impose the boundary condition on polycation composition at the solution-film interface, given by eqn. (5-66).

$$\tilde{\psi}_{CW}(z = L, t) = \tilde{\mu}_{CW}(z = L, t) + z_C\tilde{\Phi}(z = L, t) = \mu_{CW}^{\infty} \tag{5-66}$$

Since the buffer solution during the rinsing step is devoid of polymer, eqn. (5-66) implies that $\phi_C(z \geq L, t) = 0$. The mutual diffusivity of entangled neutral polymers is long known to be inversely proportional to the molecular weight squared and we expect a similarly strong dependence for polyion mutual diffusivity in the film on molecular weight. However, here we use D_{AC} = 0.1 (nm^2/sec) independent of molecular weight to assess the role of molecular weight on polycation diffusion driving force alone and on the simplified diffusion outflux given by eqn. (5-65).

A conventional implicit finite difference scheme and error relaxation was used to discretize and solve the coupled set of equations in Figure 5-5 without the constitutive equation, eqn. (5-29), and overall force balance, eqn. (5-51). Given a polycation concentration at each grid point across the film at time step p, the discretized nonlinear equations were solved using a damped Newton-Raphson method for the polycation volume fractions in the film and electrostatic potential everywhere at the next time step. The far-field was cut off at L^{∞}chosen away from the solution-film interface such that $\left|\tilde{\Phi}\right|_{z=L^{\infty}} \leq 10^{-10}$ while imposing $\left|\nabla_z\tilde{\Phi}\right|_{z=L^{\infty}} = 0$ there. A constant time step $\Delta t \sim 10^{-2}$ (sec) was used. A spatial grid size $\Delta z \sim$ 0.01-0.05 nm in the vicinity of the substrate and around the film-solution interface was used while a $\Delta z \sim$ 0.25-0.5 nm otherwise. The obtained results were polycation and electrostatic potential evolution, plotted in Figure 5-6, and were insensitive to further mesh refinements.

Despite using a constant D_{AC} for all the molecular weights studied in Figure 5-6, a clear trend emerges. The higher molecular weight polycation chains diffuse more slowly due to a reduction in the diffusion driving force. In fact, the highest molecular weight studied in Figure 5-6, N_C = 1000 appears to be trapped kinetically inside the polyanion brush layer with 80% residual

polycation after 20 minutes while there remains only 20% residual short chains with N_C = 10 after the same time period. Had we used an appropriate scaling law for D_{AC}, this trend would have been even more pronounced. In the absence of non-local and VdW interaction, the only driving force for out-diffusion the polycation a chain is the translational entropy, which drops monotonically as N_C^{-1}. Note that the electrostatic field opposes the polycation out-diffusion. In fact, it becomes progressively harder for the polycation to leave the layer as the electrostatic potential just inside the film in the vicinity of the solution-film interfaces continues to become more negative as out-diffusion progresses, see bottom panels in Figure 5-6.

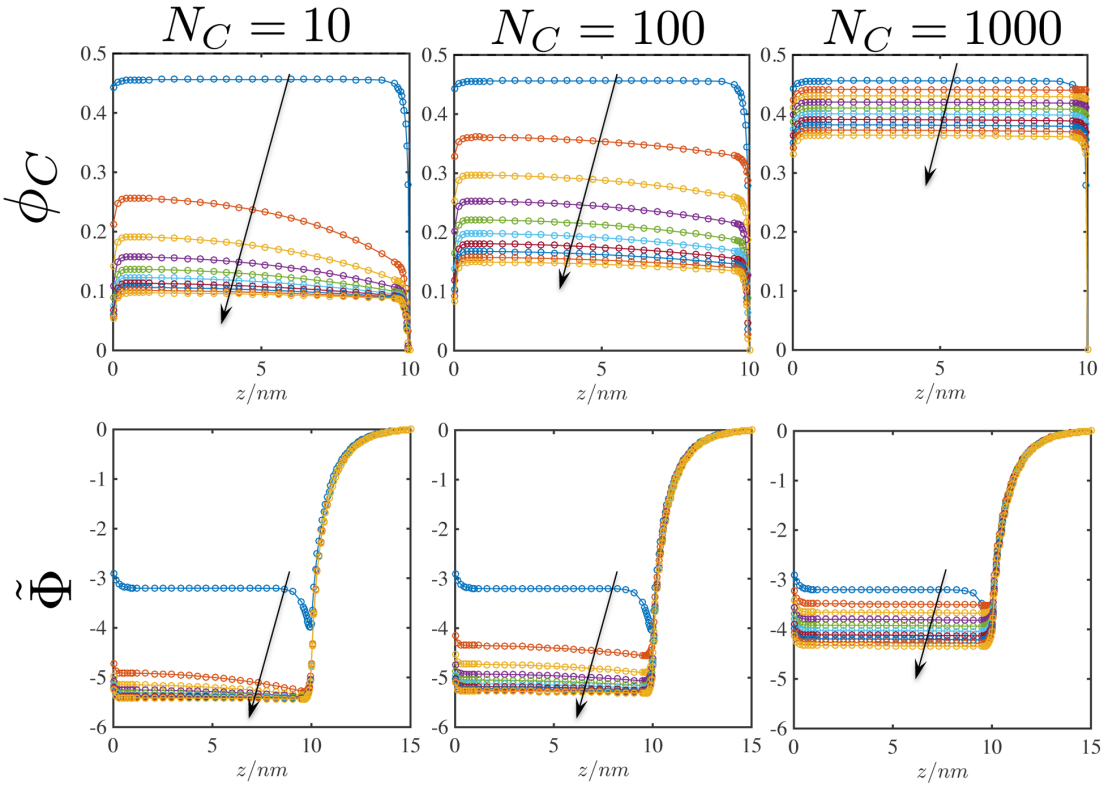

Figure 5-6: Effect of polycation polymerization index N_C on evolution of polycation volume fraction profile (top panels) and non-dimensional electrostatic potential (bottom panels) during rinsing of a rigid polyanion adsorbed layer with constant thickness L = 10 nm, uniform volume fraction 0.5 and initially saturated with polycation with pure salt solution of $C_{\pm}^{\infty}$ = 0.1M. In all simulations D_{AC} = 0.1 (nm^2/s), and E_S = 1 nm^{-1}. Total simulation time was 20 minutes. Profiles are plotted in equal 2-minute intervals starting from time zero. The arrows indicate increasing time. All FH χ parameters and stiffness coefficients in the non-local free energy density have been set to zero.

5.3.2.2 Dipping Step

In the previous section, we started with a brush layer pre-equilibrated with polycation chains absorbed from a polycation solution bath during a dipping step. In this section, we consider the

dynamics of chain absorption for N_C = 100 using D_{AC} = 0.1 (nm^2/sec) into the same rigid polyanion adsorbed layer described by the composition profile given by eqn. (5-64).

A notable distinction in the simulations for a dipping step relative to those in the previous section concerns the structure of the solution side that needs to be resolved. To this end, we assume equilibrium everywhere on the solution side up to the interface, i.e., over the range $L \leq z \leq L^{\infty}$, and thus set the polycation diffusion driving force over this range to zero. In the absence of polycation stress, we again arrive at eqn. (5-66), derived in the previous section, but this time with a finite bulk polycation concentration in the far-field at L^{∞} and an unknown polycation concentration on the solution side at L.

$$\tilde{\psi}_{CW}(z \geq L, t) = \tilde{\mu}_{CW}(z \geq L, t) + z_C\tilde{\Phi}(z \geq L, t) = \mu_{CW}^{\infty} \tag{5-67}$$

Again, the Poisson equation is solved everywhere coupled to the simplified polycation flux law, eqn. (5-65), and the polycation conservation equation that are solved only inside the film, $0 < z < L$, while eqn. (5-67) is solved for $L \leq z < L^{\infty}$. This nonlinear set of equations is solved using a combination of implicit finite difference and damped Newton-Raphson methods as described in the previous section. The results are presented in Figure 5-7.

As a function of z, a sharp jump in the composition of polycations is observed at the film-solution interface at all times in Figure 5-7A. This results from the instantaneous rush of polycations from the solution instantly to the surface of the film, where an attractive negative electrostatic potential emanates from the polyanion adsorbed layer surface, see Figure 5-7B. The electrostatic potential grows slowly less negative over time as the brush layer takes up positively charged polycations and eventually reaches the equilibrium potential given by the green curve atop all other curves in Figure 5-7B. This green curve corresponds to the equilibrium polycation volume fraction profile of the same color atop the other curves in Figure 5-7A. The total electrostatic charge density including the salt counterions is plotted in Figure 5-7C. In addition to the Debye electrostatic layer near the substrate and a double layer at the film-solution interface, an internal double layer moves inwards towards the solid substrate until it merges with the Debye layer at z ~ 0 at equilibrium.

During a dipping step, the electrostatic potential favors the in-diffusion of polycations and therefore the adsorbed layer is saturated with polycation from the solution within about two minutes into the dipping step, see Figure 5-7D. In contrast, when the same adsorbed layer

saturated with polycation with N_C = 100 after dipping step is over is rinsed with a salt solution of identical salinity as that used during the dipping step, about 30% of the initial polycations remain inside the film after 20 minutes of rinsing, as shown by the composition profile panel corresponding to N_C = 100 in Figure 5-6. The faster completion of in-diffusion during the dipping step relative to the out-diffusion of polycations in the rinsing step, despite identical molecular weight and mutual diffusivity, is a direct consequence of the electrostatic potential created by the underlying polyanion adsorbed layer, which accelerates in-diffusion, but retards out-diffusion during rinsing and dipping steps.

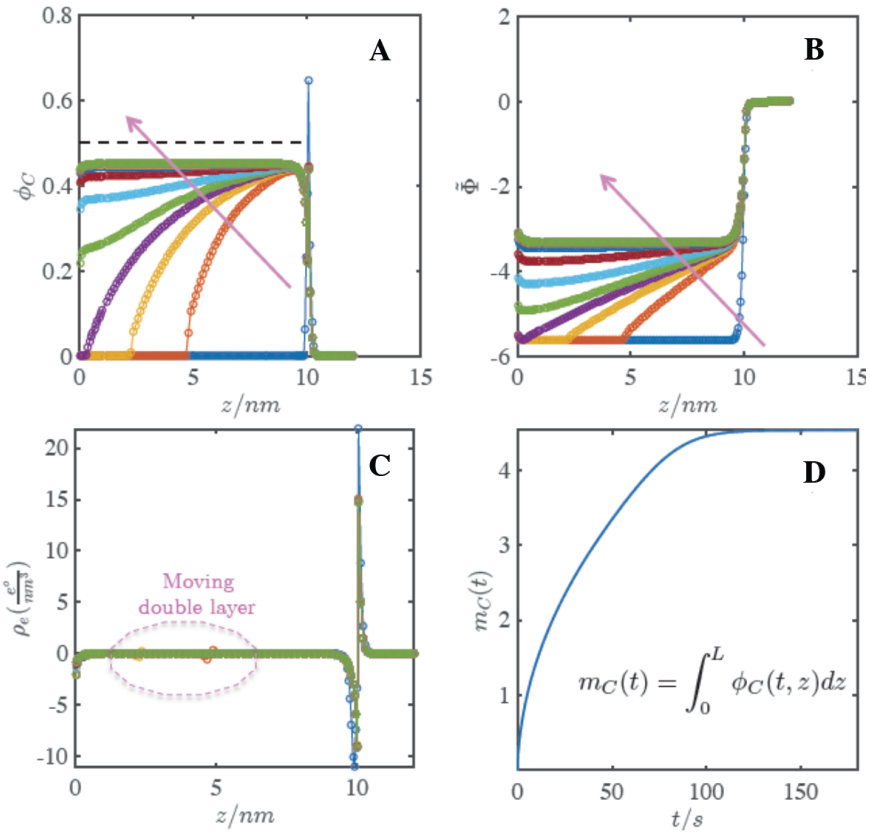

Figure 5-7: Evolution of (A) polycation composition profile, (B) non-dimensional electrostatic potential profile, and (C) total electrostatic charge density, inside a rigid polyanion adsorbed layer of fixed composition given by eqn. (5-65) during dipping step of a frozen polyanion layer, given by eqn. (5-64) and plotted as dashed black line in (A) in a solution of polycation chains with N_C = 100, 100 mM in salt and 10mM in polycation by monomer. (D) The total polycation content m_C (defined in the plot) absorbed by the layer as a function of time. In all simulations D_{AC} = 0.1 (nm^2/s), and E_S = 1 nm^{-1}. All FH χ parameters and stiffness coefficients in the non-local free energy density have been set to zero. The arrows in (A) and (B) indicate increasing time. The simulation continued for three minutes and profiles are plotted in equal 15-second intervals starting from time zero.

In the simulations presented in this section, the structure of the solution is resolved dynamically. The solution in the immediate vicinity of the film-solution interface is made up of roughly 70%

and 45% by volume polycations at the beginning and the end of the simulated dipping step, respectively; see Figure 5-7A. Just inside the film in the vicinity of the interface, polycation composition undergoes a sharp drop from the solution due to the sharp interface of the underlying polyanion adsorbed layer. The solution of Poisson equation coupled with the diffusion equation in our model allows for our predictions to converge to the true equilibrium structure during the dipping step. The framework developed here thus improves on the dynamic model of Hoda and Larson[2] by allowing for the transient evolution of electrostatic potential distribution consistent with polymer composition evolution both in the film and the solution.

5.4 Appendix

The response of the constitutive equation (5-29) in the elastic limit is obtained by setting the effective relaxation time $\tau_{eff} \to \infty$.

$$\frac{\partial \sigma}{\partial t} = (2G + \sigma)\nabla_z v_N \tag{5-A-1}$$

Using eqn. (4-21) derived in chapter 4, we can replace the gradient of network velocity in eqn. (5-A-1) by the local stretch ratio λ as below.

$$\nabla_z v^N = \frac{\partial ln\lambda}{\partial t} \tag{5-A-2}$$

Now introducing $\epsilon \equiv ln\lambda$, eqn. (5-A-1) can be rewritten in the following form where the time derivatives in (5-A-1) cancel out. As expected, time does not affect the elastic response and the elastic stress is solely as function of ϵ given by eqn. (5-A-3).

$$\frac{d\sigma}{d\epsilon} = (2G + \sigma) \to \frac{d\sigma}{d\epsilon} - \sigma = 2G \tag{5-A-3}$$

The modulus for a system of polyanions permanently anchored to a substrate and forming ion-pairs with polycation chains is taken to be of the form $G = G^o + G^o_{ip}\phi_A\phi_C$. A mixture of polyions is taken to be at rest in the initial state '^{o}' where $\epsilon = 0$. Expressing the volume fraction in terms of local stretch ratio can be done according to eqn. (5-58). Therefore, the modulus can now be expressed in terms of ϵ as below:

$$G = G^o + G^o_{ip}\phi^o_A\phi^o_C e^{-2\epsilon} \tag{5-A-4}$$

Plugging in eqn. (5-A-4) and solving the resultant ODE in terms of ϵ, we arrive at the following general solution.

$$\sigma = Ce^{-\epsilon} - 2G^o - \frac{2}{3}G^o_{ip}e^{-2\epsilon} \quad \text{(5-A-5)}$$

Applying the initial condition $\sigma(\epsilon = 0) = 0$, the integration constant *C* in eqn. (5-A-5) is obtained. The final result after some rearrangement is given by eqn. (5-A-6).

$$\sigma = 2G^o(e^{-\epsilon} - 1) + \frac{2}{3}G^o_{ip}(e^{-\epsilon} - e^{-2\epsilon}) \quad \text{(5-A-6)}$$

Replacing $\epsilon \equiv ln\lambda$ and multiplying through by $\frac{l^3}{k_BT}$, we arrive at eqn. (5-60).

5.5 References

[1] Lavalle, Ph.; Picart, C.; Mutterer, J.; Gergely, C.; Reiss, H.; Voegel, J.C.; Senger, B.; Schaaf, P. *J. Phys. Chem. B* **2004**, 108, 635-648.

[2] Hoda, N.; Larson, R.G. *J. Phys. Chem. B*. **2009**, 113, 4233-4241.

[3] Haynie, D.T.; Cho, E.; Waduge, P. *Langmuir* **2011,** 27, 5700-5704.

[4] Sclenoff, J.B.; Dubas, S.T. *Macromolecules* **2001**, 34, pp. 592-598.

[5] Spriujt, E.; Sprakel, J.; lemmers, M.; Cohen Stuart, M.A.; van der Gucht, J. *Phys. Rev. Lett.* **2010**, 105, 208301-4.

[6] Selin, V.; Ankner, J.F.; Sukhishvili, S.A. *Macromolecules* **2015**, 48, 3983-3990.

[7] Panchagnula, V.; Jeon, J.; Dobrynin, A.V. *Phys. Rev. Lett.* **2004**, 93, 037801-4.

[8] Patel, P.A.; Jeon, J.; Mather, P.T.; Dobrynin, A.V. *Langmuir* **2006**, 22, 9994-10002.

[9] Panchagnula, V.; Jeon, J.; Rusling, J.F.; Dobrynin, A.V. *Langmuir* **2005**, 21, 1118.

[10] Park, S.Y.; Rubner, M.F.; Mayes, A.M. *Langmuir* **2002**, 18, 9600-9604.

[11] Castelnovo, M.; Joanny, J.F. *Langmuir* **2000**, 16, 7524-7532.

[12] Wang, Q, *Soft Matter* **2009**, 5, 413-424.

[13] Shafir, A.; Andelman, D. *Eur. Phys. J. E.* **2006**, 19, 155-162.

[14] Borukhov, I.; Andelman, D.; Orland, H. *Macromolecules,* **1991**, 31, 1665-1671.

[15] Wang, Q. *Macromolecules* **2005**, 38, 8911-8922.

[16] Doi, M.; Onuki, A. *J. Phys. II. France* **1992**, 2, 1631-1656.

[17] Brochard, F.; Jouffroy, J.; Levinson, P. *Macromolecules* **1983**, 16, 1638-1641.

[18] Tree, D.R.; Delaney, K.T.; Ceniceros, H.D.; Iwama, T.; Fredrickson, G.H. *Soft Matter* **2017**, 13, 30133-3030.

[19] Bhave, A.V.; Armstrong, R.C.; Brown, R.A. *J. Chem. Phys.* **1991**, 95, 2988-3000.

[20] Yamamoto, M. *J. Phys. Soc. Japan* **1956**, 11, 413-421.

[21] Yamamoto, M. *J. Phys. Soc. Japan* **1957**, 12, 1148-1158.

[22] Yamamoto, M. *J. Phys. Soc. Japan* **1958**, 13, 1200-1211.

[23] Leibler, L.; Rubinstein, M.; Colby, R.H. *Macromolecules* **1991**, 24, 4701-4707.

[24] Larson, R.G., Constitutive Equations for Polymer Melts and Solutions, Butterworth Publishers, MA, **1988**.

[25] Sing, C.E. *Adv. Coll. Int. Sci.* **2017**, 239, 2-16.

[26] Onuki, A., Phase Transition Dynamics, Cambridge University Press, UK, **2002**.

[27] Drozdov, A.D.; de Claville Christiansen, J. *J. Chem. Phys.* **2015**, 142, 114904-18.

Chapter 6: Conclusions and Future Directions

6.1 Conclusions

6.1.1 Chapter 2

The physical chemistry of the PEs involved in the LbL process directly affects the strength and nature of interactions. Qualitatively, we have observed that secondary interactions, including hydrogen bonding, ion-dipole interactions and hydration of chains, can be considerably stronger than electrostatic interactions commonly believed to be the primary driving force for PE complexation. Tuning electrostatic interactions with KCl, we observed that salt alters PEM film growth kinetics and magnitude in a non-monotonic and rather "universal" fashion, at least for the three polyelectrolyte pairs studied here at pH 7, as seen in Figure 2-7. In the low salt regime, i.e. ~ 5-10% of the critical salt concentration, as well as in the high-salt regime within 40% of the critical point, there is slow and linear film growth while for KCl concentrations of around ~15-60% of the critical concentration, films grow fast and exponentially. We believe that this result reflects a trade-off between kinetic factors (diffusion coefficient) and thermodynamic ones, whose effects on film growth depend oppositely on salinity.

The type of polymer-rich phase formed upon complexation of oppositely charged PEs in bulk correlates only partially with growth kinetics of the LbL PEM films deposited from the same PEs at same concentrations, pH, and salinities. The lack of a one-to-one correspondence of precipitation and coacervation with linear and exponential growth cannot be attributed to deviation of composition of the PEM from that of the corresponding bulk mixtures, because we did not find appreciable changes in precipitation-to-coacervation transition with changes in mixing ratio. In general, however, coacervation in bulk signals high mobility of PEs in the bulk complex, which we expect to lead to correspondingly fast mutual diffusion during the build-up of PEM film. Conversely, bulk precipitation signals glassy dynamics in the bulk complex phase

and the chain diffusivity in the PEM film is expected to be correspondingly small. However, slower dynamics in PEM film growth can be caused not only by stronger interactions, leading to decreased diffusivity, but also by weaker interactions since this will produce a lower driving force for diffusion of the PEs into the PEM film. Therefore, conditions leading to precipitation provide a high thermodynamic driving force for diffusion but also slow down the diffusion by lowering the diffusivity while the converse is true for coacervation in bulk. In other words, there should be conditions intermediate between those leading to a rigid precipitate and those producing very soft coacervates, where diffusivity and thermodynamic driving force for complexation are both sufficiently high so as to produce relatively rapid migration of chains into the PEM film, resulting in exponentially growing films. At the other two extremes, slow, linear film growth kinetics prevails. Our results on the two systems are consistent with this picture, and for the systems studied here, the non-monotonicity in growth rate observed in all three systems at pH 7 can be collapsed onto a normalized "universal curve." It remains to be seen how broadly such behavior can be extended to other systems.

6.1.2 Chapter 3

Our experimentally-informed closed form free energy proposed here is shown to explain complex coacervation as a competition between three categories of association/dissociation equilibria, namely counterion condensation (CC), ion-pair formation (IP) and, for weakly dissociating polyelectrolytes (PEs), protonation or deprotonation. The strength of each of these phenomena is set by a corresponding standard free energy or equivalently an equilibrium constant defined at a reference state, taken to be the infinite dilution in water. The model presented here provides a tractable way to extend the (VO) model of coacervation by allowing for the effects of IP, CC and charge regulation, as well as van der Waals (VdW) interactions, long-range electrostatic interactions, captured by the Debye-Hückel (DH) free energy, and translational entropy of mixing. Our new theory incorporates the specificity of PE physico-chemistry and salt chemical identity, which are captured in parameters such as IP, CC, and ionization equilibrium constants, as well as the volumes of ions and monomers, Flory-Huggins interaction parameters, and composition-dependent dielectric constants. While we found a reasonable set of reference free energies to use in our model to capture the experimentally obtained binodal compositions of weak PAA/PDMAEMA systems, our model predictions

deviated from the experimental binodal diagram of the strong PSS/PDADMA system at low salt regime presumably due to the high hydrophobicity of this system which cannot be captured simply by using a constant FH χ parameter greater than 0.5. The main features and advantages of the proposed model are summarized as follows:

- Charge regulation of weak polyelectrolytes due to salt and oppositely charged PE as well as the pH drifts upon mixing of two oppositely charged PE solutions follow self-consistently from Le Châtelier's principle embedded in laws of mass action (LMA) describing protonation, CC and IP equilibria, both in mono and biphasic systems.
- The proposed model formalizes the counterion release (CR) picture of complex coacervation. While the critical salt concentration in the VO model is set solely by a competition between the translational entropy of simple counterions and long-ranged electrostatic fluctuation energy, the competition between IP and CC alone can predict complex coacervation and the presence of critical salt concentration in the present model, consistent with the CR picture. Nonetheless, long-ranged electrostatic interactions affect the critical salt concentration beyond which no coacervation occurs.
- As the propensity of counterions to condense increases at a fixed IP strength, or as IP strength is lowered for fixed CC equilibrium constants, the salt-polymer concentration binodal envelope shrinks. The strength of IP between the two ionized PE groups is found to have the most drastic effect on the binodal diagrams both for weak and strong PEs.

Thus, the inclusion of CC and IP in our model drastically changes the picture of coacervation relative to the mechanism considered by the VO-based model, in which the driving force is long-ranged electric field fluctuations. The ability of VO-based models to fit experimental phase behavior data reasonably well through adjustments in sizes of species and other parameters disguise its omission of ion pairing, which can be an equally important driver for coacervation, at least for some systems.

6.1.3 Chapter 4

The proposed model was shown to capture both Fickian and non-Fickian transport including anomalous and Case II API release profiles. Since ESM parameters can be obtained via molecular simulations, to establish a meaningful link between macroscopic and microscopic it is imperative to use ESM flux laws in analyses of experimental *in vitro* studies. Accurate

estimation of ESM API-excipient diffusivity using pseudo-binary flux laws without due consideration of API-water diffusional friction was shown to be impossible except in special cases. As a direct consequence of instantaneous thermodynamic equilibration at the interface as well as of incorporation of excipient stress into total free energy, the boundary conditions on water volume fraction and excipient stress evolve dynamically. Through the composition dependence of ESM diffusivities, the time-dependence of the boundary condition at the tablet-water interface was shown to have far-reaching implications for both water and API transport modes. Short relaxation times lead to higher levels of water in the tablet, further facilitating API and water transport. Anomalous and Case II API release are observed at intermediate relaxation times with Fickian release observed at either extreme. Excipient erosion at the tablet surface was also demonstrated to affect the API and water transport profoundly through an intricate interplay with stress relaxation. As erosion intensifies, diffusional transport through the tablet is adversely affected and the total API outflux at tablet-water interface and thus release rate is predominantly dictated by the excipient erosion rate.

Traditionally, order of magnitude analysis of two dimensionless numbers, namely Deborah number and swelling interface number defined as the ratio of swelling front velocity and API characteristic velocity in the swollen layer, given by the average API diffusivity in the swollen layer divided by the time-dependent swollen layer thickness, have been used as indicators of Fickian and non-Fickian transport. Given rheological material functions as well as relevant diffusivities, the diffusional Deborah number could be estimated. However, in our model the swelling front movement follows naturally from the rheological and diffusivity parameters and thus does not need to be considered as an independent degree of freedom. Since diffusion, relaxation and erosion are all integrated into the present model, it can be used even in systems with appreciable erosion to glean important details about transport modes of water and API, provided that the erosion velocity prefactor, k_{er} is available, which, unlike swelling front velocity, is a degree of freedom that must be specified a priori in our model.

6.1.4 Chapter 5

The constitutive equation for network of oppositely charged PEs undergoing solvent imbibition and network formation via ion pairing reaction was developed upon addition of reactive terms to the Smoluchowski equation describing the configuration probability distribution of non-reactive

network. The final equation at the first order in spatial gradients was identical to that derived in chapter 4 for non-reactive polymers undergoing solvent imbibition alone with the exception that the network modulus for the former case is controlled by ion pair reaction as well as solvent ingress.

Despite its dynamic nature, our model was shown to predict the right equilibrium behavior. PE adsorption was predicted in equilibrium limit. Higher molecular weights promote chain adsorption while non-local contributions to free energy suppress it. Our model reduces to the sequential equilibrium adsorption models of LbL assembly if LbL is assumed to be an irreversible process wherein all previously deposited chains are frozen during the subsequent steps and if dynamics is left out of our framework and RPA results for chain stiffness coefficients are used.

Instantaneous swelling of LbL assembled films in response to sudden change in surrounding medium, such as during rinsing steps was shown to be captured by our model. Equilibrium swelling structure of ultra-thin films of charged polymers was shown to be a delicate balance among mixing osmotic pressure (FH osmotic pressure), non-local (gradient) osmotic pressure, electrostatic (Maxwell) and elastic stresses present in the system. We showed that the non-local and electrostatic stresses that are typically left out of conventional models of equilibrium swelling in macroscopic systems cannot be in general ignored in LbL assembled films.

Using a mutual diffusivity between polyions independent of the molecular weight, the polycation diffusion driving force during rinsing of a rigid brush layer containing polycation chains was shown to significantly decrease with molecular weight. Electrostatic potential distribution opposes the out-diffusion of PEs during the rinsing step to such an extent that the outgoing PE is trapped kinetically inside the PEM for sufficiently high molecular weights. This prediction rationalizes the meta-stability of PEM. Time evolution of the electrostatic potential in the film cannot be ignored. As polyions invade the PEM, their charge alters the electrostatic potential significantly. During the dipping step, incoming polycation chains experience a highly negative electrostatic potential inside a polyanion brush layer at the beginning but this attractive driving forces diminishes as polycations saturate the polyanion layer and the system reaches the equilibrium at a time scale far shorter than that over which the same polycation chain can be washed off during a rinsing step. As a result, correct predictions of LbL growth rate requires self-

consistent solution of the Poisson equation (governing electrostatic potential) with mass conservation as well as constitutive equation of elastic stress and force balance equation that follows from instantaneous equilibration of simple salts and water.

6.2 Future Directions

1) The speculation that an interplay of opposing dynamic and thermodynamic effects is responsible for the observed non-monotonic and rather universal effect of salinity on LbL growth rate should be corroborated by direct measurements of interaction strength, as characterized by ion-pairing equilibrium constant, and dynamics of complex phases, chain diffusivity or the network relaxation time. Isothermal titration calorimetry and rheological tests can be used to achieve this end. Also, variation in molecular weights of polyelectrolytes should help determine possible scaling laws for molecular-weight dependence of phase behavior and PEM growth rate.

2) Chain connectivity effects in the long-ranged electrostatic free energy were largely neglected in chapter 3. Measurements of IP and CC energies through calorimetry, or indirectly through charge regulation effects measured through IR spectroscopy would help the validity envelope of counterion release picture of complex coacervation presented here. Accurate measurements of effective ionization extents in the coacervate can establish the exact contributions of long-ranged electrostatic versus IP and CC to driving force of complex coacervation. Our model can be improved and extended by allowing for composition and pH dependencies of the above parameters and their measurement through experiments and molecular simulations.

3) Future comparison with experiments of the binodal diagrams performed systematically predicted by the proposed model in chapter 3 in various systems, especially those of weakly dissociating polyelectrolytes, using the equilibrium reaction parameters obtained by direct measurement of molecular simulation will allow for a systematic evaluation of the model, which may warrant the use of composition-dependent free energies and FH χ parameters to capture subtle effects observed experimentally. Presently, binodal diagrams involving weak PEs are scarce as the concentrations of salt counterions and each PE needs be measured individually, for instance by florescent labeling and nucleic magnetic resonance (NMR) experiments.

4) ESM diffusivities, relaxation time, polymer modulus and erosion velocity are the main input parameters that need to be provided in the drug release model developed in chapter 4. However,

each of these parameters is a complicated function of composition. For instance, we took ESM diffusivities to only depend on the ratio of volume fraction of water and excipient. However, at least for certain API molecules, this might not be the case. Most of the literature on drug release focuses on API release profiles and/or polymer dissolution profiles. In order to pin down the input parameters and their composition dependence reliably, however, there is also a need for additional data sets such as tablet thickness evolution, instantaneous tablet water content. Future comparisons of our drug release model to such systematically obtained data will be helpful in assessing the accuracy of the assumptions in our model and their range of applicability.

5) In chapter 5, we derived the framework for modeling the LbL assembly. However, nonlinearities associated with the coupled set of Poisson equations, constitutive equation for elastic stress and the necessity for tracking the moving and diffuse interphase between the solution and the film need to be addressed in a future work. We demonstrated that freezing one of the polyions during rinsing or dipping step simulations reduces the computational complexity significantly. In order to extract the typical LbL growth profiles as a function of time, an efficient a numerical strategy for solving the nonlinear set of equations developed in chapter 5 simultaneously needs to be developed to be called at every time step during simulations given that a typical LbL experiment involves 10-100 depositions and rinse cycles. A similar boundary immobilization technique employed in chapter 4 can presumably be used to address the moving nature of the film-solution interphase but this requires that the computational domain extend into the solution. Therefore, a sharp interface and a jump condition could be considered especially if non-local contributions to free energy are not considered.

6) In chapter 5, we largely neglected the non-mean field effects due to severe nonlinearities they would introduce. This allowed us to fix the charge valency of PEs irrespective of composition and salinity. Once a numerical strategy for solving the LbL dynamic framework laid out in chapter 5 is devised, non-mean field effects such as charge regulation, counterion condensation, ion pairing, chain connectivity on LbL assembly could be added back into the framework. This could simply be achieved by including the relevant contributions of the free energy functional developed in chapter 3 in derivations of PE chemical potentials and osmotic pressure. Of course, inclusion of non-mean field effects will increase the non-linearity of the resulting set of equations dramatically.